Running the Gamut: From Structural Biology to HIV-1 Vaccine Design

Andrew John Borst

A dissertation

submitted in partial fulfillment of the

requirements for the degree of

Doctor of Philosophy

University of Washington

2019

Reading Committee:

David Veesler, Chair

Ning Zheng

W. Conrad Liles

Program Authorized to Offer Degree:

Department of Biochemistry

University of Washington

Abstract

Running the Gamut: From Structural Biology to HIV-1 Vaccine Design

Andrew John Borst

Chair of the Supervisory Committee:
David Veesler, Ph.D. Assistant Professor
Department of Biochemistry

Transmembrane proteins are major drug targets in bacteria, viruses, and humans. Utilizing a combination of single-particle electron microscopy, mass spectrometry, and numerous other biophysical and biochemical techniques, my thesis work has elucidated the structures and mechanisms of multiple membrane protein complexes. Specifically, the work encompassed by this dissertation focuses on uncovering the structure and mechanism of (i) a novel pathogenic bacterial ion channel, (ii) understanding the structural requirements and mode-of-action of a therapeutic antibody in complex with an angiogenic human integrin receptor, and (iii) determining the immune recognition pattern of the HIV viral spike glycoprotein for vaccine design purposes. This work aims to shed important structural and functional insights on membrane protein drug targets and their associated underlying diseases.

TABLE OF CONTENTS

LIST OF FIGURES

LIST OF TABLES

ACKNOWLEDGEMENTS

I would like to thank the following individuals for their contributions and support. Both of which allowed this thesis work to be possible.

Zachary M. James

Connor E Weidle

Matthew D Gray

Brandon Frenz

Joost Snijder

M Gordon Joyce

Ivelin S Georgiev

Guillaume BE Stewart-Jones

K. Rachael Parks

Yoni Haitin

Peter D Kwong

Andrew T McGuire

Priska D von Haller

Frank DiMaio

Mark Ginsberg

Marija Backovic

Felix A. Rey

Leonidas Stamatatos

Marie Pancera

Joel Quispe

William N. Zagotta

Rachel E. Klevit

David Veesler

DEDICATION

This body of work is hereby dedicated to my dear friend and former companion, Odin.

Without whom, I truly believe none of this would have been possible.

Odin Borst

(2009-2018)

"Your life was a gift. Your presence was a joy. Rest easy, big guy. You were my shining star."

Chapter 1. AN INTRODUCTION OF THREE PARTS

1.1 FORWARD

My experience as a graduate student at the University of Washington between the years of 2014 and 2019 emphasized the study of cryo-electron microscopy (CryoEM), glycoproteomics, protein structural heterogeneity, and the biophysical and immunological characterization of various antibody/antigen interactions. These structural data were typically supplemented with surface plasmon resonance, biolayer interferometry, and mass spectrometry data to help advance research across these diverse disciplines and biological systems.

Throughout my thesis, a common – albeit tenuous – connecting thread between each project pertained to the fact that all of these proteins were transmembrane complexes. Trans-membrane proteins are major drug targets in bacteria, viruses, and humans. Despite the enormous interest in generating therapeutic agents targeting these proteins by small molecules and protein biologics, drug design efforts are often stymied by a lack of structural and biophysical information on these complex macro-molecular machines. The recent advances in single-particle electron microscopy allowed me to visualize previously intractable membrane protein complexes to near-atomic resolution, and helped guide our understanding of numerous biochemical mechanisms and therapeutic modes-of-action. Specifically, my dissertation work focused on uncovering (i) the structures of pathogenic bacterial ion channels, (ii) understanding the structural requirements and mechanism-of-action of therapeutic protein biologics in complex with integrin receptors, and (iii) to determine the immune recognition pattern of a viral spike glycoprotein for vaccine design purposes..

The first project I completed as part of my dissertation involved the study of cyclic nucleotide-gated (CNG) ion channels (James and Borst et al., 2017). CNG and hyperpolarization-activated cyclic nucleotide-regulated (HCN) ion channels play crucial physiological roles in phototransduction, olfaction, and cardiac pace making (Craven and Zagotta, 2006). Although cyclic nucleotide binding has been shown to promote CNG and HCN channel opening, the precise mechanism underlying gating remains poorly understood. During my thesis, I used cryo-electron microscopy to determine the structure of an intact CNG channel isolated from the pathogenic bacterium, *Leptospira licerasiae*, revealing a conformation that may represent a functional state of this channel family not captured in previous studies (James and Borst et al., 2017).

The second portion of my training pertained to integrin membrane protein receptors and their interactions with therapeutic antibodies (Borst et al., 2017). The function-blocking LM609 antibody has been reported to specifically recognize αVβ3 integrin and to inhibit angiogenesis, bone resorption, and viral infections in an arginine-glycine-aspartate motif (RGD) independent manner (Charo et al., 1990; Rader et al., 1998; Wu et al., 1998). LM609 entered phase II clinical trials for the treatment of several cancers and was also successfully used for αVβ3-targeted radio-immunotherapy (Gutheil et al., 2000; Liu et al., 2011; Millard et al., 2011; Posey et al., 2001). The lack of structural information for this antibody has hindered the molecular understanding of its biochemical and therapeutic properties. By combining single-particle electron microscopy data with fluorescence size-exclusion chromatography, I demonstrated that the therapeutic properties of LM609 result from sterically hindering access of large ligands to the RGD binding pocket, without obstructing it (Borst et al., 2017). This work ultimately provided a structural framework

to expedite future efforts utilizing LM609 as a diagnostic or therapeutic tool for a variety of human diseases.

The last – and largest – portion of my dissertation heavily focused on the human immunodeficiency virus (HIV). HIV causes severe illness characterized by long incubation periods and a chronic and highly lethal final disease state known as acquired immunodeficiency syndrome. HIV infection primarily targets T-cells, causing the progressive deterioration of host immune system efficacy (Hazenberg et al., 2000). If left untreated, the mean survival time for an HIV-infected patient is approximately ten years, with mortality driven by infection of opportunistic pathogens and the onset of various malignant cancers (Patel et al., 2003). Using a combination of cryo-electron microscopy, x-ray crystallography, bio-layer interferometry, immuno-precipitation, and glycoproteomic mass spectrometry, I uncovered novel molecular determinants associated with the initial stages of immune system recognition of HIV (Borst et al., 2018). This work helped pave the way for a new avenue of epitope-based HIV vaccine design that, so far, had largely been overlooked.

Given the disparate nature of the work involved during my tenure as a graduate student (Borst et al., 2017, 2018; James and Borst et al., 2017), this introductory chapter has been hereafter divided into three major sections. Each section corresponds to one of the aforementioned biological systems I spent a significant amount of time studying and which led to at least one first author publication. The following introduction serves to provide general background knowledge for each of these systems and to outline the outstanding questions which drove the research forward at the time. Please enjoy.

1.2 Establishing a solid structural foundation: Solving an ion channel structure

My first project in graduate school focused on determining one of the first structures of an intact cyclic nucleotide-gated ion channel. In mammals, cyclic nucleotide-gated (CNG) and hyperpolarization-activated cyclic nucleotide- gated (HCN) ion channels play crucial roles in phototransduction, olfaction, cardiac pace-making, and neuronal signaling (Craven and Zagotta, 2006). CNG and HCN channels are potassium channels characterized by the presence of a carboxy-terminal cyclic nucleotide-binding domain (CNBD) that connects to the channel pore via a C-linker domain. Although previous electrophysiology studies have demonstrated that binding of cyclic nucleotides promotes channel opening (Wainger et al., 2001), the molecular mechanisms underlying CNG and HCN channel gating have thus far remained elusive due to a lack of high-resolution structural data. Full-length mammalian CNG channels have proven refractory to structural characterization due to insufficient expression levels, protein instability, and the pseudo-symmetry of the native heteromeric subunit assembly(Weitz et al., 2002; Zheng and Zagotta, 2004; Zheng et al., 2002; Zhong et al., 2002). Recently, a novel class of prokaryotic ion channels was identified which demonstrate remarkable sequence and structural similarity to mammalian CNG and HCN channels(Brams et al., 2014). Using a robust screening protocol spanning 20 prokaryotic channels, we found that the 214 kDa CNG channel orthologue LliK from the pathogenic bacteria *Leptospira licerasiae* was a promising candidate for structure determination by cryoEM. *L. licerasiae* is a spirochete known to infect humans and animals (Matthias et al., 2008), is classified as a reemerging pathogen by the National Institute of Allergy and Infectious Disease, and is a major causative agent of leptospirosis (Costa et al., 2015; Matthias et al., 2008). Despite its relatively large impact on global health (leptospirosis leads to nearly 60,000 annual deaths

worldwide (Costa et al., 2015)), leptospiral pathobiology still remains largely enigmatic. Finally, while a great deal is known regarding the biology of mammalian CNG and HCN channels and their involvement in neuronal signaling, the roles these ion channels play in bacteria remain poorly understood.

In order to elucidate the mechanisms of CNG and HCN channel gating, I utilized cryo-electron microscopy (cryoEM) to determine the structure of the LliK prokaryotic CNG channel – in the presence of cAMP – to near-atomic resolution. We uncovered a novel CNG channel structural conformation associated with gating. This ultimately provided a framework for understanding how CNG and HCN channels regulate vision, olfaction, cardiac pace-making, and neuronal signaling in mammals. Specifically, this work provided insights regarding how binding of cyclic nucleotides is coupled to potential allosteric rearrangements in the CNBD and the connected C-linker that regulate cationic flux. Completion of this work opened new avenues of biochemical research pertaining to the structural and functional characterization of bacterial ion channels.

Prokaryotic ion channels have long been used as model systems to gain fundamental insights into the structural and functional basis of neuronal signaling in mammals and humans (Martinac et al., 2008). In mammals, CNG and HCN channels are cation-permeable and are regulated by the direct binding of cyclic nucleotides (cAMP or cGMP) to the channel cytoplasmic C-terminus (Craven and Zagotta, 2006). CNG channels are present in retinal rod photoreceptors and olfactory sensory neurons, where they perform chemo-electrical energy conversion in response to light or odor stimuli, respectively (Biel and Michalakis, 2007; Fesenko et al., 1985;

Nakamura and Gold, 1987). In rod photoreceptors, absorption of light by rhodopsin is coupled to the rapid conversion of cGMP to GMP, inducing closure of CNG channels which eventually results in promotion of action potentials in the optic nerve (Biel and Michalakis, 2007; Fesenko et al., 1985). Conversely, nervous impulses in olfaction are stimulated by elevated levels of cAMP in response to binding of odorants to membrane receptors (Biel and Michalakis, 2007; Nakamura and Gold, 1987).

Given their function, mutations in human CNG channels have been associated with numerous inherited retinal degenerative disorders, achromatopsia, and anosmia (Milanesi et al., 2006). HCN channels are found in the cardiac sinoatrial node and throughout the nervous system, where they open in response to membrane hyperpolarization and generate a depolarizing current responsible for rhythmic firing (Baruscotti et al., 2005; Bucchi et al., 2012). In the heart, the activity of HCN channels is responsible for generation of the 'funny current' – a sodium-potassium current that is activated during the diastolic phase of heartbeat when hyperpolarization voltages enter a range between -70 mV and -40 mV (Milanesi et al., 2006). Cyclic nucleotide binding to HCN channels shifts this voltage dependence of activation to more depolarized potentials, increasing the rate of channel opening (Milanesi et al., 2006). Indeed, mouse model knockouts of specific HCN channels results in bradycardia, sino-atrial pausing, supraventricular and ventricular tachycardia, and significant deficits in neuronal processes and spatial memory (Baruscotti et al., 2005). In humans, HCN channel mutations and mistrafficking have been associated with several disorders, including numerous cardiac defects, epilepsy, and even autism (Baruscotti et al., 2005). CNG and HCN channels are part of a larger family that includes KCNH potassium channels. KCNH channels are distinct in that they possess a cyclic nucleotide-binding homology domain

(CNBHD) occupied by an “intrinsic ligand”, and are not directly regulated by cyclic nucleotides (Brelidze et al., 2012; Marques-Carvalho et al., 2012; Yi et al., 2016).

All members of this channel superfamily are assembled from four subunits, each comprising 6 transmembrane (TM) helices (S1-S6) that form a tetrameric assembly around a central pore (Craven and Zagotta, 2006). The S1-S4 helices are located at the periphery of the TM domain and termed as ‘voltage-sensors’ due to the ability of HCN and KCNH channels to sense and respond to the membrane potential (Craven and Zagotta, 2006). The S4 helix of voltage-sensitive channels contains several positively-charged amino acid residues that interact with a ‘charge-transfer center’ (CTC) embedded in the voltage-sensor domain (VSD) helix-bundle (Craven and Zagotta, 2006; Horn, 2004). This bundle contains alternating hydrophobic and negatively-charged residues positioned towards the polar center of this domain (Horn, 2004). While many models have been proposed regarding the mechanism of S4 voltage-sensing, all hypotheses share the common prediction that the S4 helix is able to slide down through the membrane through some unknown mechanism in response to changes in the membrane potential (Horn, 2004). This translation thus repositions the positively charged residues of the S4 helix within the CTC during activation (Horn, 2004). This, in turn, can induce the allosteric opening of the channel pore via covalent coordination between a long S4-S5 helix and the domain-swapped pore domain (Catterall, 2010; Fowler and Sansom, 2013). However, despite the availability of ion channel open-pore crystal structures (K_v 1.2-2.1) (Long et al., 2005) and numerous closed-pore structures of other channel family members (Kowal et al., 2014; Whicher and MacKinnon, 2016), all VSD segments at the time this study was undertaken only showed the S4 helix adopting in the predicted depolarized conformation, irrespective of the conformational state of the pore itself.

Coupled with biochemical and electrophysiological studies, these observations give credence to a proposed modular gating scheme whereby channel gating is believed to act as a series of coupled rearrangements and equilibria shifts within distinct modules of the channel (Craven and Zagotta, 2004). In this model, activation of the voltage sensors would shift the equilibrium of the pore to favor the open state. Alternatively, binding of cyclic nucleotides would shift the equilibrium of the CNBDs to the 'active' state, allowing for a concerted and cooperative change of the connected C-linker domain. If the system energetics are sufficient in this configuration, the pore will be driven more towards favoring the open conformation.

The CNG and HCN channel pore is comprised of helices S5-S6 and resides along the central axis of the channel tetramer (Craven and Zagotta, 2006). In potassium channels, specificity for K^+ is mediated through a 'selectivity filter' positioned near the top of the channel pore (Doyle et al., 1998), denoted as the P-loop, that contains a highly conserved TVGYG sequence motif. The inter-subunit distance and orientation of the TVGYG carbonyl groups are such that they can geometrically and chemically mimic the hydration shell of K^+ ions and allow their selective desolvation as they go through the selectivity filter. In contrast, a Na^+ ion would be too small to allow for energetically favorable contacts to form, thereby explaining the high selectivity of these channels for K^+ over Na^+.

The S6 pore helix extends through the plasma membrane and is predicted to undergo a large conformational change following gating-mediated activation (Doyle et al., 1998; Taraska et al., 2009). Given the van der Waals radius of a fully-solvated K^+ is approximately 3 Å, it is believed

that an 'active' S6 helix must adopt a pore radius approaching or exceeding 3 Å in order to allow the energetics of traversal to agree with the rapid measured ionic flux of 10^6 K^+ ions•$second^{-1}$. Indeed, the structure of the closed and open pore conformations of the KcsA (Doyle et al., 1998) and MthK (Jiang et al., 2002) channels, respectively, reveals widening of the pore relative to the closed state. This hypothesis is further corroborated by the more recent open-state structure of K_v 1.2-2.1 (Long et al., 2005) and the closed-state structures of rat Eag1 (Whicher and MacKinnon, 2016) and prokaryotic MloK (Kowal et al., 2014).

Gating of the pore in CNG and HCNs channels is modulated by the binding of cyclic nucleotides to the cyclic nucleotide-binding domain (CNBDs) located on the cytosolic C-terminus(Craven and Zagotta, 2006; Jiang et al., 2002; Wainger et al., 2001; Zagotta et al., 2003; Zheng et al., 2002). The CNBD fold is highly similar to that of other cyclic-nucleotide binding domains in mammals, including protein kinase A (PKA) and catabolite activator proteins (CAP) (Zagotta et al., 2003). Following binding of either cAMP or cGMP to the human HCN2 CNBDs, large-scale tertiary rearrangements, involving stabilization of an interaction between a C-terminal C-helix and the newly docked ligand have been observed, by comparing apo and ligand-bound structures obtained by NMR and X-ray crystallography (Lolicato et al., 2011; Saponaro et al., 2014; Zagotta et al., 2003).

Connection of the TM helices to the CNBDs occurs through a C-linker domain positioned underneath the plasma membrane (Craven and Zagotta, 2006; Zheng et al., 2002). Upon cyclic nucleotide binding, tertiary changes in the CNBDs and C-linker are result in tetramerization of CNBD/C-linker fragments (Lolicato et al., 2011; Ng et al., 2016; Zagotta et al., 2003).

Crystallization of the HCN2 channel CNBD and C-linker revealed that the C-linker is the primary site facilitating these contacts (Zagotta et al., 2003), which arise through an interface formed from an antiparallel helix-turn-helix motif of the first two C-linker helices, A' and B', of one subunit making contact with the adjacent C' and D' helices of the neighboring subunit (Zagotta et al., 2003). This interaction is referred as an 'elbow-on-shoulder' interaction due to its similarity to an 'elbow' of one neighbor resting on the 'shoulder' of another.

Despite tetramerization of the CNBDs and C-linker being likened to channel activation, binding of cyclic nucleotide antagonists to human HCN2 also results in the quaternary assembly of these subunits (Zagotta et al., 2003). Indeed, all solved crystal structures of CNG/HCN CNBDs/C-linker constructs at the time adopted a similar quaternary arrangement, regardless of whether bound to an agonist or antagonist cyclic nucleotide. The structure of the cyclic nucleotide-bound state of the HCN2 CNBDs/C-linker further revealed the presence of a highly conserved salt bridge stabilizing the compact quaternary organization of this region (Craven and Zagotta, 2004). Mutagenesis and cross-linking experiments unexpectedly revealed large rearrangements must occur in this region during gating relative to what was expected based on crystal structures (Craven and Zagotta, 2004, 2006; Zagotta et al., 2003). Specifically, disruption of this salt-bridge triad through 'charge swapping' resulted in an increase in the channel opening probability, a result that largely contradicted the hypothesis that the crystal structures of these domains represented the 'active' state (Craven and Zagotta, 2004). Instead, it thus became predicted that the contacts between the C-linker and the CNBDs must be weakened during activation structures (Craven and Zagotta, 2004, 2006; Zagotta et al., 2003).

Indeed, notwithstanding the vast amount of biochemical, biophysical, and structural data that currently exists for CNG and HCN channels, it was clear that there were a number of seemingly paradoxical experimental results requiring reconciliation in order to fully understand the mechanisms underlying channel gating. In particular, the lack of structural information pertaining to full-length CNG channels left many of the fundamental aspects of these gating mechanisms enigmatic. This included the aforementioned CNG/HCN cyclic nucleotide-bound crystal structures and the observation that disruption of a salt-bridge-triad destabilizes this quaternary organization and promotes channel activation (Craven and Zagotta, 2004). However, full-length mammalian CNG channels had historically been proven refractory to structural characterization due to insufficient expression, protein instability, and the pseudo-symmetry of the native heteromeric subunit assembly.

In 2014, a class of prokaryotic channels with remarkable sequence similarity to mammalian CNG and HCN channels was identified (Brams et al., 2014). Unlike mammalian ion channels, prokaryotic CNG channels are largely homo-tetramers and undergo minimal post-translational modifications following expression (Brams et al., 2014). In an attempt to elucidate the gating mechanisms of this medically important ion channel family, I set out to identify a prokaryotic CNG potassium channel homolog suitable for high-resolution structural studies. Furthermore, the identification of prokaryotic CNG channels represented a unique opportunity to further our knowledge of the physiological roles they perform in bacteria. I used cryoEM, a rapidly advancing technique largely bypassing the limitations of X-ray crystallography and NMR, to provide a structural framework for understanding the molecular mechanisms associated with CNG and HCN channel gating. CryoEM recently underwent a “resolution revolution” with the advent of direct-

electron detectors (Wu et al., 2016), improved computational algorithms (Li et al., 2013), and the development of automated data-collection protocols (Stagg et al., 2006). Taken together, these technical advancements have enabled high-resolution structural studies of small membrane proteins that have previously proven refractory to traditional techniques (Bai et al., 2015; Liao et al., 2013). I took advantage of these methodological advancements in order to successfully solve the structure of an activated prokaryotic CNG channel. This project marked as my first major success in graduate school, allowing me to publish one of the very first full length CNG channel structures (James and Borst et al., 2017). Moving beyond this work, I began to focus on questions pertaining to human immune system recognition of epitopes. This transition allowed me to develop skills necessary for testing hypotheses derived from structural observations made during my tenure as a graduate student.

1.3 Branching into immunobiology: Understanding an emerging cancer therapy

Following my work on ion channels (James and Borst et al., 2017), I began to diversify my training to more heavily incorporate protein biochemistry and biophysics. The biological system I chose for this transition focused on integrin membrane proteins. Integrins are heterodimeric cell-surface receptors mediating bidirectional signaling across the plasma membrane. They are assembled from non-covalently associated α and β subunits and are involved in the physiological processes of cellular adhesion, migration, growth, immunity, and differentiation (Shimaoka and Springer, 2003). Regulation of integrin activity occurs through large-scale conformational changes following ligand-binding to either the cytoplasmic or extracellular domains of the integrin heterodimer. Integrin activation entails transition from a bent, low-activity conformation, to an extended state with a significantly increased affinity for extracellular ligands (Campbell and Humphries, 2011; Ye et al., 2010). Among all integrins, $\alpha_V\beta_3$ has been highly studied for its roles in arthritis, thrombosis, and inflammation, as well as its localized expression to neovasculature and aggressive cancerous tumors (Xiong et al., 2002, 2001). In addition, many viruses have been reported to use $\alpha_V\beta_3$ integrin as a receptor or co-receptor for cellular attachment and subsequent entry (Stewart and Nemerow, 2007; Veesler et al., 2014).

Given its biomedical significance, $\alpha_V\beta_3$ has emerged as a promising therapeutic target for several human diseases (Danhier et al., 2012; Gutheil et al., 2000). Recent efforts in drug development have targeted the $\alpha_V\beta_3$ Arg-Gly-Asp (RGD) binding pocket formed at the interface between the β-propeller of the α_V subunit and the βI domain of the β_3 subunit within the integrin headpiece (Xiong et al., 2002). $\alpha_V\beta_3$ recognition of RGD-containing ligands, such as vitronectin,

fibronectin, and fibrinogen, results in rapid integrin clustering leading to platelet activation, increased bone resorption, elevated immune response, and neovascularization (Koo et al., 2002). Synthetic RGD-peptide-based strategies have yielded molecules with high affinity for the integrin RGD-binding pocket, but generally lacking integrin specificity. Since the RGD motif is recognized by nearly half of all 24 known integrin receptor types, non-specific pharmacologic recognition of numerous integrins can lead to unintended side effects.

Therapeutic antibodies provide a promising alternative, and account for most integrin-targeting drugs currently under clinical evaluation. In addition to their high specificity, therapeutic antibodies are advantageous due to their low immunogenicity and longer half-life in circulating blood relative to many small molecules and peptides (Millard et al., 2011). However, many antibodies currently used in pre-clinical and clinical trials independently target either the integrin α or β subunit, leading to recognition of any integrin heterodimer containing the target subunit (Frelinger et al., 1991). Of notable exception is LM609, a monoclonal murine antibody specific for integrin $\alpha_V\beta_3$ (Wu et al., 1998). Preclinical studies have shown that LM609 inhibits angiogenesis, bone resorption, and viral pathogenesis both *in vitro* and *in vivo* (Garrigues et al., 2008; Gavrilovskaya et al., 1998, 1999; Gramoun et al., 2007; Posey et al., 2001; Triantafilou et al., 2000). A fully humanized variant of LM609, MED-523 (Vitaxin), entered Phase I clinical trials for the treatment of cancers. Results of these trials reported no significant toxicity at any dose level (Gutheil et al., 2000). Phase II clinical trials for the treatment of colorectal cancer showed disease stabilization in 7 out of 14 patients with one patient experiencing partial regression (Gutheil et al., 2000). The second generation of Vitaxin, known as etaracizumab (Abegrin), demonstrated increased binding affinity to $\alpha_V\beta_3$ with a significant reduction in brain tumor size following $\alpha_V\beta_3$-

targeted radio-immunotherapy (Veeravagu et al., 2008). Further studies demonstrated etaracizumab can act as an effective agent for $\alpha_V\beta_3$-positive tumor-imaging (Liu et al., 2011). Etaracizumab has since entered Phase II clinical trials for the treatment of lymphoma, melanoma, renal, small intestine, and colorectal cancers, but the results of many of these trials currently remain unreported.

We sought to elucidate the molecular determinants associated with LM609 function and its mechanism of action. To this end, we determined the structure of the LM609 antigen-binding fragment (Fab) using X-ray crystallography and characterized its binding kinetics to human $\alpha_V\beta_3$ integrin. Single particle electron microscopy allowed for structural characterization of the complex formed between the Fab LM609 and the $\alpha_V\beta_3$ integrin ectodomain. Our results indicate LM609 binds with high-affinity to the apex of the integrin headpiece near but without obstructing the RGD-binding site, as confirmed by fluorescence size-exclusion chromatography. Comparison with a crystal structure of the $\alpha_V\beta_3$/fibronectin complex suggested that LM609 prevents binding of RGD-containing ligands via steric hindrance which explains the reported inhibition of angiogenesis and bone resorption mediated by this antibody in preclinical and clinical studies. This work marked my second major success in graduate school (Borst et al., 2017), and allowed me to gain a cursory understanding of the human immune system. In combination with my structural studies of ion channels (James and Borst et al., 2017), this project (Borst et al., 2017) provided me with the knowledge and skills necessary to tackle the largest aspect of my dissertation work: the development of a new HIV-1 vaccine design strategy.

1.4 TACKLING THE BEAST: DEVELOPING A NOVEL VACCINE DESIGN METHOD FOR HIV-1

Shortly upon completion of my work on integrins (Borst et al., 2017), I began to focus my efforts on a longstanding area of scientific interest: the human immunodeficiency virus. In particular, I aimed to combine structural biology, biochemistry, and biophysics to develop a new strategy for HIV-1 vaccine design against the HIV-1 envelope (Env) glycoprotein. Env is a class-I fusion protein responsible for host attachment and fusion of the viral and cellular membranes(Dalgleish et al., 1984). Following expression, Env trimerizes and undergoes furin-mediated cleavage to yield non-covalent gp120-gp41 pre-fusion trimers anchored in the viral membrane(Haim et al., 2013). As the sole target of neutralizing antibodies, Env is the focus of intense interest for current vaccine design initiatives. However, HIV-1 Env relies on multiple mechanisms of immune evasion – including dense glycosylation, sequence variation, conformational masking, and presentation of decoy epitopes(Burton and Mascola, 2015; Cuevas et al., 2015; Jardine et al., 2015; Kwong et al., 2002; Wei et al., 2003; Zhou et al., 2017). For these reasons, development of an Env-based vaccine capable of eliciting broadly neutralizing antibodies (bnAbs) has proven challenging.

The VRC01 class of bnAbs is of particular interest for HIV-1 vaccine development due to the exceptional potency and breadth of several of its well-characterized members(Huang et al., 2016; Zhou et al., 2015). These bnAbs derive from the VH1-2 variable heavy chain gene (Wu et al., 2011)(Scheid et al., 2011), have been isolated from multiple HIV-1-infected patients(Zhou et al., 2013), and putative non-mutated precursors have been identified in naïve individuals(Jardine et al., 2016). VRC01-class bnAbs are characterized by an unusually short five amino-acid light

chain complementary-determining region (CDR) L3 loop(Zhou et al., 2015) and a much higher-level of somatic hyper-mutations than antibodies targeting other pathogens(Wu et al., 2015). They bind the CD4-binding site ($CD4_{BS}$) in a way reminiscent of the interactions formed with the viral receptor CD4, making extensive CDRH2-mediated contacts while also exhibiting multiple amino acid alterations in the CDRL1 loop relative to germline precursors(Wu et al., 2015; Zhou et al., 2013). Although N-linked glycosylation sites (NLGSs) that surround the $CD4_{BS}$ sterically limit recognition by bnAbs(Zhou et al., 2017), particularly those present at position Asn276 in Loop D and along the V5 loop, mature VRC01 bnAbs overcome this barrier and potently neutralize numerous HIV-1 viral clades(Zhou et al., 2017) (Huang et al., 2016; Stewart-Jones et al., 2016; Wu et al., 2015). In contrast, the inferred germline precursors of VRC01-class bnAbs lack detectable binding to trimeric Env constructs harboring glycans at these locations(Jardine et al., 2013; McGuire et al., 2013, 2016; Medina-Ramirez et al., 2017; Stamatatos et al., 2017).

Whereas most recombinant trimeric Env antigens do not bind germline precursors of VRC01-class bnAbs, a few recently designed constructs have been shown to bind and activate this specific class of B cell receptors (BCRs)(Jardine et al., 2013; McGuire et al., 2013, 2016; Medina-Ramírez et al., 2017). We previously engineered a trimeric HIV-1 Env protein able to bind most VRC01-class precursors(McGuire et al., 2013). This construct was a trimeric gp140 protein derived from the clade C 426c virus and lacked variable loops 1, 2, and 3 along with the putative NLGSs at positions Asn276 (loop D) as well as Asn460 and Asn463 (V5 loop) (McGuire et al., 2016). Other constructs have also been engineered to engage the inferred precursors of VRC01-class bnAbs, all of which harbored mutations eliminating the NLGSs in loop D (at position Asn276) and in the V5 loop(Briney et al., 2016; Jardine et al., 2013; McGuire et al., 2013, 2016;

Medina-Ramírez et al., 2017; Tian et al., 2016). Additionally, a gp120 core derived from the 01dG5 clade virus, which naturally lacks a glycan at position Asn276, was also shown to engage the inferred germline precursor of the VRC01 antibody ($VRC01_{GL}$)(Wu et al., 2015). Although such glycan-depleted 'germline-targeting' immunogens activate B cells expressing germline VRC01-class BCRs *in vivo*(Briney et al., 2016; Dosenovic et al., 2015; Tian et al., 2016), they largely fail to elicit mature antibodies capable of bypassing the restrictions imposed by the glycan at position Asn276(Zhou et al., 2017). However, a recent study demonstrated the successful elicitation of $CD4_{BS}$-targeted antibodies, distinct from the VRC01 lineage, upon immunization of rabbits with an engineered clade C Env trimer(Dubrovskaya et al., 2017).

To better understand the potential avenues of elicitation of VRC01-class bnAbs, we first structurally characterized complexes between $VRC01_{GL}$ and two clade C Env constructs using a combination of cryo-electron microscopy (cryoEM) and X-ray crystallography. One of the constructs is a soluble trimeric 426c SOSIP with three NLGSs removed at positions Asn276, Asn460, and Asn463 based on our prior work (McGuire et al., 2013, 2016). The second construct is a monomeric 426c core containing all wild-type NLGSs (including those at positions Asn276, Asn460, and Asn463), but lacks variable loops 1, 2, and 3. The 426c strain naturally lacks NLGSs surrounding the $CD4_{BS}$ at positions Asn234 and Asn362(363), which are present in other clades. Our structural analysis revealed that the absence of these glycans leads to a reduction of local oligosaccharide density in the vicinity of the NLGS at position Asn276. Integrating this data with biolayer interferometry (BLI) assays and glycoproteomics, we demonstrate here that $VRC01_{GL}$ could bind to a 426c core construct in the presence of all naturally occurring NLGSs surrounding the $CD4_{BS,}$ including at position Asn276 and its associated glycan. We also show the affinity of

$VRC01_{GL}$ for the 426c core could be modulated by altering protein expression conditions to enrich for longer glycans, and also by shortening glycans via endoglycosidase treatment. These results suggested that priming of VRC01-class or other $CD4_{BS}$-targeting bnAbs may be possible using an HIV-1 gp120 derivative containing a glycan at position Asn276. Consequently, epitope-based vaccine design strategies utilizing a WT 426c core preserving all NLGSs quickly became a promising route for guiding elicitation of bnAbs targeting the $CD4_{BS}$ of HIV-1.

Similar to VRC01-class antibodies, bnAbs of the IOMA, 12A21, and VRC-PG20 lineages are a few other examples of $CD4_{BS}$-targeting bnAbs that have been isolated from infected patients, but have yet to be efficiently re-elicited through vaccination (Briney et al., 2016; Dosenovic et al., 2015; Dubrovskaya et al., 2017) (Jardine et al., 2016; Zhou et al., 2017). All of these mature $CD4_{BS}$-directed bnAbs effectively accommodate N-linked oligosaccharides within and near their epitopes, whereas their germline precursors largely fail to do so (Jardine et al., 2013; McGuire et al., 2013, 2016; Medina-Ramirez et al., 2017; Scharf et al., 2016; Stamatatos et al., 2017). This is, again, especially true for glycan N276, which represents a major steric barrier dampening interactions with many $CD4_{BS}$-targeting bnAb germline precursors (Borst et al., 2018; Jardine et al., 2013; McGuire et al., 2013, 2016; Medina-Ramirez et al., 2017; Scharf et al., 2016; Stamatatos et al., 2017). Although mutagenic removal of oligosaccharides in the vicinity of the $CD4_{BS}$ is widely used to promote immunogen recognition by all of these germline antibodies (Jardine et al., 2013; McGuire et al., 2013, 2014, 2016; Scharf et al., 2016)(Medina-Ramirez et al., 2017), this strategy seldomly results in elicitation of antibodies capable of robustly accommodating the reintroduced glycans for any of these lineages (Dubrovskaya et al., 2017) (Zhou et al., 2017). Indeed, the lack of a selective pressure in the absence of glycans near the $CD4_{BS}$ during the early

stages of immunization may explain some of the shortcomings guiding production of $CD4_{BS}$-directed bNAbs (Umotoy et al., 2019).

Following our discovery that $VRC01_{GL}$ binding could occur in the presence of a shortened glycan shield, we set out to investigate whether short ($GlcNAc_2Man_5$) oligosaccharides could promote recognition of a spectrum of germline antibodies recognizing the $CD4_{BS}$ and to explore if selective trimming of glycans to $GlcNAc_1$ near the $CD4_{BS}$ would enhance these interactions *in vitro* and *in vivo.* We developed a limited EndoH treatment method which allows tailoring the WT 426c core glycan shield to specifically enrich for $GlcNAc_1$ around the $CD4_{BS}$ while retaining the integrity of the high-mannose patch (a distinct supersite targeted by glycan-dependent bNAbs). We demonstrate that WT 426c core immunogens enriched for either $GlcNAc_2Man_5$ or $GlcNAc_1$ oligosaccharides both bound multiple inferred germline precursors of $CD4_{BS}$-directed bnAbs. We show immunization of $VRC01_{GL}$ heavy chain knock-in mice with these immunogens elicited $CD4_{BS}$-directed antibodies, with EndoH treatment significantly enhancing the speed of $CD4_{BS}$-targeting antibody production. These results support the logic of my rational design strategy and corroborate our accompanying *in vitro* data. Furthermore, the elicited polyclonal responses appeared to recognize the WT 426c core with mild glycan-dependency. This capstone section of my thesis ultimately outlines two immunogen production approaches yielding antibodies directed against the HIV-1 $CD4_{BS}$ upon immunization. Most importantly, this work lays the groundwork for an alternative HIV-1 vaccine design strategy allowing for retention of epitope-associated glycans during immunogenic priming.

Chapter 2. DETERMINING THE STRUCTURE OF A CYCLIC NUCLEOTIDE-GATED ION CHANNEL

2.1 CHAPTER SUMMARY

This chapter outlines the results of my first major project in graduation school. Namely, how we went about solving one of the first full-length structures of a cyclic nucleotide-gated ion channel. Cyclic nucleotide-gated (CNG) and hyperpolarization-activated cyclic nucleotide-gated (HCN) ion channels play crucial physiological roles in phototransduction, olfaction, and cardiac pace making. These channels are characterized by the presence of a carboxy-terminal cyclic nucleotide-binding domain (CNBD) that connects to the channel pore via a C-linker domain. Although cyclic nucleotide binding has been shown to promote CNG and HCN channel opening, the precise mechanism underlying gating remains poorly understood. Here we used cryo-electron microscopy (cryoEM) to determine the structure of the intact LliK cyclic nucleotide-gated channel isolated from *Leptospira licerasiae* – which shares a large sequence similarity to eukaryotic CNG and HCN channels – in the presence of a saturating concentration of cyclic AMP. A short S4-S5 linker connects nearby voltage-sensing and pore domains to produce a non-domain-swapped transmembrane architecture, which appears to be a hallmark of this channel family. We also observe major conformational changes of the LliK C-linkers and CNBDs relative to the crystal structures of isolated C-linker/CNBD fragments and the cryoEM structures of related CNG, HCN, and KCNH channels. The novel conformation of our LliK structure may represent a functional state of this channel family not captured in previous studies.

CNG and HCN channels are cation-permeable ion channels regulated by the direct binding of cyclic nucleotides (cAMP or cGMP)(Craven and Zagotta, 2006). CNG channels are present in

retinal photoreceptors and olfactory sensory neurons, where they perform chemo-electrical energy conversion in response to light or odor stimuli, respectively. Mutations in CNG channels have been associated with numerous inherited retinal degenerative disorders, achromatopsia, and anosmia(Biel and Michalakis, 2007). HCN channels are found in the cardiac sinoatrial node and throughout the nervous system, where they open in response to membrane hyperpolarization and generate a depolarizing current responsible for rhythmic firing(Craven and Zagotta, 2006). HCN channel mutations and mistrafficking have been associated with several disorders, including sinus bradycardia, epilepsy, and autism(Milanesi et al., 2006; Yi et al., 2016).

CNG and HCN channels possess a cyclic nucleotide-binding domain (CNBD) in their carboxy-terminal region and binding of cyclic nucleotide produces a large increase in the open probability of the channel pore. Cyclic nucleotide binding to HCN channels also shifts the voltage dependence of activation to more depolarized potentials, increasing the rate and extent of channel opening(Wainger et al., 2001). CNG and HCN channels are part of a family that includes KCNH potassium channels (Fig. 1a, Supplementary Figure 1). KCNH channels, however, are distinct in that they possess a cyclic nucleotide-binding homology domain (CNBHD) occupied by an "intrinsic ligand", and are not directly regulated by cyclic nucleotides(Brelidze et al., 2009, 2012; Marques-Carvalho et al., 2012).

CNG and HCN channels also harbor a C-linker domain situated between the pore and the CNBD. Based on its position along with mutagenesis and cross-linking studies, this domain is thought to transduce cyclic nucleotide binding into opening of the channel pore (Craven and Zagotta, 2004, 2006; Craven et al., 2008; Gordon and Zagotta, 1995). However, recent cryoEM

structures of apo and cAMP-bound HCN1 channel exhibit similar C-linker architectures, which resemble those observed in the crystal structures of isolated HCN C-linker/CNBD fragments (Lee and MacKinnon, 2017; Xu et al., 2010; Zagotta et al., 2003). Conversely, the recently reported open-pore cryoEM structure of a CNG channel from *C. elegans*, TAX4 (Li et al., 2017), shows a pronounced translation and rotation of the C-linker, relative to the pore domain, compared to both HCN1 structures. Despite this new structural information on CNG and HCN channels, the nature of the structural rearrangements in the C-linker/CNBD associated with channel activation remain unclear. Here, we report the structure of an intact prokaryotic CNG channel with a conformation of the C-linker/CNBD not seen in previous crystal or cryoEM structures.

2.2 IDENTIFICATION AND CHARACTERIZATION OF A FUNCTIONAL PROKARYOTIC CNG CHANNEL

Prokaryotic ion channels have historically been employed as model systems to gain fundamental insights into the structural and functional basis of neuronal signaling in mammals. To investigate the gating mechanism of the cyclic nucleotide-regulated ion channel family, we began by identifying a biochemically stable prokaryotic CNG channel variant. By utilizing a robust screening protocol implementing fluorescence-detection size-exclusion chromatography (Kawate and Gouaux, 2006), thermostability assays (Hattori et al., 2012), and negative stain EM, we found that LliK, a 214 kDa CNG channel orthologue from the pathogenic bacteria *Leptospira licerasiae,* was a promising candidate for structure determination by cryoEM **(Fig. 2.1A, Fig. 2.2, and Fig. 2.3)**. Liposome flux assays of reconstituted LliK demonstrated a robust cAMP-activated K^+ current, with an apparent affinity for cAMP of 2.4 μM, and a non-negligible channel opening probability in the absence of cyclic nucleotide **(Fig. 2.1B-C and Fig. 2.4**). These measurements confirmed the functionality of purified LliK and its permeability to K^+, as suggested by the presence of a TVGYG signature sequence responsible for the formation of the canonical potassium channel selectivity filter (Doyle et al., 1998) **(Fig. 2.2)**.

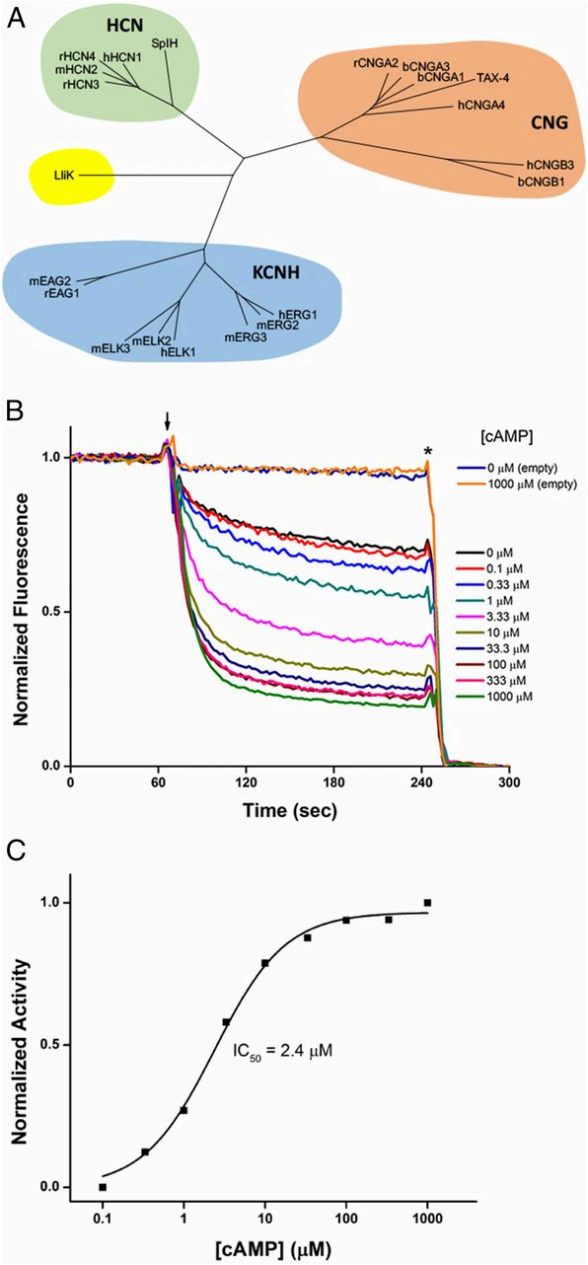

Figure 2.1. Functional characterization of the cyclic nucleotide-gated ion channel LliK. (A) Dendrogram of the CNG, HCN, and KCNH ion channel family. The position of LliK is indicated. (B) Liposome flux assay showing purified, reconstituted LliK produced a robust cyclic nucleotide-dependent K^+ current. The arrow denotes addition of the protonophore CCCP to initiate flux, while the asterisk denotes addition of the K^+ ionophore valinomycin to produce maximal ACMA quenching. (C) Normalized Hill plot used to determine that LliK apparent binding affinity (IC_{50}) for cAMP is 2.4 µM. *Adapted from (James and Borst et al., 2017)

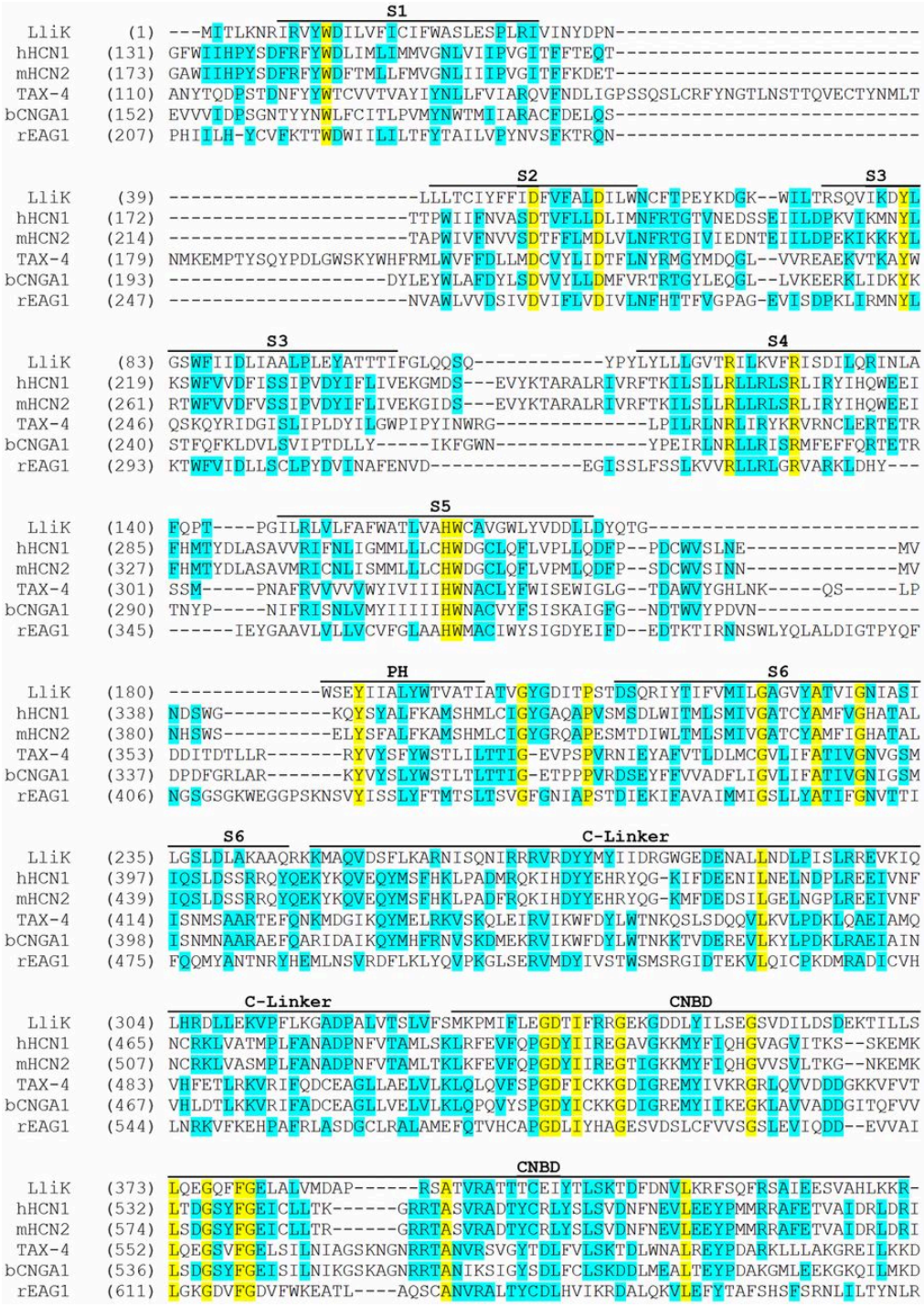

Figure 2.2. Multiple sequence alignment of CNG, HCN, and KCNH channels. LliK shares as much as 25% sequence identity with mammalian members of this protein family. Conserved residues are highlighted in cyan, whereas strictly conserved residues are highlighted in yellow. *Adapted from (James and Borst et al., 2017)

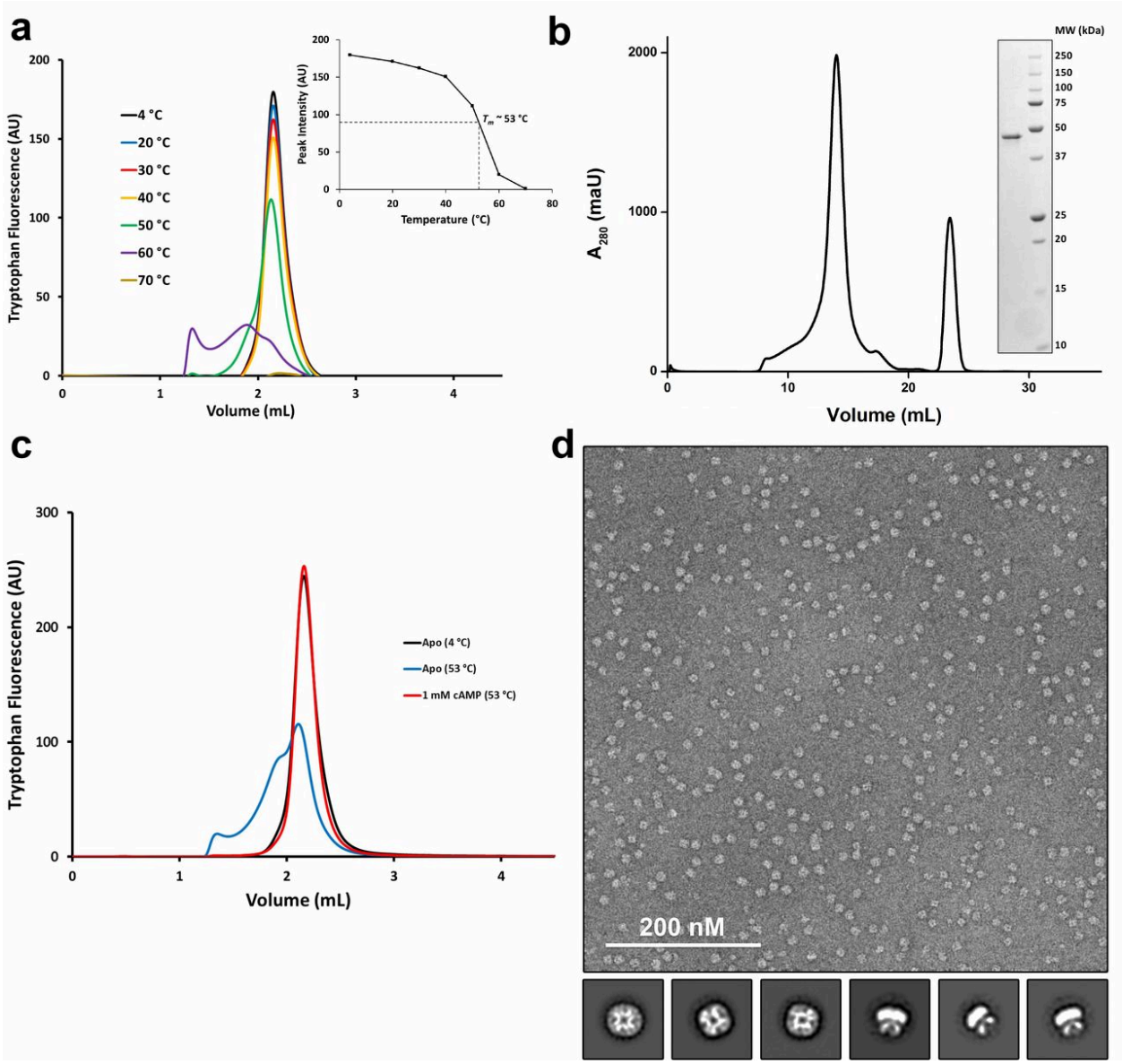

Figure 2.3. Biochemical and EM characterization of LliK.

(A) FSEC traces of purified apoLliK heated for 10 min at the indicated temperatures before injection. (*Inset*) Plot of peak intensity vs. temperature, yielding a T_m of 53 °C. (B) Size-exclusion chromatogram and SDS/PAGE gel of purified cAMP-bound LliK. The second peak of the elution trace corresponds to excess cAMP. (C) Thermostability FSEC assay. Purified LliK was heated to 53 °C for 10 min in the presence or absence of 1 mM cAMP. LliK is stabilized by cAMP, leading to a larger fraction of protein remaining stable and monodisperse following thermal challenge. (D) EM image and representative 2D class averages of negatively stained cAMP-bound LliK. *Adapted from (James and Borst et al., 2017)

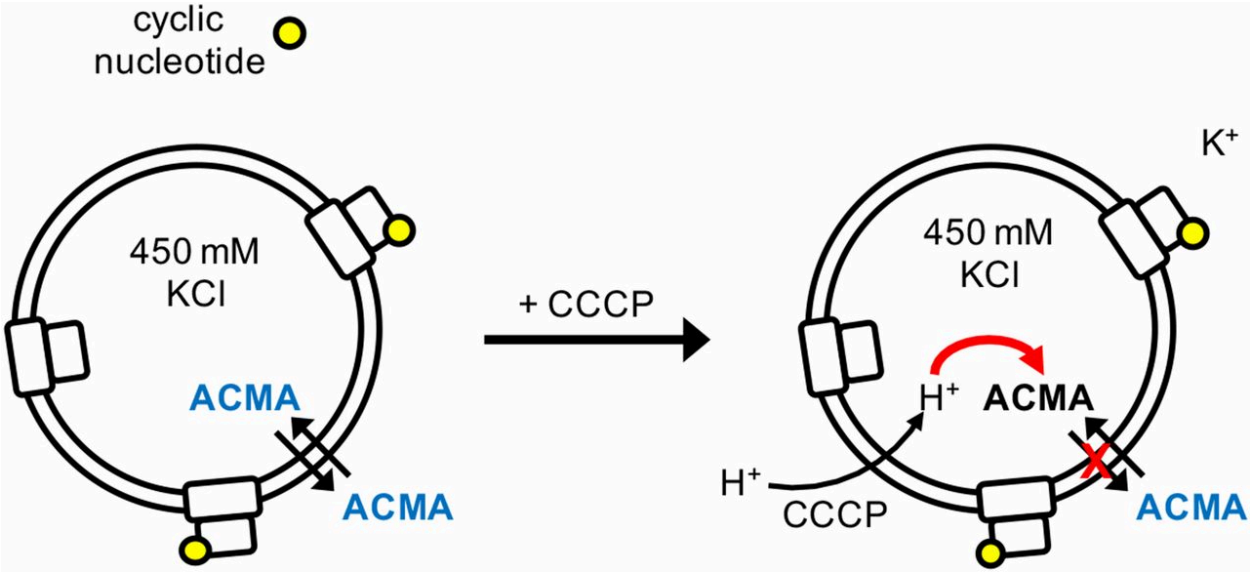

Figure 2.4. Liposome flux assay.

Following reconstitution of LliK into K^+-containing liposomes, the orientation of each molecule is expected to be random. The fluorophore ACMA diffuses into the liposome before addition of the protonophore, CCCP. cAMP binds to channels with their CNBDs facing outward, promoting channel opening and the subsequent efflux of intravesicular K^+. Simultaneously, protons will diffuse via CCCP into the liposome down their newly established electrochemical gradient to protonate and quench ACMA fluorescence. Protonation abrogates the ability of ACMA to traverse the lipid bilayer. *Adapted from (James and Borst et al., 2017)

2.3 STRUCTURE DETERMINATION OF THE LLIK CNG CHANNEL

Detergent-solubilized LilK was imaged in the presence of a saturating concentration (5 mM) of cAMP on an FEI Titan Krios electron microscope equipped with a Gatan K2 Summit direct detector **(Fig. 2.5A)**. 2D and 3D classification revealed a marked heterogeneity of the cAMP-bound LliK CNBDs relative to the well-resolved transmembrane domains (TMDs) and C-linkers. Projection-matching refinement of the best defined 3D class led to the determination of a whole-channel reconstruction at 4.5 Å resolution **(Fig. 2.5B, Fig. 2.6, and Table 2.1)**. Subsequent focusing of the refinement on the TMDs and C-linkers further improved the resolution of this region to 4.2 Å and enhanced side chain resolvability for many amino acids **(Fig. 2.5C-D, Fig. 2.6, and Table 2.1)**. A hybrid atomic model was obtained via density-guided rebuilding using RosettaCM (Song et al., 2013), hand tracing, and Rosetta iterative refinement (DiMaio et al., 2015; Wang et al., 2016) **(Fig. 2.5E-F)**. We report an all-atom model for the TMDs and C-linker A' through D' helices, whereas side chains are truncated at C_β for amino acid residues present in the remainder of the C-linker and the CNBD due to the lower resolution of the reconstruction in these regions. We are most confident about side chain assignment accuracy in the pore region whereas the quality of the reconstruction gradually decreases in other regions of the map. The final model includes residues 5 to 428 with internal breaks between 63-85 and 104-112.

Similar to the eukaryotic members of this ion channel family, LliK assembles as a four-fold symmetric tetramer situated around a centrally located pore **(Fig. 2.5E-F)**. Each subunit contains six transmembrane helices (S1-S6), with S1-S4 forming the voltage sensor domain (VSD) and S5-S6 making up the pore domain (PD). The carboxy-terminal region extends ~40 Å into the

cytoplasm and contains a tetrameric C-linker domain proximal to the membrane and CNBDs distal to the membrane.

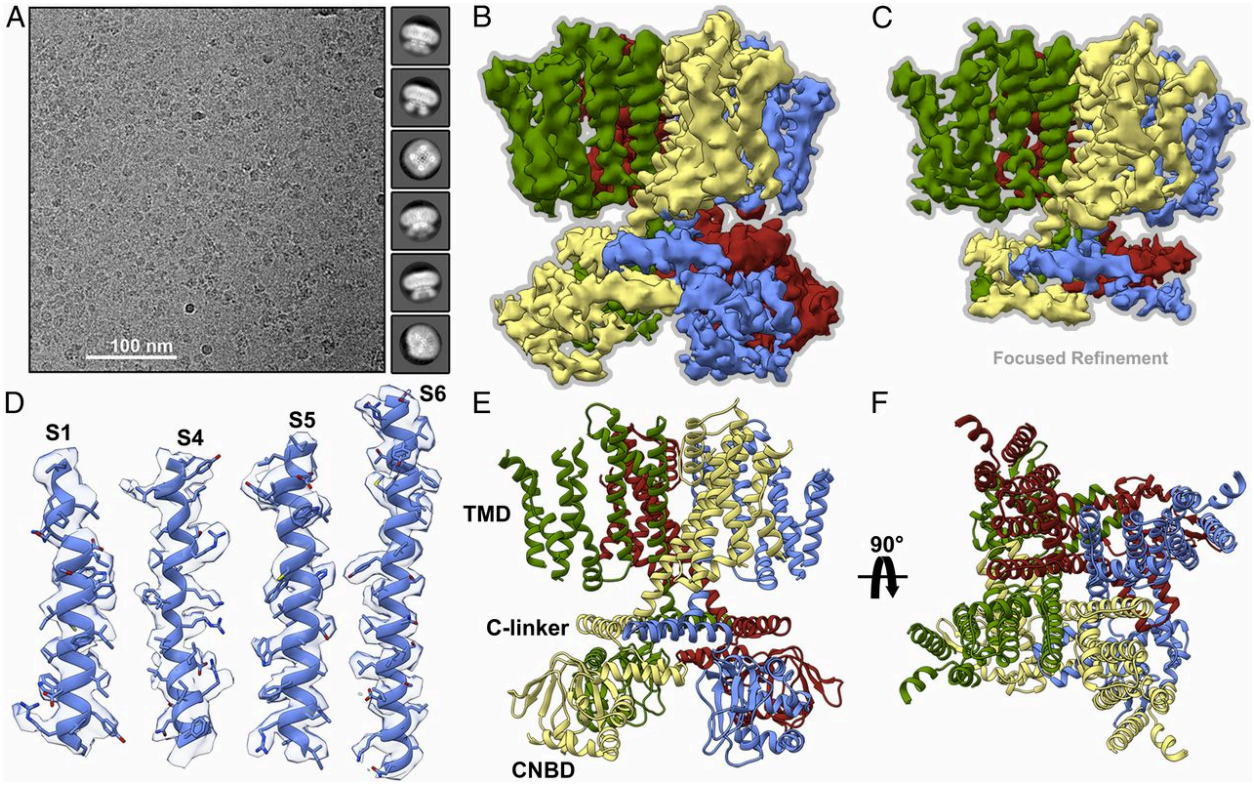

Figure 2.5. CryoEM structure of LliK.

(A) Representative cryoEM micrograph and associated 2D class averages of frozen-hydrated LliK particles. (B) 3D reconstruction at 4.5 Å resolution (sharpened with a B factor of -250Å^2) Each subunit is color coded. (C) 4.2 Å resolution cryoEM map obtained by focused refinement of the TMDs and C-linker A'-D' helices. Each subunit is color coded. (D) The atomic model is shown along with the corresponding region of the map: (from left to right) S6 helix, S5 helix, S4 helix, and S1 helix. The S6 helix and S5-S6 loop correspond to the best-defined region of the map whereas the S1 helix is much less well resolved due to its peripheral location. (E-F) Ribbon diagrams showing two orthogonal views of the LliK model with each subunit individually colored. TMDs: transmembrane domains; CNBDs: cyclic nucleotide binding domains. *Adapted from (James and Borst et al., 2017)

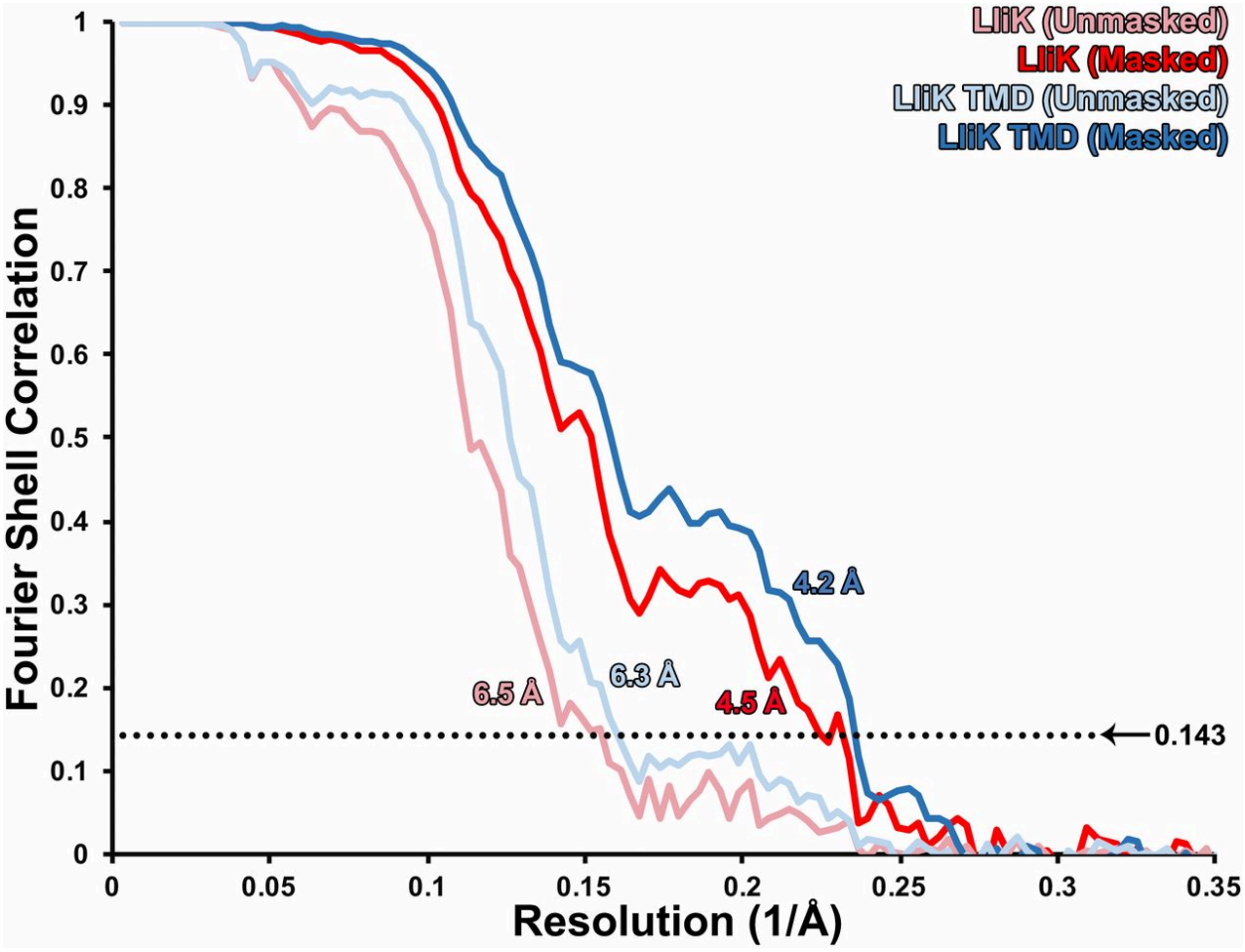

Figure 2.6. Resolution estimation of the LliK cryoEM reconstruction.

Fourier shell correlation curves for the refinements of the full channel (red) or the TMDs and C-linker A′–B′ helices only (blue). The 0.143 cutoff is indicated by a dashed line. *Adapted from (James and Borst et al., 2017)

Table 2.1. LliK refinement and model statistics

Parameter	Value
Data collection	
No. of particles	18,737
Pixel size, Å	1.1 (rescaled to 1.3655)
Defocus range, μm	1.5–3.5
Voltage, kV	300
Electron dose, $e^{-}/Å^2$	68
Refinement	
Resolution	4.5 (whole channel)/4.2 (TMDs)
Map sharpening B factor, Å2	−270 (TMD map)
Model validation	
MolProbity score (percentile)	1.53 (94th)
All-atom clash score (percentile)	2.99 (98th)
Poor rotamers, %	0
Favored rotamers, %	100
Ramachandran allowed, %	99.74
Ramachandran favored, %	93.14
Ramachandran outliers, %	0.26
rmsd bonds, Å	0.011
rmsd angles, °	1.4

2.4 TERTIARY AND QUATERNARY ORGANIZATION OF THE CYCLIC NUCLEOTIDE BINDING DOMAINS

The CNBDs in our structure adopt a canonical cAMP-bound tertiary conformation similar to that observed in all previous structures of cyclic nucleotide-bound CNBDs of CNG and HCN channels, including the recent cryoEM structures of full-length cAMP-bound HCN1 and cGMP-bound TAX4 (Kesters et al., 2015; Lee and MacKinnon, 2017; Li et al., 2017; Xu et al., 2010; Zagotta et al., 2003) (Fig. 3a, C_α rmsd = 1.0 and 1.2 Å with 98 and 93 aligned residues for HCN1 and TAX4, respectively). The CNBD consists of an α-helix (A-helix) followed by a β-roll and two additional α-helices (B- and C-helices), with the cyclic nucleotide-binding site residing between the β-roll and the C-helix. The LliK C-helix appears less ordered than in reported C-linker/CNBD crystal structures or in cAMP-bound HCN1 and in cGMP-bound TAX4 cryoEM structures, likely due to the conformational dynamics observed within this region that increase in magnitude as the density extends further towards the periphery. Comparison of our structure with previously reported apo-state CNBD structures (Akimoto et al., 2014; Goldschen-Ohm et al., 2016; Lee and MacKinnon, 2017; Saponaro et al., 2014) reveals large differences in the positions of the B- and C-helices, which are positioned away from the β-roll in the apo state **(Fig. 2.7B and Fig. 2.8)**. These observations suggest that the CNBDs of LliK are in the cyclic nucleotide-bound tertiary conformation, consistent with the high concentration of cAMP used in the cryoEM experiments. However, we could not unambiguously identify the cyclic nucleotide density, likely due to the marked heterogeneity of the CNBDs relative to the TMDs and the limited resolution of this region of the reconstruction. Overall, these results support previous models where cyclic nucleotide binding favors translation of the B- and C-helices toward the β-roll associated with channel activation (Wainger et al., 2001; Zagotta et al., 2003).

Beyond these tertiary rearrangements, our structure shows a significant quaternary reorganization of the CNBDs. Crystal structures of all CNG and HCN channel C-linker/CNBD fragments (Kesters et al., 2015; Lolicato et al., 2011; Xu et al., 2010; Zagotta et al., 2003), as well as the recent cryoEM structures of TAX4, HCN1, and CaM-inhibited Eag1 (Lee and MacKinnon, 2017; Li et al., 2017; Whicher and MacKinnon, 2016), demonstrate a compact architecture of the CNBDs and CNBHDs where each protomer forms (weak) inter-subunit contacts with neighboring subunits **(Fig. 2.7C-D)**. In contrast, the LliK CNBDs are rotated 40˚ outward relative to these previous structures, and are positioned away from each other, precluding lateral interactions **(Fig. 2.7E-F)**. This arrangement is reminiscent of what has been described for the cAMP-bound SthK C-linker/CNBD fragment**, although the swinging motion is of larger magnitude for LliK.

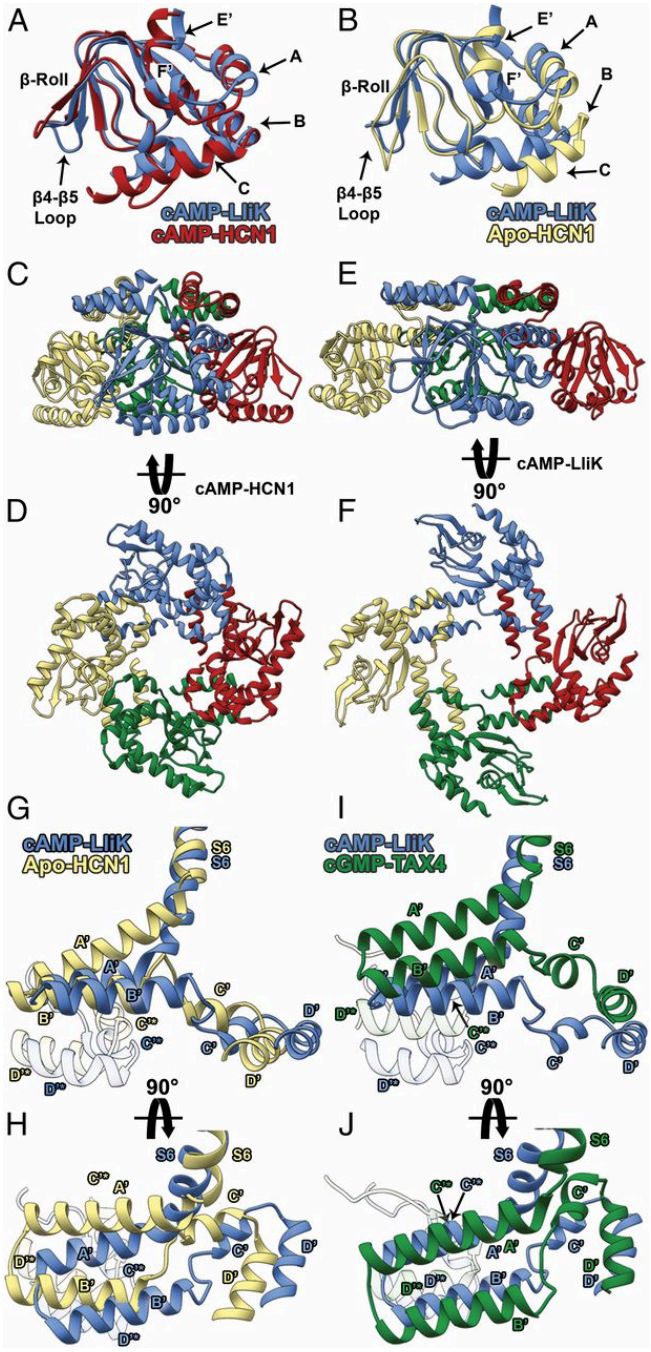

Figure 2.7. LliK undergoes large-scale tertiary and quaternary rearrangements upon cAMP binding.

(A) Superimposition of the LliK (blue) and cAMP-bound HCN1 [red; Protein Data Bank (PDB) ID code 5U6P] CNBDs showing the similarity of their tertiary structures, which extends to the carboxyl-terminal region of the C-linker. (B) Superimposition of the LliK (blue) and ligand-free

HCN1 (yellow; PDB ID code 5U6O) CNBDs showing marked differences in their tertiary structures. Key CNBD and C-linker motifs are labeled. (C and D) Two orthogonal views of the cAMP-bound HCN1 tetrameric C-linkers/CNBDs [parallel (C) and perpendicular (D) to the membrane] showing a compact architecture. (E and F) Two orthogonal views of the LliK tetrameric C-linkers/CNBDs showing the CNBDs are significantly splayed out relative to the structure of HCN1. (G) Superimposition of Apo-HCN1 (yellow) and cAMP-LliK (blue) tetrameric S6 helices revealing different relative orientations of the C-linker A′–D′ helices. (H) Orthogonal view of *G* highlighting the difference in the rotational positioning of the LliK and Apo-HCN1 C-linkers relative to S6. (I) Superimposition of cGMP-TAX4 (green) and cAMP-LliK (blue) tetrameric S6 helices showing the repositioning of the TAX4 C-linker toward the plasma membrane. (J) Orthogonal view of *I* highlighting the similarity in the rotational positioning of the LliK and cGMP-TAX4 C-linkers relative to S6. (G–J) The C-linker from a neighboring subunit is shown as semitransparent ribbon and denoted with a star. *Adapted from (James and Borst et al., 2017)

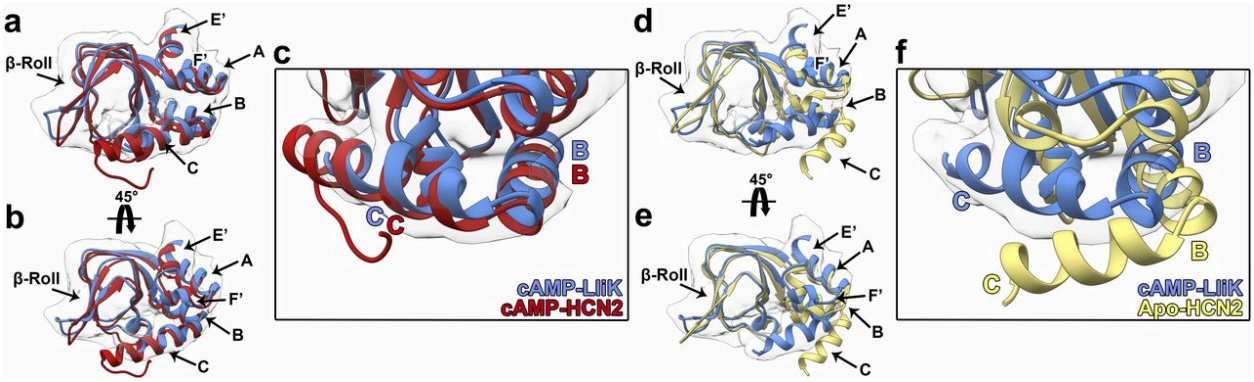

Figure 2.8. Tertiary structure of the cAMP-bound LliK CNBD.

(A) Superimposition of the crystal structure of cAMP-bound HCN2 (PDB ID code 1Q5O; red) onto the cAMP-bound LliK CNBD (blue) fit into the LliK cryoEM reconstruction. Both structures demonstrate excellent agreement with the LliK density map. (B) Orthogonal view of *A*. (C) *Inset* showing the good agreement of the fit of the B and C helices with the density. (D) Superimposition of the crystal structure of the apo-HCN2 CNBD (PDB ID code 5JON; yellow) onto the cAMP-bound LliK CNBD (blue) fit into the LliK cryoEM reconstruction. Large discrepancies between the apo-HCN2 structure and the EM map are visible. (E) Orthogonal view of *D*. (F) Inset highlighting the discrepancies of the conformation of the B and C helices of the apo-HCN2 structure with the density. *Adapted from (James and Borst et al., 2017)

2.5 ARCHITECTURE OF THE LLIK C-LINKER

The conformational change in the CNBD is coupled to a conformational change in the pore via the C-linker. The LliK C-linker begins with a 120-degree kink at the carboxy-terminal end of S6 and folds as a succession of α-helices (A'-F') that covalently link the CNBDs to the pore **(Fig. 2.5E-F)**. The C-linker is the site of all inter-subunit interactions in the carboxy-terminal region. The first two C-linker helices (A'-B') form a helix-turn-helix motif that interacts with the next two helices (C'-D') of a neighboring subunit in what has been referred to as an "elbow-on-shoulder" interaction (Zagotta et al., 2003). The inter-subunit elbow-on-shoulder contacts form a ring directly beneath the TMDs, and this interaction has been proposed to be dynamic during the cyclic nucleotide-dependent gating of CNG and HCN channels (Craven and Zagotta, 2006). The C-linker of LliK has a different conformation and quaternary organization than that observed in the crystal structures of CNG and HCN carboxy-terminal fragments (Kesters et al., 2015; Xu et al., 2010; Zagotta et al., 2003) as well as the recent cryoEM structures of TAX4, HCN1, and CaM-inhibited Eag1 (Lee and MacKinnon, 2017; Li et al., 2017; Whicher and MacKinnon, 2016) **(Fig. 2.7G-J)**. The kink between the S6 helix and the A' helix occurs about 2 helical turns later than in other cryoEM structures. In addition, the A'-B' and C'-D' helices of LliK are rotated and translated relative to each other to adopt an orientation nearly parallel to the plane of the membrane, that was not observed in previous structures.

2.6 STRUCTURE OF THE LLIK TRANSMEMBRANE DOMAIN

The LliK TMD has a similar overall architecture as TAX4, HCN1, and Eag1 (Lee and MacKinnon, 2017; Li et al., 2017; Whicher and MacKinnon, 2016) (C_α rmsd = 2.5, 3.0, and 2.9 Å with 176, 193, and 186 aligned residues respectively) **(Fig. 2.9A-D)**. In particular, LliK exhibits a non-domain swapped arrangement where each VSD associates with the PD of the same subunit, rather than the neighboring subunit as in most other known K_V channels **(Fig. 2.9A-B)**. This suggests that the non-domain-swapped architecture observed in LliK and eukayotic CNG, HCN, and KCNH channels is conserved among many members of this ion channel family and across multiple kingdoms of life.

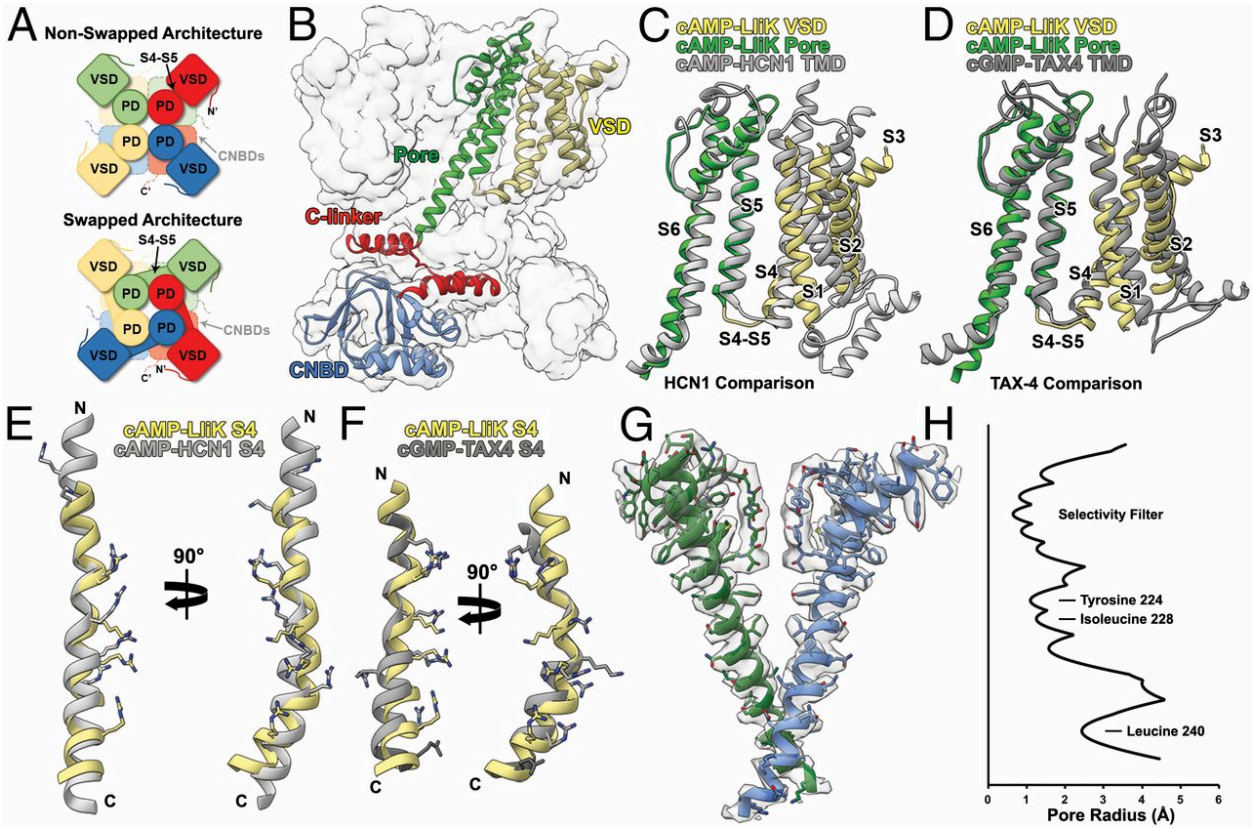

Figure 2.9. Architecture of the LliK TMD.

(A) Schematic organization of non–domain-swapped and domain-swapped K^+ channels. (B*)* Model highlighting the domain architecture of the LliK ion channel. One subunit is represented as a ribbon diagram colored by domain, whereas the other three subunits are shown as gray surfaces. (C) Superimposition of the LliK and cAMP-HCN1 (PDB ID code 5U6P), based on S5–pore helix–S6, highlighting the conserved non–domain-swapped architecture. The LliK VSD is depicted in yellow, the LliK PD in green, and cAMP-HCN1 TMD in light gray. (D) Superimposition of the LliK and cGMP-TAX4 (PDB ID code 5H3O), based on S5–pore helix–S6, highlighting the conserved non–domain-swapped architecture. The LliK VSD is depicted in yellow, the LliK PD in green, and cGMP-TAX4 TMD in dark gray. (E) Superimposition of the LliK S4 helix (yellow) with the cAMP-bound HCN1 S4 helix (light gray). (F) Superimposition of the LliK S4 helix (yellow) with the cGMP-bound TAX4 S4 helix (dark gray). Side chains of positively charged amino acid residues are shown as sticks in *E* and *F*. (G) Molecular model of the LliK pore fit into the corresponding region of the cryoEM density. Only two opposing subunits are shown for clarity. (H) Plot of the cAMP-LliK pore radius. *Adapted from (James and Borst et al., 2017)

The S4 segment is also in a generally similar conformation to that of TAX4, HCN1, and Eag1 (Lee and MacKinnon, 2017; Li et al., 2017; Whicher and MacKinnon, 2016), though is most similar in length and bend to TAX4 **(Fig. 2.9E-F)**. Of the positively charged residues in the LliK S4 helix (R122, K125, R128, and R135), four in TAX4, three in Eag1, and three in HCN1 are conserved and similarly oriented **(Fig. 2.2)**, suggesting that S4 is in the outward conformation for all these channels. The positions of these conserved charges between structures reveals that LliK and TAX4 both adopt a downwardly-oriented S4 helix relative to the structures of Eag1 and HCN1. The S2 and S3 residues forming the charge-transfer center are also conserved in LliK (F52, D55, and D89), although their role remains to be determined. Similar to what has been described for HCN1 and TAX4, the S4-S5 linker in LliK is positioned proximal to and makes putative contacts with the C-linker A'-B' helix-turn-helix motif from a neighboring subunit.

Like other members of the K_V channel superfamily, the pore of LliK is comprised of the P-loop (S5-S6 loop) and S6, which is the best-resolved region of the reconstruction **(Fig. 2.9G)**. The P-loop density is consistent with the conformation of the selectivity filter observed in other K^+-selective ion channels like Eag1 (Whicher and MacKinnon, 2016). The S6 segments form an "inverted teepee" with a narrowing at the bundle crossing on the cytoplasmic side **(Fig. 2.9G)**. The S6 helices are devoid of a kink before the S6 bundle crossing and are in a conformation similar to that observed for HCN1 and Eag1 channels (Lee and MacKinnon, 2017; Whicher and MacKinnon, 2016). However, the residue producing the greatest closure in Eag1 (Q476) is a glycine in LliK (G236) and does not constrict the pore **(Fig. 2.9C)**. The greatest constriction is produced instead by Y224 and I228, yielding a pore diameter of ~3 Å, which is about the diameter of a dehydrated

K^+. Since dehydration of K^+ is expected to be energetically unfavorable at this position, we speculate that our LliK structure has a closed pore.

2.7 CONCLUSIONS, DISCUSSION, AND FUTURE DIRECTIONS

Our LliK structure reveals major differences in the C-linkers and CNBDs relative to all other known structures of cyclic nucleotide-regulated channels. Cyclic nucleotide-dependent activation of CNG and HCN channels has been proposed to involve a series of coupled conformational changes in different channel modules (Craven and Zagotta, 2004) **(Fig. 2.10)**. Cyclic nucleotide binding is thought to promote independent conformational changes in the CNBD of each subunit, which subsequently induce a concerted conformational change in the gating ring formed by the C-linker. This conformational change in the C-linker is then coupled to an opening conformational change in the pore.

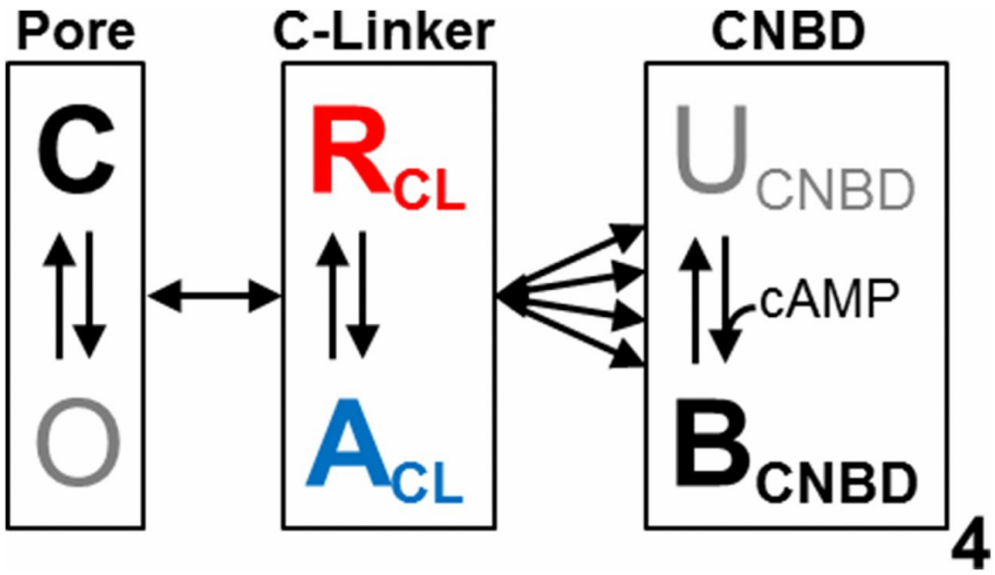

Figure 2.10. Different channel module conformational changes during activation.
*Adapted from (James and Borst et al., 2017)

In the context of this model, the CNBDs in our LliK structure appear to be in the bound and activated conformation, and the pore appears to be closed **(Fig 2.10)**. Given this unexpected pore conformation, what then is the state of the C-linker architecture we observe in our structure? Based on the finding that cAMP promotes tetramerization of isolated C-linker/CNBDs, it has been proposed that the C-linker/CNBD organization observed in all other cyclic nucleotide-bound CNG and HCN channel structures represents the activated state (Lolicato et al., 2011; Zagotta et al., 2003). Although the C-linkers are also tetramerized in our structure, they may adopt a "resting" state where the gating ring has not yet transitioned to an activated conformation, despite the CNBDs being occupied by cyclic nucleotides **(Fig. 2.10)**. This resting state may hold the CNBDs apart, preventing the compact C-linker/CNBD architecture observed in other structures.

It is also possible that our LliK structure represents a "pre-open" conformation, where the C-linker gating ring is in an active state but the pore remains closed **(Fig. 2.10)**. In line with this hypothesis, it has been shown that mutations of an inter- and intra-subunit salt bridge triad formed by residues in the B' helix, D' helix, and β-roll lead to a large increase in the favorability of pore opening in mammalian CNGA1 and HCN2 channels (Craven and Zagotta, 2004; Craven et al., 2008). This suggests that the salt bridge triad observed in the HCN2 C-linker/CNBD crystal structure is intact in the resting state of the C-linker and breaks following cAMP binding. These salt-bridge residues are conserved in LliK (R268, E299 and D339), but the salt bridge triad is partially broken in our structure due to the large distance separating the residues involved, preventing simultaneous formation of the two salt bridges. Moreover, in mammalian CNG channels, the cross-linking of the D' helix and β-roll from neighboring subunits with short linkers

favors a closed pore, whereas longer linkers permit pore opening, suggesting that these regions are further apart in the active state, as seen in our structure of LliK (Craven et al., 2008).

The recent structures of full-length eukaryotic TAX4 and HCN1 allows us to compare the organization of their C-linker/CNBDs with those of LliK. For both TAX4 and HCN1 channels it has been proposed that a rotation of the C-linker relative to the pore is coupled to cyclic nucleotide-dependent activation of these channels, eventually leading to pore opening **(Fig. 2.11)** (Lee and MacKinnon, 2017; Whicher and MacKinnon, 2016). We observe a large rotation of the LliK C-linker/CNBD relative to the pore when compared to the apo-HCN1 structure **(Fig. 2.11)**. The rotation is larger than seen for cAMP-bound HCN1 and similar in size to cGMP-bound TAX4 and Eag1 **(Fig. 2.11)**. In addition, the C-linkers of the open TAX4 structure are positioned much closer to the plasma membrane compared to the closed HCN1, Eag1, and LliK structures **(Fig. 2.11)**. These observations suggest that the observed LliK C-linker conformation could potentially be in a "pre-open" conformation. This state might be accentuated for detergent-solubilized LliK, which could have altered energetics of pore opening due to the lack of a lipid bilayer.

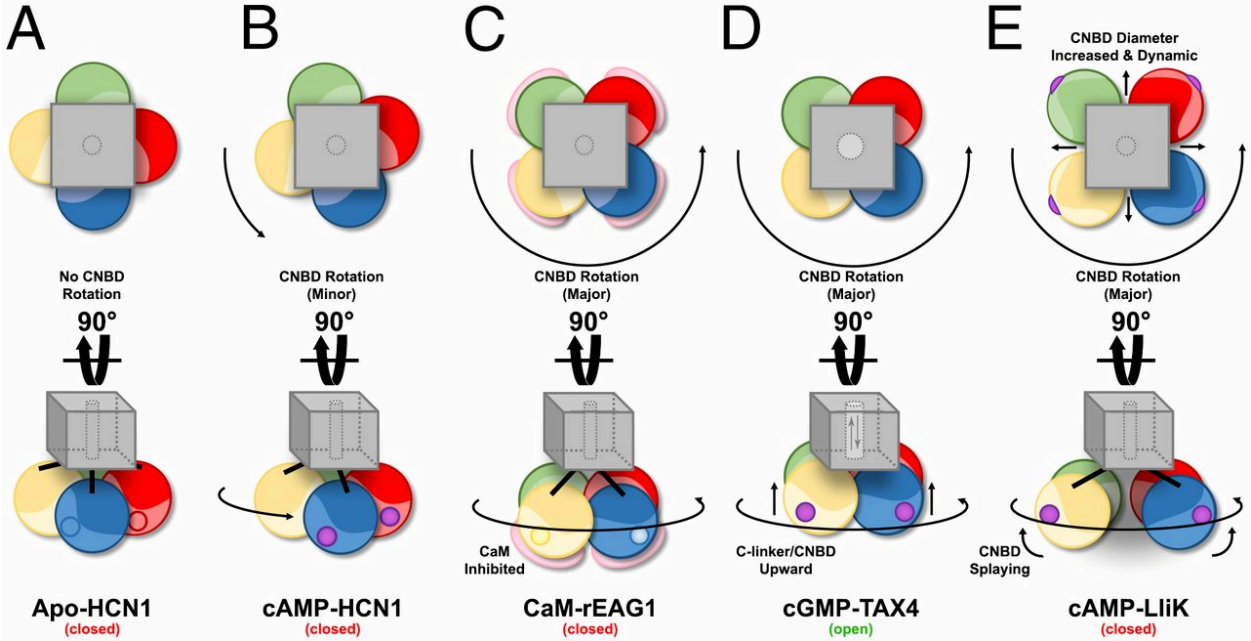

Figure 2.11. Comparison of LliK to other CNG and HCN full-length channel structures. Cartoon diagram comparing the major structural differences observed between recently solved CNG, HCN, and KCNH channel cryoEM structures. Degrees of rotational, translational, and CNBD splaying have been magnified for clarity. CNBDs and CNBHDs are color-coded by subunit. The TMD of each channel is colored in gray. The cyclic nucleotide binding pocket for Apo-HCN1 is depicted as empty circles. Cyclic nucleotides are depicted as purple circles for cAMP-HCN1, cGMP-TAX4, and cAMP-LliK. The intrinsic ligands are depicted as light yellow and light blue circles in their corresponding CNBHD subunits in Eag1, with CaM bound to the CNBHDs colored pink. (A) Apo-HCN1: closed pore. (B) cAMP-HCN1: minor rotation of the C-linker relative to the TMD and a closed pore. (C) cGMP-TAX4: major rotation of the C-linker relative to the TMD, translation of the C-linker toward the membrane, and an open pore. (D) CaM-Eag1: major rotation of the C-linker, closed pore, and inhibited by CaM. (E) cAMP-LliK: major rotation of the C-linker, closed pore, and significant splaying of the CNBDs. *Adapted from (James and Borst et al., 2017)

Finally, it is possible that our structure is in a conformation that is not observed in eukaryotic CNG or HCN channels. For example the C-linker might be in a resting or active state that is not seen in eukaryotic channels. Alternatively, the channel might reside in a desensitized state where the C-linker has “slipped”, disrupting the coupling between the CNBDs and the pore. Desensitization due to slippage is thought to occur in other ligand-gated channels and in voltage gating of HCN channels (Dürr et al., 2014; Shin et al., 2004). However, mammalian CNG and HCN channels are not known to desensitize to cyclic nucleotide, and LliK has not yet been characterized for such behavior. Future experiments will be needed to ascertain the functional state of the LliK C-linker and ultimately the full conformational trajectory associated with the allosteric regulation of CNG and HCN channels.

2.8 METHODOLOGY

2.8.1 *Protein expression and purification*

Full-length LliK was expressed from a modified pET vector encoding an N-terminal His_8 tag followed by a TEV protease cleavage site and an SGS linker. Expression was performed in C43(DE3) cells (Lucigen) grown in 2× YT medium (Formedium) to an OD_{600} of ~0.4 before induction with 0.4 mM IPTG. Cells were induced for 16–18 h at 18 °C and harvested by centrifugation. All purification steps were performed on ice or at 4 °C. Cell pellets were resuspended in lysis buffer (50 mM Tris, 150 mM KCl, pH 7.9) containing EDTA-free protease inhibitors (Roche) and lysed by three passes through an EmulsiFlex-C3 operating at 15,000–20,000 psi. The lysate was clarified by centrifugation at 25,000 × *g* for 30 min, after which membranes were isolated by ultracentrifugation at 140,000 × *g* for 1.5 h. Membrane pellets were resuspended at 1:1 (wt/vol) in resuspension buffer [50 mM Tris, 150 mM KCl, 20% (vol/vol) glycerol, pH 7.9], then divided into aliquots and flash-frozen in liquid nitrogen before storage at −80 °C. Thawed membrane aliquots were combined with an equal volume of extraction buffer (50 mM Tris, 150 mM KCl, 20 mM LMNG, 2 mM CHS, 2 mM cAMP, pH 7.9) and nutated for 2 h. Insoluble material was removed by centrifugation at 37,000 × *g* for 45 min. The supernatant was supplemented with 8 mM imidazole and combined with TALON resin (Clontech) at 10:1 sample:resin (vol/vol), followed by nutation for 2 h. The batch-bound resin was then packed into a disposable Poly-Prep column (Bio-Rad) and washed with 10 bed volumes of wash buffer (50 mM Tris, 150 mM KCl, 20 mM imidazole, 200 μM LMNG, 20 μM CHS, 1 mM cAMP, pH 7.9). Protein was eluted with wash buffer containing 250 mM imidazole and immediately applied to a PD-10 column (GE Healthcare) preequilibrated with desalting buffer (50 mM Tris, 150 mM KCl, 200 μM LMNG, 20 μM CHS, 1 mM cAMP, pH 7.9). The protein was then concentrated by using

a 100-kDa MWCO spin concentrator (GE Healthcare) and loaded onto a Superose 6 10/300 GL column (GE Healthcare) preequilibrated with SEC buffer (20 mM Tris, 150 mM KCl, 50 μM LMNG, 5 μM CHS, 0.02 mM cAMP, pH 7.9). Eluted protein (~1.0 mg/mL) was supplemented with 5 mM cAMP and used immediately for grid preparation.

2.8.2 *Thermostability assays*

For thermostability assays, LliK was purified as described earlier in the absence of cAMP. Following desalting, aliquots of purified protein were placed in a thermocycler and heated to the desired temperature for 10 min. Heat-treated samples were centrifuged for 30 min at 20,000 × *g* and 4 °C, after which the supernatants were injected onto a Superose 6 Increase 5/150 GL column (GE Healthcare) preequilibrated with SEC buffer while recording tryptophan fluorescence (λ_{Ex} = 280 nm, λ_{Em} = 325 nm). The apparent melting temperature (T_m) of apoLliK was estimated by plotting the peak intensity as a function of temperature.

2.8.3 *Reconstitution and flux assays*

For reconstitution and flux assays (Su et al., 2016), LliK was purified as described earlier in the absence of cAMP. Additionally, 40 mM DM replaced LMNG in the extraction buffer and 4 mM DM replaced LMNG in all other buffers, whereas the concentration of CHS was increased to 4 mM in the extraction buffer and 0.4 mM in all other buffers. To prepare vesicles, POPE and POPG lipids in chloroform (Avanti) were combined at 3:1 (wt/wt) and dried under argon followed by overnight storage in a vacuum desiccator. The lipid film was resuspended at 20 mg/mL in reconstitution buffer (20 mM Hepes, 450 mM KCl, 1 mM EDTA, pH 7.4) and bath-sonicated until translucent. The lipids were then combined with an equal volume of reconstitution buffer

containing 20 mM DM and 2 mM CHS, followed by 1 h nutation at room temperature. Purified protein (solubilized in DM) was added to give 100:1 lipid:protein (wt/wt), and the sample was nutated another 1 h at room temperature. The sample was transferred to 20-kDa MWCO dialysis tubing (SpectraPor) and dialyzed against reconstitution buffer for 3–4 d at 4 °C, with twice-daily buffer exchange. Protein-free "empty" vesicles were prepared identically except that SEC buffer (containing 4 mM DM) was used in place of purified protein. Immediately before flux measurements, the reconstituted vesicles were bath-sonicated 1–2 min at room temperature.

Sonicated vesicles were diluted into low K^+ buffer (20 mM Hepes, 150 mM NaCl, 1 mM EDTA, pH 7.4) containing 2 μM 9-amino-6-chloro-2-methoxyacridine (ACMA) and various cAMP concentrations. Fluorescence was recorded with a Fluorolog 3 spectrophotometer by using FluorEssence software (HORIBA Jobin Yvon). Initial ACMA fluorescence (λ_{Ex} = 410 nm, λ_{Em} = 490 nm) was recorded for 60 s before initiating flux by adding 4 μM CCCP. At 240 s, 0.04 μM valinomycin was added and the final ACMA fluorescence was recorded another 60 s. Raw flux data were normalized to the initial and final ACMA fluorescence. Relative activity was calculated as the difference between the cAMP-containing and cAMP-free flux curves at 180 s (Yang et al., 2016). Relative activity data were normalized and then fit to a Hill equation to determine an apparent affinity (i.e., IC_{50}).

2.8.4 *Negative-stain EM sample preparation.*

Purified LliK (3 μL) was negatively stained at a final concentration of 0.008 mg/mL by using Gilder Grids overlaid with a thin layer of carbon and 2% uranyl formate as previously described (Veesler et al., 2014).

2.8.5 *Negative-stain EM data collection and processing.*

Data were collected on an FEI Technai 12 Spirit 120-kV electron microscope equipped with a Gatan Ultrascan 4000 4K × 4K CCD camera. A total of 155 images were collected by using a random defocus range of 1.1–2.0 μM with a total exposure of 30 e^{-}/A^{2}. Data were automatically acquired using Leginon (Suloway et al., 2005), and data processing was carried out by using Appion (Lander et al., 2009). The parameters of the contrast transfer function (CTF) were estimated by using CTFFIND3 (Mindell and Grigorieff, 2003), and particles were picked in a reference-free manner by using DoG picker (Voss et al., 2009). Particles were extracted with a binning factor of 2 after correcting for the effect of the CTF by flipping the phases of each micrograph with EMAN 1.9 (Ludtke et al., 1999). The LliK particle stack was preprocessed in RELION/1.4 (Scheres, 2012b, 2012a) with an additional binning factor of 2 applied, resulting in a final pixel size of 6.4 Å. Approximately 61,100 particles were sorted into 128 independent classes over 25 iterations, with the best ~38,000 particles classified into 64 independent classes over an additional 25 iterations by using Relion.

2.8.6 *CryoEM sample preparation.*

We applied 2 μL of 0.9 mg/mL of cAMP-bound LliK to glow-discharged and chloroform-washed Quantifoil R 1.2/1.3 Cu 400 grids. Vitrification was performed by using an FEI Vitrobot Mark IV, using a blot time of 8 s at a temperature of 4 °C and 100% humidity.

2.8.7 *CryoEM data collection.*

Data collection was performed automatically by using Leginon (Suloway et al., 2005) to control an FEI Titan Krios Electron Microscope equipped with a K2 Summit direct detector (Li et

al., 2013) operating in electron-counting mode with a random defocus range between −1.5 and −3.5 μM. Approximately 2,100 micrographs were collected with a pixel size of 1.1 Å and a dose of 8 counts per pixel per second and 10-s acquisition time (0.2 frame per second), yielding a final measured dose of 68 $e^{-}/Å^2$ per movie.

2.8.8 *CryoEM data processing.*

Alignment of movie frames was carried out by using MotionCor2 with a B-factor of −1.000 $Å^2$ and an applied dose-weighting scheme of 1.2 electrons/$Å^2$. Each micrograph was visually inspected, and the edge from the carbon support film was manually masked in Appion (Lander et al., 2009). Omission of low-quality micrographs left a total of 1,560 micrographs for downstream data processing. A total of 500,000 particles were initially picked in a reference-free manner by using DoG picker. Global defocus and astigmatism were estimated by using GCTF (Zhang, 2016) and the non–dose-weighted aligned sums. Particles were binned to a final pixel size of 4.4 Å for an initial round of 2D classification using RELION/1.4. The best 2D classes (demonstrating unambiguous particle density) were centered, low-pass–filtered to 20 Å, and subsequently used for template picking by using FindEM (Roseman, 2004) within the Appion pipeline, yielding 379,000 total particle picks. Following 2D classification using RELION/1.4, ∼120,000 selected particles were reextracted and binned to a final pixel size of 1.3655 Å and subjected to 3D classification with RELION/1.4 using a 40-Å low-pass–filtered initial model generated with EMAN2 e2initialmodel.py (Tang et al., 2007). Of the six resulting classes, two contained defined transmembrane, C-linker, and CNBD density. The most populated and well-resolved of these classes was low-pass–filtered to 20 Å and used as an initial model during 3D refinement, using individual (local) particle defocus values estimated by using GCTF, which yielded a resolution of

5.3 Å. This reconstruction was low-pass–filtered to 20 Å and rerefined using RELION/2.0 (Kimanius et al., 2016) with a soft solvent mask, within which the resolution was calculated at each iteration. This yielded a reconstruction at 4.8-Å resolution. This map was low-pass–filtered to 8 Å and used as an initial model for a second round of 3D classification starting from the original ∼120,000 particles obtained from 2D classification. Of the eight requested classes, ∼18,700 particles resolved into a single well-defined reconstruction that was subsequently low-pass–filtered to 20 Å and refined to 4.5 Å in the presence of a soft solvent mask. This resolution was of sufficient quality to resolve several bulky amino acid side chains throughout various regions of the map.

Focused refinement of the transmembrane segment of the channel was continued from the final iteration of the refinement, leading to the 4.5-Å map, by using a soft mask surrounding only the transmembrane region and C-linker A′–B′ helices. This approach improved the local resolution of this area to 4.2 Å with significant enhancement of the quality of the helical density, including the visualization of many additional amino acid side chains. Reported resolutions are based on the gold-standard Fourier shell correlation = 0.143 criterion, and Fourier shell correction curves were corrected for the effects of soft masking by high-resolution noise substitution (Chen et al., 2013; Scheres and Chen, 2012).

2.8.9 *Model building and refinement.*

We selected a set of proteins sharing sequence similarity with LliK and for which a structure is available by using HHPred (Söding et al., 2005) (PDB ID codes 3BPZ, 3UKN, 4D7S, 4L11, 5K7L, 5H3O, and 5U6O) before threading their structures with the LliK sequence and docking them into density by using University of California, San Francisco (UCSF), Chimera

(Goddard et al., 2007). Subsequently, a LliK model accounting for the TMDs and C-linker A′–D′ helices was generated by using RosettaCM (Song et al., 2013) and the 4.2-Å resolution map. The best model was manually trimmed and edited by using Coot (Brown et al., 2015; Emsley et al., 2010) and refined by using Rosetta density-guided protocols (Wang et al., 2016) and the symmetric modeling framework in Rosetta (DiMaio et al., 2011, 2015; Wang et al., 2016). We are most confident about side-chain assignment accuracy in the pore region, whereas the quality of the reconstruction gradually decreases in other regions of the map. Residues 1–6, 33–38, 60–82, and 105–112, which are poorly resolved in the map, were omitted from the final model. The pairwise Cα rmsd among the best scoring models obtained using Rosetta density-guided iterative refinement for the equivalent residues was comprised between 0.45 and 0.85 Å. This model was combined with models output by a RosettaCM run that generated a full-length LliK structure using the 4.5-Å resolution map. Because of the gradually decreasing resolution toward the cytoplasmic region, we truncated amino acid side chains at C_β for residues present in the C-linker C′–F′ helices and the CNBD as we could not confidently assign the sequence register in these regions. The quality of the final model was analyzed with MolProbity (Chen et al., 2010a) and the pore diameter with hole (Smart et al., 1993). Figures were generated with UCSF Chimera (Pettersen et al., 2004)

Chapter 3. A THERAPEUTIC ANTIBODY SELECTIVELY INHIBITS LIGAND BINDING TO A HUMAN INTEGRIN.

3.1 CHAPTER SUMMARY

The function-blocking LM609 antibody has been reported to specifically recognize $\alpha_V\beta_3$ integrin and to inhibit angiogenesis, bone resorption, and viral infections in an arginine-glycine-aspartate motif (RGD) independent manner. LM609 entered phase II clinical trials for the treatment of several cancers and was also successfully used for $\alpha_V\beta_3$-targeted radio-immunotherapy. The lack of structural information for this antibody has hindered the molecular understanding of its biochemical and therapeutic properties. To elucidate the structural basis of recognition and the mechanisms associated with inhibition of $\alpha_V\beta_3$ integrin, we solved the structure of the LM609 antigen-binding fragment (Fab) by X-ray crystallography and determined its binding affinity for $\alpha_V\beta_3$. We also used single-particle electron microscopy to show that LM609 binds at the interface between the β-propeller domain of the α_V chain and the βI domain of the β_3 chain, near the RGD-binding site, of all observed integrin conformational states. By combining this data with fluorescence size-exclusion chromatography, we demonstrate that the therapeutic properties of LM609 result from sterically hindering access of large ligands to the RGD binding pocket, without obstructing it. This work ultimately provides a structural framework to expedite future efforts utilizing LM609 as a diagnostic or therapeutic tool for a variety of human diseases.

3.2 CRYSTAL STRUCTURE OF LM609

The structure of Fab LM609 was determined at 2.3 Å resolution using X-ray crystallography **(Fig. 3.1A-B and Table 3.2)**. Calculation of the LM609 electrostatic properties revealed that the surface formed at the apex of the Fab, containing the complementarity-determining regions (CDRs), is characterized by a marked positive potential **(Fig. 3.1C)**. This is explained by the presence of numerous basic residues directly contributed by the CDRs and by the flanking immunoglobulin framework regions. Furthermore, the amino acid composition of the LM609 CDRs follows previously reported trends with numerous aromatic, glycine and serine residues(Fellouse et al., 2004, 2007; Sidhu and Kossiakoff, 2007). The Fab elbow angle, defined as the angle between the pseudo-2-fold axes relating the two variable and the two constant domains, was determined to be 148.6˚. This structure provides a framework to rationalize a previously reported directed evolution study aimed at enhancing the affinity of Vitaxin for $\alpha_V\beta_3$ integrin(Wu et al., 1998) and for future structure-guided design studies using this antibody as a therapeutic platform.

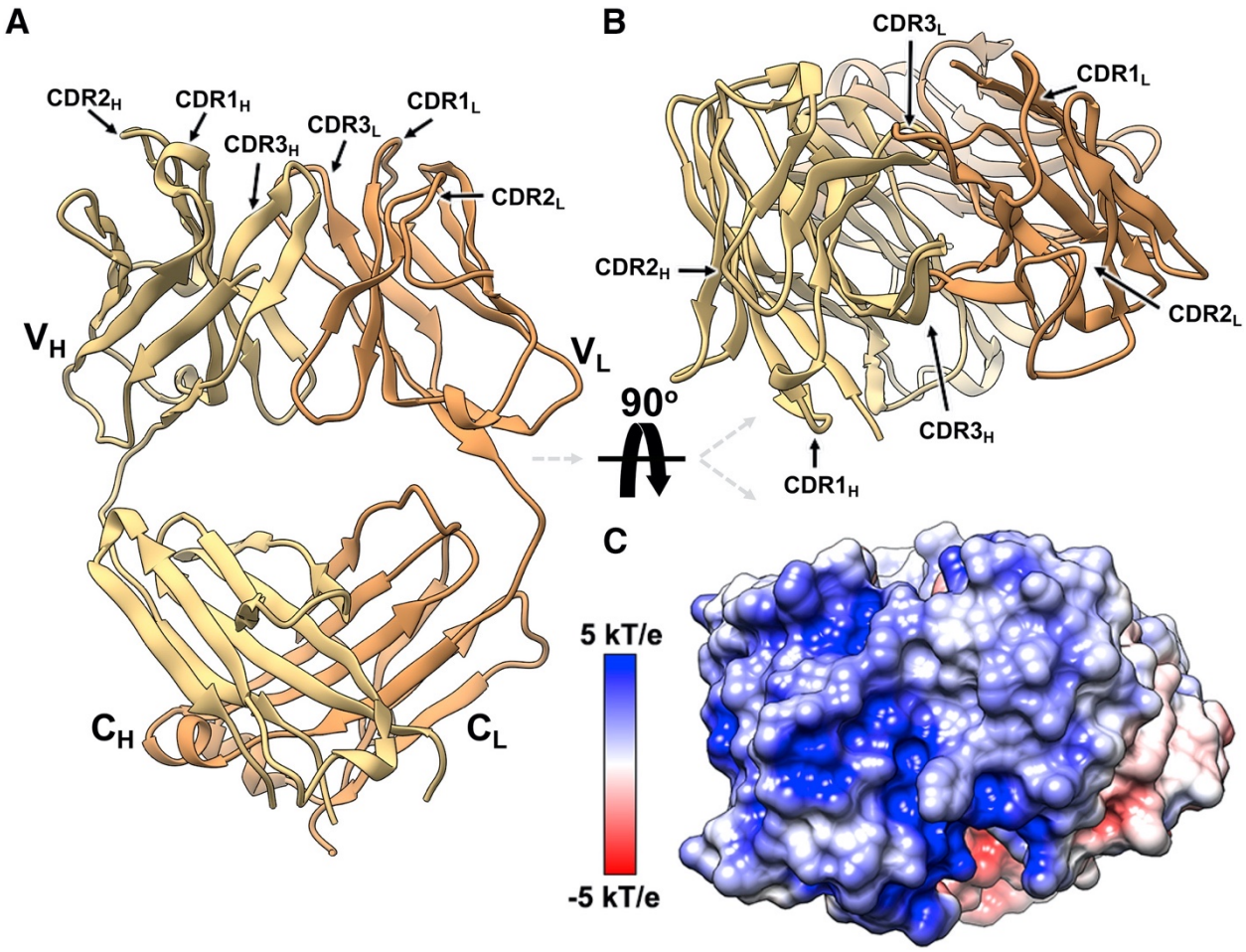

Figure 3.1. Crystal structure of Fab LM609.

(A and B) Ribbon diagrams showing two orthogonal views of the Fab LM609 colored yellow and orange for the heavy and light chains, respectively. The complementarity-determining regions (CDRs) are indicated. V_H, heavy-chain variable domain; C_H, heavy-chain constant domain; V_L, light-chain variable domain; C_L, light-chain constant domain. (C) Surface representation of LM609 colored by electrostatic potential showing the marked positive nature of the Fab apex. The orientation is identical to that in (B). *Adapted from (Borst et al., 2017)

Table 3.2. LM609 X-ray Crystallography Refinement Statistics

a–Outer-shell values are given in parentheses

b–Rfreetest set was composed of 5% randomly chosen reflections

c –Refers to number of protein / water atoms

d –Refers to overall / protein / water B-factors

e–Preferred / allowed / outliers as calculated using Coot

X-ray data processing			
Beamline	SOLEIL PX2		
Space group	P 2 2_1 2_1		
Cell constants	51.81 Å	82.35 Å	92.17 Å
a, b, c, α, β, γ	90.00°	90.00°	90.00°
Resolution (Å)	45.16-2.26 (2.33-2.26)[a]		
No. of reflections	101789 (9085)		
Multiplicity	5.3 (5.3)		
<I/σ(I)>	12.7 (3.3)		
Completeness (%)	99.8 (98.7)		
R_{merge}	0.088 (0.496)		
$CC_{1/2}$	0.997 (0.759)		
Wilson B factor ($Å^2$)	33		
Refinement			
Program	BUSTER 2.10.2		
Resolution (Å)	45.16-2.26		
No. of reflections	19063		
R_{work}/R_{free}[b]	0.213 / 0.255		
No. of atoms[c]	3255 / 183		
B-factors[d]	35 / 35 / 40		
Geometry			
***rmsd* bond lengths (Å)**	0.01		
***rmsd* bond angles (°)**	1.25		
Ramachandran plot[e] (%)	96.67 / 2.62 / 0.71		

3.3 THE FAB LM609 BINDS WITH NANOMOLAR AFFINITY TO A_VB_3 INTEGRIN

We used surface plasmon resonance to characterize the affinity of Fab LM609 to the ectodomain of human $\alpha_V\beta_3$ integrin. Immobilization of $\alpha_V\beta_3$ integrin was achieved through amine coupling with measurements performed using Fab concentrations ranging between 7.8 and 500 nM **(Figure 3.2A)**. Fab LM609 kinetic association (k_{on}) and dissociation constants (k_{off}) for $\alpha_V\beta_3$ were determined to be $1.5 \pm 0.26 \times 10^5\ M^{-1}s^{-1}$ and $3.4 \pm 0.002 \times 10^{-3}\ s^{-1}$, respectively, yielding an equilibrium dissociation constant (K_D) of $2.3 \pm 0.6 \times 10^{-8}$ M. $\alpha_V\beta_3$ binding kinetics reported here are in agreement with the previously published kinetics for the humanized therapeutic variant of Fab LM609, Vitaxin(Wu et al., 1998). These results confirm grafting of murine CDRs onto the human antibody framework had minimal impact on the binding properties of this molecule.

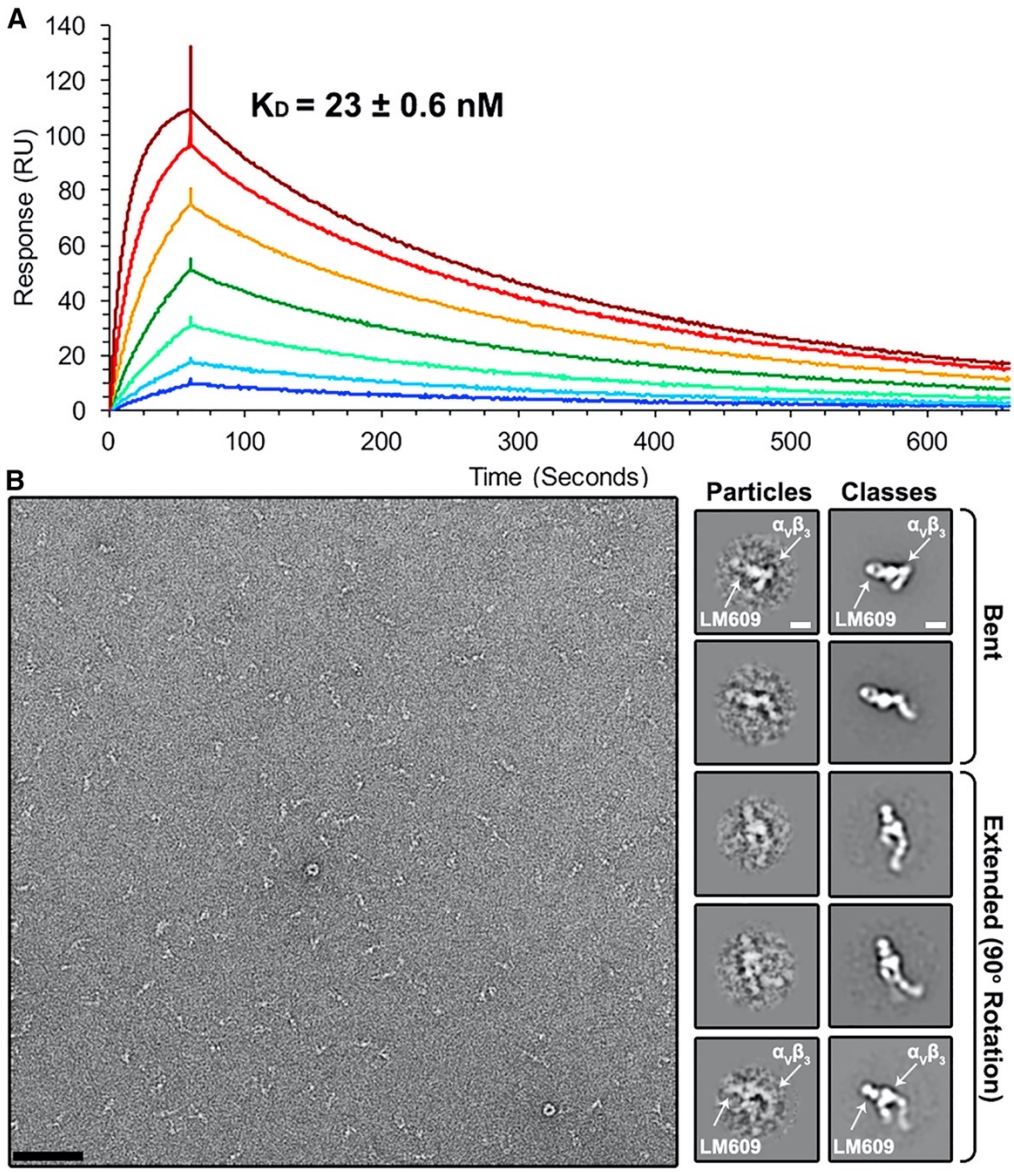

Figure 3.2. Characterization of the Fab LM609/$\alpha_V\beta_3$ Integrin Complex

(A) Kinetic analysis of LM609 binding to $\alpha_V\beta_3$ using surface plasmon resonance. Each curve on the sensorgram corresponds to a different concentration of LM609 (analyte): 7.8 nM (dark blue); 15.6 nM (light blue); 31.2 nM (light green); 62.5 nM (dark green); 125 nM (orange); 250 nM (red); 500 nM (dark red). (B) (Left) Raw electron micrograph of negatively stained Fab LM609/$\alpha_V\beta_3$ integrin complex. (Right) Raw particles (low-pass filtered to 20-Å resolution) and resulting 2D class averages of various conformations of the integrin/LM609 complex. Scale bars, 652 Å (micrograph) and 60 Å (class averages). *Adapted from (Borst et al., 2017)

3.4 LM609 SPECIFICALLY BINDS TO THE A_VB_3 INTEGRIN HEADPIECE REGION

Multiple structural studies have demonstrated the $\alpha_V\beta_3$ heterodimer can assume a bent, inactive conformation with the integrin "leg" domains wrapped around the headpiece. In addition, several different extended conformations representative of different stages of integrin activation have also been reported(Takagi et al., 2002; Xiao et al., 2004; Xiong et al., 2002, 2001). Imaging of the complex formed between human $\alpha_V\beta_3$ integrin and the Fab LM609 using negative staining electron microscopy revealed LM609 binds to all observed, bent or extended, $\alpha_V\beta_3$ conformational states **(Fig. 3.2B)**. This result suggests that complex formation with Fab LM609 does not require the $\alpha_V\beta_3$ ectodomain to be in a defined conformational state.

An iterative computational strategy was used to obtain homogeneous 2D class averages corresponding to various integrin conformational snapshots(Lyumkis et al., 2014; Veesler et al., 2014). In all resolved conformations, LM609 interacts with the $\alpha_V\beta_3$ headpiece domain **(Fig. 3.2B)**. The orientation of the Fab relative to $\alpha_V\beta_3$ was determined from the 2D class averages by identification of the typical Fab top and side views bound to the closed and open integrin conformations, respectively(Wu et al., 2012). Analysis of 2D class averages suggests the LM609 epitope is at the interface between the β-propeller domain of the α_V chain and the βI domain of the β_3 chain **(Fig. 3.2B)**; both domains could be distinguished due to the typical triangular shape of the headpiece apex region. In contrast, attempted complex formation between Fab LM609 and $\alpha_{IIb}\beta_3$ and visualization using negative staining EM yielded no detectable complexes **(Fig. 3.3)**. This result corroborates the early observation that LM609 specifically binds to $\alpha_V\beta_3$ but not to $\alpha_{IIb}\beta_3$(Wu et al., 1998), in conflict with a recent report suggesting LM609 may bind solely to the β_3 integrin subunit(Kamata et al., 2013).

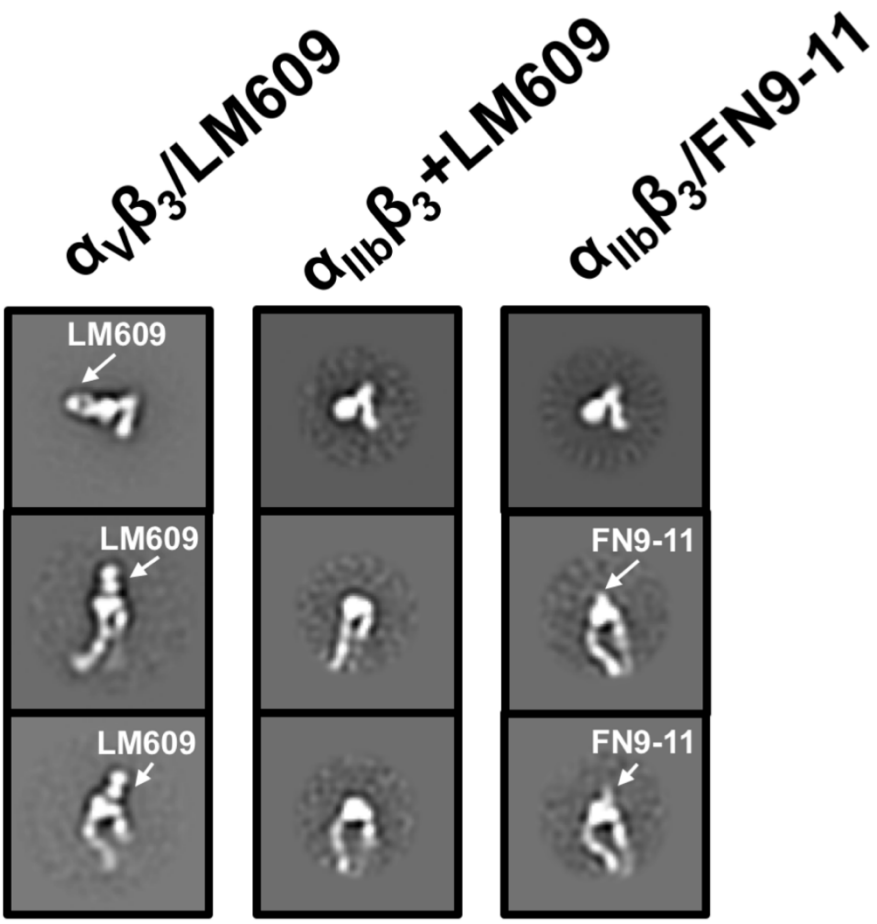

Figure 3.3. LM609 specifically binds to αVβ3but not to αIIbβ3.

2D class averages ofαVβ3 integrin in the presence of LM609 (first column), αIIbβ3 integrin in the presence of LM609 (second column) and αIIbβ3 integrin in the presence of FN9-11 (positive control, third column). *Adapted from (Borst et al., 2017)

We used the random-conical tilt (RCT) approach to compute 3D reconstructions from each independent 2D class average of the integrin conformational ensemble(Radermacher, 1988). The resulting density maps **(Fig. 3.4A-B & E-F, and Fig. 3.5)** are in excellent agreement with the corresponding class averages with observed $\alpha_V\beta_3$ conformers readily assigned to known integrin functional states(Chen et al., 2010b; Takagi et al., 2002; Zhu et al., 2008). We obtained pseudo-atomic models of the $\alpha_V\beta_3$/LM609 complex by fitting the Fab LM609 crystal structure reported here along with a previously determined $\alpha_V\beta_3$ integrin crystal structure (Xiong et al., 2001) into the 3D reconstructions using Rosetta CM (Song et al., 2013) **(Fig. 3.5C-D & G-H, Fig. 3.5A)**. These maps provide enough features to fit the LM609 Fab and determine its approximate position and orientation relative to the integrin headpiece. The 3D models support the proposed location of the LM609 epitope on the $\alpha_V\beta_3$ integrin headpiece apex at the interface between the β-propeller and βI domains, with the assigned orientation of LM609 further corroborated by the majority of contacts residing within the Fab heavy chain CDRs. However, the 2-fold pseudo-symmetry of LM609 prevents unequivocal placement of the Fab relative to the integrin apex due to the limited resolution of the RCT reconstructions. Electrostatic surface potential calculations of $\alpha_V\beta_3$ integrin show that the headpiece apex, which includes the LM609 epitope, features a predominantly negatively charged surface **(Fig. 3.4I-J)**. It is likely that the electrostatic complementarity of the paratope and epitope contributes to the high binding-affinity of LM609 for the $\alpha_V\beta_3$ integrin apex.

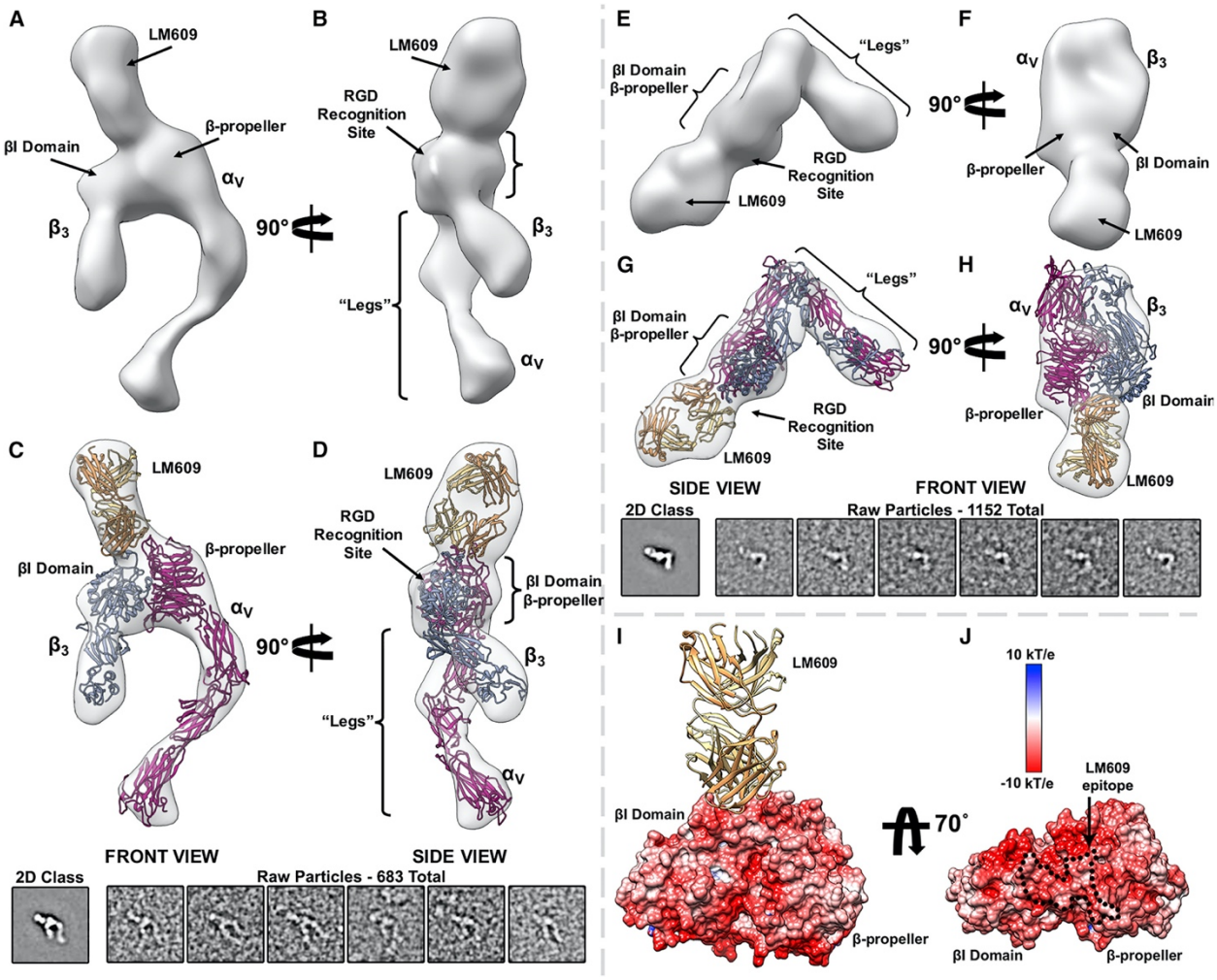

Figure 3.4. Structure of the Fab LM609/$\alpha_V\beta_3$ Integrin Complex Determined by EM

(A and B) Two orthogonal views of a random conical tilt 3D reconstruction featuring an $\alpha_V\beta_3$ integrin extended state. (C and D) Corresponding views related to (A) and (B) showing the fit of the pseudo-atomic model obtained with Rosetta (ribbon) into the reconstruction (transparent surface). The lower panel depicts the associated 2D class average and a few raw particles (low-pass filtered to 20-Å resolution) used for the RCT reconstruction of the integrin/LM609 extended state. (E and F) Two orthogonal views of a random conical tilt 3D reconstruction featuring an $\alpha_V\beta_3$ integrin bent state. (G and H) Corresponding views related to (E) and (F) showing the fit of the pseudo-atomic model obtained with Rosetta (ribbon) into the reconstruction (transparent surface). The lower panel depicts the associated 2D class average and a few raw particles (low-pass filtered to 20-Å resolution) used for the RCT reconstruction of the integrin/LM609 bent state. (I) Ribbon

diagram of the Fab LM609 bound to the integrin headpiece. Only the β propeller of the α_V subunit and the βI domain of the β_3 subunit are shown in surface representation colored by electrostatic potential. LM609 is represented as yellow and orange ribbons corresponding to the heavy and light chains, respectively. (J) Corresponding view related to (I) rotated by 70°. The approximate epitope of the LM609 Fab is indicated with black dashed lines and features a pronounced negative electrostatic potential. $\alpha_V\beta_3$ is represented as fuchsia (α_V) and light blue (β_3) ribbons in panels (C), (D), (G), and (H). *Adapted from (Borst et al., 2017)

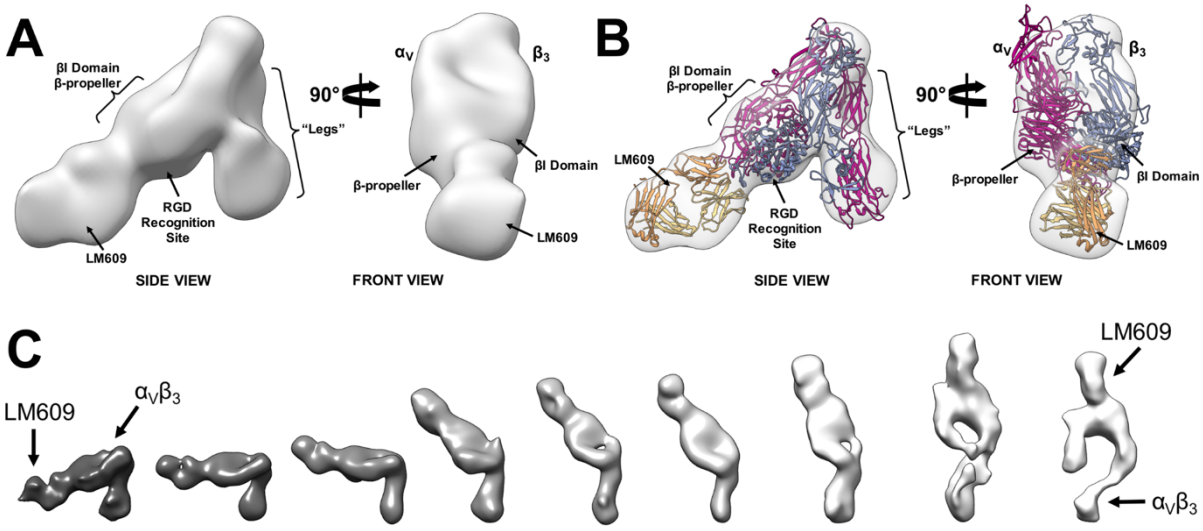

Figure 3.5. Conformational ensemble of the Fab LM609/αVβ3 integrin complex.

(A) Two orthogonal views of a random conical tilt 3D reconstruction featuring the canonicalαVβ3integrin bent/inactive state.(B) Corresponding views related to (A) showing the fit of an αVβ3crystal structure (PDB: 3IJE) and the crystal structure of the LM609 Fab (determined here) docked with Rosetta (ribbon) into the reconstruction (transparent surface).This model was used during the first stage of Rosetta refinement preceding the stepwise refinement of the more open αVβ3integrin conformational states. (C) Random conical tilt 3D reconstructions showing LM609 bound to all observed integrin conformations ranging from bent to extended states. *Adapted from (Borst et al., 2017)

3.5 THE LM609 EPITOPE DOES NOT OVERLAP WITH THE RGD LIGAND BINDING POCKET

Previous reports have shown that LM609 prevents binding of extracellular ligands to the RGD-binding pocket of $\alpha_V\beta_3$ integrin (Charo et al., 1990; Cheresh, 1987). Since the LM609 Fab does not appear to overlap with the RGD binding pocket in any of the integrin conformations observed, we set out to elucidate the mechanism associated with competitive binding. We used fluorescence size-exclusion chromatography (Hattori et al., 2012; Kawate and Gouaux, 2006) to determine if $\alpha_V\beta_3$ can bind to a fluorescein isothiocyanate-tagged RGD peptide, FITC-GRGDSPK (FITC-RGD), in the absence or presence of bound LM609 Fab **(Fig. 3.6A)**. As expected, FITC-RGD could bind to integrin $\alpha_V\beta_3$ in the absence of LM609. FITC-RGD could also bind to $\alpha_V\beta_3$, with the same magnitude, following pre-incubation of $\alpha_V\beta_3$ with a saturating amount of Fab LM609. The earlier elution volume observed for the $\alpha_V\beta_3$/FITC-RGD/LM609 peak relative to the $\alpha_V\beta_3$/FITC-RGD peak combined with tryptophan and FITC-RGD fluorescence data confirmed both ligands could simultaneously bind to $\alpha_V\beta_3$, ruling out competitive binding to the same epitope. We next showed that pre-incubation of $\alpha_V\beta_3$ with a cyclic RGD peptide prevented FITC-RGD binding, demonstrating competition would occur between LM609 and FITC-RGD if they were competing for the same epitope **(Fig. 3.7)**. Although previous studies reported that LM609 inhibits RGD-mediated ligand binding (Charo et al., 1990; Cheresh, 1987), our data further clarify that this antibody does not directly occlude the RGD-binding pocket. Instead, LM609 likely precludes binding of large RGD-ligands via steric hindrance.

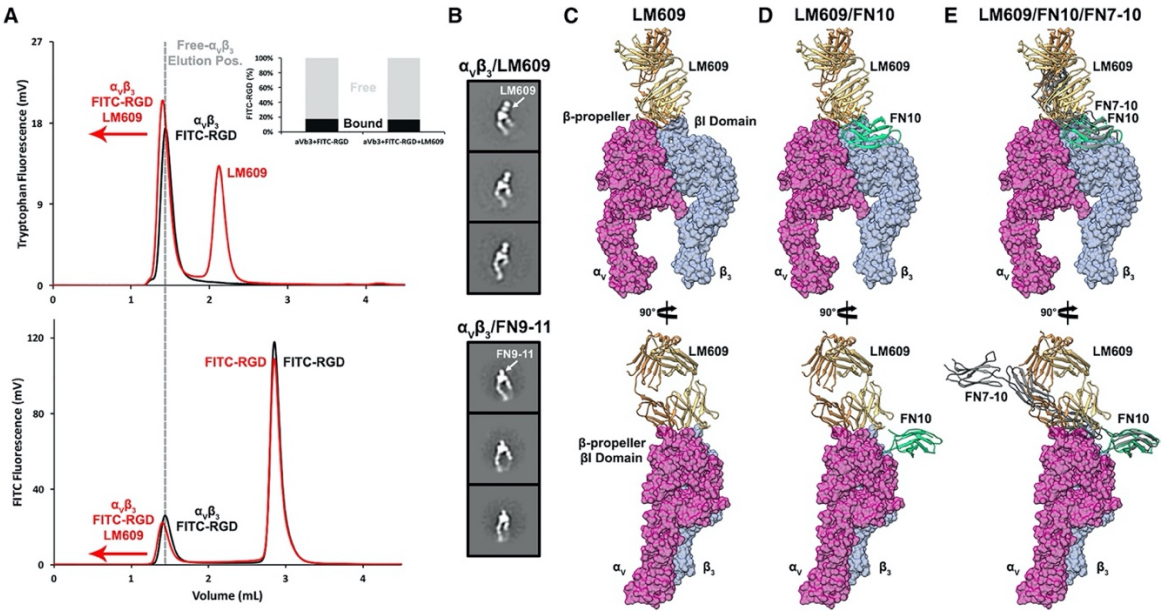

Figure 3.6. Structure of the Fab LM609/$\alpha_V\beta_3$ Integrin Complex Determined by EM

(A) Fluorescence size-exclusion chromatography profiles revealing that FITC-RGD binds integrin $\alpha_V\beta_3$ in the presence of a saturating amount of LM609 Fab. (Top) Tryptophan fluorescence elution profile of $\alpha_V\beta_3$/FITC-RGD in the absence (black) or presence (red) of LM609. (Bottom) FITC fluorescence elution profile of $\alpha_V\beta_3$/FITC-RGD in the absence (black) or presence (red) of LM609. The dotted gray line indicates the elution volume corresponding to $\alpha_V\beta_3$ in the absence of bound LM609. In both panels, binding of LM609 shifts integrin $\alpha_V\beta_3$ to earlier elution volumes. (Inset) Relative amounts of free (gray) and integrin $\alpha_V\beta_3$-bound (black) FITC-RGD peptide plotted in the absence and presence of LM609, demonstrating that LM609 does not compete with small RGD-containing ligands for binding to $\alpha_V\beta_3$ integrin. (B) LM609 binds to $\alpha_V\beta_3$ integrin in the vicinity of the region mediating attachment of physiological ligands such as fibronectin. Shown are 2D class averages of extended $\alpha_V\beta_3$ integrin in the presence of LM609 (upper column) or FN9-11 (lower column). (C–E) Two orthogonal views of a surface representation of the $\alpha_V\beta_3$ headpiece with bound LM609 (C), with bound LM609 and the domain 10 of fibronectin type III (FN10) (D), and with bound LM609, FN10, and the domains 7–10 of fibronectin type III (FN7-10) (E). Pseudo-atomic models were derived by superimposing the β-propeller and βI domains from the $\alpha_V\beta_3$/FN10 complex crystal structure (PDB: 4MMX) onto the model presented in Figure 3.4. The crystal structure of FN7-10 (PDB: 1FNF) was then superimposed onto the corresponding residues of FN10 to approximate its position and orientation relative to $\alpha_V\beta_3$ (C–E). *Adapted from (Borst et al., 2017)

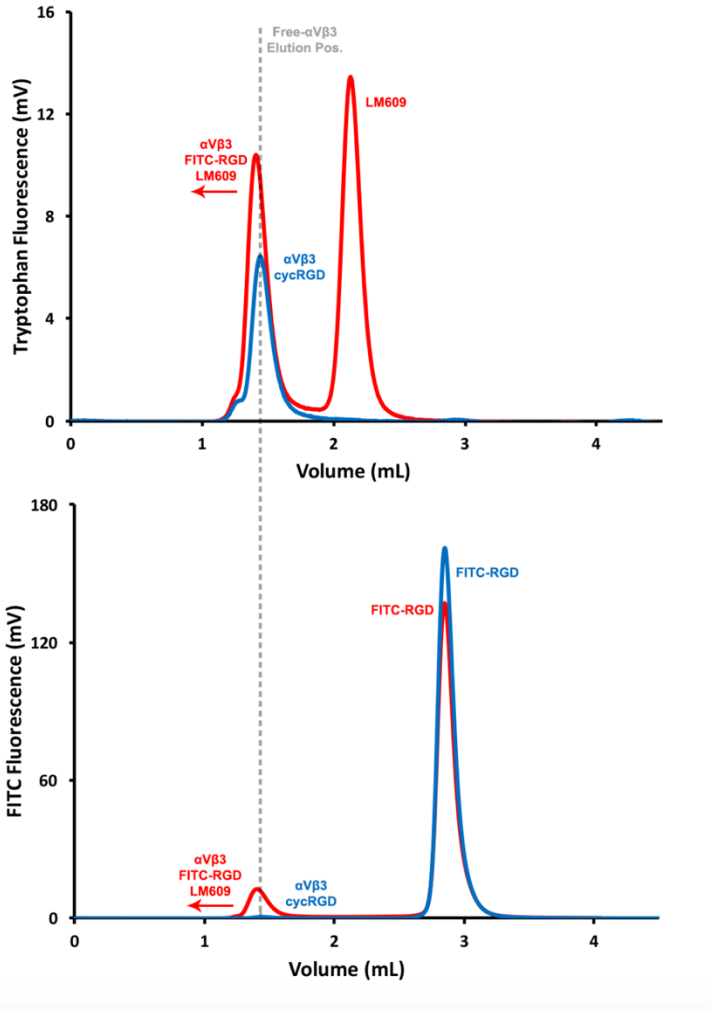

Figure 3.7. RGD peptides compete for the RGD-binding site on αVβ3, but not LM609. FSEC profiles showing FITC-RGD could bind integrin αVβ3 following pre-incubation with saturating amounts of LM609 Fab, but not following pre-incubation with saturating amounts of a competitive cyclic RGD peptide. (Top panel) Tryptophan fluorescence elution profile of αVβ3-FITC-RGD in the presence of LM609 (red) or in presence of acyclic RGD peptide (blue). (Bottom panel) FITC fluorescence elution profile of αVβ3-FITC-RGD in the presence of LM609 (red) or in the presence of a cyclic RGD-peptide (blue). The dotted grey line indicates the elution volume corresponding to αVβ3in the absence of bound LM609. Binding of LM609 shifted integrinαVβ3to earlier elution volumes, whereas binding of cyclic RGD peptide did not. When αVβ3 was pre-incubated with cyclic RGD peptide, minimal FITC fluorescence was observed in the integrin elution peak, indicating competition occurs between these two peptides, unlike with LM609, which does not directly occlude the RGD-binding site. *Adapted from (Borst et al., 2017)

3.6 CONCLUSIONS, DISCUSSION, AND FUTURE DIRECTIONS

Our EM results demonstrate LM609 binds to the $\alpha_V\beta_3$ integrin headpiece apex in the vicinity of the region mediating attachment of physiological ligands such as vitronectin, fibrinogen, or fibronectin **(Fig. 3.6B-D and Fig. 3.7)**. Whereas numerous endogenous binders rely on an exposed RGD motif for interactions with integrin, no such motif is present in LM609. Although both RGD-independent (LM609) and RGD-dependent (e.g. fibronectin) binding involve contacts with the β-propeller of the α_V subunit and the βI domain of the β_3 subunit, distinct sets of interactions mediate attachment in each case **(Fig. 3.6C)**. As a result, LM609 binding to $\alpha_V\beta_3$ does not directly occlude the RGD binding site. However, *in vitro* studies demonstrated LM609 inhibits fibronectin binding to $\alpha_V\beta_3$(Charo et al., 1990). Superposition of the fibronectin type III repeats 7-10 structure (Leahy et al., 1996) (FN7-10, PDB 1FNF) onto the corresponding domain of the $\alpha_V\beta_3$ integrin/FN10 complex structure (Van Agthoven et al., 2014) (PDB 4MMX) reveals the mechanism underlying LM609-mediated inhibition of $\alpha_V\beta_3$ (Charo et al., 1990): binding of LM609 to the integrin headpiece would likely sterically hinder subsequent attachment of fibronectin due to the expected clashes with FN domains 8 and 9 **(Fig. 3.6D and Fig. 3.8)**. Previous reports also showed LM609 can inhibit the binding of fibrinogen to $\alpha_V\beta_3$ integrin *in vitro* (Wu et al., 1998). The structural and biophysical data reported here suggest this is mediated through a mechanism of steric hindrance due to the comparably large sizes of fibrinogen and fibronectin (Mosesson, 2005), and the ability of the FITC-RGD peptide to bind to LM609-bound integrin $\alpha_V\beta_3$ **(Fig. 3.6A)**. This inhibition mechanism allows rationalizing the properties of this antibody that has been shown to inhibit angiogenesis and bone resorption *in vivo*. These results also explain why LM609 inhibits infection of RGD-containing viruses such as Parechovirus and Kaposi's Sarcoma-Associated Herpesvirus (Garrigues et al., 2008; Triantafilou et al., 2000). In our experiments, Fab LM609

could bind to all observed integrin conformational states, including the bent state. This argues that LM609 has the potential to interact with $\alpha_V\beta_3$ receptors prior to inside-out signal activation, which could be leveraged for future therapeutic strategies. Similarly to what has been proposed for the 17E6 antibody(Mahalingam et al., 2014), the full-length LM609 antibody might also interfere with integrin clustering or promote integrin internalization, therefore enhancing therapeutic effects relative to the monovalent Fab LM609.

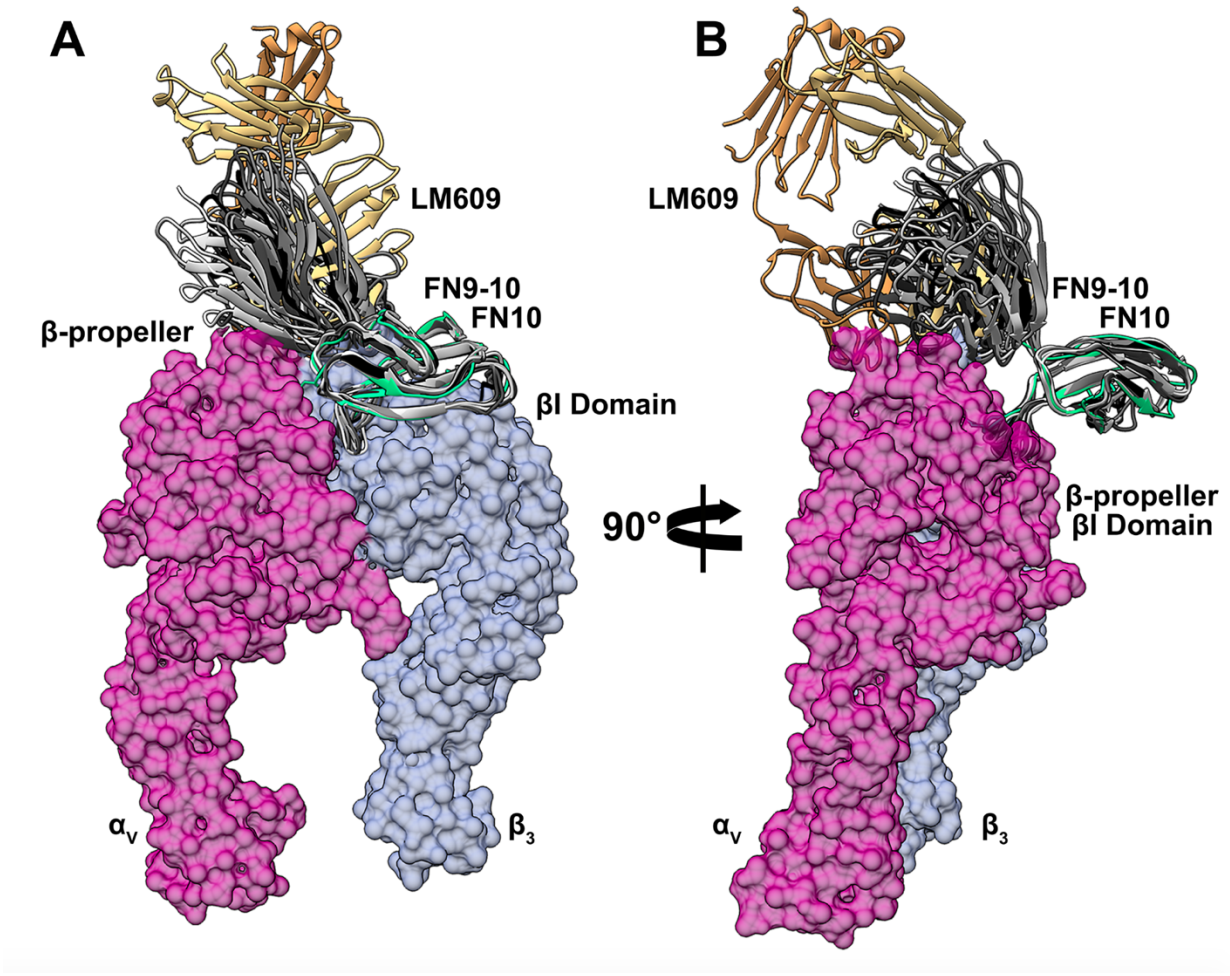

Figure 3.8. Binding of LM609 or FN9-10 to αVβ3 integrin are mutually exclusive. (A) Surface representation of the αVβ3 headpiece with both LM609 and FN9-10 bound (an ensemble of 10 models derived by NMR, PDB: 2MFN). (B) Corresponding view related to (A) rotated by 90˚. The known flexibility of the FN9-10 inter-domain linker would not circumvent the steric hindrance resulting from LM609 binding. The relative positions of LM609 and FN10 were derived by superimposing the β-propeller and β-I domains from the αVβ3/FN10 complex crystal structure (PDB: 4MMX) onto the model presented in Figure 3. The NMR ensemble structures of FN9-10 (PDB: 2MFN) were then superimposed onto the corresponding residues of FN10 to approximate their position and orientation relative to αVβ3. *Adapted from (Borst et al., 2017)

Our results shed light on the previously cryptic binding mode of an antibody that has been extensively studied for academic, preclinical, and clinical research applications. Many current RGD-based anti-integrin drugs have low specificity and act primarily as agonists for all integrins recognizing the RGD motif (Van Agthoven et al., 2014). In contrast, the high specificity of LM609 for $\alpha_V\beta_3$ and the absence of selection for activated conformational states makes it a promising antagonistic candidate for future work directed towards $\alpha_V\beta_3$-positive cancerous tumors and as a competitive binder against RGD-containing viruses targeting integrin $\alpha_V\beta_3$ as a receptor for infection. Finally, the specificity of LM609 for $\alpha_V\beta_3$ raises the possibility of developing antibody-drug conjugates directing therapeutic compounds to $\alpha_V\beta_3$ integrin-expressing cell-types. We expect the data reported here will expedite efforts utilizing LM609 as a potential diagnostic or therapeutic tool for a variety of human diseases.

3.7 METHODOLOGY

3.7.1 *Protein expression and purification*

The synthetic genes encoding human integrin α_V and β_3 subunits (NCBI accession codes NM_002210 and NM_000212), were optimized for expression in insect cells and purchased from Genscript. These genes were used as a template for PCR amplification of the regions encoding the ectodomains and comprising residues 31-987 and 27-718, for α_V and β_3 subunits, respectively (numbering corresponds to that of the immature proteins). Each amplified DNA fragment was cloned into pT350 vector(Krey et al., 2010), which contains BiP secretion signal peptide and the inducible metallothionein promoter, activated by divalent cations. *Drosophila* S2 cells were co-transfected with the plasmids carrying the α_V and β_3 ectodomain genes, and stably-transfected cell lines were established(Backovic and Krey, 2016). The protein expression was induced by 0.5mM $CuSO_4$. Supernatants containing the $\alpha_V\beta_3$ ectodomain were collected 7 days after induction.

Recombinant Fab LM609 was also produced in *Drosophila* S2 cells, using the expression strategy developed for obtaining milligram quantities of recombinant Fabs(Backovic et al., 2010). Genes encoding the variable fragments of the light and heavy chains (V_L and V_H, respectively) of the mouse LM609 antibody (Rader et al., 1998), were optimized for expression in insect cells and cloned into a bicistronic vector, that already contained the mouse IgG1 constant regions CL_1 and CH_1. Protein secretion was driven by the BiP signal peptide, and the heavy chain was tagged with a double strep tag at the C-terminus, allowing affinity purification using streptactin resin. The Fab was further purified using a Superdex 75 size exclusion column run in a buffer containing 10mM Tris pH 8 and 50mM NaCl (Backovic et al., 2010).

To obtain integrin-Fab complexes, the supernatants of S2 cells expressing the integrin were mixed with purified Fabs, and run over streptactin column. The eluted material contained the mixture of integrin-Fab complexes and the excess, unbound Fab. The two forms were separated using size exclusion chromatography, and the fractions corresponding to the peak containing the complex were concentrated. Additional $\alpha_V\beta_3$ and $\alpha_{IIb}\beta_3$ ectodomain constructs were purchased from R&D Systems.

BL21DE3 cells containing the plasmid GST-FN9-11 pGEX6P1 were grown at 37°C until an OD_{600} of 0.7 was reached. Protein expression was induced overnight at 37°C using 1mM IPTG. Cells were harvested via centrifugation, resuspended in 20 mM Tris pH 7.4, 150 mM NaCl, 5 mM DTT, 0.1 mM PMSF and kept at 4°C for 30 minutes before sonication. The cell lysate was clarified via centrifugation at 14,000 RPM for 20 minutes at 4°C and the resulting supernatant was incubated overnight at 4°C with chronic nutation in the presence of 1.5 mL of GSH-Agarose resin. The resin was subsequently poured over a disposable column to remove unbound proteins. Elution was achieved with a buffer containing 50 mM Tris-HCl pH 8.0, 15 mM GSH after a 10-minute incubation period at 4°C. Fractions containing GST-FN9-11 were dialyzed into PBS at 4°C to remove excess GSH and DTT. Cleavage of GST was performed using PreScission protease for 1 hour at 4°C. Cleaved FN9-11 was further incubated for 2 hours at 4°C with 1.5 mL GSH-Agarose resin to allow removal of free GST and uncleaved GST-FN9-11. GSH-Agarose beads were centrifuged at 4,000 RPM for 20 minutes and purified FN9-11 was collected from the supernatant.

3.7.2 *Crystal structure of LM609*

Recombinant LM609 Fab in 10mM Tris pH 8, 50mM NaCl was concentrated to 7.7 mg/ml and used for screening of crystallization conditions. Sitting drops were set up at 18°C by mixing equal volumes of protein and crystallization solutions. Crystals appeared in the condition containing 0.1M HEPES pH 7.5, 30% PEG 4,000 and 0.2M $CaCl_2$, and were cryo-cooled by plunging into liquid nitrogen, after equilibration in the same buffer containing 20% glycerol as a cryoprotectant.

X-ray data were collected at the microfocus beamline PX2 at the French national synchrotron facility (SOLEIL), and processed using the XDS package (Kabsch, 2010). Molecular replacement was done using Phaser (McCoy et al., 2007) and Fab PDB code 2ADG as a search model (Zhou et al., 2005). An atomic model was built in Coot (Emsley et al., 2010) and refined using Buster (Blanc et al., 2004). The heavy and light chains of Fab LM609 contain 217 and 214 residues, respectively, and continuous electron density accounts for the majority of both chains. No density was observed for residues 133-135 of the heavy chain, and residues 1 and 214 of the light chain, which were omitted from the model.

3.7.3 *Surface plasmon resonance*

$\alpha_V\beta_3$ integrin was reconstituted from lyophilized powder at 0.5 mg/mL in 10 mM HEPES pH 8.0, 50 mM NaCl, 2 mM $MnCl_2$, 0.05% P20 buffer. Amine coupling of 0.025mg/mL $\alpha_V\beta_3$ integrin was achieved in Sodium Acetate, pH 4.0 to a CM5 chip with a target immobilization of 1000 response units. The Fab LM609 was injected over the CM5 flow cells with a contact time of 60 seconds at a flow-rate of 60 µL/min. Fab LM609 concentrations used for kinetic analysis ranged between 7.8 nM and 500 nM. Fab LM609 dissociation from $\alpha_V\beta_3$ occurred over 600 seconds with

a flow rate of 60 µL/min. Regeneration of $\alpha_V\beta_3$ was accomplished by pulsing 10 mM glycine, pH 1.5 for 4 seconds at a flow rate of 30 µL/min. Experiments were performed in triplicate for each concentration of Fab LM609 tested.

3.7.4 *Negative-stain EM specimen preparation*

LM609/$\alpha_V\beta_3$ samples for random conical tilt experiments were negatively stained using 2% uranyl-formate on glow-discharged C-flat 2/0.5 grids overlaid with a thin layer of carbon. FN9-11/$\alpha_V\beta_3$, FN9-11/$\alpha_{IIb}\beta_3$, and LM609+$\alpha_{IIb}\beta_3$ samples were negatively stained on glow-discharged G400 Gilder grids in 10 mM Tris pH 8.0, 150 mM NaCl, 2mM $MnCl_2$ using a five-fold molar excess of FN9-11 ligand and a 2.5 molar excess of Fab LM609. All integrin complex samples were deposited on carbon grids at a determined integrin concentration of 0.008 mg/mL.

3.7.5 *EM data collection and processing*

All data were collected on an FEI Tecnai Spirit 120 kV electron microscope equipped with a Gatan Ultrascan 4000 CCD Camera. 509 image-pairs (0° and ± 55°) were collected using a random defocus range of -1.1 to -2.0 µm with a total exposure of 30 $e^-/Å^2$. The pixel size at the specimen level was 1.60 Å. Data collection was performed using Leginon (Suloway et al., 2005) with the majority of the data processing carried out in Appion (Lander et al., 2009). The parameters of the contrast transfer function (CTF) were estimated using CTFFIND3 (Mindell and Grigorieff, 2003). All particles were picked in a reference-free manner using DoG Picker (Voss et al., 2009). Correlation of particle tilt pairs was performed using Auto Tilt Picker (Voss et al., 2009). Particles were extracted with a binning factor of 2 with an initial box size of 288 pixels for the LM609/$\alpha_V\beta_3$

dataset for both the tilted and untilted particle datasets. FN9-11/integrin particles were extracted with a box size of 256 pixels. CTF-correction on the particles from the micrographs collected at 0˚ tilt was performed via phase-flipping with EMAN 1.9. The LM609/$\alpha_V\beta_3$ particle stack from the micrographs collected at 0˚ tilt was pre-processed in Relion 1.3 (Scheres, 2012a) with an additional binning factor of 2 applied, resulting in a final box size of 72 pixels and a final pixel size of 6.4 Å. A binning factor of 2 was also applied to the FN9-11/integrin datasets, resulting in a final box size of 64 pixels at 6.4 Å/pix. 2D classification was carried out in Relion 1.3 (Scheres, 2012a) on 93,992 particles from the micrographs collected at 0˚ tilt and clustered into 256 independent classes for the LM609 dataset. 27,325 selected particles were further sorted into 128 additional classes through an additional round of 2D classification. FN9-11/integrin complexes were sorted into 256 classes, with the best particles sorted into additional groups. 11 reference-free class averages representative of different integrin conformational states were centered with EMAN 2.04 (Tang et al., 2007) and uploaded to Appion as templates for reference-based alignment using SPIDER (Shaikh et al., 2008) on corresponding particle sub-stacks. Resulting alignments were further clustered using SPIDER Coran (Tang et al., 2007). Random conical tilt reconstructions were computed from the resulting clustered classes using the initial model pipeline built into Appion and particle images extracted from micrographs acquired at a 55˚ tilt angle. Final resolution estimates for all reported LM609/$\alpha_V\beta_3$ models varied between 35 and 55 Å using an FSC correlation of 0.5. Movie generation of the Fab LM609/$\alpha_V\beta_3$ conformational ensemble was performed on 3D models using the animation feature embedded within UCSF Chimera (Goddard et al., 2007). The 3D reconstructions were aligned based on the determined position, rotation, and motion of the leg domains during activation relative to the LM609/$\alpha_V\beta_3$ headpiece fiducial.

3.7.6 *Fluorescence size exclusion chromatography*

The FITC-GRGDSPK peptide (96.7% purity, FITC-RGD) was purchased from GenScript and solubilized in ultrapure water. Integrins were prepared by dissolving lyophilized $\alpha_V\beta_3$ into 10 mM HEPES pH 8, 150 mM NaCl, 4mM $MnCl_2$, 0.05% Tween 20. Samples for FSEC were prepared using a final $\alpha_V\beta_3$ integrin concentration of 100 nM in 10 mM Tris pH 8, 50 mM NaCl, 2 mM $MnCl_2$. LM609 was added to corresponding integrin samples to a final concentration of 600 nM (6-fold molar excess) and allowed to incubate on ice for 30 minutes at 4°C. Subsequently, FITC-GRGDSPK was added at a final concentration of 600 nM (6-fold molar excess) to the appropriate aliquots of $\alpha_V\beta_3$ pre-incubated either in the presence or absence of 600 nM LM609 Fab (1:1 FITC-RGD:LM609). Each sample was allowed to incubate for an additional 15 minutes, centrifuged at 16,200 x g for 10 minutes, and then transferred to a fresh 2 mL microfuge tube. Finally, all samples were injected onto a Superdex 200 Increase 5/150GL (GE Healthcare) pre-equilibrated with 10 mM Tris pH 8, 50 mM NaCl, 2 mM $MnCl_2$ buffer while recording tryptophan fluorescence (λ_{Ex}= 280 nm, λ_{Em}= 325 nm). Samples containing FITC-RGD peptide were reinjected and recorded using FITC fluorescence (λ_{Ex}= 490 nm, λ_{Em}= 520 nm). Assessment of competition between FITC-RGD and cyclic RGD was carried out as a separate run. Cyclic RGD peptide was added to a final concentration of 600 nM (6-fold molar excess relative to $\alpha_V\beta_3$ integrin) and incubated on ice for 30 minutes at 4°C prior to addition of FITC-RGD peptide and subsequent FSEC analysis.

3.7.7 *Model generation*

Pseudo-atomic models of the various conformations of the LM609/$\alpha_V\beta_3$ integrin complex were generated using Rosetta. Starting from the $\alpha_V\beta_3$ crystal structure (PDB ID: 3IJE) (Xiong et al., 2009) and the LM609 crystal structure, *RosettaDock* (Lyskov and Gray, 2008) augmented with an energy term assessing agreement to experimental density (DiMaio et al., 2009) was run. Due to the limited resolution of the RCT reconstructions, the 2-fold pseudo-symmetry of LM609 prevented unequivocal placement of the Fab relative to the integrin apex. However, this docking experiment ultimately converged on a tight ensemble of conformations. Next, these models were flexibly fit to the nine different conformations observed in the RCT reconstructions. Due to the large conformational changes between the closed and open states, and the limited radius of convergence of our refinement, these models were iteratively fit, fitting first to the most closed state, then to the second most-closed state, and so on.

Refinement of models into each state consisted of a two-step approach: first, models were minimized in torsion space using a differentiable low-resolution "centroid" energy where protein side chains are represented by single interaction centers (Song et al., 2013). Next, all-atom refinement was carried out in Cartesian space using the Rosetta *FastRelax* protocol (Conway et al., 2014). During the first stage, weak intra-domain Gaussian atom-pair distance constraints were employed to ensure each chain did not move too far from the starting conformation. No additional driving forces were added other than the experimental data. Side chains were truncated at C_β in the deposited models due to the limited resolution of the reconstructions.

Chapter 4. THE IMPACT OF GLYCAN LENGTH ON GERMLINE ANTIBODY RECOGNITION OF HIV-1

4.1 CHAPTER SUMMARY

VRC01 broadly neutralizing antibodies (bnAbs) target the CD4-binding site ($CD4_{BS}$) of the human immunodeficiency virus-1 (HIV-1) envelope glycoprotein (Env). Unlike mature antibodies, corresponding VRC01 germline precursors poorly bind to Env. Immunogen design has mostly relied on glycan removal from trimeric Env constructs and has had limited success in eliciting mature VRC01 bnAbs. To better understand elicitation of such bnAbs, we characterized the inferred germline precursor of VRC01 in complex with a modified trimeric 426c Env by cryo-electron microscopy and a 426c gp120 core by X-ray crystallography, biolayer interferometry, immunoprecipitation, and glycoproteomics. Our results show VRC01 germline antibodies interacted with a wild-type 426c core lacking variable loops 1-3 in the presence and absence of a glycan at position Asn276, with the latter form binding with higher affinity than the former. Interactions in the presence of an Asn276 oligosaccharide could be enhanced upon carbohydrate shortening, which should be considered for future vaccine design strategies targeting the $CD4_{BS}$ of HIV-1.

4.2 CRYOEM STRUCTURE OF VRC01$_{GL}$ IN COMPLEX WITH A MODIFIED 426C HIV-1 SOSIP GLYCOPROTEIN TRIMER

Based on the known enhanced ability of VRC01$_{GL}$ (and related germline antibodies) to bind 426c constructs lacking putative NLGSs at positions Asn276, Asn460 and Asn463(McGuire et al., 2013), and the lack of detectable binding to 426c DS-SOSIP **(Fig. 4.1A)**, we engineered a modified 426c DS-SOSIP trimer recapitulating the aforementioned glycan depletion mutations for structural analysis. This construct harbors the S278A, T462A and T465A mutations, abolishing the corresponding NLGSs and enabling binding to VRC01$_{GL}$ **(Fig. 4.1B and Fig. 4.2)**. It also contains the SOSIP(Sanders et al., 2002) and the 201C-433C (DS) mutations(Kwon et al., 2015) and is a chimera of 426c gp120 and BG505 gp41(Joyce et al., 2017). This glycan-depleted protein construct is henceforth referred to as 426c DS-SOSIP D3 **(Fig. 4.2)**. The VRC01$_{GL}$ construct comprises the germline VH gene reverted sequences of VH1-2*02, which includes CDRH1 and CDRH2 along with the mature CDRH3 of VRC01 and the germline VK3-11 with the mature CDR L3 of VRC01 **(Fig. 4.3)**. Initial complex formation was evaluated using negative-staining EM, which revealed sub-stoichiometric binding of VRC01$_{GL}$ Fab to 426c DS-SOSIP D3 **(Fig. 4.4A)**. The VRC01$_{GL}$ Fab appeared to have a much lower affinity for 426c DS-SOSIP D3, compared to the VRC01$_{GL}$ IgG, the latter bound with an apparent equilibrium dissociation constant of 43 nM **(Fig. 4.1B),** neglecting the effect of avidity. We next attempted to enhance binding of VRC01$_{GL}$ Fab to 426c DS-SOSIP D3 by utilizing a mild glutaraldehyde cross-linking strategy. As expected, we observed significantly increased saturation of 426c DS-SOSIP D3 trimers by VRC01$_{GL}$ Fab, indicating covalent tethering following initial engagement of VRC01$_{GL}$ to the CD4$_{BS}$ was a suitable approach to enrich for and study VRC01$_{GL}$-bound complexes **(Fig. 4.3A)**. We therefore engineered a disulfide bond between G459C$_{gp120}$ (426c DS-SOSIP D3†) and the VRC01$_{GL}$ heavy

chain A60C (denoted as 426c DS-SOSIP D3†-VRC01$_{GL}$) **(Fig. 4.2 and Fig. 4.3)**. This strategy was previously employed to enhance binding of VRC01$_{MAT}$ to SOSIP trimers without altering interface contacts(Stewart-Jones et al., 2016). Using this method, we purified an enriched fraction of Fab-bound trimers and used this sample for structural characterization **(Fig. 4.1C, Fig. 4.4)**. This strategy led us to determine two cryoEM reconstructions of the 426c DS-SOSIP D3†-VRC01$_{GL}$ complex **(Fig. 4.1D-E, Fig. 4.3E-F, Fig. 4.4, and Table 4.3)**: one with three bound Fabs at 3.8Å resolution **(Fig. 4.1D, Table 4.3, Fig. 4.3E, Fig. 4.4A-B)**, and one with two bound Fabs at 4.8 Å resolution **(Fig. 4.1E, Fig. 4.3F, Fig. 4.4C-D)**.

Similarly to what was reported for the B41 SOSIP trimer(Ozorowski et al., 2017), the 426c DS-SOSIP D3†-VRC01$_{GL}$ V1/V2 apex is closed under cryoEM conditions **(Fig. 4.1D,E,F)** whereas it is open in the conditions we used for negative-staining sample preparation(Ozorowski et al., 2017) **(Fig. 4.3B)**. We note that the closed 426c DS-SOSIP D3†-VRC01$_{GL}$ trimeric Env conformation observed in cryoEM lacks a formed gp120 bridging sheet, which is reminiscent of other closed SOSIP trimer structures **(Fig. 4.1G)** (Julien et al., 2015; Lyumkis et al., 2013a; Pancera et al., 2014; Stewart-Jones et al., 2016). VRC01$_{GL}$-class antibodies have recently been shown to also bind to core gp120 constructs in the presence of a bridging sheet(Scharf et al., 2016). Our data reveals that VRC01$_{GL}$ could also bind a prefusion closed conformation, which had previously only been reported for its mature counterpart, VRC01$_{MAT}$(Stewart-Jones et al., 2016) **(Fig. 4.1G)**.

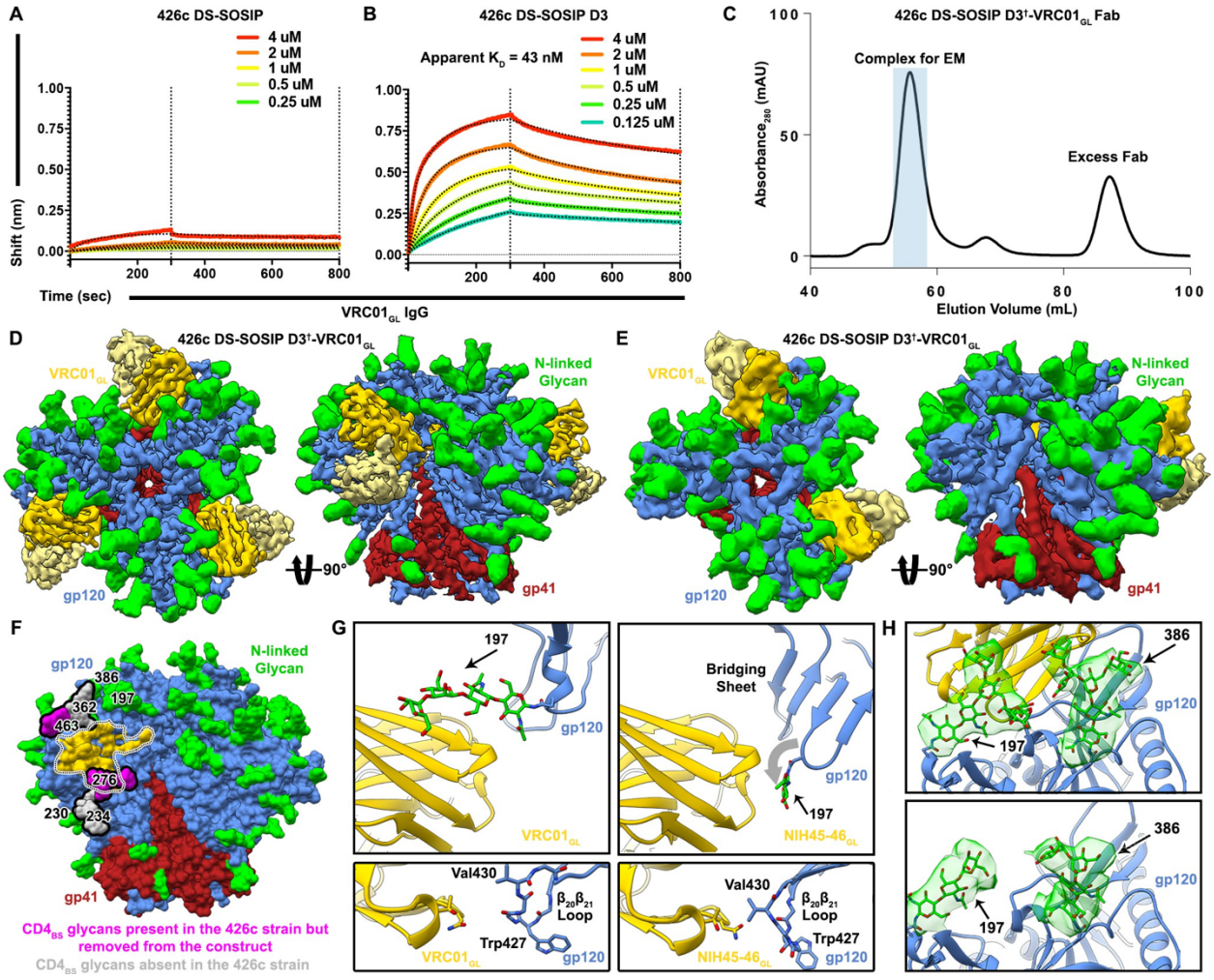

Figure 4.1. Structural characterization of the 426c DS-SOSIP D3†-VRC01$_{GL}$ complex. (A–B) BLI binding data of immobilized VRC01$_{GL}$ IgGs binding to WT 426c DS-SOSIP (A) or 426c DS-SOSIP D3 trimers. The concentrations of 426c DS-SOSIP trimers injected are indicated on each panel. Fit curves are colored as black dotted lines. A K_D could not be determined in (A) due to the weak responses observed. The vertical dotted lines indicate the transition between association and dissociation phases. (C) Size-exclusion chromatogram of the purified 426c DS-SOSIP D3†-VRC01$_{GL}$ complex used for cryoEM structure determination. The pooled fractions used for cryoEM are highlighted in light blue. (D) Two orthogonal views of the 3.8 Å cryoEM reconstruction sharpened with a B-factor of −250 Å^2 whereas the glycan density is shown unsharpened. (E) Two orthogonal views of the asymmetric 4.8 Å reconstruction with two bound Fabs. (F) Surface representation of the 426c SOSIP trimer highlighting differences in glycosylation compared to the BG505 SOSIP. Glycans not present in 426c are colored light-gray and outlined.

Glycans present in the 426c strain but removed by mutation from the 426c DS-SOSIP D3† construct are colored magenta and outlined. The gp120 surface buried at the interface with VRC01$_{GL}$ is indicated as a dotted outline and is colored yellow. (G) Comparison of the gp120 bridging sheet conformation when VRC01$_{GL}$-class Fabs are bound to either 426c DS-SOSIP D3† trimer (*Top-left*) or a previously solved 426c gp120 core lacking selected NLGSs, such as the Asn276 NLGS (PDB: 5IGX) (*Top-right*). Comparisons of $\beta_{20}\beta_{21}$ loop conformations of each complex are shown below corresponding top panels. (H) Comparison of glycan density and position between VRC01$_{GL}$-bound and VRC01$_{GL}$-free protomers in the asymmetric cryoEM reconstruction shown in (E). (*Top*) Asn197 and Asn386 glycan density is stronger for protomers bound to VRC01$_{GL}$ Fab than for the gp120 protomer not bound to VRC01$_{GL}$ (*Bottom*). In panels D-H, gp120 protomers are shown in blue, gp41 in red, N-linked glycans in green and VRC01$_{GL}$ in dark and light yellow for the heavy and light chains, respectively. *Adapted from (Borst et al., 2018)

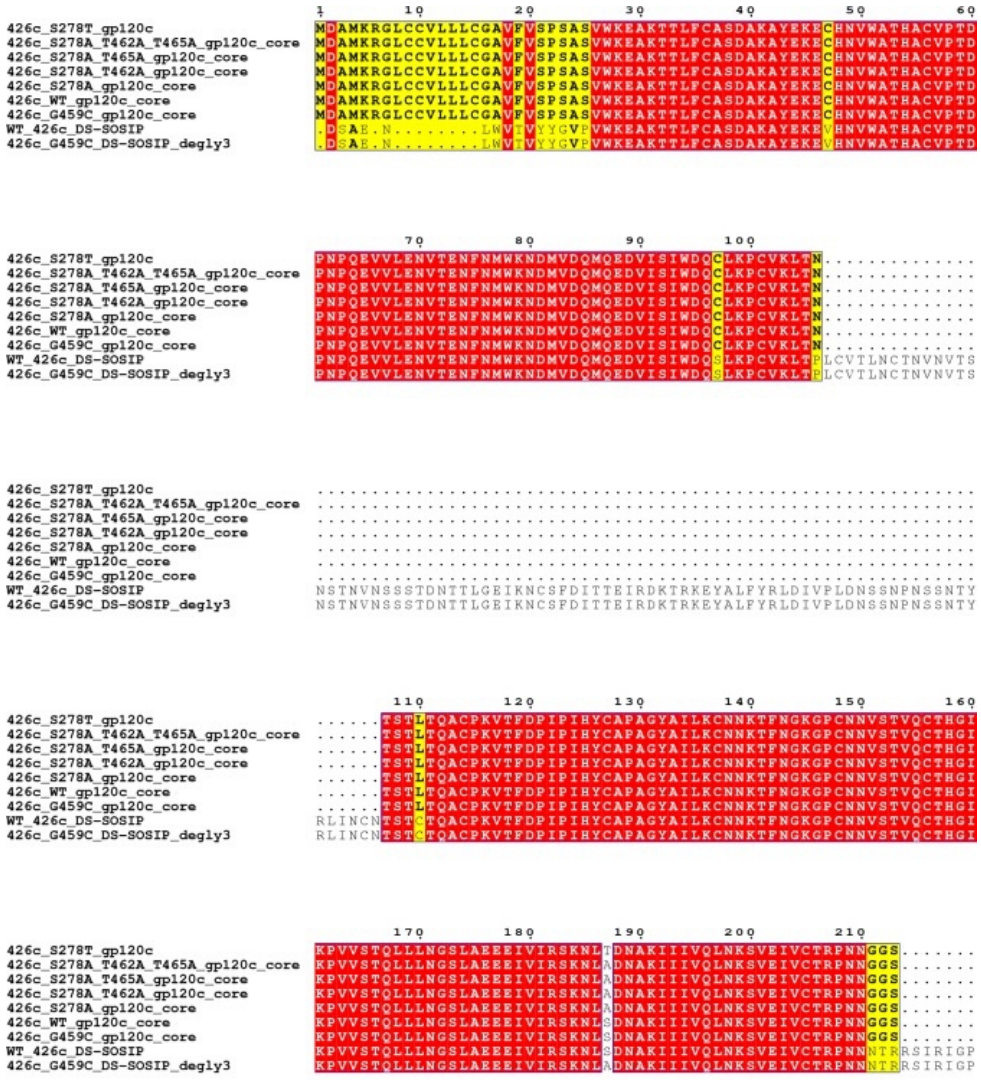

Figure 4.2.1 Multiple Sequence alignment of analyzed HIV-1 constructs.

HIV-1 constructs derived from the 426c strain used in this study were subjected to multiple sequence alignment using Clustal Omega and rendered using ESPript (Gouet et al., 1999; Sievers and Higgins, 2014). Residues highlighted in red signify identical amino acids conserved across all aligned constructs. Similar residues are highlighted in bold and colored yellow. *Adapted from (Borst et al., 2018)

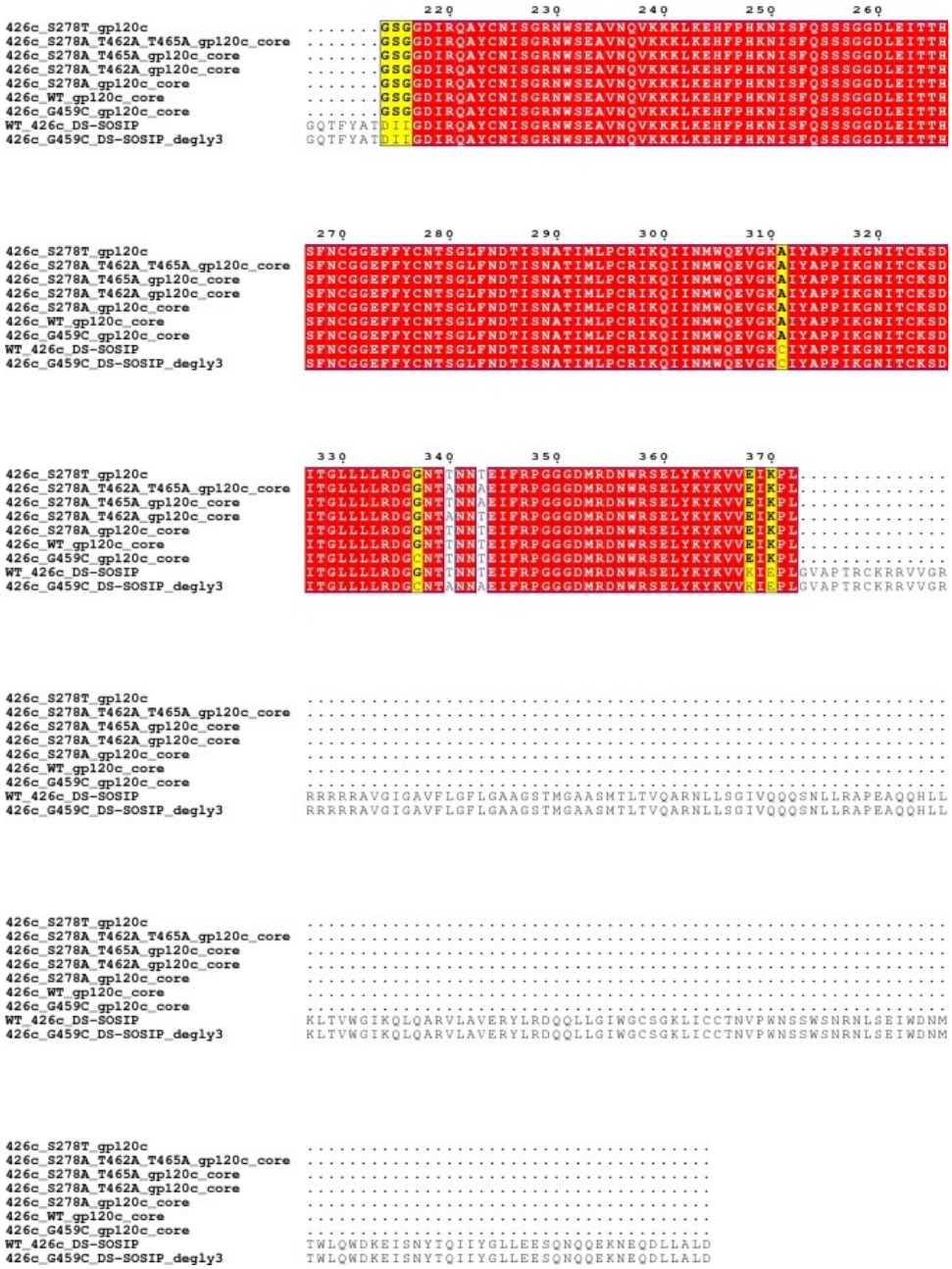

Figure 4.3.2 Multiple Sequence alignment of analyzed HIV-1 constructs.

HIV-1 constructs derived from the 426c strain used in this study were subjected to multiple sequence alignment using Clustal Omega and rendered using ESPript (Gouet et al., 1999; Sievers and Higgins, 2014). Residues highlighted in red signify identical amino acids conserved across all aligned constructs. Similar residues are highlighted in bold and colored yellow. *Adapted from (Borst et al., 2018)

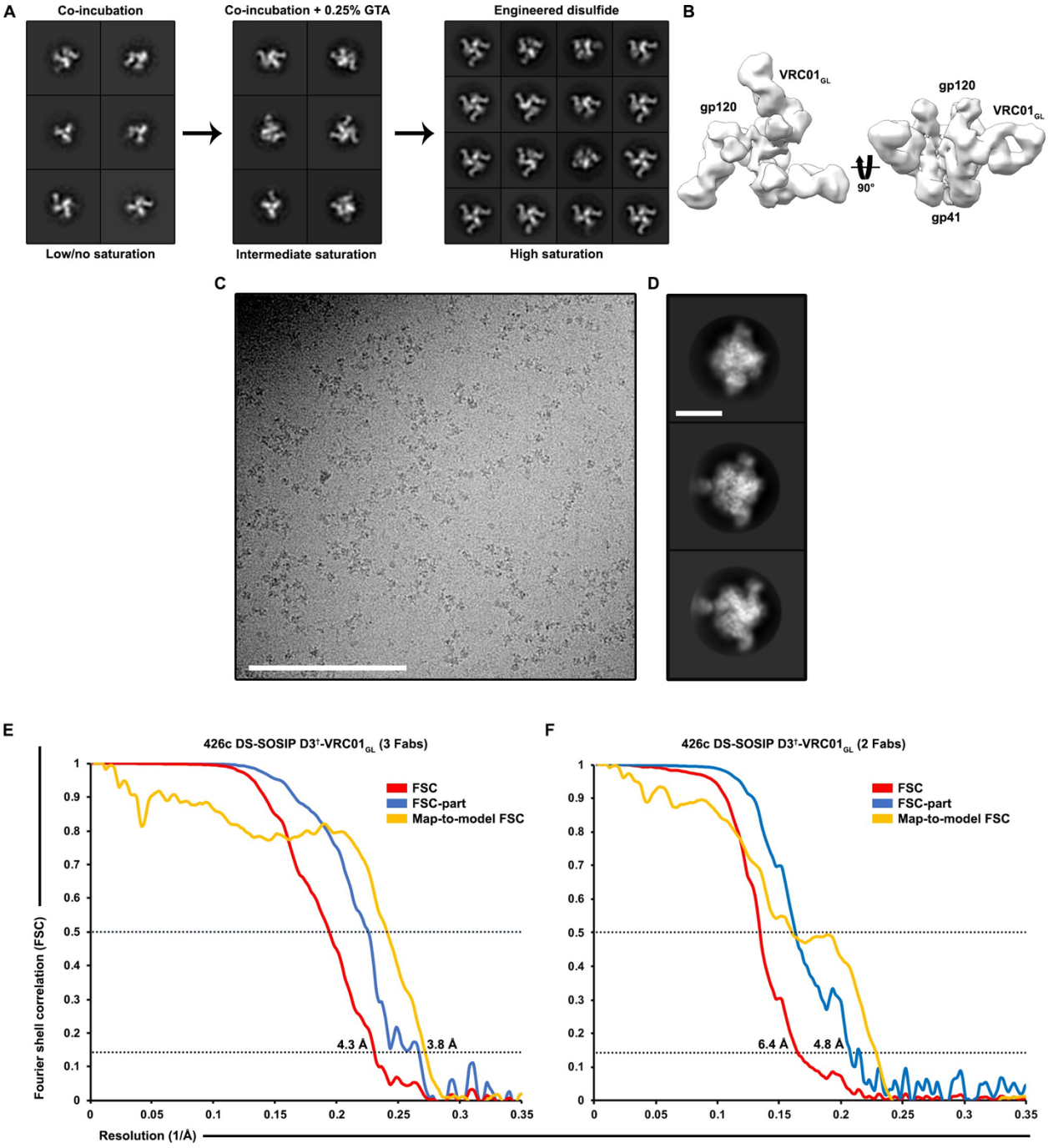

Figure 4.4. Further structural characterization of the 426c DS-SOSIP D3†-VRC01$_{GL}$ complex. (A) Strategy implemented to increase the occupancy of VRC01$_{GL}$ Fab for structural studies. VRC01$_{GL}$ can engage 426c DS-SOSIP D3, but its low apparent affinity relative to VRC01$_{GL}$ IgG precludes saturation at the concentrations used for negative staining EM imaging (*Left*). Mild

glutaraldehyde (GTA) crosslinking (0.25% GTA for 45 s followed by quenching with 1M Tris) increased $VRC01_{GL}$ saturation of 426c DS-SOSIP D3 (*Middle*). Engineering a disulfide bond between 426c DS-SOSIP D3 ($G459C_{gp120}$) and the heavy chain of $VRC01_{GL}$ ($A60C_{HC}$) further increased gp120 saturation of the trimer (*Right*). (B) 3D reconstruction of negatively stained 426c DS-SOSIP $D3^{\dagger}$-$VRC01_{GL}$. (C–D) Representative micrograph (E) and 2D class averages (F) of frozen-hydrated 426c DS-SOSIP $D3^{\dagger}$-$VRC01_{GL}$. Scale bars represent 200 nm (E) or 200 Å (F). (E) Fourier shell correlation (FSC) curves of the 426c DS-SOSIP $D3^{\dagger}$-$VRC01_{GL}$ complex with three Fabs bound showing an estimated resolution of 3.8 Å. (F) Fourier shell correlation curves of the 426c DS-SOSIP $D3^{\dagger}$-$VRC01_{GL}$ complex with two Fabs bound showing an estimated resolution of 4.8 Å. The top and bottom horizontal dashed lines show the 0.5 and 0.143 cutoffs used for resolution estimates for map-to-model or gold-standard FSC, respectively. Both conventional FSC and FSC-part, as reported in Frealign, are shown. *Adapted from (Borst et al., 2018)

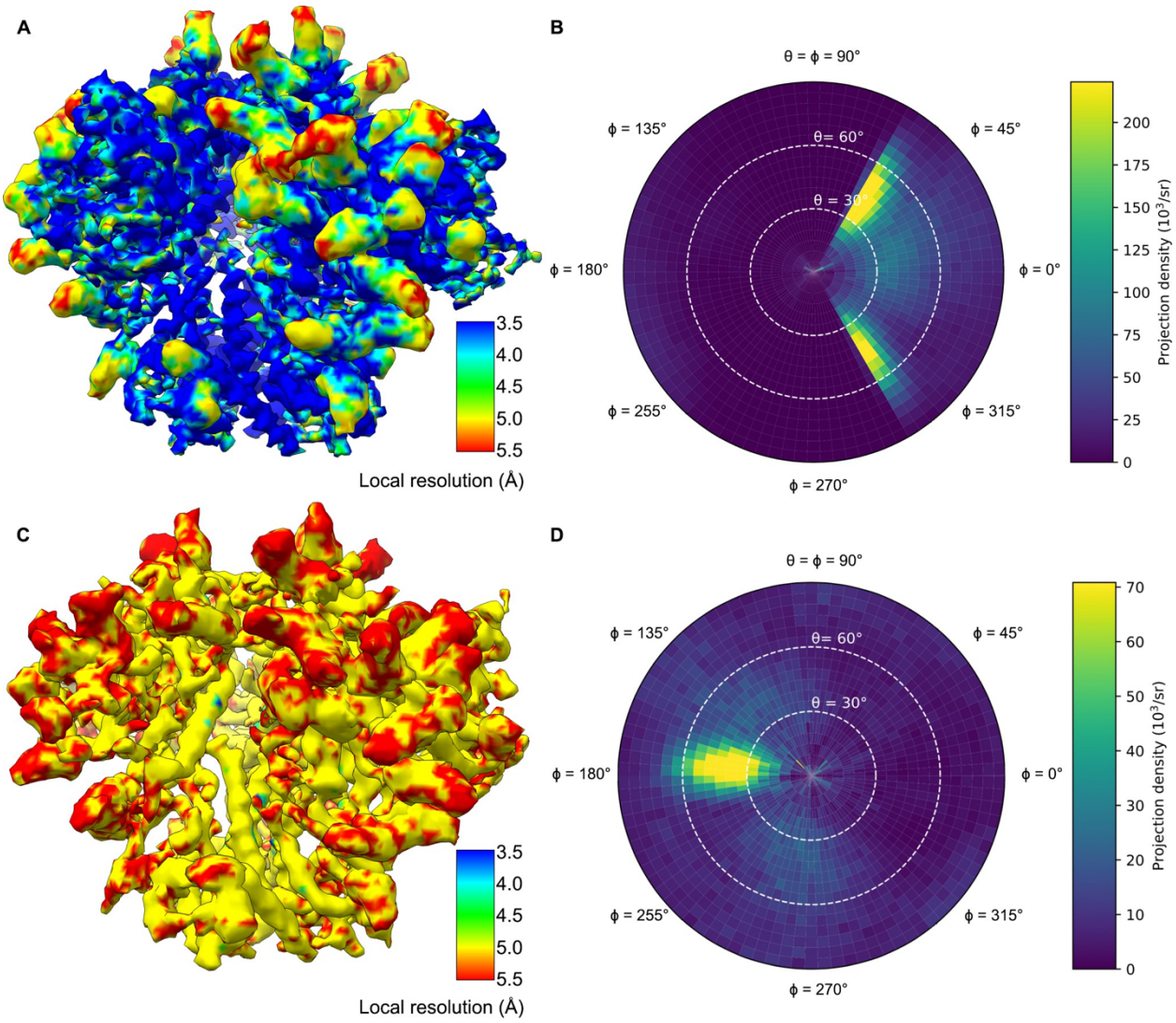

Figure 4.5. Validation of the 426c DS-SOSIP D3†-VRC01$_{GL}$ cryoEM reconstructions (A) Local resolution estimates of 426c DS-SOSIP D3† bound to three copies of VRC01$_{GL}$-A60C$_{HC}$ as determined using ResMap (Kucukelbir et al., 2014). (B) Graphical plot depicting distribution of particle image orientations. (C) Local resolution estimates of 426c DS-SOSIP D3† bound to two copies of VRC01$_{GL}$-A60C$_{HC}$ as determined using ResMap (Kucukelbir et al., 2014). (D) Graphical plot depicting distribution of particle image orientations. *Adapted from (Borst et al., 2018)

Table 4.3. CryoEM data collection, refinement, and model validation statistics

*Adapted from (Borst et al., 2018)

Parameter	Value
Data Collection	
No. of Micrographs	1,993
No. of Particles	134,443
Pixel size, Å	1.36
Defocus range, μM	2.0-3.5
Voltage, kV	300
Dose Rate, counts/pix/sec	8
Electron dose, $e^-/Å^2$	80
Refinement	
Resolution, Å	3.8
Map-sharpening B factor, $Å^2$	-230
Model validation (3 Fab structure)	
Favored rotamers, %	98.21%
Poor rotamers, %	0.30%
Ramachandran outliers, %	0.27%
Clash Score	1.92
Molprobity score	1.17
EM ringer score	2.00

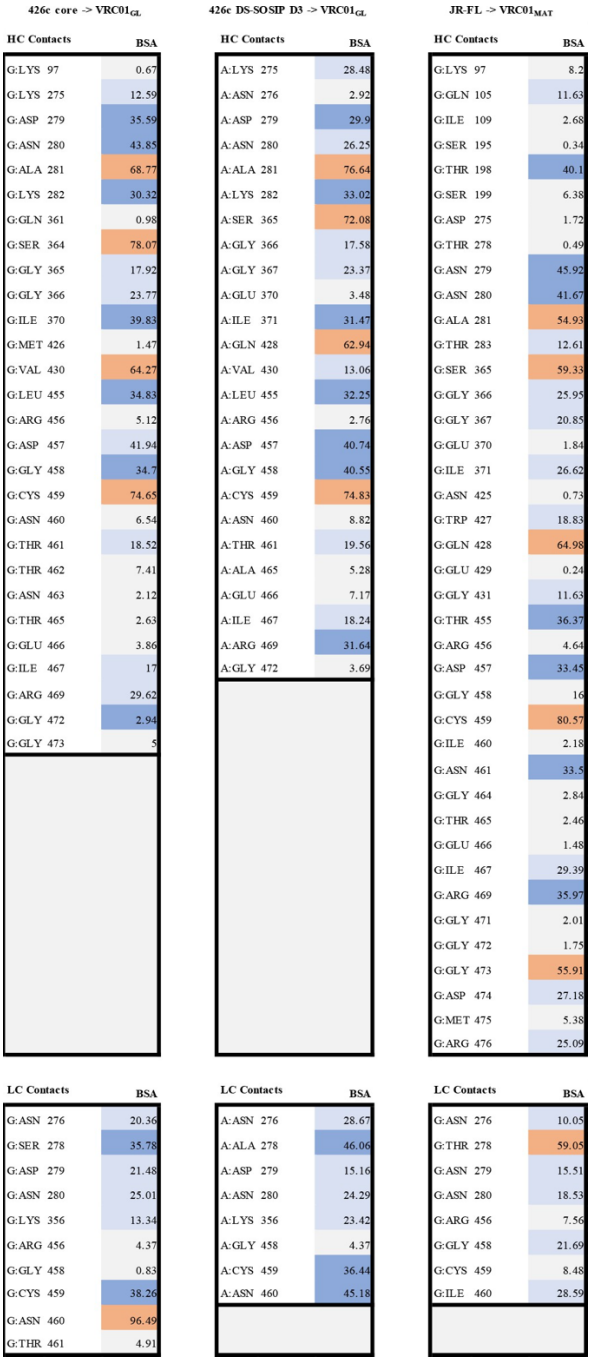

426c core -> VRC01$_{GL}$

HC Contacts	BSA
G:LYS 97	0.67
G:LYS 275	12.59
G:ASP 279	35.59
G:ASN 280	43.85
G:ALA 281	68.77
G:LYS 282	30.32
G:GLN 361	0.98
G:SER 364	78.07
G:GLY 365	17.92
G:GLY 366	23.77
G:ILE 370	39.83
G:MET 426	1.47
G:VAL 430	64.27
G:LEU 455	34.83
G:ARG 456	5.12
G:ASP 457	41.94
G:GLY 458	34.7
G:CYS 459	74.65
G:ASN 460	6.54
G:THR 461	18.52
G:THR 462	7.41
G:ASN 463	2.12
G:THR 465	2.63
G:GLU 466	3.86
G:ILE 467	17
G:ARG 469	29.62
G:GLY 472	2.94
G:GLY 473	5

LC Contacts	BSA
G:ASN 276	20.36
G:SER 278	35.78
G:ASP 279	21.48
G:ASN 280	25.01
G:LYS 356	13.34
G:ARG 456	4.37
G:GLY 458	0.83
G:CYS 459	38.26
G:ASN 460	96.49
G:THR 461	4.91

426c DS-SOSIP D3 -> VRC01$_{GL}$

HC Contacts	BSA
A:LYS 275	28.48
A:ASN 276	2.92
A:ASP 279	29.9
A:ASN 280	26.25
A:ALA 281	76.64
A:LYS 282	33.02
A:SER 365	72.08
A:GLY 366	17.58
A:GLY 367	23.37
A:GLU 370	3.48
A:ILE 371	31.47
A:GLN 428	62.94
A:VAL 430	13.06
A:LEU 455	32.25
A:ARG 456	2.76
A:ASP 457	40.74
A:GLY 458	40.55
A:CYS 459	74.83
A:ASN 460	8.82
A:THR 461	19.56
A:ALA 465	5.28
A:GLU 466	7.17
A:ILE 467	18.24
A:ARG 469	31.64
A:GLY 472	3.69

LC Contacts	BSA
A:ASN 276	28.67
A:ALA 278	46.06
A:ASP 279	15.16
A:ASN 280	24.29
A:LYS 356	23.42
A:GLY 458	4.37
A:CYS 459	36.44
A:ASN 460	45.18

JR-FL -> VRC01$_{MAT}$

HC Contacts	BSA
G:LYS 97	8.2
G:GLN 105	11.63
G:ILE 109	2.68
G:SER 195	0.34
G:THR 198	40.1
G:SER 199	6.38
G:ASP 275	1.72
G:THR 278	0.49
G:ASN 279	45.92
G:ASN 280	41.67
G:ALA 281	54.93
G:THR 283	12.61
G:SER 365	59.33
G:GLY 366	25.95
G:GLY 367	20.85
G:GLU 370	1.84
G:ILE 371	26.62
G:ASN 425	0.73
G:TRP 427	18.83
G:GLN 428	64.98
G:GLU 429	0.24
G:GLY 431	11.63
G:THR 455	36.37
G:ARG 456	4.64
G:ASP 457	33.45
G:GLY 458	16
G:CYS 459	80.57
G:ILE 460	2.18
G:ASN 461	33.5
G:GLY 464	2.84
G:THR 465	2.46
G:GLU 466	1.48
G:ILE 467	29.39
G:ARG 469	35.97
G:GLY 471	2.01
G:GLY 472	1.75
G:GLY 473	55.91
G:ASP 474	27.18
G:MET 475	5.38
G:ARG 476	25.09

LC Contacts	BSA
G:ASN 276	10.05
G:THR 278	59.05
G:ASN 279	15.51
G:ASN 280	18.53
G:ARG 456	7.56
G:GLY 458	21.69
G:CYS 459	8.48
G:ILE 460	28.59

Figure 4.6. Comparison of gp120 interface contacts between VRC01$_{GL}$ and VRC01$_{MAT}$ Tables highlighting gp120 residues and their associated buried surface area (BSA) which comprise the interface with VRC01-class antibodies, as determined by PISA. BSA values are colored light gray for values ranging between 0.1 and 10.0, light blue for values between 10.1 and 30.0, dark blue for values between 30.1 and 50.0, and red for values > 50.0 Å^2. HC: heavy chain; LC: light chain. *Adapted from (Borst et al., 2018)

4.3 STRUCTURAL ANALYSIS OF THE REGION SURROUNDING THE $CD4_{BS}$ IN 426C DS-SOSIP D3

Removal of $CD4_{BS}$-surrounding carbohydrates has been shown to enhance binding of $CD4_{BS}$-targeted germline VRC01-class antibodies and to increase the antigenicity of this region(McGuire et al., 2013, 2016; Stamatatos et al., 2017; Zhou et al., 2017). Our structural analysis reveals that the 426c DS-SOSIP naturally lacks an NLGS at position Asn234 near the $CD4_{BS}$, which is otherwise conserved in 80% of known circulating HIV-1 strains(Crooks et al., 2015). Instead, 426c features a glycan at Asn230 that is more remote from the VRC01 epitope than glycan Asn234 (Jardine et al., 2016) **(Fig. 4.1F)**. The oligosaccharide at position Asn230 appears to be highly dynamic, since only the two proximal N-acetyl-glucosamine (GlcNAc) moieties are resolved in the reconstruction **(Fig. 4.7)** and does not interact with $VRC01_{GL}$ or other glycans in the complex. Previous structural characterization of clades A and G SOSIP trimers established that glycans at positions Asn276 and Asn234 are in close proximity to each other and likely restrain each others' conformational freedom (Jardine et al., 2016)(Stewart-Jones et al., 2016; Zhou et al., 2017). The absence of glycan Asn234 in 426c gp120 reduces local carbohydrate crowding near the $CD4_{BS}$ and could increase accessibility of this neutralization supersite(Stewart-Jones et al., 2016) and lead to altered local glycan processing(Behrens et al., 2018; Bonomelli et al., 2011).

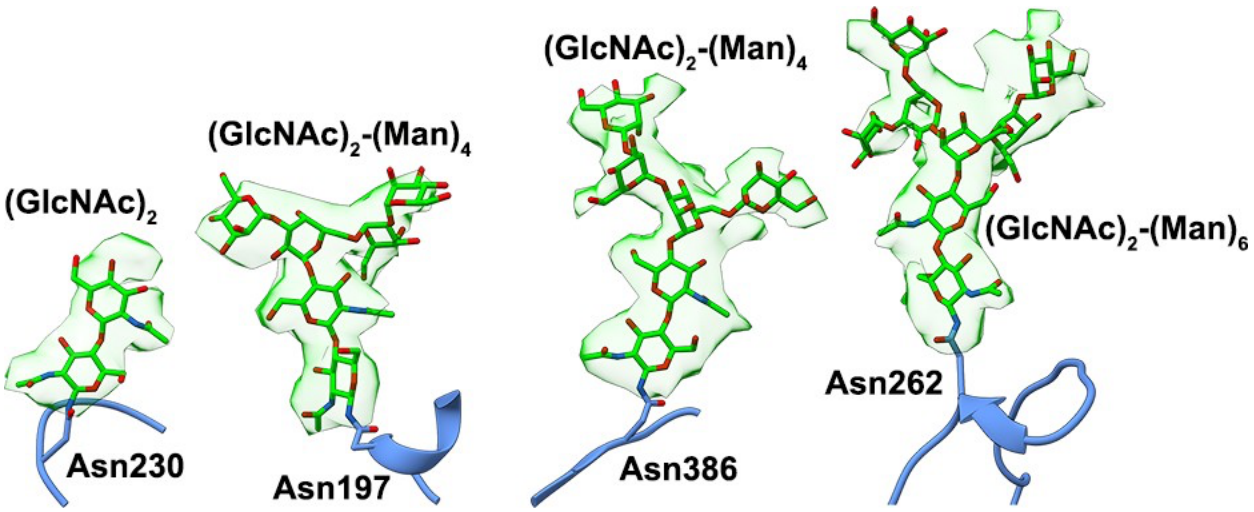

Figure 4.7. Example of glycans resolved in the 426c DS-SOSIP D3†-VRC01$_{GL}$ structure. CryoEM density (green semi-transparent surface) and atomic model for glycans at positions Asn230, Asn197, Asn386 and Asn262 are shown. *Adapted from (Borst et al., 2018)

The 426c DS-SOSIP also lacks an NLGS at position Asn362(363), which is present in 42% of strains deposited in the HIV database(Gaschen et al., 2018) **(Fig. 4.1F)**. This oligosaccharide is located distally from the viral membrane side of the SOSIP trimer **(Fig. 4.1F)** and is sandwiched between the $VRC01_{MAT}$ heavy chain and glycan Asn386 in the structure of $VRC01_{MAT}$ bound to the JR-FL SOSIP trimer (clade B)(Stewart-Jones et al., 2016). Analysis of the asymmetric 426c DS-SOSIP $D3^{\dagger}$-$VRC01_{GL}$ structure, comprising two Fabs, revealed that Fab-bound protomers feature slightly better-resolved density for glycan Asn386 than the free protomer when visualized at the same contour level **(Fig. 4.1H)**. These observations suggest that $VRC01_{GL}$ may stabilize the Asn386 glycan either through reduction of its conformational freedom and/or via direct interactions with the Fab framework region. The absence of glycan Asn362 or other topologically equivalent oligosaccharides in the 426c gp120 sequence likely contributes to increased accessibility of the $CD4_{BS}$ to $VRC01_{GL}$-class bnAbs due to the close proximity of this glycan to the epitope(Stewart-Jones et al., 2016) **(Fig. 4.1F)**.

Similarly to what is observed in available $VRC01_{MAT}$/SOSIP complex structures(Stewart-Jones et al., 2016), glycan Asn197 density is also strongest when bound to $VRC01_{GL}$, but appears weaker in the unbound protomer **(Fig. 4.1H)**, again indicating either Fab-induced stabilization or restriction of movement. The position of glycan Asn197 differs substantially between available structures of monomeric gp120 epitope-based constructs bound to $VRC01_{GL}$-class Fabs and the conformation of the $VRC01_{GL}$-bound SOSIP trimer reported here **(Fig. 4.1G)** (Scharf et al., 2016). This variation in Asn197 positioning is guided by the formation of the gp120 bridging sheet in monomeric gp120, which would otherwise only form following CD4 receptor binding in the context of trimeric Env **(Fig. 4.1G)** (Kwon et al., 2012; Zhou et al., 2010). This conformational

difference includes the β_{20}/β_{21} loop, whose orientation in the 426c DS-SOSIP D3†-VRC01$_{GL}$ complex differs relative to crystal structures of VRC01$_{GL}$-class antibodies in complex with monomeric gp120 **(Fig. 4.1G)** (Scharf et al., 2016). Although the β_{20}/β_{21} loop is close to the VRC01 paratope, VRC01$_{MAT}$ was reported to have minimal preference in the conformation of the bridging sheet or β_{20}/β_{21} region, as 87% of its contact surface area includes the conformationally invariant outer domain of gp120(Zhou et al., 2010). Whether or not the conformation of the β_{20}/β_{21} region directly impacts germline VRC01-class antibody binding affinities remains unclear. However, VRC01$_{GL}$ in complex with gp120 constructs lacking this domain have been determined (eOD-GT6 and eOD-GT8), demonstrating that these germline mAbs do not strictly require this region for CD4$_{BS}$ recognition when glycans surrounding the CD4$_{BS}$ are also removed (Jardine et al., 2013).

4.4 V5 LOOP NLGSS OF THE 426C CORE DID NOT HINDER BINDING TO $VRC01_{GL}$ FABS

One of the mechanisms by which HIV-1 Env has evolved to avoid detection by the progenitors of VRC01-class bnAbs is by selection of V5 loop NLGSs(Huang et al., 2016; Li et al., 2011; Zhou et al., 2010) which sterically limit access to the $CD4_{BS}$. The observation that $VRC01_{GL}$ may accommodate carbohydrates surrounding the $CD4_{BS}$ in our 426c DS-SOSIP $D3^{\dagger}$-$VRC01_{GL}$ cryoEM structure prompted us to assess the effect on binding of the two V5 loop putative NLGSs mutated in 426c DS-SOSIP $D3^{\dagger}$-$VRC01_{GL}$. With 426c Env trimers, we previously found that $VRC01_{GL}$ binding could be detected following removal of glycan Asn276, and was further enhanced following removal of wild-type NLGSs at positions Asn460 and Asn463 (McGuire et al., 2013). We also demonstrated that removing the V1/V2, and V3 loops in gp140 Env trimers further increased binding of multiple VRC01-class germline antibodies relative to trimers only containing glycan-depleting mutations(McGuire et al., 2014, 2016). However, the effects of V1/V2 and V3 loops deletion on $VRC01_{GL}$ binding to 426 core constructs in the presence of glycans remains unclear. Here we reintroduced the two NLGSs at positions Asn460 and Asn463 (in the V5 loop) and assessed their individual and cumulative effects on $VRC01_{GL}$ engagement of the 426c core construct comprised of gp120 residues 44 to 492 and lacking the V1/V2 and V3 variable loops(Kwon et al., 2012). Expanding on our prior work (McGuire et al., 2016), the following four 426c core glycan-deleted combinations were tested using HEK293F-expressed protein constructs: S278A/T462A/T465A, S278A/T465A, S278A/T462A, and S278A **(Fig. 4.2, Fig. 4.8A-D, and Table 4.4)**.

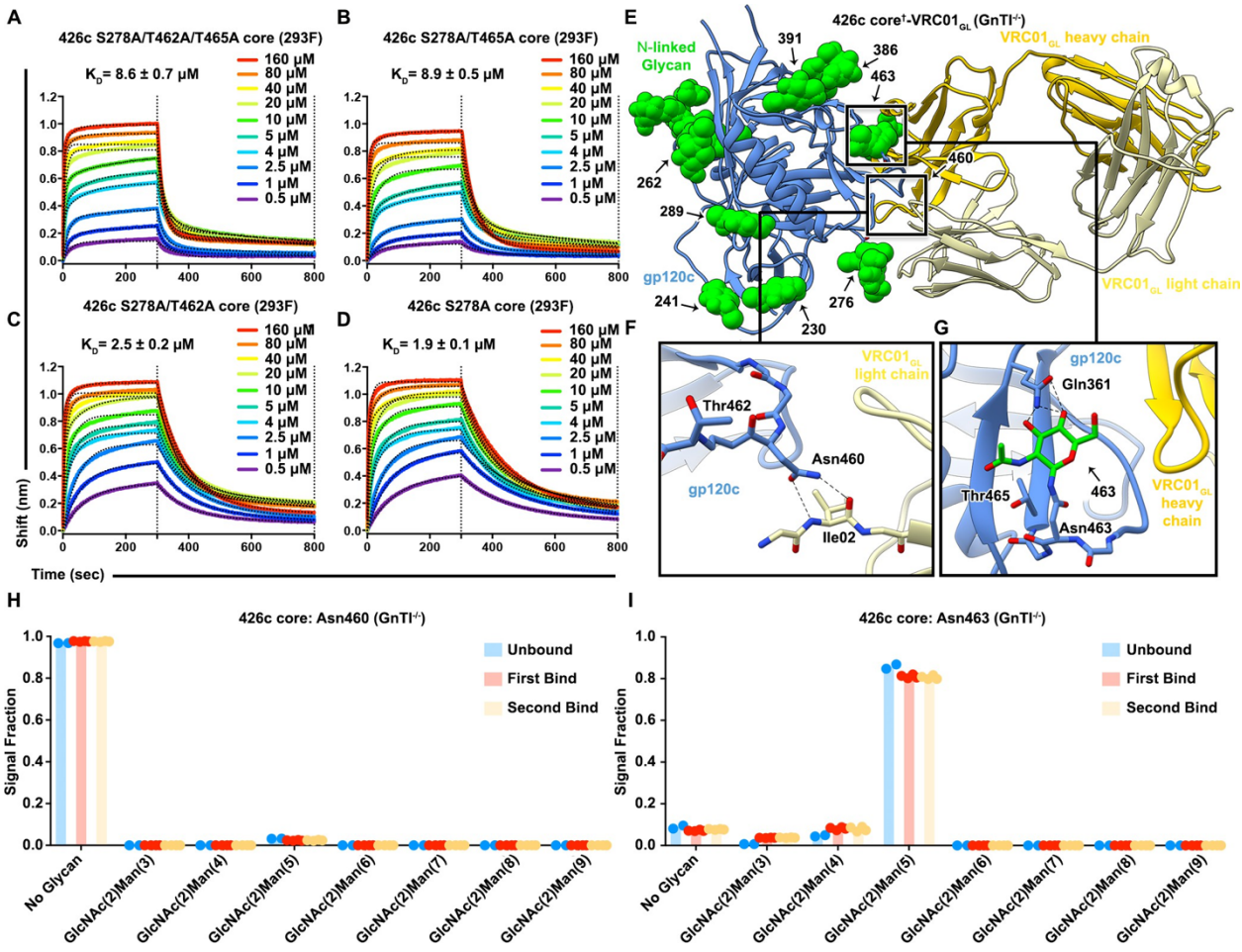

Figure 4.8. Native V5 loop NLGSs do not hinder VRC01$_{GL}$ binding to the 426c core. (A–D) BLI curves and the corresponding equilibrium dissociation constants for VRC01$_{GL}$ IgG binding to the S278A/T462A/T465A (A), S278A/T462A (B), S278A/T465A (C), and S278A (D) 426c core constructs lacking either one or several glycans in the V5 and D loops. The concentrations of 426c core injected and the color key is indicated on each panel. Fitted curves are colored as black dotted lines. The vertical dashed lines indicate the transition between association and dissociation phases. (E) Ribbon diagram of the 426c core†-VRC01$_{GL}$ complex crystal structure. gp120 is colored blue, VRC01$_{GL}$ Fab is colored yellow (heavy chain: dark yellow; light chain: light yellow), and resolved gp120 glycans are shown in surface representation and colored green. (F) Close-up view of the gp120 Asn460 contacts with the backbone carbonyl and amide groups of the light chain VRC01$_{GL}$ residue Ile02. (G) Close-up view of the $(GlcNAc)_1$ at position Asn463 of gp120. Oligosaccharides are labeled by the corresponding Asn residue they are linked to. Hydrogen bonds are represented as dashed lines. (H–I) Semi-quantitative LC-MS/MS analysis

of VRC01$_{GL}$-based IP experiments depicting the relative signal intensities for identified Asn460 (H) and Asn463 (I) glycoforms in unbound (blue), first binding event (red), and second binding event (yellow) fractions. The 'unbound' material indicates 426c core glycoforms that did not bind VRC01$_{GL}$ well following three binding steps. The 'first' binding event corresponds to 426c core elution fractions following collection of the sample flow-through and three rigorous wash cycles. The 'second' binding event follows a rebinding of the aforementioned flow-through, performing three additional washes, and eluting any residual bound material from the VRC01$_{GL}$ affinity column and collecting this fraction. Colored dots associated with their corresponding histogram bars represent individual values extracted from each experimental replicate, with the bar itself representing the experimental mean signal fraction. *Adapted from (Borst et al., 2018)

Table 4.4. BLI kinetics parameters of various 426c core constructs expressed using HEK293F cells

*Adapted from (Borst et al., 2018)

	Average Kinetic Values						
VRC01$_{GL}$ Fab vs 426c core (293)	KD (M)	KD Error	kon(1/Ms)	kon Error	kdis(1/s)	kdis Error	Full R^2
426c core S278A	1.89E-06	1.04E-07	3.02E+03	1.08E+02	4.81E-03	9.06E-05	0.9972
426c core S278A/T462A	2.50E-06	1.79E-07	3.40E+03	1.74E+02	6.63E-03	1.53E-04	0.9635
426c core S278A/T465A	8.90E-06	5.19E-07	2.92E+03	1.62E+02	1.36E-02	2.23E-04	0.9626
426c core S278A/T462A/T465A	8.61E-06	6.88E-07	5.49E+03	4.86E+02	2.58E-02	6.00E-04	0.9460

Reintroduction of the NLGS at position Asn460 (S278A/T465A) in the 426c core had no detectable impact on $VRC01_{GL}$ binding affinity despite the predicted overlap of a putative carbohydrate at position Asn460 with the bound $VRC01_{GL}$ Fab(Guo et al., 2012) **(Fig. 4.8A-B and Table 4.4)**. Indeed, our previous work removing NLGSs at positions Asn460 and Asn463 via the N460D/N463D mutations had only a relatively minor impact on $VRC01_{GL}$ engagement to trimeric 426c constructs compared to the large increase in binding observed following removal of the native Asn276 NLGS (McGuire et al., 2013, 2016). To better understand the molecular rationale of these observations with the monomeric 426c core construct, we engineered a disulfide-linked 426c $core^{\dagger}$-$VRC01_{GL}$ complex containing all wild-type NLGSs (426c $core^{\dagger}$-$VRC01_{GL}$). We co-expressed these proteins using HEK293 $GnTI^{-/-}$ cells, which lack N-acetyl-glucosaminyltransferase I activity and thus are unable to generate complex *N*-linked carbohydrates(Wright and Morrison, 1994). We then determined its crystal structure at 2.3 Å resolution after endoglycosidase H (EndoH) treatment to facilitate crystallization(Depetris et al., 2012; Freeze and Kranz, 2010) **(Fig. 4.8E, and Table 4.5)**. Despite harboring an NLGS, no glycan density could be resolved at position Asn460 in either of the two molecules of the asymmetric unit. Instead, the Asn460 side chain is hydrogen bonded to the backbone amide and carbonyl groups of the $VRC01_{GL}$ light-chain residue, Ile02 ($Ile02_{LC}$) **(Fig. 4.8F)**. In support of this observation, we detected only unglycosylated Asn460 peptide fragments when analyzing tryptic digests of this sample with liquid chromatography coupled to electron transfer/high-energy collision-dissociation tandem mass-spectrometry (LC-MS/MS) **(Fig. 4.8H, Fig. 4.9A,B)**. Furthermore, only low levels of glycosylation were detected at Asn460 by qualitative LC-MS/MS analysis of unliganded 426c core (lacking the G459C mutation) **(Fig. 4.9C)**. Additionally, we performed $VRC01_{GL}$-based immunoprecipitation (IP) experiments utilizing a $VRC01_{GL}$ affinity column and the same 426c

core construct. Semi-quantitative LC-MS/MS comparison of the 426 gp120 core samples from fractions that did not bind to $VRC01_{GL}$ ("unbound" flow-through), and those that did ("bound" elution), revealed no difference in glycan occupancy of the Asn460 NLGS (**Fig. 4.8H)**. This indicated this sequon is rarely glycosylated in 426c core and explains its negligible impact on $VRC01_{GL}$ binding. The predicted overlap of a glycan Asn460 with $VRC01_{GL}$ and the absence of a resolved proximal GlcNAc in the crystal structure of 426c core†-$VRC01_{GL}$ also suggests a likely strict preference for the unglycosylated Asn460 glycoform of the 426c gp120 for binding **(Fig. 4.8F)**.

Table 4.5. RMSD Table comparing ligand-free and ligand-bound $VRC01_{GL}$ CDRL1 loop conformations.

*Adapted from (Borst et al., 2018)

Cα RMSD for residues 26-32 (Atoms)	WT426c core - $VRC01_{GL}$ chain L	WT426c core - $VRC01_{GL}$ chain B
4JPI (unliganded $VRC01_{GL}$) chain L	1.637 (2.687)	1.759 (2.598)
4JPI (unliganded $VRC01_{GL}$) chain B	0.379 (1.271)	0.667 (1.530)
4JPK chain L	0.909 (1.731)	1.066 (1.879)
5IGX chain L	1.601 (2.600)	1.700 (2.446)

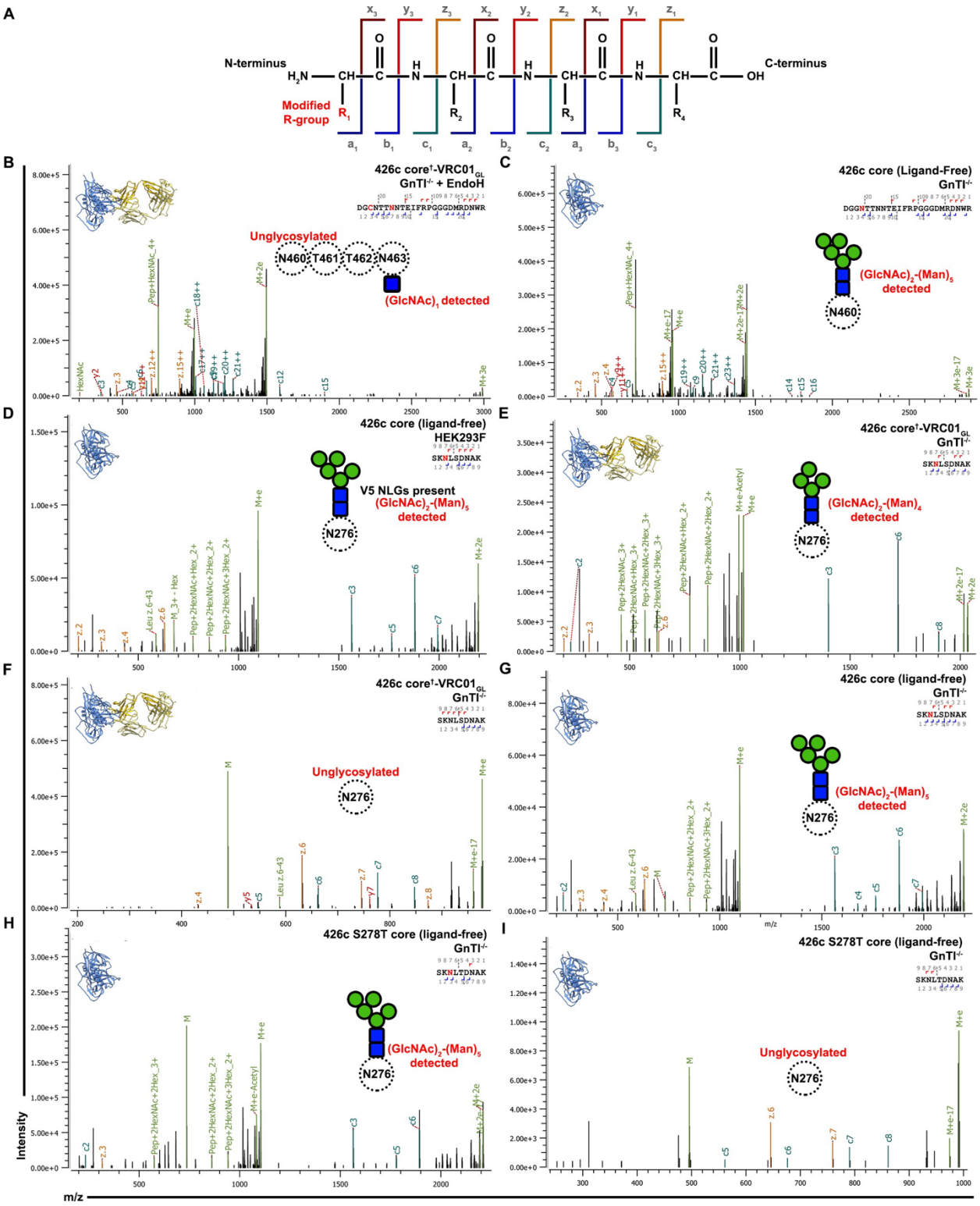

Figure 4.9. Representative LC-MS/MS glycan identifications of 426c core constructs. The top-left ribbon diagram corresponds to the sample analyzed. The LC-MS/MS fragmentation pattern is indicated in the top-right inset. A graphical depiction of the Asn276 residue (dotted white

circle) and its associated identified glycan (blue: N-acetyl glucosamine, green: mannose) are represented on the spectrum. Green peak labels correspond to precursor peptides with/without LC-MS/MS fragmentation occurring within the glycan. Red/orange peak labels represent identified x, y, and z fragments. Blue/teal peak labels highlight identified a, b, and c fragments. (A) Schematic of possible LC-MS/MS peptide fragmentation patterns. The peptide N- and C-termini are labeled. Possible fragmentation positions are denoted as grey text, with x, y, and z fragments represented as red/orange labels and blue/teal fragments representing a, b, and c fragments. Modified R-groups are denoted in red text. (B–C) Representative LC-MS/MS spectra of detected V5 glycosylation profile of the 426c core†-VRC01$_{GL}$ (GnTI$^{-/-}$-expressed) (B) and a ligand-free 426c core containing a glycan at position Asn460 (GnTI$^{-/-}$-expressed) (C). (D–J) Various additional representative LC-MS/MS spectra of an Asn276 glycopeptide containing a (GlcNAc)$_2$-(Man)$_5$ oligosaccharide from ligand-free 426c core (HEK293F-expressed) (D), an Asn276 glycopeptide of the 426c core†-VRC01$_{GL}$ complex with a detectable (GlcNAc)$_2$-(Man)$_4$ sugar (GnTI$^{-/-}$-expressed) (E), an Asn276 peptide from the 426c core†-VRC01$_{GL}$ complex that is unglycosylated at position Asn276 (GnTI$^{-/-}$-expressed) (F), a 426c core Asn276 glycopeptide containing a (GlcNAc)$_2$-(Man)$_5$ oligosaccharide (GnTI$^{-/-}$-expressed) (G), a 426c S278T core Asn276 glycopeptide containing a (GlcNAc)$_2$-(Man)$_5$ oligosaccharide (GnTI$^{-/-}$-expressed) (H), and an Asn276 peptide of a 426c S278T core that is unglycosylated at position Asn276 (GnTI$^{-/-}$-expressed) (I). *Adapted from (Borst et al., 2018)

We furthermore observed that reintroduction of the Asn463 NLGS (S278A/T462A or S278A) also did not result in a reduction in $VRC01_{GL}$ binding relative to the 426c S278A/T462A/T465A core **(Fig. 4.8A,C,D and Table 4.4)**. This result was unexpected, as V5 glycosylation of Env trimers containing all variable loops have been reported to negatively affect $VRC01_{GL}$ recognition of the $CD4_{BS}$ (Huang et al., 2016; Li et al., 2011; McGuire et al., 2013; Zhou et al., 2010). We observed electron density for the proximal GlcNAc linked to Asn463 in one of the two molecules of the asymmetric unit of the 426c core†-$VRC01_{GL}$ crystal structure and cross-validated the presence of this post-translational modification using LC-MS/MS **(Fig. 4.8G)**. $VRC01_{GL}$-based IP experiments followed by semi-quantitative LC-MS/MS validated these structural observations by detecting Asn463 glycosylation which was undistinguishable between "bound" elution and "unbound" flow-through fractions **(Fig. 4.8I)**. This supports our BLI data suggesting the Asn463 glycan does not hinder $VRC01_{GL}$ binding in the context of the 426c core and that this site is glycosylated.

4.5 VRC01$_{GL}$ FAB BOUND TO THE ASN276 GLYCAN-CONTAINING 426C CORE CONSTRUCT

A hallmark of VRC01-class bnAb maturation is the shortening of the CDR L1 loop length and/or the addition of glycine residues, both of which have been proposed to enable accommodation of the Asn276 glycan near the CD4$_{BS}$(Jardine et al., 2016; Scharf et al., 2016; Wu et al., 2015; Zhou et al., 2010). Although VRC01$_{MAT}$ was shown to bind to the trimeric Env CD4$_{BS}$ in the presence of glycan Asn276, its removal significantly increased binding affinity and neutralization potency (Jardine et al., 2013; McGuire et al., 2013, 2016; Medina-Ramírez et al., 2017; Stamatatos et al., 2017). Removal of the Asn276 NLGS from certain trimeric SOSIP constructs by either N276D or (S/T)278(A/R) mutations significantly enhanced the antigenicity of the VRC01 epitope(McGuire et al., 2013, 2016). However, when such glycan-depleted trimeric Env constructs were used as immunogens, the antibodies they elicit fail to overcome the glycan present at position Asn276 of wild-type viruses(Briney et al., 2016; Dosenovic et al., 2015). Removal of glycan Asn276 through N276A substitution abrogated VRC01$_{GL}$ interactions, indicating this residue was critical for binding (McGuire et al., 2016). These observations suggest that initial engagement of VRC01-class bnAb precursors in infected individuals occurs with an asparagine at position 276 and may also be possible, at low levels, in the presence of a glycan at this NLGS (Scharf et al., 2016).

Considering the reduced glycan shielding of the 426c strain, the deletion of variable loops 1, 2, and 3 in our 426c core constructs, and the minimal impact V5 loop NLGSs had on VRC01$_{GL}$ binding, we tested whether the wild type 426c core construct could interact with VRC01$_{GL}$ in the presence of the Asn276 NLGS **(Fig. 4.2)**. BLI analysis revealed VRC01$_{GL}$ bound similarly to both

the HEK293F and HEK293 GnTi$^{-/-}$-expressed 426c cores with equilibrium dissociation constants of 11 μM and 15 μM, respectively **(Fig. 4.10A,B)**. The crystal structure of the disulfide engineered 426c core†-VRC01$_{GL}$ complex expressed in GnTi$^{-/-}$ cells further reveals the presence of a resolved glycan at position Asn276 in one of the two molecules of the asymmetric unit, indicating VRC01$_{GL}$ bound to both Asn276 glycosylated and unglycosylated species **(Fig. 4.10C-J)**.

Analysis of this structure highlights distinct sets of interactions observed between the light chains of VRC01$_{GL}$ or VRC01$_{MAT}$ and glycan Asn276, which is rotated ~90˚ when comparing the two structures **(Fig. 4.10C-D)**. In line with our previous observation that Asn276 is important for VRC01$_{GL}$ recognition(McGuire et al., 2016), we observed that Asn276 is hydrogen bonded to the VRC01$_{GL}$ light chain residue Tyr91 in our 426c core†-VRC01$_{GL}$ and 426c DS-SOSIP D3†-VRC01$_{GL}$ structures but not in the JR-FL SOSIP~VRC01$_{MAT}$ crosslinked complex structure **(Fig. 4.10C-E)** (PDB: 5FYK)(Stewart-Jones et al., 2016). The CDRL1 of VRC01$_{GL}$ has been shown to adopt multiple conformations both when ligand-free and when bound to eOD-GT6, the latter lacked a glycan at position Asn276(Jardine et al., 2013). The CDRL1 loop of NIH45-46$_{GL}$ (a germline VRC01-class antibody) bound to the 426c core TM4 adopts a similar orientation as the one observed for the CDRL1 loop of VRC01$_{GL}$ bound to eOD-GT6 (Scharf et al., 2016) (Jardine et al., 2013) **(Table 4.5).** Comparisons between the structures of our 426c core†-VRC01$_{GL}$ complex, a putatively authentic germline VRC01/eOD-GT6 complex (PDB ID 4JPK(Jardine et al., 2013)) and the unliganded VRC01$_{GL}$ (PDB ID 4JPI)(Jardine et al., 2013), indicate that the CDRL1 of VRC01$_{GL}$ accommodates the Asn276 oligosaccharide in a conformation similar to the CDRL1 of unliganded VRC01$_{GL}$ (chain B) **(Table 4.5)**(Jardine et al., 2013)**,** but differs from a complex with a gp120 core lacking this glycan **(Fig. 4.10F-H)**. This observation supports that

disulfide crosslinking of 426c core†-VRC01$_{GL}$ did not distort the CDRL1 of VRC01$_{GL}$ into a non-native conformation for the accommodation of glycan Asn276 in our structure **(Fig. 4.10C)**. LC-MS/MS analysis of the sample used for crystallization revealed *N*-linked carbohydrates at position Asn276 of 426c core†-VRC01$_{GL}$ ranged from $(GlcNAc)_2$-$(Man)_4$ to $(GlcNAc)_2$-$(Man)_5$ **(Fig. 4.11A-B and Fig. 4.9E)**. Unglycosylated Asn276 peptides were also identified, corroborating the presence of two populations of molecules in the crystal structure and the ability of VRC01$_{GL}$ to recognize both species **(Fig. 4.11A and Fig. 4.9F)**.

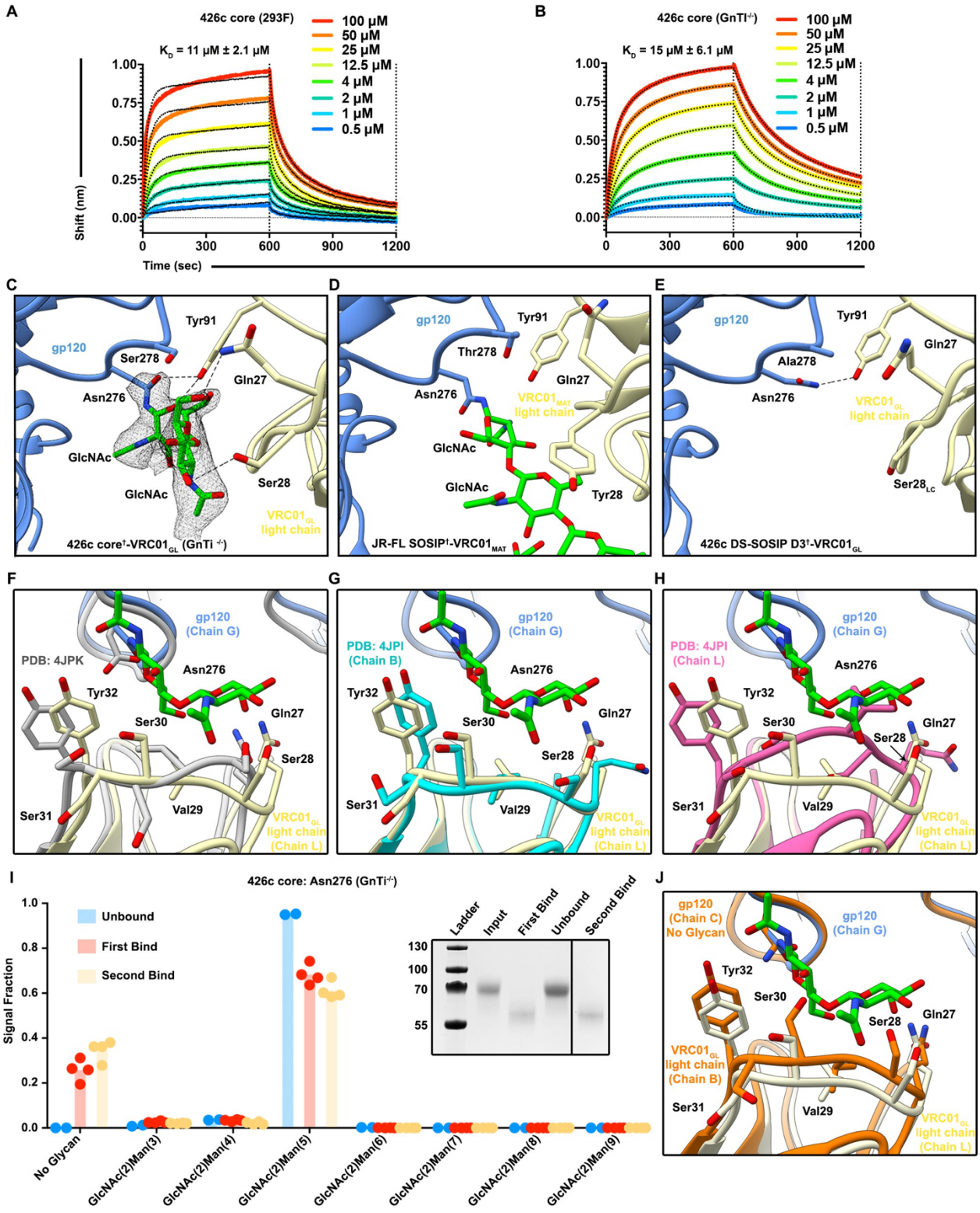

Figure 4.10. The $VRC01_{GL}$ Fab bound to the WT 426c core in presence of a glycan Asn276. (A–B) BLI binding data of the immobilized $VRC01_{GL}$ Fab with the 426c core expressed in either HEK293F (A) or HEK293 GnTI$^{-/-}$ cells (B). (C) Crystal structure of 426c core†-$VRC01_{GL}$

highlighting glycan electron density at position Asn276 (grey mesh: $2F_O$-Fc map contoured at 1.0σ) and amino-acid contacts for one molecule of the asymmetric unit. (D) Structure of $VRC01_{MAT}$ in complex (crosslinked) with the HIV-1 JR-FL SOSIP trimer (PDB ID: 5FYK) (Stewart-Jones et al., 2016) in the same orientation as in panel (C) and focusing on the glycan at position Asn276. (E) CryoEM structure of the 426c DS-SOSIP $D3^{\dagger}$-$VRC01_{GL}$ complex in the same orientation as in panel (C) and focusing on Asn276. Hydrogen bonds spanning 2.8–3.5 Å are depicted as dashed lines. (F–H) Comparison of $VRC01_{GL}$ CDRL1 conformations in the presence or absence of a glycan at position Asn276. In the three panels, gp120 is shown in blue cartoon representation and $VRC01_{GL}$ light chain in light yellow for our crystal structure of 426c $core^{\dagger}$-$VRC01_{GL}$. Residues Gln27 to Tyr32 of $VRC01_{GL}$ light chain are shown as sticks and labeled. (F) $VRC01_{GL}$ bound to eODGT6 (PDB ID: 4JPK) (Jardine et al., 2013) is shown in grey. (G) Chain B of unliganded $VRC01_{GL}$ (PDB ID: 4JPI) (Jardine et al., 2013) is shown in cyan. (H) Chain L of unliganded $VRC01_{GL}$ (PDB ID: 4JPI) (Jardine et al., 2013) is shown in pink. (I) Semi-quantitative LC-MS/MS analysis depicting the relative signal intensities for identified Asn276 glycoforms in unbound (blue), after the first binding event (red), and after the second binding event (yellow) fractions taken from $VRC01_{GL}$-based IP experiments. The 'unbound' material indicates 426c core glycoforms that did not bind $VRC01_{GL}$ following three binding events. Colored dots on corresponding histogram bars represent individual values extracted from each experimental replicate, with the bar itself representing the experimental mean signal fraction. (*Inset)* SDS-PAGE depicting the average molecular weight difference between wild-type 426c core species in 'unbound' flow-through and 'bound' elution fractions. (**J**) Structural comparison of $VRC01_{GL}$ CDRL1 conformations in the presence or absence of a glycan at position Asn276 in each of the molecules present in the asymmetric unit of our 426c $core^{\dagger}$-$VRC01_{GL}$ crystal structure. *Adapted from (Borst et al., 2018)

A

Construct	No Glycan	(GlcNAc)1	(GlcNAc)2	(GlcNAc)2-(Man)3	(GlcNAc)2-(Man)4	(GlcNAc)2-(Man)5	(GlcNAc)2-(Man)6	(GlcNAc)2-(Man)7	(GlcNAc)2-(Man)8	(GlcNAc)2-(Man)9	Hybrid/Complex
426c core†-VRC01$_{GL}$ (GnTI + EndoH)	✓	X	X	X	✓	✓	X	X	X	X	X
426c core (GnTI + EndoH)	✓	✓	X	✓	X	X	X	X	X	X	X

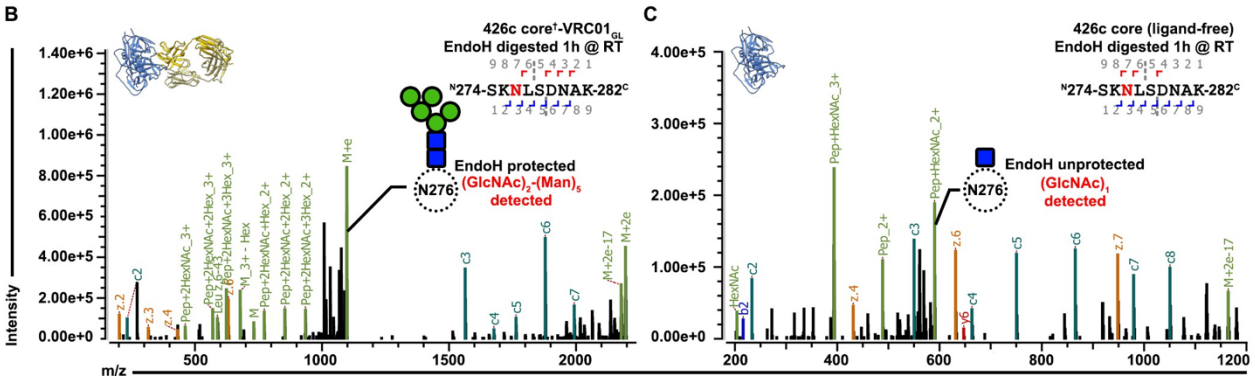

Figure 4.11. VRC01$_{GL}$ binding in the presence of a glycan at position Asn276 and protection against EndoH-mediated digestion.

(A) Summary of identifications for 426c Asn276 glycopeptides. 426c core constructs that were subjected to qualitative LC-MS/MS are indicated on the left. Glycopeptide identifications detected using the Byonic software (Bern et al., 2012) are listed in blue and denoted with a check-mark (✓). (B–C) Representative LC-MS/MS spectra from panel (A) of glycan Asn276 identifications from the cross-linked 426c core†-VRC01$_{GL}$ and unliganded 426c core complex following EndoH digestion. The top-left ribbon diagram corresponds to the sample analyzed. The LC-MS/MS fragmentation pattern is indicated in the top-right inset. A graphical depiction of the Asn276 residue (dotted circle) and its associated identified glycan (blue: N-Acetylglucosamine, green : Mannose) are represented on the spectrum. The black line indicates identification of the precursor mass with neutral losses corresponding to the identified glycopeptide. Green peak labels correspond to precursor peptides with/without LC-MS/MS fragmentation occurring within the glycan. Red/orange peak labels represent identified x, y, and z fragments. Blue/teal peak labels highlight identified a, b, and c fragments. After EndoH digestion, a (GlcNAc)$_2$-(Man)$_5$ glycan was the predominant glycoform identified at position Asn276 with the sample used for crystallization (B) whereas a (GlcNAc)$_1$ glycan prevailed with the unliganded 426c core (C). *Adapted from (Borst et al., 2018)

Despite the EndoH treatment used to promote crystallization of 426c core†-VRC01$_{GL}$, no $(GlcNAc)_1$ glycopeptides were detected at the Asn276 NLGS by LC-MS/MS **(Fig. 4.11A)**. In contrast, we detected digested glycopeptides containing $(GlcNAc)_1$ moieties for other NLGSs, confirming the efficiency of the EndoH treatment **(Fig. 4.9B)**. These observations validated the Asn276 glycan density observed in the crystal structure and suggested that bound VRC01$_{GL}$ protected the glycan Asn276 from enzymatic digestion **(Fig. 4.11A-B)**, but not other oligosaccharides, such as glycan Asn463 **(Fig. 4.8E,G and Fig. 4.9B)**. We further corroborated this hypothesis by analyzing EndoH-treated 426c core in the absence of co-expressed VRC01$_{GL}$ and confirmed the presence of $(GlcNAc)_1$ moieties at position Asn276 by LC-MS/MS **(Fig. 4.11A,C)**, supporting that digestion of this glycan was possible if not sterically hindered by the binding of this Fab(Yet et al., 1988).

To probe whether the disulfide cross-link promoted artificial accommodation of glycan Asn276, we performed an additional analysis with samples obtained from IP experiments using the 426c core construct lacking the G459C mutation. 426 core samples from the "unbound" flow-through and "bound" elution fractions had distinct migration profiles by SDS-PAGE **(Fig. 4.10I)**, with the bound fraction exhibiting higher electrophoretic mobility than the unbound species. LC-MS/MS revealed the bound fraction was enriched for unglycosylated Asn276 peptides, suggesting this subspecies was the preferred VRC01$_{GL}$ binder **(Fig. 4.10I)**. This result corroborates reports of VRC01$_{GL}$ binding occurring preferentially in the absence of a glycan at position 276(Jardine et al., 2013; McGuire et al., 2013, 2016; Medina-Ramírez et al., 2017; Scharf et al., 2016; Stamatatos et al., 2017). However, we also detected that the majority of the Asn276 peptide signal was of the $(GlcNAc)_2$-$(Man)_5$ Asn276 glycoform in bound fractions (approximately twice as much as the

unglycosylated Asn276 signal) **(Fig. 4.10I)**, suggesting VRC01$_{GL}$ could indeed bind in the presence of this glycan and in the absence of an engineered cross-link. This experiment, along with our crosslinked 426c core†-VRC01$_{GL}$ crystal structure and qualitative LC-MS/MS, confirm both the glycosylated **(Fig. 4.10C,F-I)** and unglycosylated Asn276 glycoforms are present following expression and that VRC01$_{GL}$ could accommodate both. In summary, VRC01$_{GL}$ bound a 426c core with wild-type NLGSs, was sterically compatible with glycans present at positions Asn276 and Asn463, and strictly interacted with a subspecies of gp120 lacking a glycan at position Asn460.

4.6 MODULATION OF GLYCAN COMPOSITION ALTERED $VRC01_{GL}$ ANTIBODY RECOGNITION OF THE WT 426C CORE

Irrespective of the chosen expression system (HEK293F or HEK293 GnTI$^{-/-}$), our LC-MS/MS analyses showed that 426c core constructs all contained detectable levels of both the unglycosylated and the $(GlcNAc)_2$-$(Man)_5$ oligosaccharide variants at position Asn276 **(Fig. 4.10I, Fig. 4.11A-B, and Fig. 4.9D-G)**. Since $(GlcNAc)_2$-$(Man)_5$ is a short glycan produced in mammalian cells(Hossler et al., 2009), and was the major detectable glycosylated form in $VRC01_{GL}$-based IP "bound" elution fractions, we interrogated whether differential expression conditions known to enrich for $(GlcNAc)_2$-$(Man)_9$ glycans could negatively impact the binding of $VRC01_{GL}$ IgGs to 426c core. We thus compared $VRC01_{GL}$ binding to HEK293 GnTI$^{-/-}$-produced 426c core constructs expressed in the absence or presence of 100 μM kifunensine to yield a range of $(GlcNAc)_2$-$(Man)_5$ to $(GlcNAc)_2$-$(Man)_9$ glycans or to enrich for $(GlcNAc)_2$-$(Man)_9$ glycans, respectively(Depetris et al., 2012).

The efficacy of this strategy was confirmed by two orthogonal methods: 1) SDS-PAGE, which demonstrated the two expression conditions yielded samples with distinct migration profiles, and 2) LC-MS/MS, which confirmed enrichment for $(GlcNAc)_2$-$(Man)_9$ glycans in the presence of kifunensine **(Fig. 4.12A and Fig. 4.13A-C)**. Importantly, binding affinities for the 426c core were improved by ~10 fold in the context of immobilized full-length $VRC01_{GL}$ IgGs relative to immobilized VRC01 Fabs. The 426c core expressed using HEK293 GnTI$^{-/-}$ in the absence of kifunensine bound $VRC01_{GL}$ IgG with a K_D of 2 μM **(Fig. 4.12B and Table 4.6)**, whereas binding was significantly reduced when the 426c core was expressed in the presence of kifunensine **(Fig. 4.12C and Table 4.6)**. The $VRC01_{GL}$ IgG binding affinity to 426c core

expressed in GnTI$^{-/-}$ cells in the presence of kifunensine was enhanced following treatment with EndoH **(**K_D=245 nM, **Fig. 4.12D and Table 4.6)**, confirming recognition of gp120 by $VRC01_{GL}$ IgGs can occur in the presence of a proximal GlcNAc at position Asn276. This $VRC01_{GL}$ IgG binding affinity was similar to the HEK293 GnTI$^{-/-}$-expressed 426c S278A core construct (K_D = 204 nM), although the kinetics of binding differed for the two samples **(Fig. 4.12E)**.

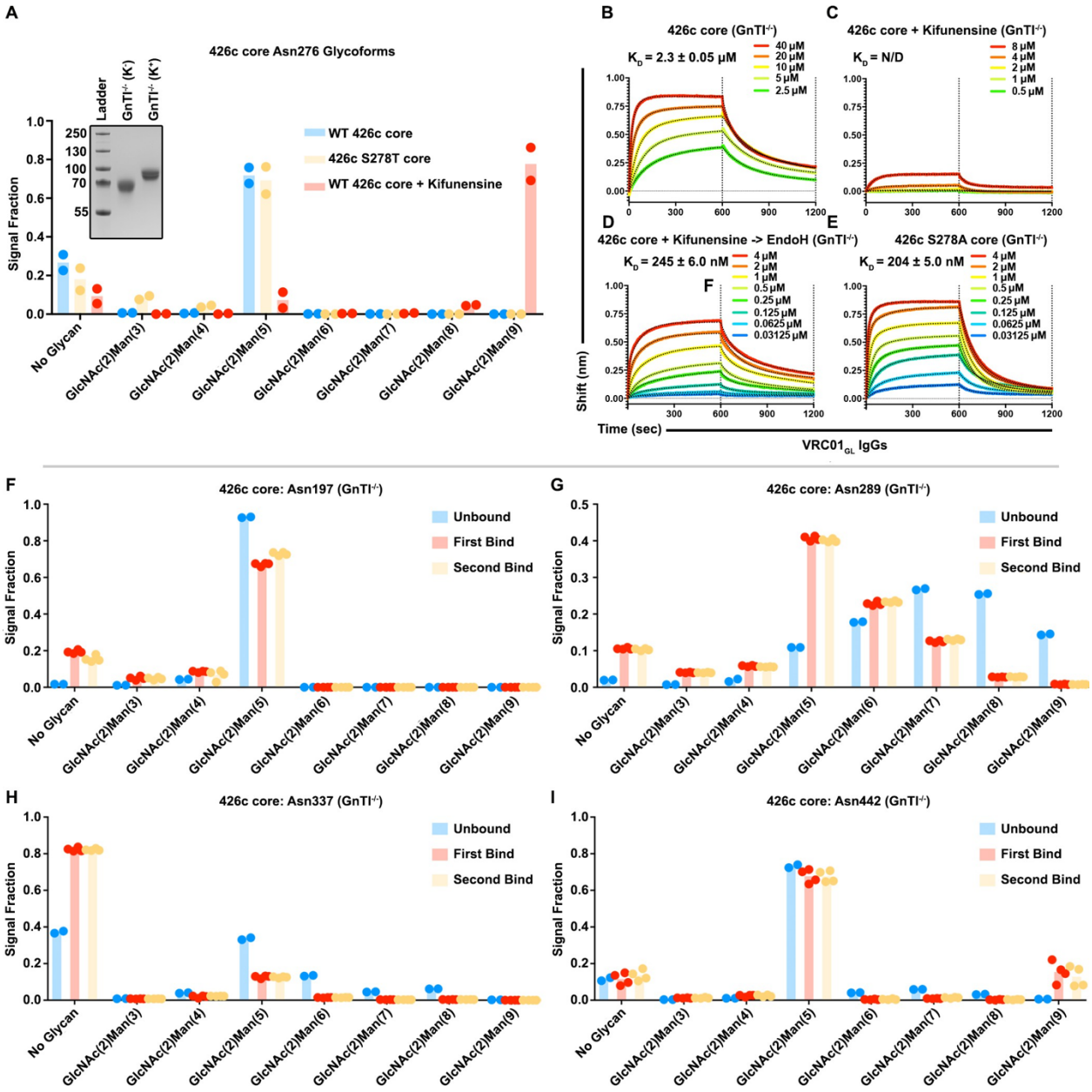

Figure 4.12. Glycan length impacted VRC01$_{GL}$ IgG recognition of the WT 426c core.

(A) Semi-quantitative LC-MS/MS analysis depicting the relative signal intensities for identified Asn276 glycoforms in 426c core (blue), 426c S278T core (yellow), and 426c core expressed in the presence of 100 μM kifunensine (red). (*Inset*) SDS-PAGE demonstrating the molecular weight difference between the 426c core expressed in the absence (K^-) or presence (K^+) of 100 μM kifunensine. The molecular weights of the protein standards are indicated on the left. (B–E) BLI binding data and determined equilibrium dissociation constant values of VRC01$_{GL}$ IgG binding to the 426c core expressed using HEK293 GnTI$^{-/-}$ cells (B), the 426c core expressed using HEK293

GnTI$^{-/-}$ cells in the presence of 100 μM kifunensine (C), the 426c core expressed using HEK293 GnTI$^{-/-}$ cells and digested with EndoH (D), and the 426c S278A core expressed using HEK293 GnTI$^{-/-}$ cells (E). The concentrations of 426c core injected are indicated on each panel. Fitted curves are colored as black dotted lines. The vertical dotted lines indicate the transition between association and dissociation phases. N/D: not determined. (F–I) Semi-quantitative LC-MS/MS analysis depicting the relative signal intensities of unbound (blue), first binding event (red), and second binding event (yellow) fractions taken from VRC01$_{GL}$-based IP experiments. Glycoforms were analyzed for NLGSs Asn197 (G), Asn289 (H), Asn337 (I), and Asn442 (J). Colored dots in panels A and F-I represent individual values extracted from each experimental replicate, with the bar itself representing the experimental mean signal fraction. *Adapted from (Borst et al., 2018)

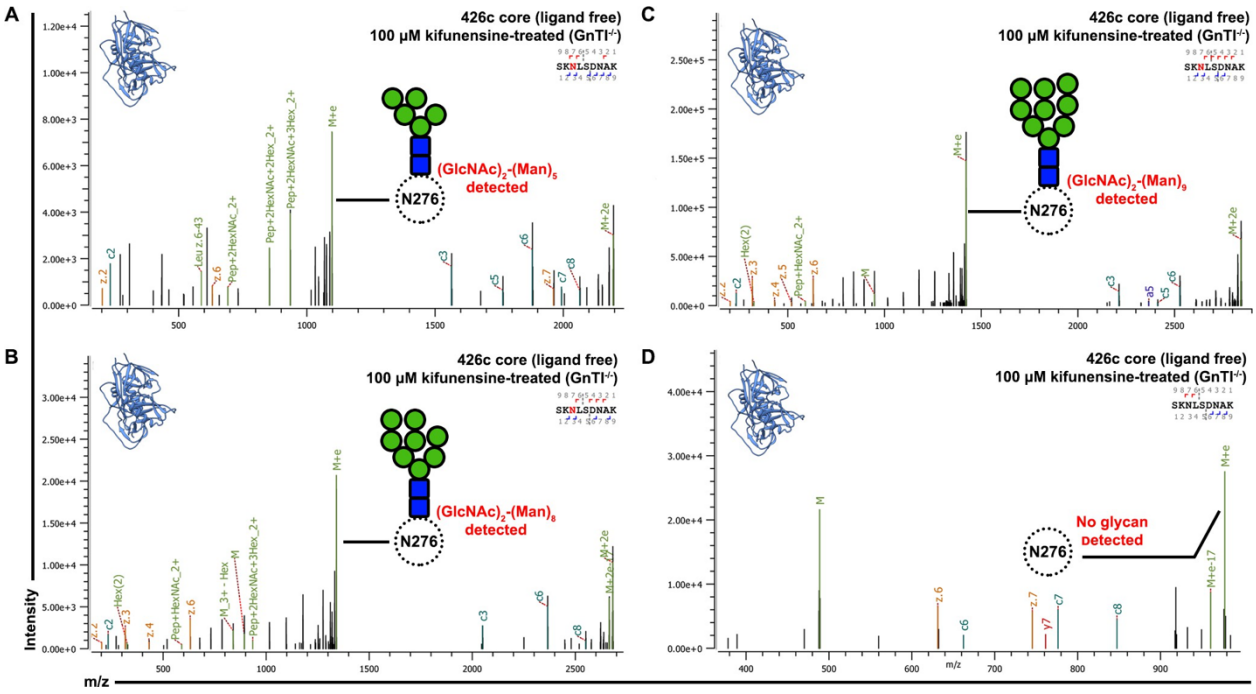

Figure 4.13. LC-MS/MS glycan identifications of kifunensine-treated WT 426c core constructs. Representative LC-MS/MS spectra of glycan Asn276 identifications from the kifunensine-treated 426c core sample used for BLI experiments. The top-left ribbon diagram corresponds to the sample analyzed. The LC-MS/MS fragmentation pattern is indicated in the top-right inset. A graphical depiction of the Asn276 residue (dotted white circle) and its associated identified glycan (blue: N-acetyl glucosamine; green: mannose;) are represented on the spectrum. Green peak labels correspond to precursor peptides with/without LC-MS/MS fragmentation occurring within the glycan. Red/orange peak labels represent identified x, y, and z fragments. Blue/teal peak labels highlight identified a, b, and c fragments. (A–D) Representative LC-MS/MS spectra of an Asn276 glycopeptide with a $(GlcNAc)_2$-$(Man)_5$ oligosaccharide from the 426c core expressed in $GnTI^{-/-}$ cells in the presence of 100 µM kifunensine (A), an Asn276 glycopeptide with a $(GlcNAc)_2$-$(Man)_8$ oligosaccharide (B), an Asn276 glycopeptide with a $(GlcNAc)_2$-$(Man)_9$ oligosaccharide (C), and an unglycosylated Asn276 peptide (D). All these identifications were made from the same kifunensine-treated sample. *Adapted from (Borst et al., 2018)

Table 4.6. BLI kinetics parameters of various 426c core constructs expressed using GnTI$^{-/-}$ cells

*Adapted from (Borst et al., 2018)

	Average Kinetic Values						
$VRC01_{GL}$ IgG vs 426c core (GNTi$^{-/-}$)	KD (M)	KD Error	kon(1/Ms)	kon Error	kdis(1/s)	kdis Error	Full R^2
426c core	2.25E-06	4.18E-08	1.26E+03	2.18E+01	2.69E-03	1.62E-05	0.9804
426c core +kif	N/D	N/D	N/D	N/D	N/D	N/D	N/D
426c core (100 μM kifunensin) +EndoH	2.45E-07	6.03E-09	1.17E+04	2.76E+02	2.51E-03	2.23E-05	0.9547
426c S278A core	2.04E-07	4.95E-09	3.58E+04	7.95E+02	5.31E-03	3.94E-05	0.9804

Previous studies demonstrated enhanced $VRC01_{MAT}$ binding following glycan Asn276 removal although $VRC01_{MAT}$ could accommodate Asn276 glycans (Jardine et al., 2013; McGuire et al., 2013; Medina-Ramírez et al., 2017) (McGuire et al., 2013, 2016; Scharf et al., 2016; Stamatatos et al., 2017; Zhou et al., 2017). Similarly to $VRC01_{MAT}$, $VRC01_{GL}$ binding was previously detected in the absence of the Asn276 glycan (McGuire et al., 2013, 2016). In this present study, $VRC01_{GL}$ binding was also observed under typical expression conditions with the native Asn276 NLGS retained, but was dramatically reduced following expression in the presence of kifunensine **(Table 4.6 , Fig. 4.12A-C, and Fig. 4.13)**. This may indicate that kifunensine treatment results in dramatically more efficient glycosylation of some NLGSs or that differences in glycan length influence recognition of $VRC01_{GL}$-class antibodies to the $CD4_{BS}$, or both **(Fig. 4.12A)**. In line with these hypotheses, the $VRC01_{GL}$-based IP and subsequent semi-quantitative LC-MS/MS of the 426c core expressed in the absence of kifunensine revealed a consistent preference for short and/or unglycosylated species bound to $VRC01_{GL}$ **(Fig. 4.10I and Fig. 4.12F-I).** These findings explain the observed increase in electrophoretic mobility of 426c core species in $VRC01_{GL}$-based IP fractions that bound this antibody compared to the unbound fraction **(Fig. 4.10I)**.

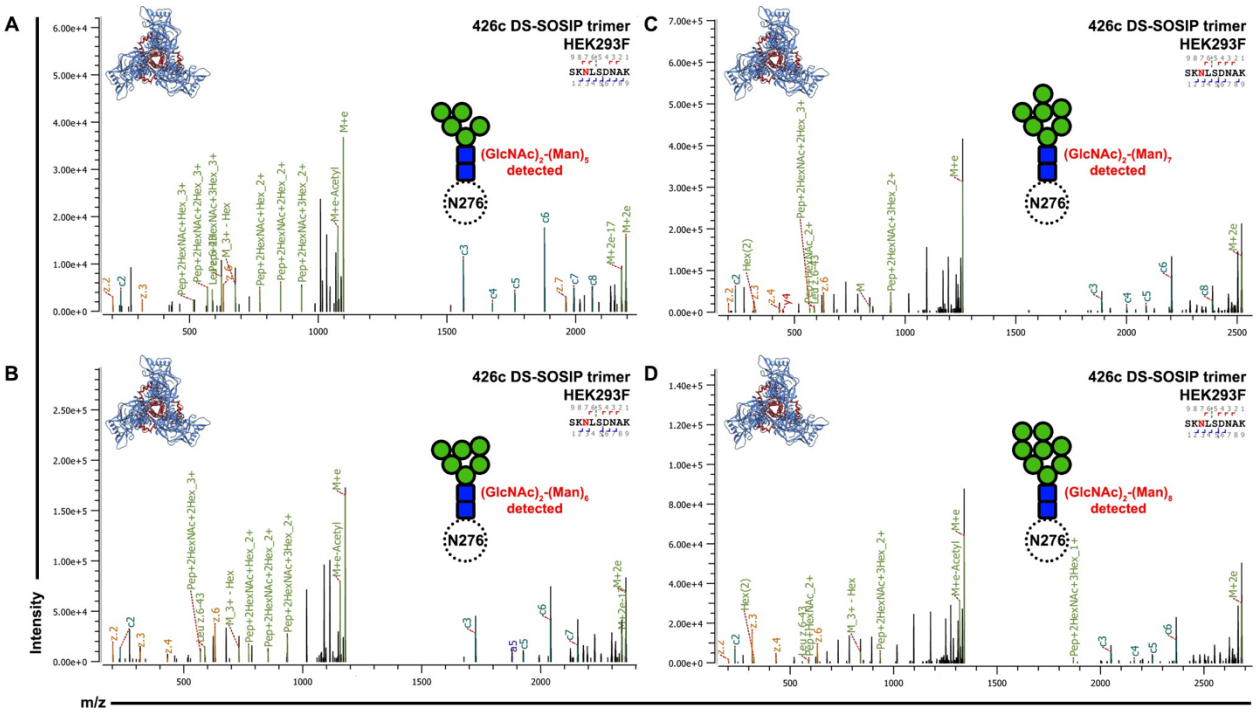

Figure 4.14. Trimeric 426c DS-SOSIP has a variable glycan length at position Asn276. Representative LC-MS/MS spectra of glycan Asn276 identifications from the 426c DS-SOSIP. The top-left ribbon diagram corresponds to the sample analyzed. The LC-MS/MS fragmentation pattern is indicated in the top-right inset. A graphical depiction of the Asn276 residue (dotted white circle) and its associated identified glycan (green circle = Mannose; blue = N Acetylglucosamine) are represented on the spectrum. Green peak labels correspond to precursor peptides with/without LC-MS/MS fragmentation occurring within the glycan. Red/orange peak labels represent identified x, y, and z fragments. Blue/teal peak labels highlight identified a, b, and c fragments. (A–D) Representative LC-MS/MS spectrum of an Asn276 glyco-peptide of a detectable $(GlcNAc)_2$-$(Man)_5$ glycan (A), a $(GlcNAc)_2$-$(Man)_6$ glycan (B), a $(GlcNAc)_2$-$(Man)_7$ glycan (C), and a $(GlcNAc)_2$-$(Man)_8$ glycan (D). *Adapted from (Borst et al., 2018)

While many 426c core glycans are likely to be affected by either kifunensine or EndoH treatment, the Asn276 oligosaccharide is expected to have a pronounced negative effect on $VRC01_{GL}$ binding due to its direct overlap with the $VRC01_{GL}$ epitope(Stewart-Jones et al., 2016; Zhou et al., 2017). The 426c core†-$VRC01_{GL}$ crystal structure does not resolve ordered mannose rings at position Asn276, despite their high detected abundance by LC-MS/MS, and thus only the two proximal GlcNAc moieties were modeled in our structure **(Fig. 4.11C)**. This indicates the Asn276 mannose moieties are likely not directly involved in binding to $VRC01_{GL}$ light chain, but rather act as a steric barrier $VRC01_{GL}$ must overcome to interact with the $CD4_{BS}$. Qualitative LC-MS/MS analyses of the 426c DS-SOSIP trimer, expressed in the absence of kifunensine, revealed longer glycans at the Asn276 NLGS, which correlated with a poorer binding affinity, relative to the 426c core also expressed in the absence of kifunensine **(Fig. 4.1A and Fig. 4.13)**. Indeed, interactions with the Asn276-linked mannose moieties might be restricted to $VRC01_{MAT}$, as these rings are well-resolved in corresponding crystal structures. $VRC01_{GL}$-specificity and compatibility for proximal GlcNAcs is made evident by the increased affinity of $VRC01_{GL}$ for the 426c core following digestion with EndoH **(Fig. 4.12D)**. These results indicate binding of several germline antibodies to gp120 core constructs could potentially be modulated by tailoring protein expression conditions, oligosaccharide length, and/or by endoglycosidase treatment, as opposed to strict mutations aimed at abolishing NLGSs (Kong et al., 2010).

4.7 THE AMINO ACID SEQUENCE OF AN INTACT 426C CORE ASN276 NLGS MODULATED VRC01$_{GL}$ ANTIBODY RECOGNITION

Considering our prior work demonstrating that amino acid composition of the Asn276 NLGS impacted VRC01$_{GL}$ recognition independently of glycan presence(McGuire et al., 2016), and our observation that VRC01$_{GL}$ could bind to 426c core in the presence of a native NLGS at position Asn276 (with a preferential selection for the unglycosylated variant), we decided to test whether altering the identity of the Asn276 NLGS at the 278 position could impact VRC01$_{GL}$-class antibody binding. Whereas 82% of sequenced HIV-1 clades harbor a threonine residue at position 278 of gp120, 426c gp120 contains a serine at this position. Since recent reports suggested NXT NLGS sites are more efficiently glycosylated relative to NXS sites(Huang et al., 2017), we compared the binding kinetics of full-length VRC01$_{GL}$-class IgGs, VRC01$_{GL}$ and 12A21$_{GL}$, to HEK293 GnTI$^{-/-}$-expressed 426c core and an 426c S278T core mutant **(Supplementary Fig. 4.2 and Fig. 4.3)**. BLI experiments demonstrated the S278T mutation reduced the equilibrium dissociation constant by 10-fold relative to the wild type NLGS, mainly by decreasing association kinetics **(Fig. 4.15A-D and Fig. 4.16A)**. The S278T mutation did not abrogate VRC01$_{GL}$-class antibody binding, despite an expected improvement in Asn276 glycosylation efficiency (Huang et al., 2017)**.** Moreover, semi-quantitative LC-MS/MS revealed $(GlcNAc)_2$-$(Man)_5$ oligosaccharides were predominantly detected at position Asn276 in the S278T mutant, though some unglycosylated peptides were still present at low levels **(Fig. 4.12A and Fig. 4.9H,I)**.

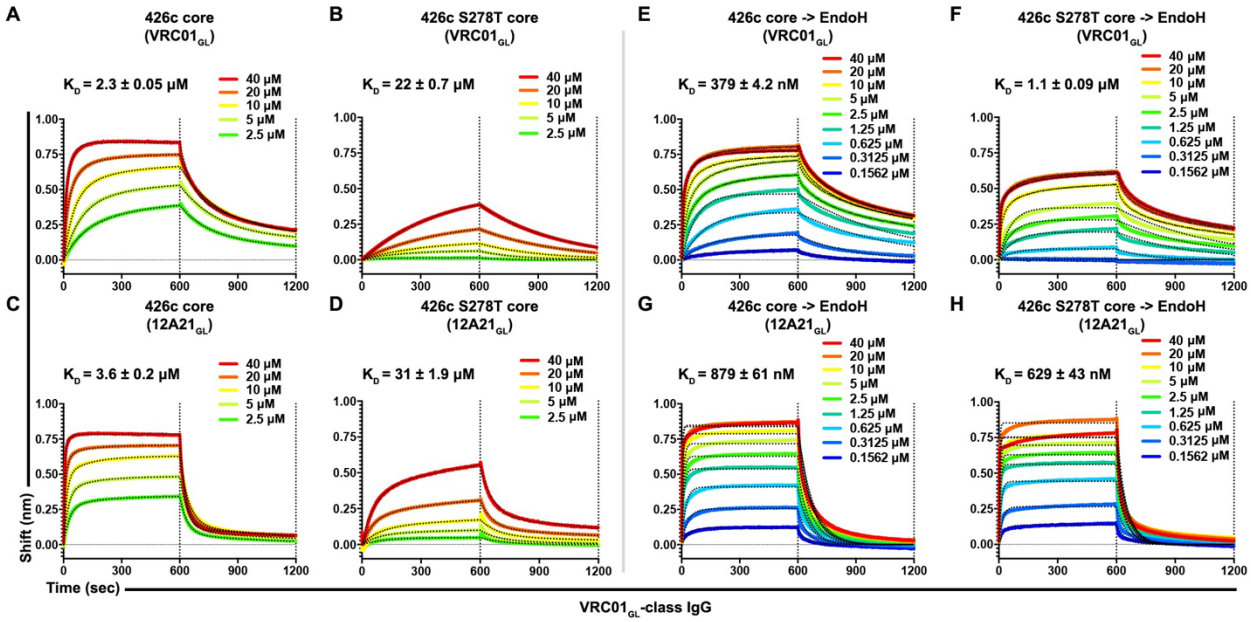

Figure 4.15. Asn276 glycosylation frequency modulated VRC01$_{GL}$-class IgGs recognition of the WT 426c core.

(A–D) BLI binding data and associated K_D values of 426c core constructs, expressed in HEK293 GnTI$^{-/-}$ cells, with two immobilized VRC01$_{GL}$-class IgGs. VRC01$_{GL}$ IgG binding was assessed against the 426c core (A) and the 426c S278T core **(**B). 12A21$_{GL}$ binding to the 426c core (C) and 426c S278T core (D) were also tested. (E–H) BLI binding data and corresponding K_D values of 426c core constructs, expressed using HEK293 GnTI$^{-/-}$ cells and treated with EndoH, with VRC01$_{GL}$-class IgGs. VRC01$_{GL}$ IgG binding was assessed against the EndoH-treated 426c core (E) and the 426c S278T core (F). 12A21$_{GL}$ interactions with the EndoH-treated 426c core (G) and 426c S278T core (H) were also tested. The concentrations of 426c core injected and the color key are indicated on each panel. Fit curves are colored as black dotted lines. The vertical dotted lines indicate the transition between association and dissociation phases. *Adapted from (Borst et al., 2018)

To rule out any potential impact residue identity at position 278 might have on $VRC01_{GL}$-class antibody binding affinities (irrespective of glycosylation status), we mutated the Asn276 NLGS using substitutions S278A, S278V, and S278R **(Fig. 4.2)**. Although the magnitude of binding was improved relative to both 426c core constructs containing a glycan at position Asn276, no appreciable difference in affinities was detected among any of these NLGS-depleted 426 core mutants **(Fig. 4.16A-F)**. Since binding was reduced following introduction of the S278T mutation, these results collectively suggest that a significant fraction of the interactions observed by BLI between the 426c core (containing an intact Asn276 NXS NLGS) and $VRC01_{GL}$ occurred with the unglycosylated Asn276 subspecies. This construct is expected to be less-frequently glycosylated at position Asn276 relative to the S278T mutant (Huang et al., 2017). However, $VRC01_{GL}$-class IgG binding was also detected with the 426c S278T core **(Fig. 4.15A-D, and Fig. 4.16A)**, and EndoH treatment (which retains core GlcNAcs) of both the S278 and S278T constructs significantly improved IgG binding relative to their untreated counterparts **(Fig. 4.15E-H and Fig. 4.16A)**. Although these findings support that binding is dampened by the Asn276 mannose moieties in the absence of $VRC01_{GL}$ CDRL1 loop shortening and/or glycine insertions, interactions were still possible, as underscored by the presence of this carbohydrate in the crystal structure **(Fig. 4.10C)**, the EndoH protection assay **(Fig. 4.11B-C)**, and $VRC01_{GL}$-based IP LC-MS/MS analyses of non-crosslinked samples **(Fig. 4.10I)**. The ability of $VRC01_{GL}$-class antibodies to recognize a $CD4_{BS}$ containing an NLGS at position Asn276 and the linked oligosaccharide is unprecedented, and highlights a potentially unique feature of the 426c core construct containing all native NLGSs for engagement of $VRC01_{GL}$ antibodies.

A

$VRC01_{GL}$ IgG -> 426c core (GnTI-/-)	Average Kinetic Values						
	KD (M)	KD Error	kon(1/Ms)	kon Error	kdis(1/s)	kdis Error	Full R^2
426c S278 core	2.25E-06	4.18E-08	1.26E+03	2.18E+01	2.69E-03	1.62E-05	0.9804
426c S278T core	2.24E-05	7.36E-07	3.72E+02	1.15E+01	8.33E-03	8.98E-05	0.9801
426c S278 core +EndoH	3.79E-07	9.41E-09	6.84E+03	1.40E+02	2.34E-03	1.60E-05	0.9684
426c S278T core +EndoH	1.11E-06	9.34E-08	4.02E+03	1.32E+02	3.07E-03	2.87E-05	0.9555
426c S278A core	4.18E-07	1.04E-08	1.20E+04	2.61E+02	2.82E-03	1.96E-05	0.9726
426c S278V core	3.95E-07	7.31E-09	7.82E+03	9.64E+01	2.05E-03	1.01E-05	0.9749
426c S278R core	4.01E-07	1.11E-08	1.35E+04	2.91E+02	2.92E-03	2.10E-05	0.9713
$12A21_{GL}$ IgG -> 426c core (GnTI-/-)							
426c S278 core	3.57E-06	1.80E-07	3.64E+03	1.64E+02	1.23E-02	1.93E-04	0.9725
426c S278T core	3.10E-05	1.87E-06	4.75E+02	3.10E+01	1.68E-02	2.27E-04	0.9669
426c S278 core +EndoH	8.79E-07	6.09E-08	2.72E+04	1.39E+03	1.77E-02	2.47E-04	0.9875
426c S278T core +EndoH	6.29E-07	4.28E-08	5.02E+04	3.20E+03	2.04E-02	3.64E-04	0.9820
426c S278A core	3.52E-07	3.15E-08	5.87E+04	3.76E+03	5.54E-03	9.90E-05	0.9041
426c S278V core	2.72E-07	1.76E-08	4.47E+04	1.96E+03	5.18E-03	6.47E-05	0.9492
426c S278R core	3.69E-07	3.22E-08	6.05E+04	3.83E+03	6.81E-03	1.23E-04	0.9241

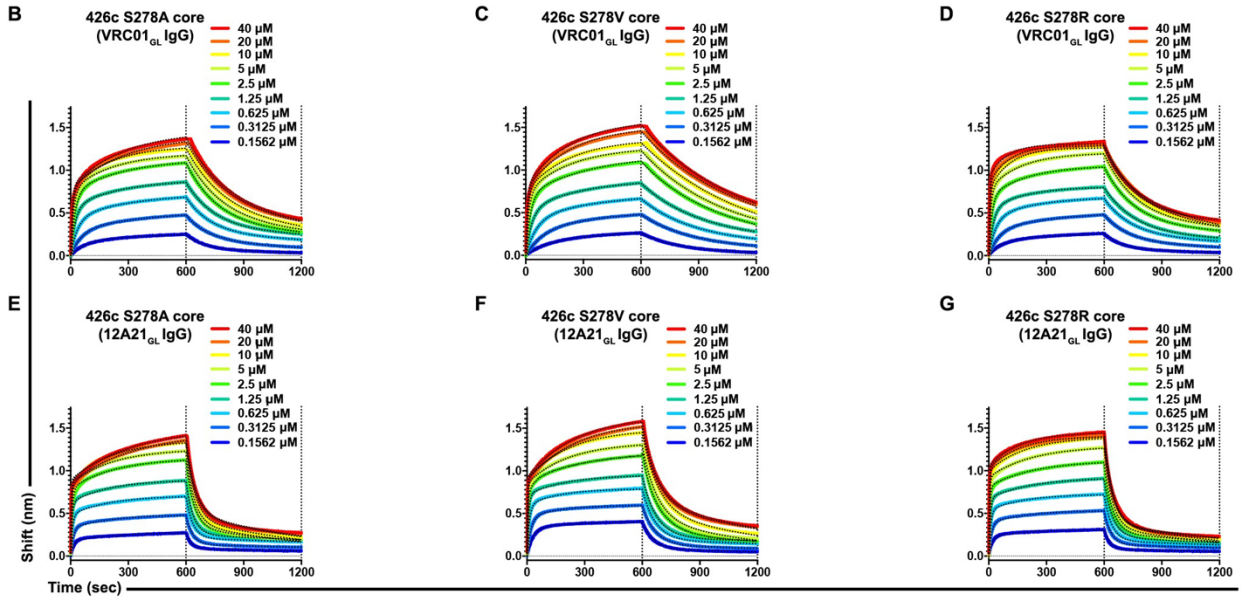

Figure 4.16. $VRC01_{GL}$ binding affinity was not significantly affected by the identity of the residue 278 in the absence of a glycan at position Asn276.

(A) BLI kinetics parameters determined from panels (B–G) and Figure 4.15. (B–D) BLI binding data and determined equilibrium dissociation constants for $VRC01_{GL}$ IgG binding to 426c S278A core (A), 426c S278V core (B**)**, and 426c S278R core. (E–G) BLI binding data and determined equilibrium dissociation constants of $12A21_{GL}$ IgG binding to 426c S278A core (**A**), 426c S278V core (B), and 426c S278R core. The concentrations of 426c core injected are indicated on each panel. Fit curves are colored black. The vertical dashed lines indicate the transition between association and dissociation phases. *Adapted from (Borst et al., 2018)

4.8 CONCLUSIONS, DISCUSSION, AND FUTURE DIRECTIONS

Broad-spectrum and potent neutralization of HIV-1 by naturally occurring VRC01 bnAbs targeting the $CD4_{BS}$ is possible in humans(Huang et al., 2016). However, mature VRC01-class bnAbs are produced only in a small fraction of infected individuals and only after up to a decade following the initial infection(Wu et al., 2015). Due to the negligible binding of germline VRC01-class antibodies to "wild-type" stabilized prefusion-closed SOSIP trimers, we sought out to understand putative mechanisms of primary engagement of this class of germline antibodies by various HIV-1 immunogens. To this end, we first engineered a disulfide bond between the glycan depleted 426c DS-SOSIP $D3^{\dagger}$ and $VRC01_{GL}$ to promote complex formation. This tethering approach was recently described for $VRC01_{MAT}$ and led to native structures that do not suffer from any distortions(Stewart-Jones et al., 2016). It is unlikely that the engineered disulfide would force the $VRC01_{GL}$ and 426 gp120 to interact in a homogeneous way. An engineered disulfide would only prevent the dissociation of the two proteins (similarly to what we previously described for mature VRC01 (Stewart-Jones et al, Cell 2016)), but will not force them to interact uniformly (Stewart-Jones et al., 2016). Using this crosslinking strategy, we demonstrated that $VRC01_{GL}$ bound to the deglycosylated 426c DS-SOSIP $D3^{\dagger}$ trimer in the absence of a formed bridging sheet and that this binding stabilized surrounding $CD4_{BS}$ carbohydrates at position Asn197 and Asn386. Considering there was a minor enrichment for the unglycosylated Asn197 glycoform in "bound" fractions following $VRC01_{GL}$-based immunoprecipitation of the 426c core, there could be an entropic cost associated with binding in the presence of this particular oligosaccharide. Additionally, we found that 426c naturally lacks glycans at positions Asn234 and Asn362, which likely enhanced accessibility of the $CD4_{BS}$ to bnAbs and could affect processing of nearby carbohydrates(Behrens et al., 2018), including glycan Asn276. We propose this is one of the

reasons explaining the ability of 426c DS-SOSIP D3 and 426c core constructs to bind $VRC01_{GL}$-class antibodies.

Immunogen design efforts focusing on VRC01-class bnAbs have thus far largely relied on the mutagenic removal of NLGSs during priming followed by their reinsertion during subsequent boost (McGuire et al., 2013; Medina-Ramírez et al., 2017; Zhou et al., 2017). This strategy may not recapitulate the conditions of *bona fide* infections, as several $CD4_{BS}$ NLGSs are conserved amongst circulating HIV-1 strains(Crooks et al., 2015; Lavine et al., 2012; Pritchard et al., 2015; Stewart-Jones et al., 2016). The complete absence of these NLGSs during the priming phase may also remove a selection pressure guiding proper accommodation of these glycans during antibody maturation, and could explain the limited success of elicitation of VRC01-class bnAbs capable of neutralizing natively glycosylated wild-type viruses. As a result, alternative priming and boost strategies retaining these native NLGSs may need to be considered.

Specifically, HIV-1 gp120 core constructs have previously been shown to have differential processing of NLGSs around the $CD4_{BS}$ relative to their trimeric SOSIP counterparts(Bonomelli et al., 2011). We observed that reintroduction of 426c gp120 V5 loop NLGSs did not negatively impact $VRC01_{GL}$ binding to the 426c core in contrast with what was detected for trimeric 426c gp140 (McGuire et al., 2013). We found that $VRC01_{GL}$ Fabs and IgGs could bind to the 426c core (containing a wild-type Asn276 NLGS) but, as expected, not to a trimeric 426c DS-SOSIP construct containing all wild type NLGSs (Huang et al., 2016). We put forward this interaction is likely permitted in the WT 426 core in part due to the absence of variable loops 1, 2, and 3 and could potentially be further augmented by the natural absence of glycans at position Asn234 and

Asn362. It is also possible that stabilized trimeric pre-fusion closed SOSIP constructs impart additional negative steric effects not present in the monomeric gp120 core epitopes. This is supported by our observation that there is a reduced amount of trimming of the Asn276 glycan in the 426c DS-SOSIP trimer relative to the 426c core monomer. This could arise from steric properties of the trimer which would be absent in soluble monomeric constructs, thereby limiting unfettered access of the glycosylation machinery to this site during expression. It also remains to be determined if the conformation of the gp120 bridging sheet influences the recognition efficacy of this germline antibody.

We found that $VRC01_{GL}$ binding to WT 426c core constructs preferentially occurred using expression systems allowing for production of short glycans and provided a structural framework for accommodation of the Asn276 oligosaccharide by the $VRC01_{GL}$ CDRL1. As is the case for $VRC01_{MAT}$ (Jardine et al., 2013; McGuire et al., 2013, 2016; Medina-Ramírez et al., 2017; Stamatatos et al., 2017), we would like to emphasize that the unglycosylated Asn276 variant is the preferred $VRC01_{GL}$ binding partner and likely had an important contribution the interactions observed by BLI. However, we detected glycosylation at position Asn276, both structurally and by LC-MS/MS following $VRC01_{GL}$-based IP experiments, in the $VRC01_{GL}$-bound fractions, in the presence and absence of cysteine cross-linking, respectively. This indicated accommodation of this oligosaccharide could occur during $VRC01_{GL}$ binding in the absence of CDRL1 loop shortening and/or glycine addition, arguing in favor of its retention in epitope-based constructs derived from the 426c strain of HIV-1.

The structural and biophysical data reported here provide a foundation for understanding how bnAbs targeting the HIV-1 $CD4_{BS}$ may be elicited in humans in the presence of a native Asn276 NLGS. We demonstrated structurally that $VRC01_{GL}$ binding to a 426c core is possible and appears to occur both in the absence and presence of a glycan at position Asn276, supporting recently proposed hypotheses (Jardine et al., 2016)(Scharf et al., 2016). Introduction of an NXS NLGS at position Asn276 of g120 core constructs lacking selected variable loops and in absence of glycans Asn234, Asn362(363), and Asn460 could prove a useful strategy to elicit VRC01-class antibodies during the priming phase of immunization. Additionally, the stark differences in binding observed between $VRC01_{GL}$ and 426c DS-SOSIP or 426c core constructs suggests "germline-targeting" vaccine design strategies starting with an epitope-based gp120 immunogen may be a promising alternative to current priming strategies focusing on glycan-depleted HIV-1 SOSIP trimers. Indeed, a remarkable success using site-directed epitope-based immunogens targeting other antigenic regions of HIV-1 Env has been recently achieved (Xu et al., 2018). In the context of $VRC01_{GL}$-targeted immunogens, the use of insect cell expression systems may further benefit recognition of the HIV-1 $CD4_{BS}$ due to the abundance of paucimannose sugars (Altmann et al., 1999). This approach has already been reported to enhance the immunogenicity of the $CD4_{BS}$ for other HIV-1 antibodies, but has yet to be shown for antibodies of the VRC01 lineage(Kong et al., 2010). We highlight here the advantages of using an HIV-1 WT 426c core construct for enhancing VRC01-class germline antibody binding relative to the glycan-depleted 426c trimeric Env SOSIP construct and propose that these observations be considered in future vaccine design efforts targeting the $CD4_{BS}$ of HIV-1.

4.9 METHODS

4.9.1 *Protein purification*

426c core†-VRC01$_{GL}$

426c core†-VRC01$_{GL}$ was expressed using HEK293S GnTI$^{-/-}$ cells. Cells were cultured in suspension and transfected with equal parts of 426c G459C core, VRC01$_{GL}$-A60C$_{HC}$, and VRC01$_{GL}$ light chain plasmids (500 µg total/L) using 293 Free Transfection Reagent (Novagen). After 6 days, cells were centrifuged at 4,500 rpm for 20 minutes and supernatant was filter-sterilized. A His-tag on the Fab heavy chain was utilized for purification by suspending His60 Ni-Superflow Resin (Takata) in the supernatant at 4^{o} C overnight. The Ni resin was washed with a solution of 150mM NaCl, 20mM Tris pH 8.0, 20mM Imidazole pH 7.0 and eluted with a solution of 300mM NaCl, 50mM Tris pH 8.0, 250mM Imidazole pH 7.0. The sample was further purified by Size-exclusion chromatography (SEC) using a HiLoad 16/600 Superdex 200pg (GE) column removing non-specific proteins and excess Fab. Fractions containing the complex were concentrated and treated with an excess of EndoH for one hour at 37^{o}C. The complex was then rerun over an SEC S200 column and concentrated to ~10mg/mL for crystallization trials.

426c DS-SOSIP D3†-VRC01$_{GL}$

HEK293S GnTI$^{-/-}$ cells were transfected with 426c DS-SOSIP D3†, VRC01$_{GL}$-A60C$_{HC}$, VRC01$_{GL}$ light chain and furin plasmids at a ratio of 3:1:1:1, as described above and previously(Stewart-Jones et al., 2016). Complexes were purified by the His-tag on the VRC01$_{GL}$ fragment as described above. Complexes were further purified on SEC as previously described and the peak containing both SOSIP and VRCO1$_{GL}$ were concentrated for cryoEM.

426c DS-SOSIP variants

426c DS-SOSIP D3 (non-crosslinked G459 variant with C-terminal strep-his tag) was expressed using HEK293F cells by co-transfection of 426c DS.SOSIP D3 and furin plasmids at a 5:1 ratio. 426c DS-SOSIP D3 was purified first by Ni- and then by Streptactin-affinity, followed by enzymatic digestion and separation of the cleaved tag from the trimer by SEC using a HiLoad 16/600 Superdex 200pg (GE).

426c core constructs

All 426c core constructss were expressed by the transfection protocol described above. Agarose Bound Galanthus Nivalis Lectin (Vector) was used to separate the cores from the supernatant. The resin was washed with 20mM Tris pH 7.5, 100 mM NaCl, 1 mM EDTA and elution used a buffer containing 20mM Tris pH 7.5, 100 mM NaCl, 1 mM EDTA, and 1M Methyl α-D-mannopyranoside. Samples were further purified by SEC using a HiLoad 16/600 Superdex 200pg (GE) column.

Antibodies

All antibodies were expressed by the transfection protocol described above using equal ratios of heavy and light chain encoding plasmids. Protein A Agarose (Pierce) resin was used to separate IgG from the supernatant. Protein A beads were washed with phosphate buffer saline (PBS) and elution used a commercially available IgG elution buffer at pH 2.0 (Pierce). Samples were buffer exchanged into PBS.

4.9.2 *Biolayer interferometry.*

BLI assays were performed with an Octet Red 96 instrument (ForteBio, Inc, Menlo Park, CA) at 29ºC with shaking at 500 r.p.m. All measurements were corrected by subtracting the background signal obtained from duplicate traces generated with an irrelevant negative control IgG or Fab. For standard BLI assays, IgGs were immobilized on anti-AHC biosensors (at 20 µg/ml in PBS), or Fabs on anti-human Fab-CH1 (FAB2G, ForteBio) biosensors (at 40 µg/ in PBS), for 240s. Sensors were then incubated for 1 min in kinetic buffer (KB: 1X PBS, 0.01% BSA, 0.02% Tween 20 and 0.005% NaN3) to establish the baseline signal (nm shift). Antibody-loaded sensors were then immersed into solutions of purified recombinant samples for kinetic analysis. Analyses of DS-SOSIP trimers and 426c core constructs was performed by BLI using $VRC01_{GL}$ IgG and an extensive dilution series to determine accurate K_D estimates. Samples expressed in the presence of 100µM kifunensin and EndoH-digested were first buffer exchanged into PBS prior to dilution and kinetic analyses. Curve fitting to determine relative apparent antibody affinities for the samples was performed using a 1:1 binding model and the ForteBio data analysis software. Mean k_{on} , k_{off} , and K_D values were determined by averaging all binding curves within a dilution series having R^2 values of greater than 95% confidence level.

4.9.1 *Crystallization*

Crystallization conditions for the 426c core†-$VRC01_{GL}$ were screened using a Mosquito (ttplabtech)-dispensing robot. Screening was done with Rigaku Wizard Precipitant Synergy block no. 2, Molecular Dimensions Proplex screen HT-96, and Hampton Research Crystal Screen HT using the vapor diffusion method. Initial crystals were further optimized with Hampton Research Additive Screen to grow large and well-diffracting crystals. Final crystals were grown in a solution

of 0.09M $MgCl_2$, 0.09M Na-Citrate pH 5.0, 13.5% PEG 4000, 0.1M $LiCl_2$. Crystals were cryoprotected in solutions containing 30% molar excess of their original reagents and 20% glycerol. Crystals diffracted to 2.3A. Data was collected at ALS 5.0.2 and processed using HKL2000(Otwinowski and Minor, 1997).

4.9.2 *Structure solution and refinement.*

The structure of 426c core†-VRC01$_{GL}$ Fab was solved through molecular replacement using Phaser in CCP4(Collaborative Computational Project, 1994). The structure was further refined with COOT(Emsley and Cowtan, 2004) and Phenix(Adams et al., 2010). The refinement statistics are summarized in Table 1.

4.9.3 *Negative-stain EM sample preparation*

All 426c DS-SOSIP constructs in this study (3 μL) were negatively stained at a final concentration of 0.008 mg/mL using Gilder Grids overlaid with a thin layer of carbon and 2% uranyl formate as previously described (Veesler et al., 2014).

4.9.4 *Negative-Stain EM data collection and processing*

Data were collected on an FEI Technai 12 Spirit 120kV electron microscope equipped with a Gatan Ultrascan 4000 CCD camera. A total of 150-300 images were collected per sample by using a random defocus range of 1.1–2.0 μm with a total exposure of 45 e−/A^2. Data were automatically acquired using Leginon (Suloway et al., 2005), and data processing was carried out using Appion (Lander et al., 2009). The parameters of the contrast transfer function (CTF) were estimated using

CTFFIND4 (Mindell and Grigorieff, 2003), and particles were picked in a reference-free manner using DoG picker(Voss et al., 2009). Particles were extracted with a binning factor of 2 after correcting for the effect of the CTF by flipping the phases of each micrograph with EMAN 1.9 (Ludtke et al., 1999). The 426c DS-SOSIP D3†-VRC01$_{GL}$ stack was pre-processed in RELION/2.1(Kimanius et al., 2016; Scheres, 2012d, 2012c) with an additional binning factor of 2 applied, resulting in a final pixel size of 6.4 Å. Resulting particles were sorted by reference-free 2D classification over 25 iterations. The best particles were chosen for 3D classification into 6 classes using RELION/2.1(Kimanius et al., 2016). C3 symmetry was applied for 426c DS-SOSIP D3†-VRC01$_{GL}$, with the best 3D classes refined further in RELION/2.1(Kimanius et al., 2016) using the gold-standard approach.

4.9.5 *CryoEM sample preparation*

We applied 2μL of 0.7 mg/mL of DS-SOSIP D3†-VRC01$_{GL}$ in 10 mM HEPES pH 7.5, 50 mM NaCl, 0.085 mM dodecyl-maltoside to glow-discharged C-flat CF-1.2/1.3-4C-T-grids. Vitrification was performed by using an FEI Vitrobot Mark IV, using a blot time of 6 s at a temperature of 22 °C and 100% humidity.

4.9.6 *CryoEM data collection*

Data collection was performed automatically using Leginon(Suloway et al., 2005) to control an FEI Titan Krios Electron Microscope equipped with a Gatan Quantum GIF energy filter and a K2 Summit direct electron detector(Li et al., 2013) operating in electron-counting mode spanning a random defocus range between 2.0 and 3.5 μm. Approximately 2,000 micrographs

were collected with a pixel size of 1.36 Å at a dose rate of 8 counts per pixel per second and 15-s acquisition time (0.2 frame per second), yielding a final measured dose of 80 e−/Å^2 per movie.

4.9.7 *CryoEM data processing*

Alignment of movie frames was carried out using MotionCor2(Zheng et al., 2017) with a B-factor of -100 Å^2 and an applied dose-weighting scheme of 0.95 electrons/Å^2/frame. Omission of low-quality micrographs left a total of 1,724 micrographs for downstream data processing. ~567,000 particles were picked in a reference-free manner using DoG picker(Voss et al., 2009). Global defocus and astigmatism were estimated using GCTF(Zhang, 2016) on the non-dose weighted aligned sums. Dose-weighted particles were binned to a final pixel size of 5.44 Å for an initial round of 2D classification using RELION/2.1(Kimanius et al., 2016). 200,000 selected particles were re-centered, re-extracted, and unbinned to a final pixel size of 1.36 Å and subjected to 3D classification with RELION/2.1(Kimanius et al., 2016) using the 30 Å low-pass filtered initial model generated from the DS-SOSIP D3†-VRC01$_{GL}$ negative-stain dataset. Out of the eight resulting classes, five classes contained well defined secondary structure elements and three bound Fabs. These classes were low-pass filtered to 20 Å and the best-resolved class was used as an initial model during 3D refinement using C3 symmetry. Refined angles for all particles were subsequently imported into FREALIGN (Grigorieff, 2016; Lyumkis et al., 2013b) and further refined with an applied particle weighting scheme. An additional iteration of refinement was performed by adjusting only the X/Y shifts. This refinement scheme resulted in a final estimated resolution of 3.8 Å for the three-Fab complex. The VRC01$_{GL}$ constant domains of the Fab were masked out during the final rounds of refinement and omitted from the final model due to the inherent flexibility of the elbow region(Stanfield et al., 2006). This same strategy was used for 3D

classes of DS-SOSIP D3†-VRC01$_{GL}$ containing only two Fabs (C1 symmetry), leading to a final estimated resolution of 4.8 Å. Reported resolutions are based on the gold-standard FSC = 0.143 criterion . Local resolution estimates were generated using the ResMap software (Kucukelbir et al., 2014).

4.9.8 *Model building and refinement*

We selected a clade A HIV-1 BG505 SOSIP.664 trimer(Stewart-Jones et al., 2016) and the 426c.TM1deltaV1-V3gp120 in complex with germline NIH46-46(Scharf et al., 2016) as initial reference models for building 426c DS-SOSIP D3†-VRC01$_{GL}$. This model was manually trimmed and edited using COOT (Emsley and Cowtan, 2004; Emsley et al., 2010) and RosettaES(Frenz et al., 2017). We then further refined the structure in Rosetta using density-guided protocols (Wang et al., 2016) for the 3.8 Å resolution C3 reconstruction. This process was repeated iteratively until convergence and high agreement with the map was achieved. The Fab constant domains were masked out during refinemen and omitted from the final model. Following refinement of protein coordinates, identified *N*-linked glycans were manually docked into their corresponding density and refined using Rosetta (DiMaio et al., 2011). Multiple rounds of minimization were performed on the complete glycoprotein model and manually inspected for errors. Throughout this process, we applied strict non-crystallographic symmetry constraints in Rosetta (DiMaio et al., 2011). The 4.8 Å asymmetric 426c DS-SOSIP D3†-VRC01$_{GL}$ structure bound to only two Fabs was built by removing one of the VRC01$_{GL}$-A60C Fabs bound to the aforementioned C3 model and was minimized using Rosetta without applying symmetry. Glycans not resolved by density in the unbound protomer were manually trimmed. Final model quality was analyzed using

Molprobity(Chen et al., 2010a) and EM ringer(Barad et al., 2015). All figures were generated with UCSF Chimera(Pettersen et al., 2004).

4.9.9 *$VRC01_{GL}$-based immunoprecipitation*

Purified recombinant $VRC01_{GL}$ IgG was covalently coupled to Dnyabeads MyOne Tosylactivated beads (Life Technologies), and immunoprecipitation using magnetic separation was carried out according to the manufacturer's protocol. 5 mg of 426c core produced using HEK293S $GnTI^{-/-}$ cells were incubated with 100 μg of $VRC01_{GL}$-beads for 15 minutes (first bind), after which the beads were removed and unbound material (flow through) was incubated with a second fresh 100 μg aliquot of $VRC01_{GL}$-beads for an additional 15 minutes (second bind). $VRC01_{GL}$-beads from first and second binding were washed 3x before acidic elution and pH neutralization of affinity-purified samples. Unbound material was further depleted by incubation with a third 100 μg of $VRC01_{GL}$-beads, which were removed, before analysis. Samples of the original input 426c core, and $VRC01_{GL}$-bound and unbound fractions were resolved by SDS gel electrophoresis under reducing conditions and the remainder subjected to LC-MS/MS analysis, as described above.

4.9.10 *Mass Spectrometry*

For analysis of *N*-linked glycosylation profiles, an estimated 250 pmol of each HIV-1 426c-based construct analyzed in this paper was denatured, reduced, and alkylated by dilution to 5 μM in 50 μL of buffer containing 100 mM Tris (pH 8.5), 10 mM Tris(2-carboxyethylphosphine (TCEP), 40 mM iodoacetamide or 40 mM iodoacetic acid, and 2% (wt/vol) sodium deoxycholate.

Samples were first heated to 95 °C for 10 min and then incubated for an additional 30 min at room temperature in the dark. The samples were digest with trypsin (Sigma Aldrich), by diluting 20µL of sample to total volume of 100µL 50 mM ammonium bicarbonate (pH 8.5). Protease was added to the samples in a ratio of 1:75 by weight and left to incubate at 37 °C overnight. After digestion, 2µL of formic acid was added to the samples to precipitate the sodium deoxycholate from the solution. After centrifugation at 17,000×g for 25 min, 85 µL of the supernatant was collected and centrifuged again at 17,000×g for 5 min to ensure removal of any residual precipitated deoxycholate. 80 µL of this supernatant was collected. For each sample, 8µL was injected on a Thermo Scientific Orbitrap Fusion Tribrid mass spectrometer. A 35-cm analytical column and a 3-cm trap column filled with ReproSil-Pur C18AQ 5µM (Dr. Maisch) beads were used. Nanospray LC-MS/MS was used to separate peptides over a 90-min gradient from 5 to 30% acetonitrile with 0.1% formic acid. A positive spray voltage of 2,100 was used with an ion transfer tube temperature of 350 °C. An electron-transfer/higher-energy collision dissociation ion-fragmentation scheme(Frese et al., 2013) was used with calibrated charge-dependent entity-type definition (ETD) parameters and supplemental higher-energy collision dissociation energy of 0.15. A resolution setting of 120,000 with an AGC target of 2×10^5 was used for MS1, and a resolution setting of 30,000 with an AGC target of 1×10^5 was used for MS2. Data were searched with the Protein Metrics Byonic software(Bern et al., 2012), using a small custom database of recombinant protein sequences including the proteases used to prepare the glycopeptides. Reverse decoy sequences were also included in the search. Specificity of the search was set to C-terminal cleavage at R/K (trypsin), allowing up to two missed cleavages, with EthcD fragmentation (b/y- and c/z-type ions). We used a precursor mass and product mass tolerance of 12 ppm and 24 ppm, respectively. Carbamidomethylation of cysteines was set as fixed modification, carbamidomethylation of the

lysines and N-terminal amines were set as variable modifications, methionine oxidation as variable modification, pyroglutamate identification was set for both N-terminal glutamines and glutamates as a variable modification, and a concatenated N-linked glycan database (derived from the four software-included databases) was used to identify glycopeptides. All analyzed glycopeptide hits were manually inspected to ensure for quality and accuracy. Semi-quantitative LC-MS/MS of VRC01-based immunoprecipitation experiments were performed using Skyline(MacLean et al., 2010) with peak integration and LC-MS/MS searches imported from Byonic. Missed cleavages and post-translational modifications listed above for qualitative LC-MS/MS searches were included in the quantification of glycopeptides. All MS1 peak areas used for integration were manually inspected to ensure for quality and accuracy. Unbound fractions from two experimental replicates were pooled and injected as two technical replicates, whereas each “bound” fraction (first bind and second bind) were performed as two experimental and two technical replicates each.

Chapter 5. GLYCAN TAILORING MODULATES IMMUNE RECOGNITION OF THE HIV-1 CD4 RECEPTOR BINDING SITE

5.1 CHAPTER SUMMARY

We now enter into the final part of the thesis work, which expands upon the promising results of the previous chapter. Since the first case of the human immunodeficiency virus (HIV) was reported in the United States in 1981, HIV has infected over 75 million individuals worldwide and has caused over 32 million deaths. Although progress have been made in managing this disease, no vaccine against HIV currently exists. Rare broadly neutralizing HIV antibodies have been isolated from select infected patients. Some of these antibodies block the HIV envelope CD4-receptor binding ($CD4_{BS}$) site, which enables viral attachment and initiation of entry into host T-cells. As a result, recent efforts have focused on reverse-engineering this protective immune response in order to obtain a vaccine. While some encouraging successes have been recently reported, numerous studies have highlighted the difficulty in producing antibodies capable of bypassing the glycan shield surrounding the $CD4_{BS}$, which facilitates immune evasion. In this study, we developed a strategy to selectively tailor the HIV gp120 glycan shield and increase exposure of the $CD4_{BS}$. We assessed the efficacy of this approach both *in vitro* and *in vivo* and determined that glycan trimming enhanced immune recognition of the gp120 $CD4_{BS}$. Thus, this chapter introduces glycan tailoring as a novel approach to HIV vaccine design.

5.2 EndoH digestion preferentially targets oligosaccharides surrounding the $CD4_{BS}$

Glycoproteins typically exhibit a high degree of oligosaccharide heterogeneity at each N-linked glycosylation site(Struwe et al., 2018; Walls et al., 2019; Watanabe et al., 2018). Furthermore, enrichment for specific saccharides at selected glycosylation sites is non-trivial. As a result, site-specific tailoring of the glycan shield of an antigen is a long-sought goal of protein engineering. We recently demonstrated that WT 426c core production in HEK293S $GnTI^{-/-}$ cells resulted in a predominance of $GlcNAc_2Man_5$ glycans near the $CD4_{BS,}$ whereas other regions of the core had more diversified oligosaccharide lengths (Borst et al., 2018). Moreover, the HIV-1 Env oligosaccharide density has been shown to inversely correlate with the site-specific activity of glycoside hydrolases in the cell secretory pathway due to restrictions imparted by carbohydrate accessibility (Behrens et al., 2016; Coss et al., 2016; Pritchard et al., 2015). Although Env is heavily glycosylated, the glycan density varies considerably across the surface of this protein, likely explaining the observed glycan shield heterogeneity. We previously reported that $VRC01_{GL}$ utilizes CDRL1 and CDRL3 to contact the two proximal GlcNAc of the oligosaccharide at position N276 (Borst et al., 2018). The lower carbohydrate density detected around the $CD4_{BS}$ – compared to other regions of Env – led us to postulate EndoH could trim these specific oligosaccharides to $GlcNAc_1$ while retaining glycan integrity at other sites. Thus, a protocol enabling region-specific glycan digestion could allow for retention of key contacts between germline $CD4_{BS}$ antibodies and the gp120 glycan shield, while avoiding exposure of additional non-native epitopes.

To test the feasibility of selective glycan trimming and enrichment for $GlcNAc_1$ near the $CD4_{BS}$, we first investigated the rate of enzymatic digestion of the WT 426c core using a limited EndoH

digestion protocol **(Fig. 5.1A)**. EndoH-treated samples were collected at various time points and were denatured and/or frozen to halt enzymatic activity. SDS-PAGE analysis showed the undigested WT 426c core expressed using HEK293S GnTI$^{-/-}$ cells had an electrophoretic migration profile corresponding to a molecular weight of 67 kDa, comprising a 39kDa polypeptide and up to 15 putative N-linked glycans. Individual gel bands had a smeared appearance, likely resulting from the heterogeneity of glycan occupancy and length at each N-linked glycosylation sequon (Borst et al., 2018). A marked enhancement of the WT 426c core electrophoretic mobility was detected after 2.5 minutes of EndoH treatment, followed by smaller incremental increases in mobility at subsequent timepoints **(Fig. 5.1A)**. These results revealed limited EndoH treatment of the WT 426c core resulted in a rapid initial glycan trimming step followed by a slower digestion phase.

To assess whether EndoH treatment preferentially targeted regions of low oligosaccharide density on the WT 426c core, we quantified glycans present at individual N-linked glycosylation sequons for each EndoH digestion timepoint with liquid chromatography coupled to electron transfer/high-energy collision-dissociation tandem mass-spectrometry (LC-MS/MS) (Frese et al., 2013). We evaluated the glycosylation status of glycopeptides detected at positions N197, N276, N289, N332, N337, N442, N460 and/or N463 **(Fig. 5.1B)**. Oligosaccharide trimming occurred at distinct rates for different sites on the surface of the WT 426c core. Specifically, glycans located near the $CD4_{BS}$, such as N197, N276, and N460/N463, were virtually entirely cleaved to $GlcNAc_1$ between 2.5 and 20 minutes after initiating the reaction **(Fig. 5.1B)**. Glycan N442, which is located near the gp120 apex, also underwent rapid digestion **(Fig. 5.1C)**. Conversely, oligosaccharides located within the densely glycosylated high-mannose patch (positions N289, N332, and N337) were trimmed at

much slower rates **(Figure 5.1C)**. The extent of site-specific cleavage inversely correlated with the carbohydrate density at the surface of the WT 426c core **(Figure 5.1C)**. This confirmed the accessibility of EndoH to glycans of the high-mannose patch was severely dampened relative to oligosaccharides located near the $CD4_{BS}$.

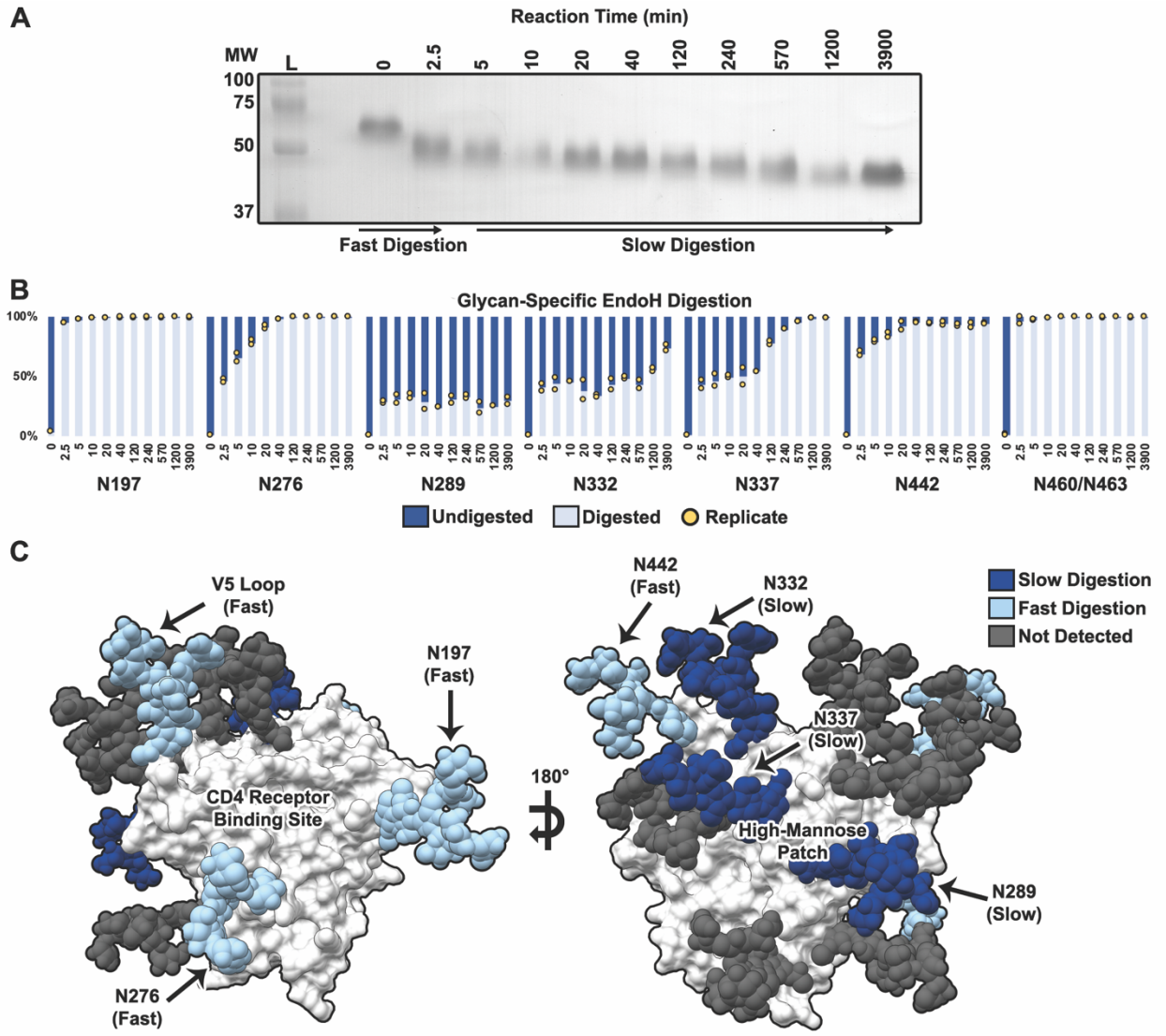

Figure 5.1. Limited EndoH-treatment of the WT 426c core selectively trims oligosaccharides near the $CD4_{BS}$.

(A) SDS-PAGE analysis of the WT 426c core digested with EndoH at a ratio of 1:50 (w/w) EndoH:WT 426c core at various timepoints comprised between 0 (pre-treatment) and 3,900 minutes (post-treatment). L: molecular weight ladder (expressed in kDa) (B) Semi-quantitative analysis of the EndoH-treated WT 426c core by LC-MS/MS. Samples were analyzed at multiple timepoints following addition of EndoH. Seven glycosylation sites were detected and quantitation included undigested glycopeptides ($GlcNAc_2Man_3$ through $GlcNAc_2Man_8$) and digested glycopeptides ($GlcNAc_1$). Average undigested and digested glycopeptide signal fractions are represented in dark-blue and light-blue, respectively. Technical replicates are indicated as yellow

circles. X-axis represents time in minutes post-EndoH treatment. Y-axis is the fraction of total signal for all detected glycoforms combined at each site. V5 loop corresponds to both N460/N463 glycosylation sequons. (C) Mapping of the WT 426c core glycan shield susceptibility to EndoH treatment. Glycans that were digested slowly are colored dark-blue. Glycans rapidly digested are indicated in light-blue. For visualization of undigested oligosaccharide density across regions of the WT 426c core, amino acid coordinates were derived from PDB 6MFT, with glycans modeled separately as putative $GlcNAc_2Man_9$ sugars (with the exception of glycan N276, which was modeled as $GlcNAc_2Man_5$)(Borst et al., 2018).

5.3 GLYCAN TRIMMING ENHANCES BINDING OF GERMLINE $CD4_{BS}$-TARGETING ANTIBODIES

To evaluate the ability of multiple germline $CD4_{BS}$-targeting antibodies to interact with the WT 426 core, and the impact of limited EndoH glycan trimming on recognition, we analyzed WT 426 core binding to immobilized $CD4_{BS}$-directed antibodies ($VRC01_{GL,}$ $12A21_{GL,}$ $VRC\text{-}PG20_{GL,}$ $IOMA_{GL}$ and 179NC75) using biolayer interferometry. To verify that other regions of the WT 426c core glycan shield were not deleteriously impacted by EndoH treatment at early timepoints, we also assessed binding to antibody 2G12, a bnAb which recognizes oligosaccharides in the densely glycosylated high mannose patch(Calarese et al., 2003; Trkola et al., 1995). Measurements were taken at different time points following initiation of the reaction to assess the evolution of antibody binding.

The undigested WT 426 core weakly interacted with $VRC01_{GL}$ and bound very weakly to $12A21_{GL}$(Klein et al., 2013; Scheid et al., 2011) prior to EndoH treatment **(Fig. 5.2A-B)**. $VRC\text{-}PG20_{GL}$(Zhou et al., 2013) **(Fig. 5.2C)** and 179NC75 (a glycan N276 dependent bnAb) **(Fig. 5.2D)** both bound to the untreated WT 426c core more efficiently relative to the two aforementioned germline antibodies. As expected, antibody 2G12 also engaged the undigested WT 426c core **(Fig. 5.2E)**. In contrast, the germline $CD4_{BS}$-targeting antibody, $IOMA_{GL}$ (Gristick et al., 2016), did not bind to the WT 426c core under any condition tested **(Fig. 5.2F)**. 15 minutes post reaction initiation, $VRC01_{GL}$, $12A21_{GL}$, and $VRC\text{-}PG20_{GL}$ binding levels were universally enhanced **(Fig. 5.2A-C)**. Conversely, 179NC75(Freund et al., 2015) showed rapid reduction in $CD4_{BS}$ recognition after 15 minutes, followed by a complete loss of binding after 60 minutes of EndoH-mediated trimming, due to digestion of glycan N276 from $GlcNAc_2Man_5$ to $GlcNAc_1$ **(Fig. 5.1B and Fig.**

5.2D). 2G12 binding, however, was unchanged at similar timepoints, indicating enzymatic activity did not affect the epitope of this bnAb for short reaction times **(Fig. 5.2E).** These findings concur with the LC-MS/MS data, which show virtually complete oligosaccharide digestion near the $CD4_{BS}$ between 10 and 40 minutes, but not for oligosaccharides within the high-mannose patch **(Fig. 5.1B-C)**. The data further indicate that prior to EndoH treatment, the WT 426c core bound to several germline bnAb precursors targeting the $CD4_{BS}$, even though all native N-linked glycosylation sequons were retained.

No further modulation of binding to any of the $CD4_{BS}$-directed germline antibodies was detected at later timepoints, whereas 2G12 recognition levels decreased substantially with increasing reaction times **(Fig. 5.2A-E)**. We explain the latter observation as a loss of critical antibody-glycan contacts upon trimming of oligosaccharides in the high-mannose patch **(Fig. 5.1B-C)**. These observations confirm that shortly after addition of EndoH, a rapid initial phase of oligosaccharide trimming took place near the WT 426c core $CD4_{BS}$ resulting in (i) binding enhancement to several germline $CD4_{BS}$-targeting antibodies and (ii) decreased engagement of the glycan-dependent bnAb 179NC75. The subsequent, slower cleavage phase affected the more densely glycosylated high-mannose patch, thereby validating the limited EndoH treatment strategy outlined above.

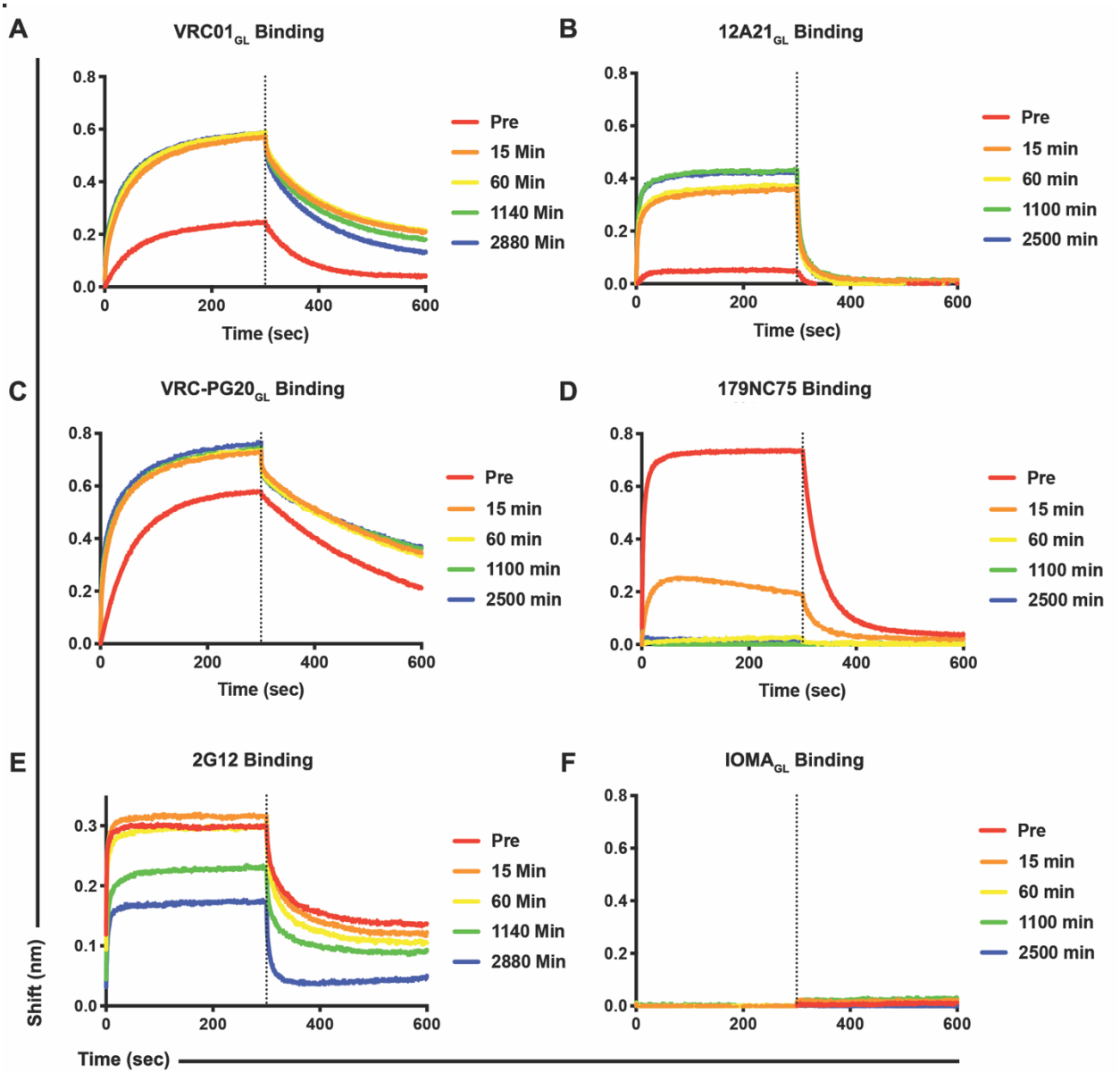

Figure 5.2. Limited EndoH trimming promotes binding of the HIV-1 WT 426c core to several germline precursors of $CD4_{BS}$ bnAbs.

Biolayer interferometry analysis of binding of 10 μM WT 426c core to immobilized $VRC01_{GL}$ (A), $12A21_{GL}$ (B), $VRC\text{-}PG20_{GL}$ (C), 179NC75 (D), 2G12 (E), and $IOMA_{GL}$ (F) antibodies before and after initiation of EndoH treatment (as indicated by the color key). Transition from association to dissociation phases are indicated by a vertical dotted black line. 2G12 binds to the high-mannose patch and was used as a control.

5.4 IMMUNIZATION WITH WT 426C CORE NANOPARTICLES ELICITED $CD4_{BS}$-DIRECTED ANTIBODIES

We next evaluated the capacity of the WT 426c core to elicit $CD4_{BS}$-targeting antibodies and if limited EndoH treatment of this antigen correlated with stronger humoral immune responses. Based on the previously reported quantitative and qualitative benefits of multivalent display for immunogen design (Kanekiyo et al., 2013; Marcandalli et al., 2019; Sliepen et al., 2015; Yan et al., 2019), we opted to multimerize SpyTagged WT 426c core antigens using a ferritin nanoparticle fused to SpyCatcher(Zakeri et al., 2012) **(Fig. 5.3A)**. Purified antigens were either untreated (to preserve the $GlcNAc_2$-Man_5 oligosaccharides near the $CD4_{BS}$), or incubated with EndoH for 15 minutes at room temperature followed by size-exclusion chromatography, to halt the reaction and specifically enrich for $GlcNAc_1$ near the $CD4_{BS}$ **(Fig. 5.3A)**. Following nanoparticle assembly and size-exclusion chromatography, the antigens were negatively stained for single-particle electron microscopy quality control. As expected, both samples contained resolved nanoparticles with flexibly tethered WT 426c core antigens protruding from the ferritin scaffold **(Fig. 5.3B-C)**.

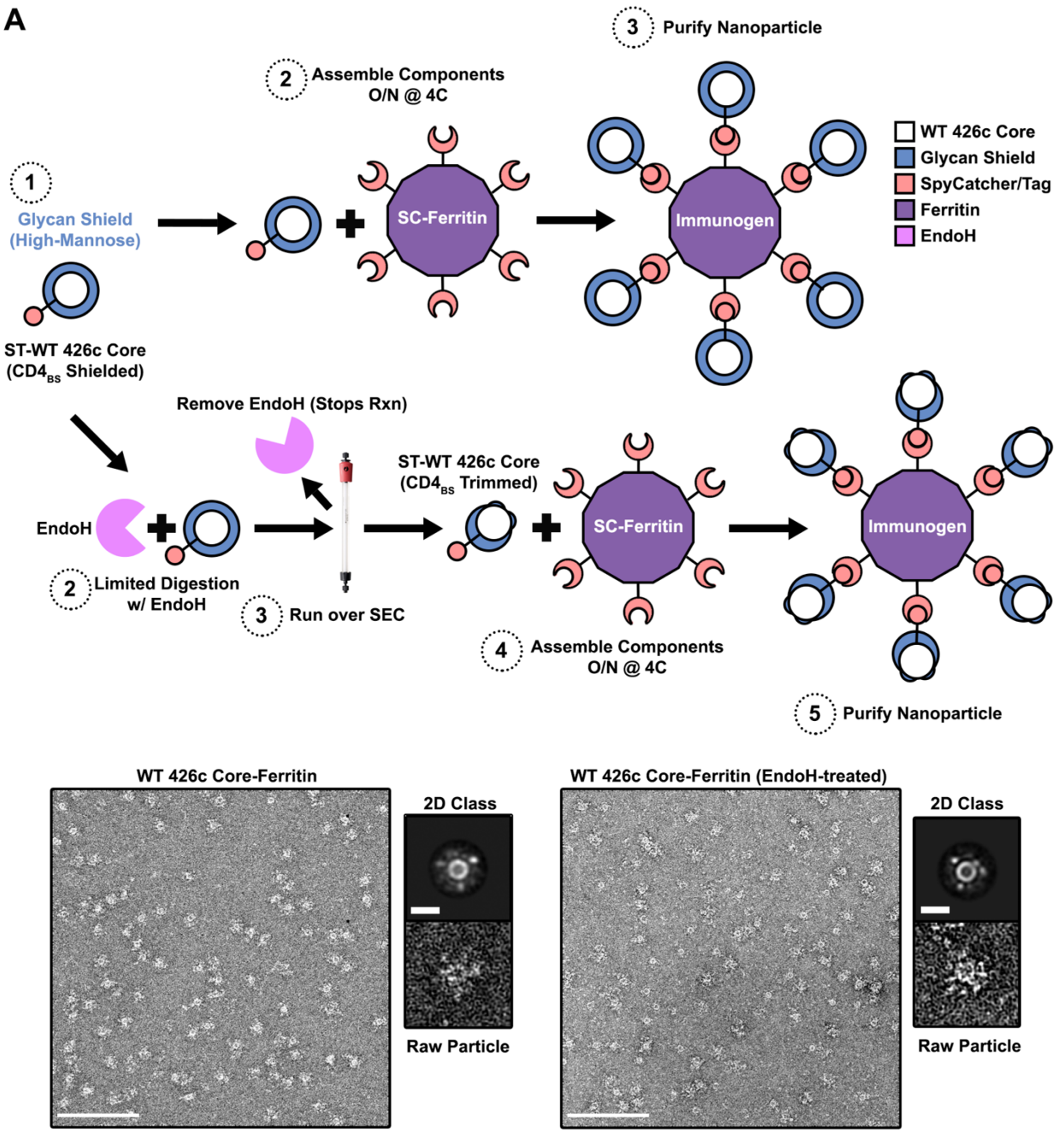

Figure 5.3. Assembly and analysis of multivalent WT 426c core nanoparticles.

(A) Assembly strategy for untreated (top) and EndoH-treated (bottom) WT 426c core-ferritin nanoparticles. (B-C) Negative stain electron microscopy images (Scale bar = 200 nm), 2D class averages (Scale bar = 165 Å), and raw particle images of WT 426c core-ferritin (B) and EndoH-treated WT 426c core-ferritin (C). ST: spy tag, SC: spy catcher, SEC: size-exclusion chromatography.

Immunizations were carried out using $VRC01_{GL}$ heavy chain knock-in mice to allow for the potential production of chimeric VRC01-like antibodies alongside murine antibodies. These mice harbor the human $VRC01_{GL}$ heavy chain gene and five amino-acid long light chain CDR3 gene (typical of VRC01 bNAbs) in ~80% and 0.1% of their naïve B cell receptors, respectively (Dosenovic et al., 2015)(Verkoczy et al., 2017)(Jardine et al., 2015). The first group of five mice was immunized with untreated WT 426c core nanoparticles (predominantly N-linked to $GlcNAc_2Man_5$ oligosaccharides near the $CD4_{BS}$) **(Fig. 5.4A)**. The second group of four mice was immunized with WT 426c core nanoparticles enriched for $GlcNAc_1$ near the $CD4_{BS}$ via limited EndoH digestion **(Fig. 5.4A)**. Although all immunogens were produced using HEK293S $GnTI^{-/-}$ cells (to enrich for high mannose glycans), ELISAs utilized antigens (i) prepared using HEK293F cells to interrogate binding of polyclonal antibodies in the presence of a complex glycan shield and (ii) without a SpyTag fusion to rule out reactivity toward this protein domain.

As expected, no binding was observed using pre-immune sera from any animal against any antigen **(Fig. 5.4B and Fig. 5.5)**. In contrast, increasingly higher binding responses to the WT 426c core were detected with sera from both groups at weeks two (post-prime) **(Fig. 5.4B and Fig. 5.6)**, four (post boost #1) **(Fig. 5.4B and Fig. 5.7)**, and six (post-boost #2) **(Fig. 5.4B and Fig. 5.8)**. To test for the presence of $CD4_{BS}$-directed antibodies, we utilized a $CD4_{BS}$-epitope knock-out mutant construct, which harbors the D279A, D368R and E370A substitutions (Gray et al., 2009; Sather et al., 2014). The equivalent binding response of 2G12 to this $CD4_{BS}$-epitope knock-out mutant and to the WT 426c core validated proper folding of the former antigen and provided an internal loading control for the ELISA experiments **(Fig. 5.4B)**. Sera from the untreated ($GlcNac_2Man_5$) group revealed a significant population of $CD4_{BS}$-specific antibodies beginning

after the second injection, i.e. at week 4 **(Fig. 5.4B-D and Figs. 5.6-5.8)**. In contrast, EndoH treatment enabled a significant $CD4_{BS}$-targeted response immediately following the first immunization which was maintained after each subsequent autologous boost **(Fig. 5.4B-D and Figs. 5.6-5.8)**. We detected a reduction of the $CD4_{BS}$-focused responses at week six in both groups despite increased overall antibody titers, which might indicate a rise in a non-$CD4_{BS}$-targeting response following three autologous injections **(Fig. 5.4B-D)**.

To probe for specific production of VRC01-class antibodies, we carried out serum ELISAs using two HEK293F-expressed antigens: eOD-GT8 and eOD-GT8 VRC01-epitope knock-out (276-NFTA/DWRD-279 and D368R) **(Fig. 5.9A)**. eOD-GT8 comprises the gp120 outer domain of the HIV-1 clade B Hxb2 gp120 glycoprotein and is a derivative of eOD-GT6, which was initially designed as a germline-targeting immunogen to induce VRC01-class bNAbs (Havenar-Daughton et al., 2018; Jardine et al., 2013, 2016; Umotoy et al., 2019). We detected negligible binding to eOD-GT8 with immune sera from all nine mice for all weeks tested, indicating that the $CD4_{BS}$ antibodies produced here were likely distinct from the canonical human $VRC01_{GL}$ lineage **(Fig 5.9A)**. As expected, mature VRC01 tightly engaged eOD-GT8 (positive control), but not the eOD-GT8 VRC01-epitope knock-out (negative control). Finally, 2G12 also did not bind eOD-GT8 (negative control) due to the absence of the epitope of this bnAb on this antigen **(Fig. 5.9A)**. To assess the impact of the retained glycans surrounding the $CD4_{BS}$ of the WT 426c core on antibody recognition, we tested the reactivity of the immune sera against a 426c core construct lacking N-linked glycosylation sequons at positions N276, N460, and N463. The observed reduction of antibody binding to this 426c core construct compared to WT 426c core, which was

most obvious at week four (**Fig. 5.4B-D and Figs 5.6-5.8)**, was not statistically significant, and will be further investigated in future studies.

Collectively, these data indicate that retention of all native N-linked glycosylation sequons of the WT 426c core immunogen enabled elicitation of antibodies targeting the $CD4_{BS}$, with EndoH treatment enhancing this effect.

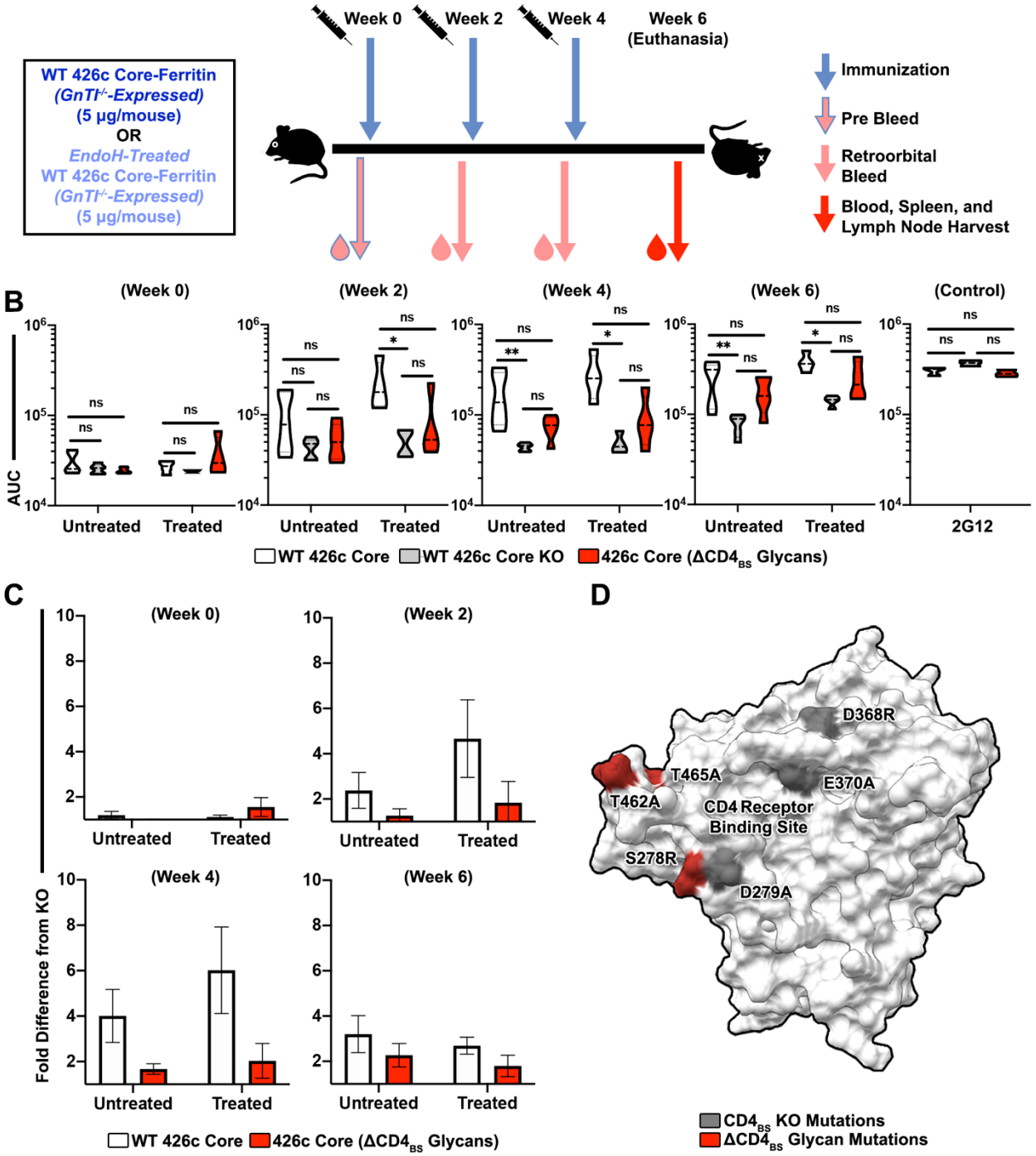

Figure 5.4. Multivalent WT 426c cores rapidly elicit a $CD4_{BS}$-directed immune response. (A) Immunization scheme utilizing WT 426c core-ferritin and EndoH-treated WT 426c core-ferritin nanoparticles. (B) Violin plots depicting serum ELISA data at weeks zero, two, four, and six representing calculated median titers (dashed line) for all mice in each cohort. Data represent

areas under the curve for each mouse in each group for the three antigens tested (n=5 for the group with untreated immunogen and n=4 for the group with EndoH treated immunogen). First and third quartile ranges are depicted as dotted lines. Antigens coated on ELISA wells were expressed in HEK293F cells to allow for production of complex glycans. Tests for significance on biological replicates were performed using a paired nonparametric Friedman two-tailed t-test (ns = not significant, * = $p \leq 0.05$). Antibody 2G12 was used as a control, with technical replicates analyzed using an unpaired nonparametric Wilcoxon two-tailed t-test (ns = not significant). (C) Histogram plots highlighting the fold-change in area under the curve values calculated in (B) for the WT 426c core and the 426c core ($\Delta CD4_{BS}$ Glycans) relative to the WT 426c core KO (error bars = SEM). In panels (B) and (C) the plots are color-coded as follows: white: WT 426c core; grey: WT 426c core KO ($CD4_{BS}$-epitope knock-out mutant, D279A, D368R and E370A); red: 426c core $\Delta CD4_{BS}$ glycans (lacking N-linked glycosylation sequons at positions N276, N460, and N463). (D) Surface rendering of the WT 426c core showing the amino acid positions mutated in the different constructs used for ELISAs (grey = $CD4_{BS}$ KO mutations, red = $\Delta CD4_{BS}$ glycan mutations [S278R/T462A/T465A]).

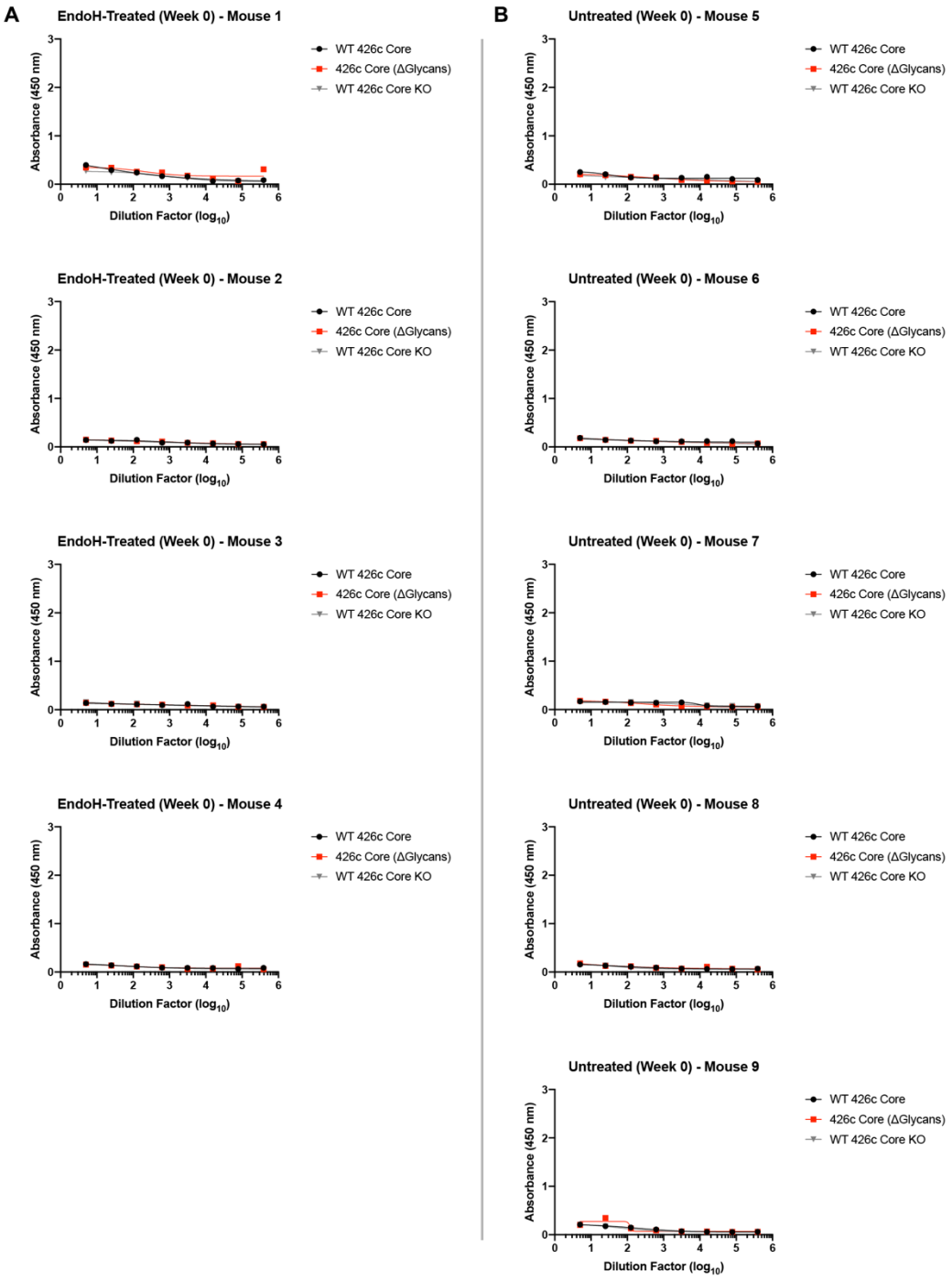

Figure 5.5. Serum ELISA of naïve mice (Week 0, pre-immunization).

Serum responses for antigens expressed in HEK293F cells for (A) the GlcNAc(1)-enriched cohort and (B) the GlcNAc(2)Man(5)-enriched cohort, prior to immunogenic priming. (Black = WT 426c core response; Grey = WT 426c core $CD4_{BS}$-KO response; Red = 426c core [$\Delta CD4_{BS}$ Glycans] response).

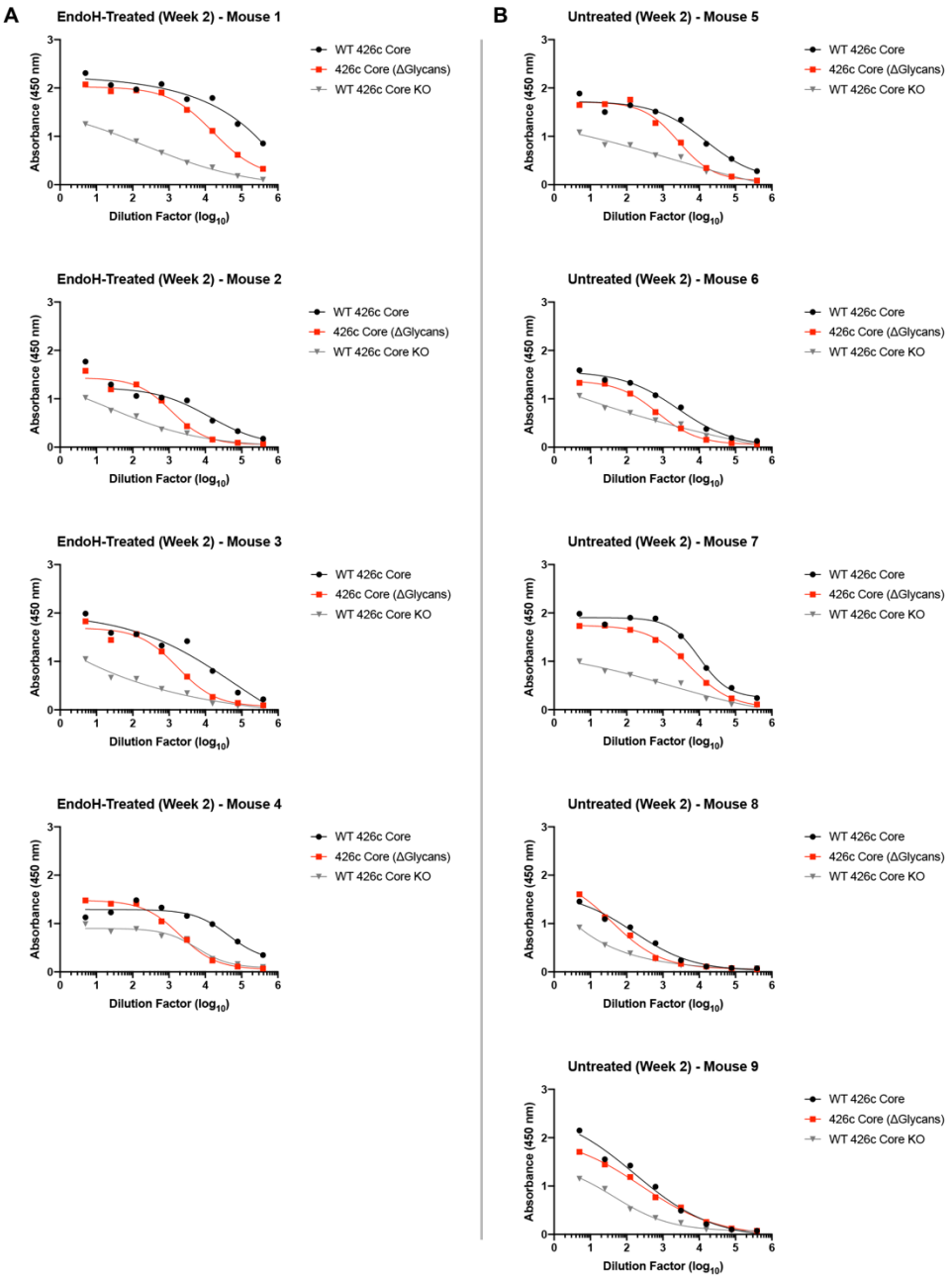

Figure 5.6. Supplementary figure 2. Serum ELISA of primed mice (week 2, post-prime). Serum responses for antigens expressed in HEK293F cells for (A) the GlcNAc(1)-enriched cohort and (B) the GlcNAc(2)Man(5)-enriched cohort two weeks after immunogenic priming. For mouse #2, the first data-point for the WT 426c core was omitted from the calculation for generation of a sigmoidal fit. (Black = WT 426c core response; Grey = WT 426c core $CD4_{BS}$-KO response; Red = 426c core [$\Delta CD4_{BS}$ Glycans] response).

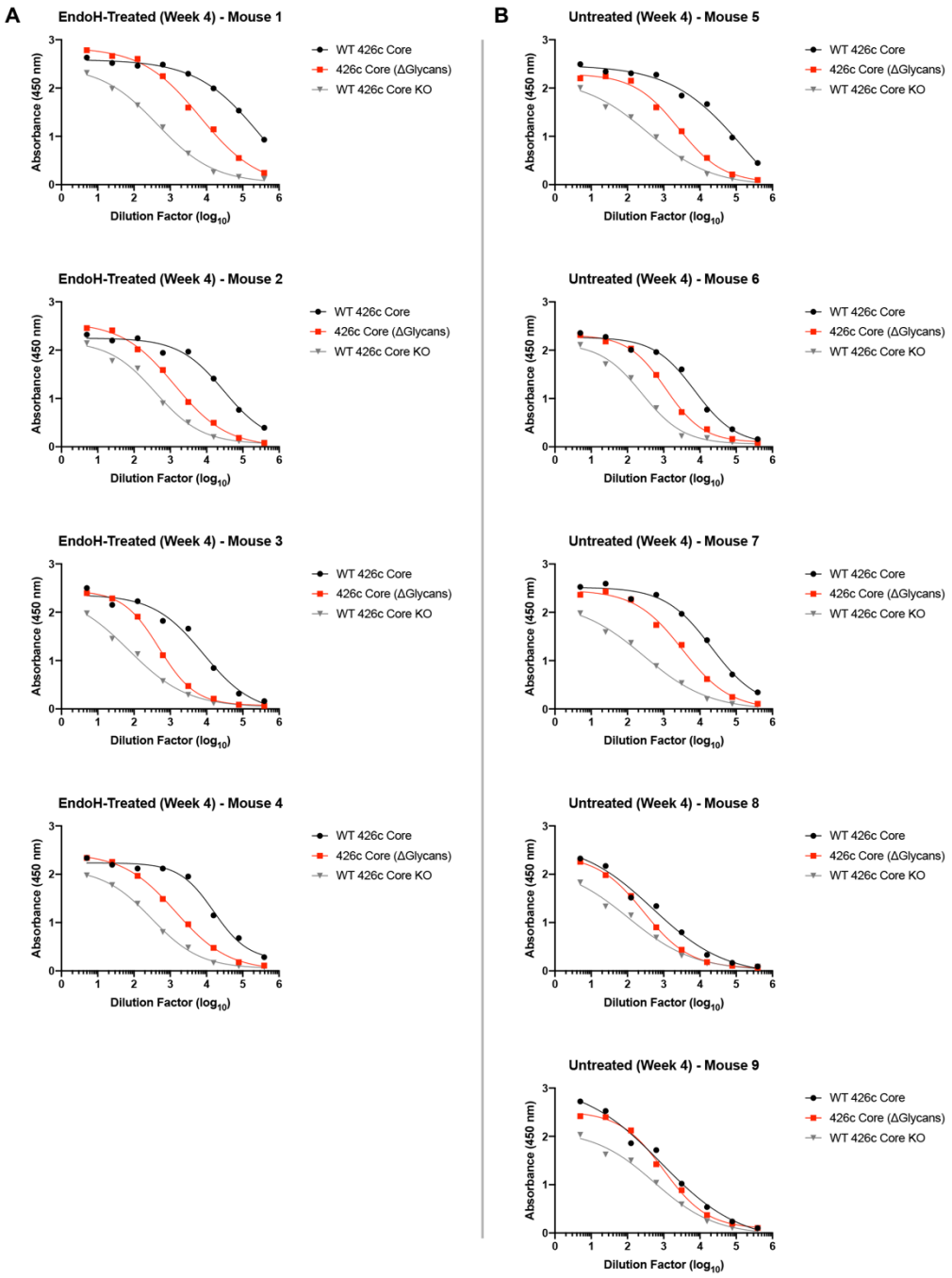

Figure 5.7. Serum ELISA of boosted mice (week 4, post-autologous boost #1).

Serum responses for antigens expressed in HEK293F cells for (A) the GlcNAc(1)-enriched cohort and (B) the GlcNAc(2)Man(5)-enriched cohort two weeks after the first autologous antigenic boost. (Black = WT 426c core response; Grey = WT 426c core $CD4_{BS}$-KO response; Red = 426c core [$\Delta CD4_{BS}$ Glycans] response).

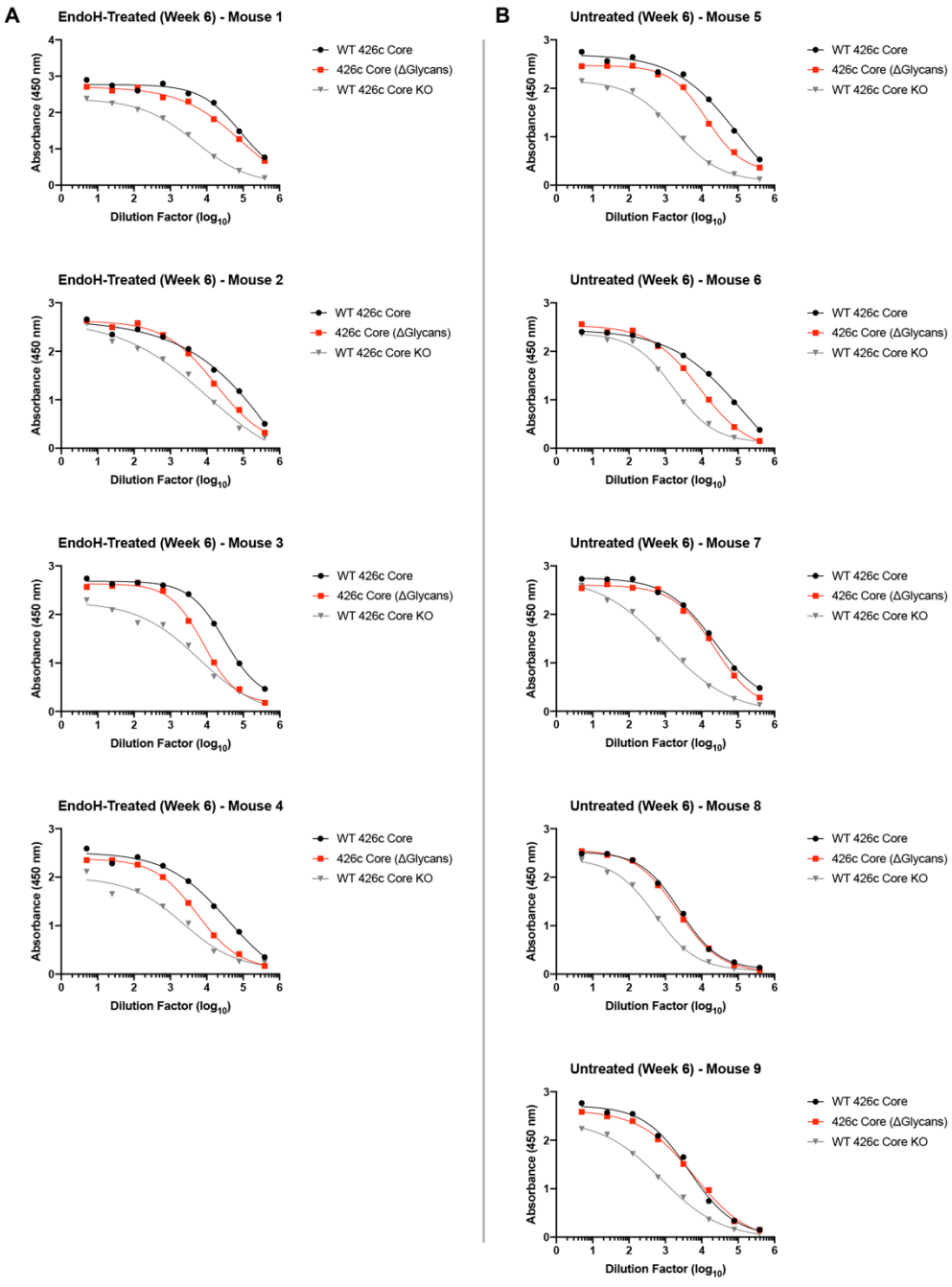

Figure 5.8. Serum ELISA of twice-boosted mice (week 6, post-autologous boost #2). Serum responses for antigens expressed in HEK293F cells for (A) the GlcNAc(1)-enriched cohort and (B) the GlcNAc(2)Man(5)-enriched cohort two weeks after the second autologous antigenic boost. (Black = WT 426c core response; Grey = WT 426c core $CD4_{BS}$-KO response; Red = 426c core [$\Delta CD4_{BS}$ Glycans] response).

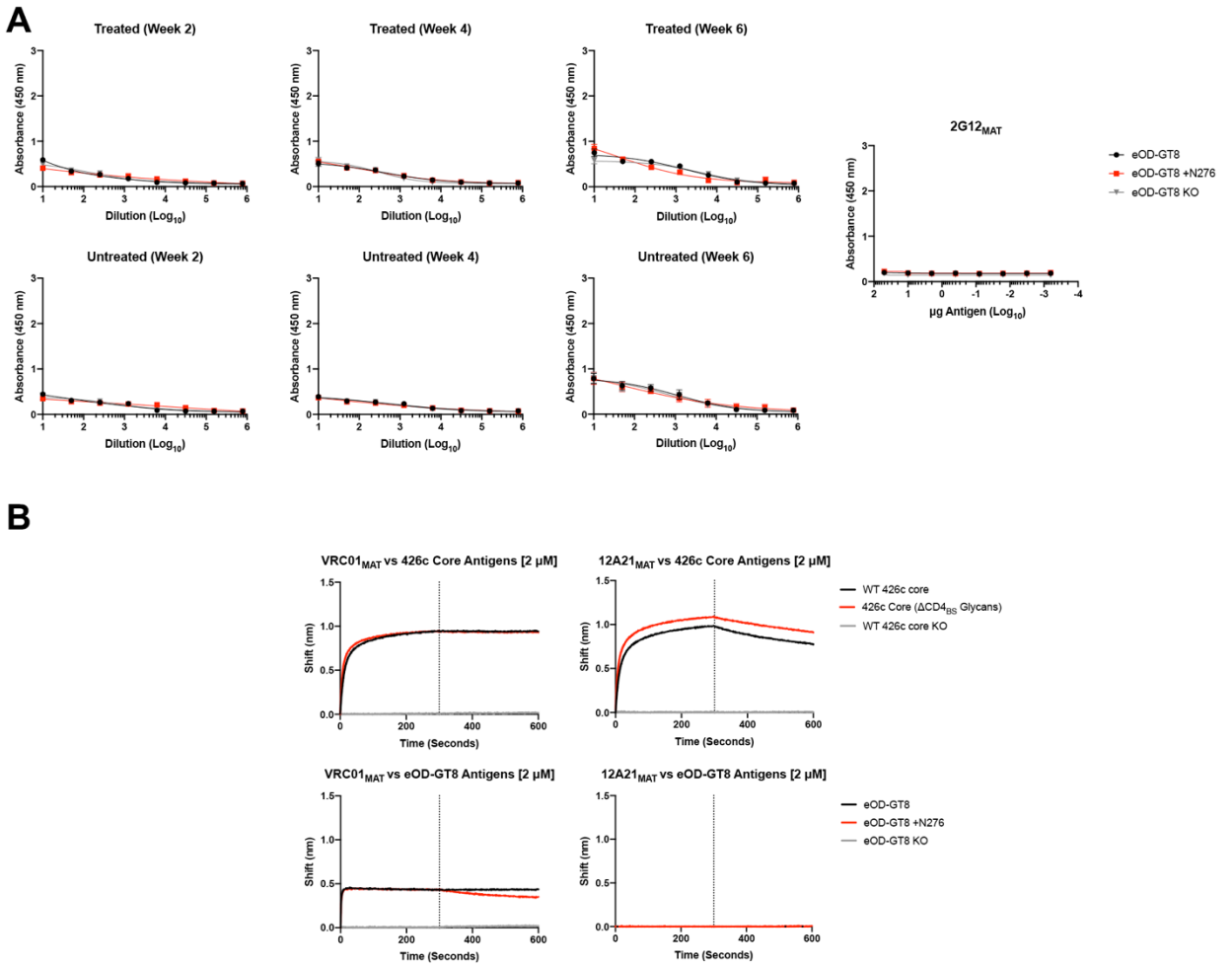

Figure 5.9. Immune sera and VRC01-class bNAb reactivity against eOD-GT8 antigens. (A) Serum ELISAs at weeks two, four, and six against eOD-GT8 antigens representing calculated mean titers for all mice in each group (error bars: SEM). Antigens coated on ELISA wells were expressed in HEK293F cells to allow for production of complex glycans. The 2G12 control represents average mean response values from three technical replicates starting at 50 µg bNAb diluted 8-times using a 5-fold serial dilution factor (error bars: SEM). (B) BLI binding data for VRC01-class mature VRC01 and 12A21 bNAbs against various WT 426c core. All antigen were expressed in HEK293F cells. (Top: Black = WT 426c core response; Grey = WT 426c core $CD4_{BS}$-KO response; Red = 426c core [$\Delta CD4_{BS}$ Glycans] response; Bottom: (Black = eOD-GT8 response; Grey = eOD-GT8-KO response; Red = eOD-GT8+N276 response).

5.5 CONCLUSIONS, DISCUSSION, AND FUTURE DIRECTIONS

In chapter 4 of this dissertation, we discovered that $VRC01_{GL}$ could accommodate and interact with the WT 426c core N276 glycan through contacts with the two proximal GlcNAc moieties(Borst et al., 2018). We further demonstrated that binding to $VRC01_{GL}$ in the presence of an N276 oligosaccharide could be enhanced following enrichment for $GlcNAc_2$-Man_5 oligosaccharides, and was substantially increased upon glycan trimming to $GlcNAc_1$ using EndoH (Borst et al., 2018). In this chapter, we developed a protocol to selectively enrich for $GlcNAc_1$ near the $CD4_{BS}$ of the WT 426c core and analyzed the potential of this approach to increase the recognition of several $CD4_{BS}$-targeting bnAb germline precursors. We observed varying magnitudes of WT 426c core binding to $VRC01_{GL}$, $12A21_{GL}$ and $VRC\text{-}PG20_{GL}$ in the presence of all native N-linked glycosylation sequons around the $CD4_{BS}$. Furthermore, these binding levels were universally enhanced upon limited EndoH treatment, indicating improved access of these antibodies to their epitopes without resorting to mutagenesis.

For immunization with EndoH-treated antigens, we had to first consider the possible impacts associated with non-specific digestion of the native HIV-1 gp120 glycan shield. Specifically, extended EndoH-treatment of an HIV-1 SOSIP trimer was previously described to abrogate binding of the glycan dependent 2G12 bnAb targeting the high-mannose patch (Depetris et al., 2012). This was likely due to the loss of key glycan contacts in this region following prolonged enzymatic activity. This finding emphasized that non-specific oligosaccharide trimming could (i) abolish epitopes of glycan-dependent bNAbs and dampen their elicitation, as well as (ii) expose non-native epitopes normally occluded by glycans, resulting in production of off-target non-neutralizing antibodies. Both of these outcomes are undesirable. The limited EndoH trimming

strategy reported here circumvents these two shortcomings by preferentially digesting oligosaccharides near the $CD4_{BS}$ that otherwise severely dampen or hinder access to several germline reverted bnAbs. This method led to the specific binding enhancement of multiple $CD4_{BS}$-directed bnAb germline precursors while not impacting recognition of the high-mannose patch-directed antibody, 2G12.

We corroborated these *in vitro* findings by analyzing the polyclonal response of mice immunized with multivalently-displayed WT 426c core nanoparticles. Strikingly, antigens harboring either $GlcNac_2Man_5$ or $GlcNAc_1$ oligosaccharides near the $CD4_{BS}$ were both capable of eliciting $CD4_{BS}$-directed responses upon immunization. Moreover, limited EndoH treatment of the antigen accelerated the production of $CD4_{BS}$-directed antibodies, as revealed by a marked $CD4_{BS}$-specific response immediately after priming. Importantly, this limited EndoH treatment strategy did not negatively skew the humoral response away from the $CD4_{BS}$, confirming that it successfully averted exposure of additional non-native epitopes.

Despite utilizing a $VRC01_{GL}$ knock-in mouse model, neither the untreated nor the EndoH-treated antigens elicited antibodies binding to eOD-GT8. Of note, while many VRC01-class antibodies bind with high affinity to eOD-GT8(Jardine et al., 2016), this behavior is not universal. A recent longitudinal study identified VRC01-class PCIN63 bNAbs that did not engage eOD-GT8 (Jardine et al., 2016; Umotoy et al., 2019) and our results show the VRC01-class $12A21_{GL}$ bound to the WT 426c core, but not to eOD-GT8. Sequencing and characterization of the 426c-specific monoclonal antibodies elicited during our immunization campaign will be the focus of future studies in order to unveil their precise modes-of-recognition.

Our study harnesses unique features of the 426c core including its natural lack and/or repositioning of oligosaccharides at positions N234 and N362 found in many other gp120 orthologues. This resulting "glycan hole" near the $CD4_{BS}$ putatively favors access to many germline antibodies and an accompanied accommodation of glycan N276. Given the autologous nature of our prime-boost-boost protocol, it is probable that the polyclonal responses observed here are 426c strain-specific. This is supported by the absence of reactivity observed with eOD-GT8 and the fact that gp120 from numerous HIV-1 strains exhibit a denser glycan shield near the $CD4_{BS}$ relative to 426c. Reintroduction of oligosaccharides absent in 426c via subsequent, heterologous boost immunizations could be implemented in future studies to expand the breadth of the polyclonal response. To conclude, our data provide the proof-of-concept for using the WT 426c core – which retains all native N-linked glycosylation sequons – for immunogenic priming. By utilizing the WT 426c core in combination with region-specific engineering of the glycan shield, we propose glycan tailoring as an alternative approach in vaccine design to prime elicitation of $CD4_{BS}$-directed antibodies in HIV-1.

5.6 METHODOLOGY

5.6.1 *Protein purification.*

WT 426c cores and SpyTagged-WT 426c cores were expressed using HEK293S GnTI$^{-/-}$ cells. After 6 days, cells were centrifuged at 4,500 rpm for 20 minutes and supernatant was filter-sterilized. Agarose Bound Galanthus Nivalis Lectin (Vector) was used to separate the cores from the supernatant. The resin was washed with 20mM Tris pH 7.5, 100 mM NaCl, 1 mM EDTA and elution used a buffer containing 20mM Tris pH 7.5, 100 mM NaCl, 1 mM EDTA, and 1M Methyl α-D-mannopyranoside. Samples were further purified by SEC using a HiLoad 16/600 Superdex 200pg (GE) column.

5.6.2 *Limited endoH digestion and SDS-PAGE analysis.*

Undigested WT 426c core was frozen in liquid nitrogen for mass spectrometry analysis. An additional sample was prepared for SDS-PAGE in the presence of reducing loading buffer and snap frozen at the same time. EndoH was then added in a separate tube at 1:50 molar ratio (EndoH : WT 426c core) and incubated at 25^{o}C. For each digestion timepoint, samples were taken and immediately frozen in liquid nitrogen for mass spectrometry and SDS-PAGE in the same manner as the undigested sample. All pre/post digestion timepoints were performed in duplicate using two separate tubes. 10 uL of each EndoH digestion timepoint for one experimental replicates was loaded on an 15% SDS-PAGE gel and run at 200 V for 45 minutes. Samples were stained using Coomassie Brilliant Blue XX and de-stained overnight at room temperature.

5.6.3 *Mass spectrometry.*

For analysis of *N*-linked glycosylation profiles, an estimated 250 pmol of each WT 426c core digestion timepoint were thawed and immediately denatured, reduced, and alkylated by dilution to 5 µM in 50 µL of buffer containing 100 mM Tris (pH 8.5), 10 mM Tris(2-carboxyethylphosphine (TCEP), 40 mM iodoacetamide or 40 mM iodoacetic acid, and 2% (wt/vol) sodium deoxycholate. Samples were first heated to 95 °C for 10 min and then incubated for an additional 30 min at room temperature in the dark. The samples were digested with trypsin (Sigma Aldrich), by diluting 20µL of sample to total volume of 100µL 50 mM ammonium bicarbonate (pH 8.5). Protease was added to the samples in a ratio of 1:75 by weight and left to incubate at 37 °C overnight. After digestion, 2µL of formic acid was added to the samples to precipitate the sodium deoxycholate from the solution. After centrifugation at 17,000×g for 25 min, 85 µL of the supernatant was collected and centrifuged again at 17,000×g for 5 min to ensure removal of any residual precipitated deoxycholate. 80 µL of this supernatant was collected. For each sample, 12µL was injected on a Thermo Scientific Orbitrap Fusion Tribrid mass spectrometer. A 35-cm analytical column and a 3-cm trap column filled with ReproSil-Pur C18AQ 5µM (Dr. Maisch) beads were used. Nanospray LC-MS/MS was used to separate peptides over a 90-min gradient from 5 to 30% acetonitrile with 0.1% formic acid. A positive spray voltage of 2,100 was used with an ion transfer tube temperature of 350 °C. An electron-transfer/higher-energy collision dissociation ion-fragmentation scheme(Frese et al., 2013) was used with calibrated charge-dependent entity-type definition (ETD) parameters and supplemental higher-energy collision dissociation energy of 0.15. A resolution setting of 120,000 with an AGC target of 2×10^5 was used for MS1, and a resolution setting of 30,000 with an AGC target of 1×10^5 was used for MS2. Data were searched with the Protein Metrics Byonic software(Bern et al., 2012), using a small custom

database of recombinant protein sequences including the proteases used to prepare the glycopeptides. Reverse decoy sequences were also included in the search. Specificity of the search was set to C-terminal cleavage at R/K (trypsin), allowing up to two missed cleavages, with EthcD fragmentation (b/y- and c/z-type ions). We used a precursor mass and product mass tolerance of 12 ppm and 24 ppm, respectively. Carbamidomethylation of cysteines was set as fixed modification, carbamidomethylation of the lysines and N-terminal amines were set as variable modifications, methionine oxidation as variable modification, pyroglutamate identification was set for both N-terminal glutamines and glutamates as a variable modification, and a concatenated N-linked glycan database (derived from the four software-included databases) was used to identify glycopeptides. All analyzed glycopeptide hits were manually inspected to ensure for quality and accuracy. Semi-quantitative LC-MS/MS analysis of EndoH-treated samples was performed using Skyline(MacLean et al., 2010) with peak integration and LC-MS/MS searches imported from Byonic. Missed cleavages far from PNGS sequences, carbamidomethylation of the lysines and N-terminal amines, and pyroglutamate modifications were omitted from the final quantitative analysis. All MS1 peak areas used for integration were manually inspected to ensure for quality and accuracy. Quantification of undigested glycans were measured as the sum integrated signal for GlcNAc(2)-Man(3) through GlcNAc(2)-Man(9) oligosaccharides of each PNGS. Digested glycans were quantified as integrated signal values for GlcNAc(1) species. Unglycosylated PNGS peptides were omitted from this analysis. Two independent experimental replicates were pooled, injected, and analyzed.

5.6.4 *Biolayer interferometry*

BLI assays were performed with an Octet Red 96 instrument (ForteBio, Inc, Menlo Park, CA) at 25ºC with shaking at 1000 r.p.m. All measurements were corrected by subtracting the background signal obtained from duplicate traces generated with a sensor not loaded with an antibody to remove any non-specific binding signal. IgGs were immobilized on anti-AHC biosensors (at 20 µg/ml in PBS) for 60s. Sensors were then incubated for 1 min in kinetic buffer (KB: 1X PBS, 0.01% BSA, 0.02% Tween-20) to establish the baseline signal (nm shift). Antibody-loaded sensors were then immersed into solutions of purified recombinant WT 426c core (10 uM) for analysis. For measurements taken during the course of enzymatic treatment, 200 nM EndoH was added directly to well containing WT 426c core. Readings were collected at 15, 60, and 1110 minutes following the beginning of the reaction. Plate was kept at 25ºC during the entire course of the reaction. To prevent evaporation of sample for measurement of the 1100 timepoint, plates were stored and covered with parafilm. BLI measurements of VRC01-class antibodies against eOD-GT8 were performed as outlined above (minus the EndoH-treatment). Mature VRC01 and 12A21 antibodies were immobilized on anti-AHC biosensors and 2 µM of corresponding eOD-GT8 ligand was suspended in each well.

5.6.5 *Nanoparticle assembly*

2 mg of purified SpyTag-WT 426c Core (expressed in GnTi$^{-/-}$ cells) were digested with EndoH for 15 minutes at room temperature at a 1:50 molar ratio of enzyme:antigen. To halt the reaction and remove EndoH, the mixture was immediately run over an Superdex 200 Increase 10/300 GL column. Fractions containing partially digested antigen were pooled and concentrated to at least 3.5 mg/mL prior to assembly with Spycatcher-Ferritin. Two mixtures were prepared: 1) Spytag-

WT 426c core with Spycatcher-Ferritin, and 2) EndoH-treated WT 426c core with Spycatcher ferritin. 1 μg of Spycatcher-Ferritin was mixed with every 2.5 μg of antigen. Mixtures were allowed to incubate overnight with mild nutation at 4C. Assembled complexes were subsequently purified the following morning using an Superdex 200 Increase 10/300 GL column and analyzed by negative stain electron microscopy.

5.6.6 *Negative-stain EM sample preparation*

All nanoparticles used in this study (3 μL) were negatively stained at a final concentration of 0.015 mg/mL using Gilder Grids overlaid with a thin layer of carbon and 2% uranyl formate as previously described (Veesler et al., 2014).

5.6.7 *Negative-Stain EM data collection and processing*

Data were collected on an FEI Technai 12 Spirit 120kV electron microscope equipped with a Gatan Ultrascan 4000 CCD camera. A total of approximately 150 images were collected per sample by using a random defocus range of 1.5–2.5 μm with a total exposure of 45 $e-/A^2$. Data were automatically acquired using Leginon(Suloway et al., 2005), and data processing was carried out using Appion (Lander et al., 2009). The parameters of the contrast transfer function (CTF) were estimated using CTFFIND4 (Mindell and Grigorieff, 2003), and particles were picked in a reference-free manner using DoG picker(Voss et al., 2009). Particles were extracted with a binning factor of 2 after correcting for the effect of the CTF by flipping the phases of each micrograph with EMAN 1.9 (Ludtke et al., 1999). The particle stacks were pre-processed in RELION/2.1(Kimanius et al., 2016; Scheres, 2012d, 2012c; Zivanov et al., 2018) with an

additional binning factor of 2 applied, resulting in a final pixel size of 6.4 Å. Resulting particles were sorted by reference-free 2D classification over 25 iterations.

5.6.8 *Mouse immunizations*

Immunizations were performed in the glH-VRC01 mouse(Jardine et al., 2015). This mouse is heterozygous for the glVRC01 heavy chain (mature VRC01 CDRH3). The light chains expressed in this mouse are the endogenous mouse light chains. Female and male mice were immunized intramuscularly with a dose of 5 μg of protein and 60 μg of Poly (I:C) (InvivoGen, Cat# tlrl-pic-5) split between the rear hind legs. Blood was collected retro-orbitally at week two and four and via cardiac puncture at week six.

5.6.9 *Serum enzyme-linked immunosorbent assay*

30 uL of 5 μg /mL of either WT 426c core, and WT 426c Core KO were absorbed onto a 384-well Immulon 2HB ELISA plates at 37C for 2 hours in 10 mM Tris pH 7.5, 150 mM NaCl buffer. Plates were then washed four times with ELISA washing buffer (TBS+0.02% Tween 20) prior to blocking at 37C for 1 hour with 100 μL per well of blocking buffer containing 2% Bovine Serum Albumin. After blocking, plates were washed 4 times with ELISA washing buffer. Serum was serial diluted started at a 1:5 dilution 8X in washing buffer and allowed to incubate for 1 hour at 37C with final volumes of 30 μL/well. For the 2G12 control, 50 μg of 2G12 was added to the first well and serial diluted 8X with a 1:5 dilution factor with a final volume of 30 μL/well. Following 4 additional washes with ELISA washing buffer, a 1:4000 dilution of goat anti-mouse IgG HRP in wash buffer was added to each well and incubated at 37C for 1 hour followed by four washes

with wash buffer at 30 µL/well. For the 2G12 control, a 1:4000 dilution of goat anti-human IgG HRP in wash buffer was added to each well instead. 30 µl/well of SureBlue Reserve TMB Microwell Peroxidase substrate was added. After 6 min, 30 µL/well of 1N Hydrochloric Acid was added and the A450 of each well was read on a Biotek 405 Select microplate reader. The same protocol was used for the eOD-GT8 analysis, except that the final SureBlue Reserve TMB Microwell Peroxidase substrate reaction step was extended to 10 minutes prior to quenching with 30 uL/well of 1N Hydrochloric acid.

5.6.10 *Ethics statement*

All animal experiments were approved by the Fred Hutchinson Cancer Research Center's Institutional Animal Care and Use Committee (IACUC) guidelines as per protocol number 50879 and follow the recommendations in the Guide for the Care and Use of Laboratory Animals of the National Institutes of Health. The Fred Hutchinson Cancer Research Center (Fred Hutch) IACUC complies will all applicable regulations, including the Public Health Service (PHS) Policy on Humane Care and Use of Laboratory Animals (Policy), the Guide for the Care and Use of Laboratory Animals (Guide), and the Animal Welfare Act (AWA) regulations. The Fred Hutch IACUC has an approved Animal Welfare Assurance on file with the Office of Laboratory Animal Welfare (OLAW). The Assurance number is D16-00142 (Legacy # A3226-01). Fred Hutch IACUC is AAALAC accredited. The most recent AAALAC site visit occurred June 12-13, 2018. Fred Hutch IACUC is registered with the USDA, Registration #91-R-0025.

Chapter 6. THESIS SUMMARY AND FUTURE DIRECTIONS

During the first phase of my dissertation work (chapter 2), I outlined how we solved the structure of one of the first fully intact cyclic nucleotide-gated (CNG) ion channels to near-atomic resolution. At the time, the lack of structural data for any full-length CNG or HCN channel had largely limited our understanding of the molecular mechanisms associated with sensory transduction, as well as the molecular mechanisms associated with cardiac and neuronal excitability. This structure of a CNG channel with cAMP bound displayed a novel conformation of the C-terminal region containing the cyclic nucleotide-binding domain. This configuration was significantly different from the X-ray crystal structures of isolated C-terminal fragments, as well as CryoEM structures of orthologous CNG channels determined around the same time. We observed that the voltage-sensor domain was not domain 'swapped', a configuration that had – at the time – only been seen in a few other ion channel structures. This unexpected finding suggested that this architecture might be a common feature for this family of ion channels. We anticipated that these results would have a strong impact on the field of ion channel biology and their associated fields of neuroscience, as conserved quaternary rearrangements likely contribute to gating in all CNG, HCN and KCNH channels. Furthermore, we believe these results will provide a structural framework for future drug design initiatives aimed at modulating the function of these medically important membrane protein complexes.

Chapter 3 of this dissertation focused on uncovering the molecular mode-of-action for an antibody-based cancer therapy. LM609, also named Vitaxin, Etaracizumab, Abegrin and MEDI-522, is an antibody which specifically targets human αVβ3 integrin and is currently evaluated in

phase II clinical trials by several pharmaceutical companies for the treatment of lymphoma, melanoma, renal, small intestine and colorectal cancers. The current lack of structural and mechanistic information for this antibody had severely limited rationale engineering approaches for specific biomedical applications. In chapter 2 of this thesis, I highlighted the biophysical and structural characterization of the complex formed between human $\alpha_V\beta_3$ integrin and the antigen-binding region (Fab) of the LM609 antibody. Throughout this chapter, we demonstrated that LM609 binds with high-affinity to the apex of the integrin headpiece in the vicinity of but without obstructing the RGD-binding site used by numerous endogeneous ligands. These results also show that LM609 prevents binding of RGD-containing ligands via steric hindrance, rather than by integrin conformational selection. This thoroughly explained the reported inhibition of angiogenesis and bone resorption mediated by this antibody in preclinical and clinical studies. I believe this work represented a significant step forward in unveiling the mode of action of the LM609 antibody and in providing a structural framework for future rational engineering of this therapeutic binder. It is expected that these results will have a broad impact – both in basic research and in medicine – due to the tremendous importance of integrins and their involvement in various human diseases.

Chapter 4 began my focus on HIV-1 vaccine development. HIV-1 is a leading cause of mortality and morbidity worldwide, with a death toll approaching over 1.1 million human lives as of 2015. A major challenge in HIV-1 vaccine design is the elicitation of broadly neutralizing antibodies (bnAbs) targeting conserved epitopes on the viral envelope (Env) glycoprotein. Env decorates the virus surface of the virion and is the sole target of virus-neutralizing antibodies during infection. Given its importance for viral infectivity, Env has evolved several immune

evasion strategies preventing development of acquired immunity in the vast majority of HIV-infected individuals. These include rapid antigenic evolution, masking of epitopes with glycans or conformational changes and exposure of non-neutralizing immuno-dominant "decoy" epitopes. Of all known HIV-1 bnAbs, $CD4_{BS}$-targeting antibodies have been isolated from multiple HIV-1-infected patients and are of particular interest for HIV-1 vaccine development due to their exceptional potency and breadth. These antibodies bind the $CD4_{BS}$ and prevent interactions between Env and host CD4 receptors.

Although N-linked glycosylation sites surrounding the CD4-binding site typically limit recognition by antibodies, mature $CD4_{BS}$-directed bnAbs can overcome this barrier and potently neutralize numerous HIV-1 viral clades. In contrast, their inferred germline precursors lack detectable binding to trimeric Env constructs harboring glycans at these locations. As a result, vaccinology initiatives aiming to elicit $CD4_{BS}$ bnAbs have largely relied on removal of these glycans by way of mutagenesis. Unfortunately, the antibodies these immunizations scheme tend to produce typically do not neutralize the wild-type virus. Those that do, only tend to do so weakly. This is largely due to these elicited antibodies failing to overcome the glycan shield of wild-type viruses with high efficacy. This is especially true for the oligosaccharide at position Asn276, which resides at the center of the epitope for many $CD4_{BS}$-targeting antibodies. In chapter 4, I highlighted work leading to the first reported near-atomic resolution cryoEM structure of the inferred germline precursor of a $CD4_{BS}$-targeting bnAb, germline VRC01 ($VRC01_{GL}$) in complex with a modified 426c HIV-1 SOSIP trimer.

Based on our structural observations, we suggested that a naturally occurring reduction of local oligosaccharide density in the vicinity of the $CD4_{BS}$ and sequence specific features were responsible for the unique ability of 426c Env-derived protein constructs to engage $VRC01_{GL}$. We subsequently determined a crystal structure of $VRC01_{GL}$ in complex with a fully glycosylated 'wild-type' 426c gp120 core construct. Surprisingly, this construct demonstrated the ability to bind to $VRC01_{GL}$ via interactions with the oligosaccharide at position Asn276 – a result which had long been thought to be impossible. These results challenged a major immunological dogma, and represented a paradigm shift in the field of HIV-1 vaccine design. By combining biosensor assays and glycoproteomics, we also demonstrated the affinity of $VRC01_{GL}$ for 426c gp120 could be modulated by altering the length of N-linked carbohydrates.

Given these results, we next set out to tailor the glycan shield of the wild-type 426c gp120 core to enzymatically enrich for short glycans specifically around the $CD4_{BS}$ while retaining the integrity of other sites targeted by bNAbs. Following a robust biochemical and biophysical analytic pipeline, chapter 5 outlined the development of a limited endoglycosidase H digestion strategy promoting selective trimming of oligosaccharides located near the $CD4_{BS}$ of a wild-type 426c gp120 core. The resulting enhanced accessibility of the $CD4_{BS}$ led to increased engagement of multiple $CD4_{BS}$-directed bNAb germline precursors *in vitro* compared to an untreated control. Given the ability of a breadth of germline precursors to interact with this enzymatically treated wild-type 426c core, we injected mice with multivalently displayed 426c gp120 core antigens expressed in HEK293S cells. Immunized $VRC01_{GL}$ heavy-chain knock-in mice elicited strong $CD4_{BS}$-directed responses, with EndoH treatment of antigens significantly enhancing this effect.

Given the results of this study, it has become clear that the chemistry associated with protein glycosylation can have significant impacts on protein-protein interactions.

The collective results outlined in chapters 4 and 5 of this dissertation underscore the importance of continued research in the areas of glycoproteomics, glycan-protein interactions, and vaccine design against glycosylated membrane proteins. It is probable that many biochemical interactions – beyond just those reported here – are impacted and regulated heavily by protein surface glycan chemistry. It is well-known that protein expression within cells produces large variances in glycan profiles between individual molecules transcribed and translated from a same genomic sequence. Thus, it is imperative that future studies determine if the observations observed for HIV-1 can be extended and applied to a broader spectrum of molecular processes, diseases, and their emerging associated treatment options.

Chapter 7. REFERENCES

Adams, P.D., Afonine, P. V, Bunkóczi, G., Chen, V.B., Davis, I.W., Echols, N., Headd, J.J., Hung, L.-W., Kapral, G.J., Grosse-Kunstleve, R.W., et al. (2010). PHENIX: a comprehensive Python-based system for macromolecular structure solution. Acta Crystallogr. D. Biol. Crystallogr. *66*, 213–221.

Van Agthoven, J.F., Xiong, J.-P., Alonso, J.L., Rui, X., Adair, B.D., Goodman, S.L., and Arnaout, M.A. (2014). Structural basis for pure antagonism of integrin αVβ3 by a high-affinity form of fibronectin. Nat. Struct. Mol. Biol. *21*, 383–388.

Akimoto, M., Zhang, Z., Boulton, S., Selvaratnam, R., VanSchouwen, B., Gloyd, M., Accili, E.A., Lange, O.F., and Melacini, G. (2014). A mechanism for the auto-inhibition of hyperpolarization-activated cyclic nucleotide-gated (HCN) channel opening and its relief by cAMP. J. Biol. Chem. *289*, 22205–22220.

Altmann, F., Staudacher, E., Wilson, I.B., and März, L. (1999). Insect cells as hosts for the expression of recombinant glycoproteins. Glycoconj. J. *16*, 109–123.

Backovic, M., and Krey, T. (2016). Stable Drosophila Cell Lines: An Alternative Approach to Exogenous Protein Expression. Methods Mol. Biol. *1350*, 349–358.

Backovic, M., Johansson, D.X., Klupp, B.G., Mettenleiter, T.C., Persson, M.A.A., and Rey, F.A. (2010). Efficient method for production of high yields of Fab fragments in Drosophila S2 cells. Protein Eng. Des. Sel. *23*, 169–174.

Bai, X.-C., Yan, C., Yang, G., Lu, P., Ma, D., Sun, L., Zhou, R., Scheres, S.H.W., and Shi, Y. (2015). An atomic structure of human γ-secretase. Nature *525*, 212–217.

Barad, B.A., Echols, N., Wang, R.Y.-R., Cheng, Y., DiMaio, F., Adams, P.D., and Fraser, J.S. (2015). EMRinger: side chain-directed model and map validation for 3D cryo-electron microscopy. Nat. Methods *12*, 943–946.

Baruscotti, M., Bucchi, A., and Difrancesco, D. (2005). Physiology and pharmacology of the

cardiac pacemaker (“funny”) current. Pharmacol. Ther. *107*, 59–79.

Behrens, A.-J., Vasiljevic, S., Pritchard, L.K., Harvey, D.J., Andev, R.S., Krumm, S.A., Struwe, W.B., Cupo, A., Kumar, A., Zitzmann, N., et al. (2016). Composition and Antigenic Effects of Individual Glycan Sites of a Trimeric HIV-1 Envelope Glycoprotein. Cell Rep. *14*, 2695–2706.

Behrens, A., Kumar, A., Medina-Ramirez, M., Cupo, A., Marshall, K., Cruz Portillo, V.M., Harvey, D.J., Ozorowski, G., Zitzmann, N., Wilson, I.A., et al. (2018). Integrity of Glycosylation Processing of a Glycan-Depleted Trimeric HIV-1 Immunogen Targeting Key B-Cell Lineages. J. Proteome Res. *17*, 987–999.

Bern, M., Kil, Y.J., and Becker, C. (2012). Byonic: advanced peptide and protein identification software. Curr. Protoc. Bioinforma. *Chapter 13*, Unit13.20.

Biel, M., and Michalakis, S. (2007). Function and dysfunction of CNG channels: insights from channelopathies and mouse models. Mol. Neurobiol. *35*, 266–277.

Blanc, E., Roversi, P., Vonrhein, C., Flensburg, C., Lea, S.M., and Bricogne, G. (2004). Refinement of severely incomplete structures with maximum likelihood in BUSTER-TNT. Acta Crystallogr. D. Biol. Crystallogr. *60*, 2210–2221.

Bonomelli, C., Doores, K.J., Dunlop, D.C., Thaney, V., Dwek, R.A., Burton, D.R., Crispin, M., and Scanlan, C.N. (2011). The glycan shield of HIV is predominantly oligomannose independently of production system or viral clade. PLoS One *6*, 1–7.

Borst, A.J., James, Z.M., Zagotta, W.N., Ginsberg, M., Rey, F.A., DiMaio, F., Backovic, M., and Veesler, D. (2017). The Therapeutic Antibody LM609 Selectively Inhibits Ligand Binding to Human αVβ3Integrin via Steric Hindrance. Structure *25*, 1732-1739.e5.

Borst, A.J., Weidle, C.E., Gray, M.D., Frenz, B., Snijder, J., Joyce, M.G., Georgiev, I.S., Stewart-Jones, G.B., Kwong, P.D., McGuire, A.T., et al. (2018). Germline VRC01 antibody recognition of a modified clade C HIV-1 envelope trimer and a glycosylated HIV-1 gp120 core. Elife *7*.

Brams, M., Kusch, J., Spurny, R., Benndorf, K., and Ulens, C. (2014). Family of prokaryote

cyclic nucleotide-modulated ion channels. Proc. Natl. Acad. Sci. U. S. A. *111*, 7855–7860.

Brelidze, T.I., Carlson, A.E., and Zagotta, W.N. (2009). Absence of direct cyclic nucleotide modulation of mEAG1 and hERG1 channels revealed with fluorescence and electrophysiological methods. J. Biol. Chem. *284*, 27989–27997.

Brelidze, T.I., Carlson, A.E., Sankaran, B., and Zagotta, W.N. (2012). Structure of the carboxy-terminal region of a KCNH channel. Nature *481*, 530–533.

Briney, B., Sok, D., Jardine, J.G., Nemazee, D., Burton, D.R., Schief, W.R., Briney, B., Sok, D., Jardine, J.G., Kulp, D.W., et al. (2016). Tailored Immunogens Direct Affinity Maturation toward HIV Neutralizing Antibodies Article Tailored Immunogens Direct Affinity Maturation toward HIV Neutralizing Antibodies. Cell *166*, 1459-1464.e11.

Brown, A., Long, F., Nicholls, R.A., Toots, J., Emsley, P., and Murshudov, G. (2015). Tools for macromolecular model building and refinement into electron cryo-microscopy reconstructions. Acta Crystallogr. D. Biol. Crystallogr. *71*, 136–153.

Bucchi, A., Barbuti, A., Difrancesco, D., and Baruscotti, M. (2012). Funny Current and Cardiac Rhythm: Insights from HCN Knockout and Transgenic Mouse Models. Front. Physiol. *3*, 240.

Burton, D.R., and Mascola, J.R. (2015). Antibody responses to envelope glycoproteins in HIV-1 infection. Nat. Immunol. *16*, 571–576.

Calarese, D.A., Scanlan, C.N., Zwick, M.B., Deechongkit, S., Mimura, Y., Kunert, R., Zhu, P., Wormald, M.R., Stanfield, R.L., Roux, K.H., et al. (2003). Antibody domain exchange is an immunological solution to carbohydrate cluster recognition. Science *300*, 2065–2071.

Campbell, I.D., and Humphries, M.J. (2011). Integrin structure, activation, and interactions. Cold Spring Harb. Perspect. Biol. *3*.

Catterall, W.A. (2010). Ion channel voltage sensors: structure, function, and pathophysiology. Neuron *67*, 915–928.

Charo, I.F., Nannizzi, L., Smith, J.W., and Cheresh, D.A. (1990). The vitronectin receptor alpha

v beta 3 binds fibronectin and acts in concert with alpha 5 beta 1 in promoting cellular attachment and spreading on fibronectin. J. Cell Biol. *111*, 2795–2800.

Chen, S., McMullan, G., Faruqi, A.R., Murshudov, G.N., Short, J.M., Scheres, S.H.W., and Henderson, R. (2013). High-resolution noise substitution to measure overfitting and validate resolution in 3D structure determination by single particle electron cryomicroscopy. Ultramicroscopy *135*, 24–35.

Chen, V.B., Arendall, W.B., Headd, J.J., Keedy, D.A., Immormino, R.M., Kapral, G.J., Murray, L.W., Richardson, J.S., and Richardson, D.C. (2010a). MolProbity: all-atom structure validation for macromolecular crystallography. Acta Crystallogr. D. Biol. Crystallogr. *66*, 12–21.

Chen, X., Xie, C., Nishida, N., Li, Z., Walz, T., and Springer, T.A. (2010b). Requirement of open headpiece conformation for activation of leukocyte integrin alphaXbeta2. Proc. Natl. Acad. Sci. U. S. A. *107*, 14727–14732.

Cheresh, D.A. (1987). Human endothelial cells synthesize and express an Arg-Gly-Asp-directed adhesion receptor involved in attachment to fibrinogen and von Willebrand factor. Proc. Natl. Acad. Sci. U. S. A. *84*, 6471–6475.

Collaborative Computational Project, N. 4 (1994). The CCP4 suite: programs for protein crystallography. Acta Crystallogr. D. Biol. Crystallogr. *50*, 760–763.

Conway, P., Tyka, M.D., DiMaio, F., Konerding, D.E., and Baker, D. (2014). Relaxation of backbone bond geometry improves protein energy landscape modeling. Protein Sci. *23*, 47–55.

Coss, K.P., Vasiljevic, S., Pritchard, L.K., Krumm, S.A., Glaze, M., Madzorera, S., Moore, P.L., Crispin, M., and Doores, K.J. (2016). HIV-1 Glycan Density Drives the Persistence of the Mannose Patch within an Infected Individual. J. Virol. *90*, 11132–11144.

Costa, F., Hagan, J.E., Calcagno, J., Kane, M., Torgerson, P., Martinez-Silveira, M.S., Stein, C., Abela-Ridder, B., and Ko, A.I. (2015). Global Morbidity and Mortality of Leptospirosis: A Systematic Review. PLoS Negl. Trop. Dis. *9*, e0003898.

Craven, K.B., and Zagotta, W.N. (2004). Salt bridges and gating in the COOH-terminal region of

HCN2 and CNGA1 channels. J. Gen. Physiol. *124*, 663–677.

Craven, K.B., and Zagotta, W.N. (2006). CNG and HCN channels: two peas, one pod. Annu. Rev. Physiol. *68*, 375–401.

Craven, K.B., Olivier, N.B., and Zagotta, W.N. (2008). C-terminal movement during gating in cyclic nucleotide-modulated channels. J. Biol. Chem. *283*, 14728–14738.

Crooks, E.T., Tong, T., Chakrabarti, B., Narayan, K., Georgiev, I.S., Menis, S., Huang, X., Kulp, D., Osawa, K., Muranaka, J., et al. (2015). Vaccine-Elicited Tier 2 HIV-1 Neutralizing Antibodies Bind to Quaternary Epitopes Involving Glycan-Deficient Patches Proximal to the CD4 Binding Site. PLoS Pathog. *11*, 1–34.

Cuevas, J.M., Geller, R., Garijo, R., López-Aldeguer, J., and Sanjuán, R. (2015). Extremely High Mutation Rate of HIV-1 In Vivo. PLoS Biol. *13*, 1–19.

Dalgleish, A.G., Beverley, P.C.L., Clapham, P.R., Crawford, D.H., Greaves, M.F., and Weiss, R.A. (1984). The CD4 (T4) antigen is an essential component of the receptor for the AIDS retrovirus. Nature *312*, 763–767.

Danhier, F., Le Breton, A., and Préat, V. (2012). RGD-based strategies to target alpha(v) beta(3) integrin in cancer therapy and diagnosis. Mol. Pharm. *9*, 2961–2973.

Depetris, R.S., Julien, J.P., Khayat, R., Lee, J.H., Pejchal, R., Katpally, U., Cocco, N., Kachare, M., Massi, E., David, K.B., et al. (2012). Partial enzymatic deglycosylation preserves the structure of cleaved recombinant HIV-1 envelope glycoprotein trimers. J. Biol. Chem. *287*, 24239–24254.

DiMaio, F., Tyka, M.D., Baker, M.L., Chiu, W., and Baker, D. (2009). Refinement of protein structures into low-resolution density maps using rosetta. J. Mol. Biol. *392*, 181–190.

DiMaio, F., Leaver-Fay, A., Bradley, P., Baker, D., and André, I. (2011). Modeling symmetric macromolecular structures in Rosetta3. PLoS One *6*, e20450.

DiMaio, F., Song, Y., Li, X., Brunner, M.J., Xu, C., Conticello, V., Egelman, E., Marlovits, T.,

Cheng, Y., and Baker, D. (2015). Atomic-accuracy models from 4.5-Å cryo-electron microscopy data with density-guided iterative local refinement. Nat. Methods *12*, 361–365.

Dosenovic, P., Von Boehmer, L., Escolano, A., Jardine, J., Freund, N.T., Gitlin, A.D., McGuire, A.T., Kulp, D.W., Oliveira, T., Scharf, L., et al. (2015). Immunization for HIV-1 Broadly Neutralizing Antibodies in Human Ig Knockin Mice. Cell *161*, 1505–1515.

Doyle, D.A., Morais Cabral, J., Pfuetzner, R.A., Kuo, A., Gulbis, J.M., Cohen, S.L., Chait, B.T., and MacKinnon, R. (1998). The structure of the potassium channel: molecular basis of K+ conduction and selectivity. Science *280*, 69–77.

Dubrovskaya, V., Guenaga, J., de Val, N., Wilson, R., Feng, Y., Movsesyan, A., Karlsson Hedestam, G.B., Ward, A.B., and Wyatt, R.T. (2017). Targeted N-glycan deletion at the receptor-binding site retains HIV Env NFL trimer integrity and accelerates the elicited antibody response. PLOS Pathog. *13*, e1006614.

Dürr, K.L., Chen, L., Stein, R.A., De Zorzi, R., Folea, I.M., Walz, T., Mchaourab, H.S., and Gouaux, E. (2014). Structure and dynamics of AMPA receptor GluA2 in resting, pre-open, and desensitized states. Cell *158*, 778–792.

Emsley, P., and Cowtan, K. (2004). Coot: model-building tools for molecular graphics. Acta Crystallogr. D. Biol. Crystallogr. *60*, 2126–2132.

Emsley, P., Lohkamp, B., Scott, W.G., and Cowtan, K. (2010). Features and development of Coot research papers. 486–501.

Fellouse, F.A., Wiesmann, C., and Sidhu, S.S. (2004). Synthetic antibodies from a four-amino-acid code: a dominant role for tyrosine in antigen recognition. Proc. Natl. Acad. Sci. U. S. A. *101*, 12467–12472.

Fellouse, F.A., Esaki, K., Birtalan, S., Raptis, D., Cancasci, V.J., Koide, A., Jhurani, P., Vasser, M., Wiesmann, C., Kossiakoff, A.A., et al. (2007). High-throughput generation of synthetic antibodies from highly functional minimalist phage-displayed libraries. J. Mol. Biol. *373*, 924–940.

Fesenko, E.E., Kolesnikov, S.S., and Lyubarsky, A.L. (1985). Induction by cyclic GMP of cationic conductance in plasma membrane of retinal rod outer segment. Nature *313*, 310–313.

Fowler, P.W., and Sansom, M.S.P. (2013). The pore of voltage-gated potassium ion channels is strained when closed. Nat. Commun. *4*, 1872.

Freeze, H.H., and Kranz, C. (2010). Endoglycosidase and glycoamidase release of N-linked glycans. Curr. Protoc. Mol. Biol. *Chapter 17*, Unit 17.13A.

Frelinger, A.L., Du, X.P., Plow, E.F., and Ginsberg, M.H. (1991). Monoclonal antibodies to ligand-occupied conformers of integrin alpha IIb beta 3 (glycoprotein IIb-IIIa) alter receptor affinity, specificity, and function. J. Biol. Chem. *266*, 17106–17111.

Frenz, B., Walls, A.C., Egelman, E.H., Veesler, D., and Di Maio, F. (2017). RosettaES: A sampling strategy enabling automated interpretation of difficult cryo-EMmaps. Nat. Methods *14*, 797–800.

Frese, C.K., Zhou, H., Taus, T., Altelaar, A.F.M., Mechtler, K., Heck, A.J.R., and Mohammed, S. (2013). Unambiguous phosphosite localization using electron-transfer/higher-energy collision dissociation (EThcD). J. Proteome Res. *12*, 1520–1525.

Freund, N.T., Horwitz, J.A., Nogueira, L., Sievers, S.A., Scharf, L., Scheid, J.F., Gazumyan, A., Liu, C., Velinzon, K., Goldenthal, A., et al. (2015). A New Glycan-Dependent CD4-Binding Site Neutralizing Antibody Exerts Pressure on HIV-1 In Vivo. PLoS Pathog. *11*, e1005238.

Garrigues, H.J., Rubinchikova, Y.E., Dipersio, C.M., and Rose, T.M. (2008). Integrin alphaVbeta3 Binds to the RGD motif of glycoprotein B of Kaposi's sarcoma-associated herpesvirus and functions as an RGD-dependent entry receptor. J. Virol. *82*, 1570–1580.

Gaschen, B., Kuiken, C., Korber, B., and Foley, B. (2018). Retrieval and on-the-fly alignment of sequence fragments from the HIV database. Bioinformatics *17*, 415–418.

Gavrilovskaya, I.N., Shepley, M., Shaw, R., Ginsberg, M.H., and Mackow, E.R. (1998). beta3 Integrins mediate the cellular entry of hantaviruses that cause respiratory failure. Proc. Natl. Acad. Sci. U. S. A. *95*, 7074–7079.

Gavrilovskaya, I.N., Brown, E.J., Ginsberg, M.H., and Mackow, E.R. (1999). Cellular entry of hantaviruses which cause hemorrhagic fever with renal syndrome is mediated by beta3 integrins. J. Virol. *73*, 3951–3959.

Goddard, T.D., Huang, C.C., and Ferrin, T.E. (2007). Visualizing density maps with UCSF Chimera. J. Struct. Biol. *157*, 281–287.

Goldschen-Ohm, M.P., Klenchin, V.A., White, D.S., Cowgill, J.B., Cui, Q., Goldsmith, R.H., and Chanda, B. (2016). Structure and dynamics underlying elementary ligand binding events in human pacemaking channels. Elife *5*.

Gordon, S.E., and Zagotta, W.N. (1995). Localization of regions affecting an allosteric transition in cyclic nucleotide-activated channels. Neuron *14*, 857–864.

Gouet, P., Courcelle, E., Stuart, D.I., and Métoz, F. (1999). ESPript: analysis of multiple sequence alignments in PostScript. Bioinformatics *15*, 305–308.

Gramoun, A., Shorey, S., Bashutski, J.D., Dixon, S.J., Sims, S.M., Heersche, J.N.M., and Manolson, M.F. (2007). Effects of Vitaxin, a novel therapeutic in trial for metastatic bone tumors, on osteoclast functions in vitro. J. Cell. Biochem. *102*, 341–352.

Gray, E.S., Taylor, N., Wycuff, D., Moore, P.L., Tomaras, G.D., Wibmer, C.K., Puren, A., DeCamp, A., Gilbert, P.B., Wood, B., et al. (2009). Antibody specificities associated with neutralization breadth in plasma from human immunodeficiency virus type 1 subtype C-infected blood donors. J. Virol. *83*, 8925–8937.

Grigorieff, N. (2016). Frealign: An Exploratory Tool for Single-Particle Cryo-EM. Methods Enzymol. *579*, 191–226.

Gristick, H.B., von Boehmer, L., West Jr, A.P., Schamber, M., Gazumyan, A., Golijanin, J., Seaman, M.S., Fätkenheuer, G., Klein, F., Nussenzweig, M.C., et al. (2016). Natively glycosylated HIV-1 Env structure reveals new mode for antibody recognition of the CD4-binding site. Nat. Struct. Mol. Biol. *23*, 906–915.

Guo, D., Shi, X., Arledge, K.C., Song, D., Jiang, L., Fu, L., Gong, X., Zhang, S., Wang, X., and

Zhang, L. (2012). A single residue within the V5 region of HIV-1 envelope facilitates viral escape from the broadly neutralizing monoclonal antibody VRC01. J. Biol. Chem. *287*, 43170–43179.

Gutheil, J.C., Campbell, T.N., Pierce, P.R., Watkins, J.D., Huse, W.D., Bodkin, D.J., and Cheresh, D.A. (2000). Targeted antiangiogenic therapy for cancer using Vitaxin: a humanized monoclonal antibody to the integrin alphavbeta3. Clin. Cancer Res. *6*, 3056–3061.

Haim, H., Salas, I., and Sodroski, J. (2013). Proteolytic processing of the human immunodeficiency virus envelope glycoprotein precursor decreases conformational flexibility. J. Virol. *87*, 1884–1889.

Hattori, M., Hibbs, R.E., and Gouaux, E. (2012). A fluorescence-detection size-exclusion chromatography-based thermostability assay for membrane protein precrystallization screening. Structure *20*, 1293–1299.

Havenar-Daughton, C., Sarkar, A., Kulp, D.W., Toy, L., Hu, X., Deresa, I., Kalyuzhniy, O., Kaushik, K., Upadhyay, A.A., Menis, S., et al. (2018). The human naive B cell repertoire contains distinct subclasses for a germline-targeting HIV-1 vaccine immunogen. Sci. Transl. Med. *10*.

Hazenberg, M.D., Hamann, D., Schuitemaker, H., and Miedema, F. (2000). T cell depletion in HIV-1 infection: How CD4+ T cells go out of stock. Nat. Immunol. *1*, 285–289.

Horn, R. (2004). How S4 segments move charge. Let me count the ways. J. Gen. Physiol. *123*, 1–4.

Hossler, P., Khattak, S.F., and Li, Z.J. (2009). Optimal and consistent protein glycosylation in mammalian cell culture. Glycobiology *19*, 936–949.

Huang, J., Kang, B.H., Ishida, E., Zhou, T., Griesman, T., Sheng, Z., Wu, F., Doria-Rose, N.A., Zhang, B., McKee, K., et al. (2016). Identification of a CD4-Binding-Site Antibody to HIV that Evolved Near-Pan Neutralization Breadth. Immunity *45*, 1108–1121.

Huang, Y.W., Yang, H.I., Wu, Y.T., Hsu, T.L., Lin, T.W., Kelly, J.W., and Wong, C.H. (2017).

Residues Comprising the Enhanced Aromatic Sequon Influence Protein N-Glycosylation Efficiency. J. Am. Chem. Soc. *139*, 12947–12955.

James, Z.M., Borst, A.J., Haitin, Y., Frenz, B., Dimaio, F., Zagotta, W.N., and Veesler, D. (2017). CryoEM structure of a prokaryotic cyclic nucleotide-gated ion channel. 2–7.

Jardine, J., Julien, J.-P., Menis, S., Ota, T., Kalyuzhniy, O., McGuire, A., Sok, D., Huang, P.-S., MacPherson, S., Jones, M., et al. (2013). Rational HIV immunogen design to target specific germline B cell receptors. Science *340*, 711–716.

Jardine, J.G., Ota, T., Sok, D., Pauthner, M., Kulp, D.W., Kalyuzhniy, O., Skog, P.D., Thinnes, T.C., Bhullar, D., Briney, B., et al. (2015). HIV-1 VACCINES. Priming a broadly neutralizing antibody response to HIV-1 using a germline-targeting immunogen. Science *349*, 156–161.

Jardine, J.G., Kulp, D.W., Havenar-Daughton, C., Sarkar, A., Briney, B., Sok, D., Sesterhenn, F., Ereño-Orbea, J., Kalyuzhniy, O., Deresa, I., et al. (2016). HIV-1 broadly neutralizing antibody precursor B cells revealed by germline-targeting immunogen. Science *351*, 1458–1463.

Jiang, Y., Lee, A., Chen, J., Cadene, M., Chait, B.T., and MacKinnon, R. (2002). The open pore conformation of potassium channels. Nature *417*, 523–526.

Joyce, M.G., Georgiev, I.S., Yang, Y., Mcdermott, A.B., Mascola, J.R., Kwong, P.D., Joyce, M.G., Georgiev, I.S., Yang, Y., Druz, A., et al. (2017). Soluble Prefusion Closed DS-SOSIP . 664-Env. CellReports *21*, 2992–3002.

Julien, J.-P., Lee, J.H., Ozorowski, G., Hua, Y., Torrents de la Peña, A., de Taeye, S.W., Nieusma, T., Cupo, A., Yasmeen, A., Golabek, M., et al. (2015). Design and structure of two HIV-1 clade C SOSIP.664 trimers that increase the arsenal of native-like Env immunogens. Proc. Natl. Acad. Sci. U. S. A. *112*, 11947–11952.

Kabsch, W. (2010). XDS. Acta Crystallogr. D. Biol. Crystallogr. *66*, 125–132.

Kamata, T., Handa, M., Takakuwa, S., Sato, Y., Kawai, Y., Ikeda, Y., and Aiso, S. (2013). Epitope mapping for monoclonal antibody reveals the activation mechanism for αVβ3 integrin. PLoS One *8*, e66096.

Kanekiyo, M., Wei, C.-J., Yassine, H.M., McTamney, P.M., Boyington, J.C., Whittle, J.R.R., Rao, S.S., Kong, W.-P., Wang, L., and Nabel, G.J. (2013). Self-assembling influenza nanoparticle vaccines elicit broadly neutralizing H1N1 antibodies. Nature *499*, 102–106.

Kawate, T., and Gouaux, E. (2006). Fluorescence-detection size-exclusion chromatography for precrystallization screening of integral membrane proteins. Structure *14*, 673–681.

Kesters, D., Brams, M., Nys, M., Wijckmans, E., Spurny, R., Voets, T., Tytgat, J., Kusch, J., and Ulens, C. (2015). Structure of the SthK carboxy-terminal region reveals a gating mechanism for cyclic nucleotide-modulated ion channels. PLoS One *10*, e0116369.

Kimanius, D., Forsberg, B.O., Scheres, S.H.W., and Lindahl, E. (2016). Accelerated cryo-EM structure determination with parallelisation using GPUS in RELION-2. Elife *5*, 1–21.

Klein, F., Diskin, R., Scheid, J.F., Gaebler, C., Mouquet, H., Georgiev, I.S., Pancera, M., Zhou, T., Incesu, R.B., Fu, B.Z., et al. (2013). Somatic mutations of the immunoglobulin framework are generally required for broad and potent HIV-1 neutralization. Cell *153*, 126–138.

Kong, L., Sheppard, N.C., Stewart-Jones, G.B.E., Robson, C.L., Chen, H., Xu, X., Krashias, G., Bonomelli, C., Scanlan, C.N., Kwong, P.D., et al. (2010). Expression-System-Dependent Modulation of HIV-1 Envelope Glycoprotein Antigenicity and Immunogenicity. J. Mol. Biol. *403*, 131–147.

Koo, L.Y., Irvine, D.J., Mayes, A.M., Lauffenburger, D.A., and Griffith, L.G. (2002). Co-regulation of cell adhesion by nanoscale RGD organization and mechanical stimulus. J. Cell Sci. *115*, 1423–1433.

Kowal, J., Chami, M., Baumgartner, P., Arheit, M., Chiu, P.-L., Rangl, M., Scheuring, S., Schröder, G.F., Nimigean, C.M., and Stahlberg, H. (2014). Ligand-induced structural changes in the cyclic nucleotide-modulated potassium channel MloK1. Nat. Commun. *5*, 3106.

Krey, T., D'Alayer, J., Kikuti, C.M., Saulnier, A., Damier-Piolle, L., Petitpas, I., Johansson, D.X., Tawar, R.G., Baron, B., Robert, B., et al. (2010). The disulfide bonds in glycoprotein E2 of hepatitis C virus reveal the tertiary organization of the molecule. PLoS Pathog. *6*, e1000762.

Kucukelbir, A., Sigworth, F.J., and Tagare, H.D. (2014). Quantifying the local resolution of cryo-EM density maps. Nat. Methods *11*, 63–65.

Kwon, Y. Do, Pancera, M., Acharya, P., Georgiev, I.S., Crooks, E.T., Gorman, J., Joyce, M.G., Guttman, M., Ma, X., Narpala, S., et al. (2015). Crystal structure , conformational fixation and entry-related interactions of mature ligand-free HIV-1 Env. Nat. Publ. Gr. *22*, 522–531.

Kwon, Y.D., Finzi, A., Wu, X., Dogo-Isonagie, C., Lee, L.K., Moore, L.R., Schmidt, S.D., Stuckey, J., Yang, Y., Zhou, T., et al. (2012). Unliganded HIV-1 gp120 core structures assume the CD4-bound conformation with regulation by quaternary interactions and variable loops. Proc. Natl. Acad. Sci. *109*, 5663–5668.

Kwong, P.D., Doyle, M.L., Casper, D.J., Cicala, C., Leavitt, S.A., Majeed, S., Steenbeke, T.D., Venturi, M., Chaiken, I., Fung, M., et al. (2002). HIV-1 evades antibody-mediated neutralization through conformational masking of receptor-binding sites. Nature *420*, 678–682.

Lander, G.C., Stagg, S.M., Voss, N.R., Cheng, A., Fellmann, D., Pulokas, J., Yoshioka, C., Irving, C., Mulder, A., Lau, P.-W., et al. (2009). Appion: an integrated, database-driven pipeline to facilitate EM image processing. J. Struct. Biol. *166*, 95–102.

Lavine, C.L., Lao, S., Montefiori, D.C., Haynes, B.F., Sodroski, J.G., Yang, X., and the NIAID Center for HIV/AIDS Vaccine Immunology (2012). High-Mannose Glycan-Dependent Epitopes Are Frequently Targeted in Broad Neutralizing Antibody Responses during Human Immunodeficiency Virus Type 1 Infection. J. Virol. *86*, 2153–2164.

Leahy, D.J., Aukhil, I., and Erickson, H.P. (1996). 2.0 A crystal structure of a four-domain segment of human fibronectin encompassing the RGD loop and synergy region. Cell *84*, 155–164.

Lee, C.-H., and MacKinnon, R. (2017). Structures of the Human HCN1 Hyperpolarization-Activated Channel. Cell *168*, 111-120.e11.

Li, M., Zhou, X., Wang, S., Michailidis, I., Gong, Y., Su, D., Li, H., Li, X., and Yang, J. (2017). Structure of a eukaryotic cyclic-nucleotide-gated channel. Nature *542*, 60–65.

Li, X., Mooney, P., Zheng, S., Booth, C.R., Braunfeld, M.B., Gubbens, S., Agard, D. a, and Cheng, Y. (2013). Electron counting and beam-induced motion correction enable near-atomic-resolution single-particle cryo-EM. Nat. Methods *10*, 584–590.

Li, Y., O'Dell, S., Walker, L.M., Wu, X., Guenaga, J., Feng, Y., Schmidt, S.D., McKee, K., Louder, M.K., Ledgerwood, J.E., et al. (2011). Mechanism of Neutralization by the Broadly Neutralizing HIV-1 Monoclonal Antibody VRC01. J. Virol. *85*, 8954–8967.

Liao, M., Cao, E., Julius, D., and Cheng, Y. (2013). Structure of the TRPV1 ion channel determined by electron cryo-microscopy. Nature *504*, 107–112.

Liu, Z., Jia, B., Zhao, H., Chen, X., and Wang, F. (2011). Specific targeting of human integrin α(v)β (3) with (111)In-labeled Abegrin™ in nude mouse models. Mol. Imaging Biol. *13*, 112–120.

Lolicato, M., Nardini, M., Gazzarrini, S., Möller, S., Bertinetti, D., Herberg, F.W., Bolognesi, M., Martin, H., Fasolini, M., Bertrand, J.A., et al. (2011). Tetramerization dynamics of C-terminal domain underlies isoform-specific cAMP gating in hyperpolarization-activated cyclic nucleotide-gated channels. J. Biol. Chem. *286*, 44811–44820.

Long, S.B., Campbell, E.B., and Mackinnon, R. (2005). Crystal structure of a mammalian voltage-dependent Shaker family K+ channel. Science *309*, 897–903.

Ludtke, S.J., Baldwin, P.R., and Chiu, W. (1999). EMAN: semiautomated software for high-resolution single-particle reconstructions. J. Struct. Biol. *128*, 82–97.

Lyskov, S., and Gray, J.J. (2008). The RosettaDock server for local protein-protein docking. Nucleic Acids Res. *36*, W233-8.

Lyumkis, D., Julien, J., Val, N. De, Cupo, A., Potter, C.S., Klasse, P., Burton, D.R., Sanders, R.W., Moore, J.P., Carragher, B., et al. (2013a). Cryo-EM Structure of a Fully Glycosylated Soluble Cleaved HIV-1 Envelope Trimer. Science (80-.). *342*, 1484–1490.

Lyumkis, D., Brilot, A.F., Theobald, D.L., and Grigorieff, N. (2013b). Likelihood-based classification of cryo-EM images using FREALIGN. J. Struct. Biol. *183*, 377–388.

Lyumkis, D., Oliveira dos Passos, D., Tahara, E.B., Webb, K., Bennett, E.J., Vinterbo, S., Potter, C.S., Carragher, B., and Joazeiro, C.A.P. (2014). Structural basis for translational surveillance by the large ribosomal subunit-associated protein quality control complex. Proc. Natl. Acad. Sci. U. S. A. *111*, 15981–15986.

MacLean, B., Tomazela, D.M., Shulman, N., Chambers, M., Finney, G.L., Frewen, B., Kern, R., Tabb, D.L., Liebler, D.C., and MacCoss, M.J. (2010). Skyline: an open source document editor for creating and analyzing targeted proteomics experiments. Bioinformatics *26*, 966–968.

Mahalingam, B., Van Agthoven, J.F., Xiong, J.-P., Alonso, J.L., Adair, B.D., Rui, X., Anand, S., Mehrbod, M., Mofrad, M.R.K., Burger, C., et al. (2014). Atomic basis for the species-specific inhibition of αV integrins by monoclonal antibody 17E6 is revealed by the crystal structure of αVβ3 ectodomain-17E6 Fab complex. J. Biol. Chem. *289*, 13801–13809.

Marcandalli, J., Fiala, B., Ols, S., Perotti, M., de van der Schueren, W., Snijder, J., Hodge, E., Benhaim, M., Ravichandran, R., Carter, L., et al. (2019). Induction of Potent Neutralizing Antibody Responses by a Designed Protein Nanoparticle Vaccine for Respiratory Syncytial Virus. Cell *176*, 1420-1431.e17.

Marques-Carvalho, M.J., Sahoo, N., Muskett, F.W., Vieira-Pires, R.S., Gabant, G., Cadene, M., Schönherr, R., and Morais-Cabral, J.H. (2012). Structural, biochemical, and functional characterization of the cyclic nucleotide binding homology domain from the mouse EAG1 potassium channel. J. Mol. Biol. *423*, 34–46.

Martinac, B., Saimi, Y., and Kung, C. (2008). Ion channels in microbes. Physiol. Rev. *88*, 1449–1490.

Matthias, M.A., Ricaldi, J.N., Cespedes, M., Diaz, M.M., Galloway, R.L., Saito, M., Steigerwalt, A.G., Patra, K.P., Ore, C.V., Gotuzzo, E., et al. (2008). Human leptospirosis caused by a new, antigenically unique Leptospira associated with a Rattus species reservoir in the Peruvian Amazon. PLoS Negl. Trop. Dis. *2*, e213.

McCoy, A.J., Grosse-Kunstleve, R.W., Adams, P.D., Winn, M.D., Storoni, L.C., and Read, R.J. (2007). Phaser crystallographic software. J. Appl. Crystallogr. *40*, 658–674.

McGuire, A.T., Hoot, S., Dreyer, A.M., Lippy, A., Stuart, A., Cohen, K.W., Jardine, J., Menis, S., Scheid, J.F., West, A.P., et al. (2013). Engineering HIV envelope protein to activate germline B cell receptors of broadly neutralizing anti-CD4 binding site antibodies. J. Exp. Med. *210*, 655–663.

McGuire, A.T., Dreyer, A.M., Carbonetti, S., Lippy, A., Glenn, J., Scheid, J.F., Mouquet, H., and Stamatatos, L. (2014). HIV antibodies. Antigen modification regulates competition of broad and narrow neutralizing HIV antibodies. Science *346*, 1380–1383.

McGuire, A.T., Gray, M.D., Dosenovic, P., Gitlin, A.D., Freund, N.T., Petersen, J., Correnti, C., Johnsen, W., Kegel, R., Stuart, A.B., et al. (2016). Specifically modified Env immunogens activate antibodies in transgenic mice. Nat. Commun. *7*, 1–10.

Medina-Ramirez, M., Garces, F., Escolano, A., Skog, P., Del Moral-Sanchez, I., Dosenovic, P., Hua, Y., McGuire, A.T., Gitlin, A.D., Freund, N.T., et al. (2017). Design and crystal structure of a native-like HIV-1 envelope trimer that engages multiple broadly neutralizing antibody precursors in vivo. J. Exp. Med. *214*, 2573–2590.

Medina-Ramírez, M., Garces, F., Escolano, A., Skog, P., de Taeye, S.W., Del Moral-Sanchez, I., McGuire, A.T., Yasmeen, A., Behrens, A.-J., Ozorowski, G., et al. (2017). Design and crystal structure of a native-like HIV-1 envelope trimer that engages multiple broadly neutralizing antibody precursors in vivo. J. Exp. Med. *214*, 2573–2590.

Milanesi, R., Baruscotti, M., Gnecchi-Ruscone, T., and DiFrancesco, D. (2006). Familial sinus bradycardia associated with a mutation in the cardiac pacemaker channel. N. Engl. J. Med. *354*, 151–157.

Millard, M., Odde, S., and Neamati, N. (2011). Integrin targeted therapeutics. Theranostics *1*, 154–188.

Mindell, J.A., and Grigorieff, N. (2003). Accurate determination of local defocus and specimen tilt in electron microscopy. J. Struct. Biol. *142*, 334–347.

Mosesson, M.W. (2005). Fibrinogen and fibrin structure and functions. J. Thromb. Haemost. *3*, 1894–1904.

Nakamura, T., and Gold, G.H. (1987). A cyclic nucleotide-gated conductance in olfactory receptor cilia. Nature *325*, 442–444.

Ng, L.C.T., Putrenko, I., Baronas, V., Van Petegem, F., and Accili, E.A. (2016). Cyclic Purine and Pyrimidine Nucleotides Bind to the HCN2 Ion Channel and Variably Promote C-Terminal Domain Interactions and Opening. Structure *24*, 1629–1642.

Otwinowski, Z., and Minor, W. (1997). Processing of X-ray diffraction data collected in oscillation mode. Methods Enzymol. *276*, 307–326.

Ozorowski, G., Pallesen, J., de Val, N., Lyumkis, D., Cottrell, C.A., Torres, J.L., Copps, J., Stanfield, R.L., Cupo, A., Pugach, P., et al. (2017). Open and closed structures reveal allostery and pliability in the HIV-1 envelope spike. Nature *547*, 360–363.

Pancera, M., Zhou, T., Druz, A., Georgiev, I.S., Soto, C., Gorman, J., Huang, J., Acharya, P., Chuang, G.-Y., Ofek, G., et al. (2014). Structure and immune recognition of trimeric pre-fusion HIV-1 Env. Nature *514*, 455–461.

Patel, P., Hanson, D.L., Sullivan, P.S., Novak, R.M., and Moorman, A.C. (2003). Annals of Internal Medicine Incidence of Types of Cancer among HIV-Infected Persons Compared with the General Population in the United States , 1992 – 2003. Ann. Intern. Med. *148*, 728–744.

Pettersen, E.F., Goddard, T.D., Huang, C.C., Couch, G.S., Greenblatt, D.M., Meng, E.C., and Ferrin, T.E. (2004). UCSF Chimera--a visualization system for exploratory research and analysis. J. Comput. Chem. *25*, 1605–1612.

Posey, J.A., Khazaeli, M.B., DelGrosso, A., Saleh, M.N., Lin, C.Y., Huse, W., and LoBuglio, A.F. (2001). A pilot trial of Vitaxin, a humanized anti-vitronectin receptor (anti alpha v beta 3) antibody in patients with metastatic cancer. Cancer Biother. Radiopharm. *16*, 125–132.

Pritchard, L.K., Vasiljevic, S., Ozorowski, G., Seabright, G.E., Cupo, A., Ringe, R., Kim, H.J., Sanders, R.W., Doores, K.J., Burton, D.R., et al. (2015). Structural Constraints Determine the Glycosylation of HIV-1 Envelope Trimers. Cell Rep. *11*, 1604–1613.

Rader, C., Cheresh, D.A., and Barbas, C.F. (1998). A phage display approach for rapid antibody

humanization: designed combinatorial V gene libraries. Proc. Natl. Acad. Sci. U. S. A. *95*, 8910–8915.

Radermacher, M. (1988). Three-dimensional reconstruction of single particles from random and nonrandom tilt series. J. Electron Microsc. Tech. *9*, 359–394.

Roseman, A.M. (2004). FindEM — a fast , efficient program for automatic selection of particles from electron micrographs. *145*, 91–99.

Sanders, R.W., Vesanen, M., Schuelke, N., Schiffner, L., Kalyanaraman, R., Berkhout, B., Maddon, P.J., Olson, W.C., Lu, M., Moore, J.P., et al. (2002). Stabilization of the Soluble , Cleaved , Trimeric Form of the Envelope Glycoprotein Complex of Human Immunodeficiency Virus Stabilization of the Soluble , Cleaved , Trimeric Form of the Envelope Glycoprotein Complex of Human Immunodeficiency Virus Type 1. J. Virol. *76*, 8875–8889.

Saponaro, A., Pauleta, S.R., Cantini, F., Matzapetakis, M., Hammann, C., Donadoni, C., Hu, L., Thiel, G., Banci, L., Santoro, B., et al. (2014). Structural basis for the mutual antagonism of cAMP and TRIP8b in regulating HCN channel function. Proc. Natl. Acad. Sci. U. S. A. *111*, 14577–14582.

Sather, D.N., Carbonetti, S., Malherbe, D.C., Pissani, F., Stuart, A.B., Hessell, A.J., Gray, M.D., Mikell, I., Kalams, S.A., Haigwood, N.L., et al. (2014). Emergence of broadly neutralizing antibodies and viral coevolution in two subjects during the early stages of infection with human immunodeficiency virus type 1. J. Virol. *88*, 12968–12981.

Scharf, L., West, A.P., Sievers, S.A., Chen, C., Jiang, S., Gao, H., Gray, M.D., McGuire, A.T., Scheid, J.F., Nussenzweig, M.C., et al. (2016). Structural basis for germline antibody recognition of HIV-1 immunogens. Elife *5*, 1–24.

Scheid, J.F., Mouquet, H., Ueberheide, B., Diskin, R., Klein, F., Oliveira, T.Y.K., Pietzsch, J., Fenyo, D., Abadir, A., Velinzon, K., et al. (2011). Sequence and structural convergence of broad and potent HIV antibodies that mimic CD4 binding. Science *333*, 1633–1637.

Scheres, S.H.W. (2012a). RELION: implementation of a Bayesian approach to cryo-EM structure determination. J. Struct. Biol. *180*, 519–530.

Scheres, S.H.W. (2012b). A Bayesian view on cryo-EM structure determination. J. Mol. Biol. *415*, 406–418.

Scheres, S.H.W. (2012c). RELION : Implementation of a Bayesian approach to cryo-EM structure determination. J. Struct. Biol. *180*, 519–530.

Scheres, S.H.W. (2012d). A Bayesian View on Cryo-EM Structure Determination. J. Mol. Biol. *415*, 406–418.

Scheres, S.H.W., and Chen, S. (2012). Prevention of overfitting in cryo-EM structure determination. Nat. Methods *9*, 853–854.

Shaikh, T.R., Gao, H., Baxter, W.T., Asturias, F.J., Boisset, N., Leith, A., and Frank, J. (2008). SPIDER image processing for single-particle reconstruction of biological macromolecules from electron micrographs. Nat. Protoc. *3*, 1941–1974.

Shimaoka, M., and Springer, T.A. (2003). Therapeutic antagonists and conformational regulation of integrin function. Nat. Rev. Drug Discov. *2*, 703–716.

Shin, K.S., Maertens, C., Proenza, C., Rothberg, B.S., and Yellen, G. (2004). Inactivation in HCN channels results from reclosure of the activation gate: desensitization to voltage. Neuron *41*, 737–744.

Sidhu, S.S., and Kossiakoff, A.A. (2007). Exploring and designing protein function with restricted diversity. Curr. Opin. Chem. Biol. *11*, 347–354.

Sievers, F., and Higgins, D.G. (2014). Clustal Omega, accurate alignment of very large numbers of sequences. Methods Mol. Biol. *1079*, 105–116.

Sliepen, K., Ozorowski, G., Burger, J.A., van Montfort, T., Stunnenberg, M., LaBranche, C., Montefiori, D.C., Moore, J.P., Ward, A.B., and Sanders, R.W. (2015). Presenting native-like HIV-1 envelope trimers on ferritin nanoparticles improves their immunogenicity. Retrovirology *12*, 82.

Smart, O.S., Goodfellow, J.M., and Wallace, B.A. (1993). The pore dimensions of gramicidin A.

Biophys. J. *65*, 2455–2460.

Söding, J., Biegert, A., and Lupas, A.N. (2005). The HHpred interactive server for protein homology detection and structure prediction. Nucleic Acids Res. *33*, W244-8.

Song, Y., DiMaio, F., Wang, R.Y.-R., Kim, D., Miles, C., Brunette, T., Thompson, J., and Baker, D. (2013). High-resolution comparative modeling with RosettaCM. Structure *21*, 1735–1742.

Stagg, S.M., Lander, G.C., Pulokas, J., Fellmann, D., Cheng, A., Quispe, J.D., Mallick, S.P., Avila, R.M., Carragher, B., and Potter, C.S. (2006). Automated cryoEM data acquisition and analysis of 284742 particles of GroEL. *155*, 470–481.

Stamatatos, L., Pancera, M., and McGuire, A.T. (2017). Germline-targeting immunogens. Immunol. Rev. *275*, 203–216.

Stanfield, R.L., Zemla, A., Wilson, I.A., and Rupp, B. (2006). Antibody elbow angles are influenced by their light chain class. J. Mol. Biol. *357*, 1566–1574.

Stewart-Jones, G.B.E., Soto, C., Lemmin, T., Chuang, G.Y., Druz, A., Kong, R., Thomas, P. V., Wagh, K., Zhou, T., Behrens, A.J., et al. (2016). Trimeric HIV-1-Env Structures Define Glycan Shields from Clades A, B, and G. Cell *165*, 813–826.

Stewart, P.L., and Nemerow, G.R. (2007). Cell integrins: commonly used receptors for diverse viral pathogens. Trends Microbiol. *15*, 500–507.

Struwe, W.B., Chertova, E., Allen, J.D., Seabright, G.E., Watanabe, Y., Harvey, D.J., Medina-Ramirez, M., Roser, J.D., Smith, R., Westcott, D., et al. (2018). Site-Specific Glycosylation of Virion-Derived HIV-1 Env Is Mimicked by a Soluble Trimeric Immunogen. Cell Rep. *24*, 1958-1966.e5.

Su, Z., Brown, E.C., Wang, W., and MacKinnon, R. (2016). Novel cell-free high-throughput screening method for pharmacological tools targeting K+ channels. Proc. Natl. Acad. Sci. U. S. A. *113*, 5748–5753.

Suloway, C., Pulokas, J., Fellmann, D., Cheng, A., Guerra, F., Quispe, J., Stagg, S., Potter, C.S.,

and Carragher, B. (2005). Automated molecular microscopy: The new Leginon system. J. Struct. Biol. *151*, 41–60.

Takagi, J., Petre, B.M., Walz, T., and Springer, T.A. (2002). Global conformational rearrangements in integrin extracellular domains in outside-in and inside-out signaling. Cell *110*, 599–11.

Tang, G., Peng, L., Baldwin, P.R., Mann, D.S., Jiang, W., Rees, I., and Ludtke, S.J. (2007). EMAN2: an extensible image processing suite for electron microscopy. J. Struct. Biol. *157*, 38–46.

Taraska, J.W., Puljung, M.C., Olivier, N.B., Flynn, G.E., and Zagotta, W.N. (2009). Mapping the structure and conformational movements of proteins with transition metal ion FRET. Nat. Methods *6*, 532–537.

Tian, M., Cheng, C., Chen, X., Haynes, B.F., Mascola, J.R., Alt, F.W., Tian, M., Cheng, C., Chen, X., Duan, H., et al. (2016). Induction of HIV Neutralizing Antibody Lineages in Mice with Diverse Precursor Repertoires. Cell *166*, 1471-1484.e18.

Triantafilou, K., Triantafilou, M., Takada, Y., and Fernandez, N. (2000). Human parechovirus 1 utilizes integrins alphavbeta3 and alphavbeta1 as receptors. J. Virol. *74*, 5856–5862.

Trkola, A., Pomales, A.B., Yuan, H., Korber, B., Maddon, P.J., Allaway, G.P., Katinger, H., Barbas, C.F., Burton, D.R., and Ho, D.D. (1995). Cross-clade neutralization of primary isolates of human immunodeficiency virus type 1 by human monoclonal antibodies and tetrameric CD4-IgG. J. Virol. *69*, 6609–6617.

Umotoy, J., Bagaya, B.S., Joyce, C., Schiffner, T., Menis, S., Saye-Francisco, K.L., Biddle, T., Mohan, S., Vollbrecht, T., Kalyuzhniy, O., et al. (2019). Rapid and Focused Maturation of a VRC01-Class HIV Broadly Neutralizing Antibody Lineage Involves Both Binding and Accommodation of the N276-Glycan. Immunity *51*, 141-154.e6.

Veeravagu, A., Liu, Z., Niu, G., Chen, K., Jia, B., Cai, W., Jin, C., Hsu, A.R., Connolly, A.J., Tse, V., et al. (2008). Integrin alphavbeta3-targeted radioimmunotherapy of glioblastoma multiforme. Clin. Cancer Res. *14*, 7330–7339.

Veesler, D., Cupelli, K., Burger, M., Gräber, P., Stehle, T., and Johnson, J.E. (2014). Single-particle EM reveals plasticity of interactions between the adenovirus penton base and integrin αVβ3. Proc. Natl. Acad. Sci. U. S. A. *111*, 8815–8819.

Verkoczy, L., Alt, F.W., and Tian, M. (2017). Human Ig knockin mice to study the development and regulation of HIV-1 broadly neutralizing antibodies. Immunol. Rev. *275*, 89–107.

Voss, N.R., Yoshioka, C.K., Radermacher, M., Potter, C.S., and Carragher, B. (2009). DoG Picker and TiltPicker : Software tools to facilitate particle selection in single particle electron microscopy. J. Struct. Biol. *166*, 205–213.

Wainger, B.J., DeGennaro, M., Santoro, B., Siegelbaum, S.A., and Tibbs, G.R. (2001). Molecular mechanism of cAMP modulation of HCN pacemaker channels. Nature *411*, 805–810.

Walls, A.C., Xiong, X., Park, Y.-J., Tortorici, M.A., Snijder, J., Quispe, J., Cameroni, E., Gopal, R., Dai, M., Lanzavecchia, A., et al. (2019). Unexpected Receptor Functional Mimicry Elucidates Activation of Coronavirus Fusion. Cell *176*, 1026-1039.e15.

Wang, R.Y.-R., Song, Y., Barad, B.A., Cheng, Y., Fraser, J.S., and DiMaio, F. (2016). Automated structure refinement of macromolecular assemblies from cryo-EM maps using Rosetta. Elife *5*.

Watanabe, Y., Raghwani, J., Allen, J.D., Seabright, G.E., Li, S., Moser, F., Huiskonen, J.T., Strecker, T., Bowden, T.A., and Crispin, M. (2018). Structure of the Lassa virus glycan shield provides a model for immunological resistance. Proc. Natl. Acad. Sci. U. S. A. *115*, 7320–7325.

Wei, X., Decker, J.M., Wang, S., Hui, H., Kappes, J.C., Wu, X., Salazar-Gonzalez, J.F., Salazar, M.G., Kilby, J.M., Saag, M.S., et al. (2003). Antibody neutralization and escape by HIV-1. Nature *422*, 307–312.

Weitz, D., Ficek, N., Kremmer, E., Bauer, P.J., and Kaupp, U.B. (2002). Subunit stoichiometry of the CNG channel of rod photoreceptors. Neuron *36*, 881–889.

Whicher, J.R., and MacKinnon, R. (2016). Structure of the voltage-gated K^+ channel Eag1 reveals an alternative voltage sensing mechanism. Science *353*, 664–669.

Wright, A., and Morrison, S.L. (1994). Effect of altered CH2-associated carbohydrate structure on the functional properties and in vivo fate of chimeric mouse-human immunoglobulin G1. J Exp Med *180*, 1087–1096.

Wu, H., Beuerlein, G., Nie, Y., Smith, H., Lee, B.A., Hensler, M., Huse, W.D., and Watkins, J.D. (1998). Stepwise in vitro affinity maturation of Vitaxin, an alphav beta3-specific humanized mAb. Proc. Natl. Acad. Sci. U. S. A. *95*, 6037–6042.

Wu, S., Avila-Sakar, A., Kim, J., Booth, D.S., Greenberg, C.H., Rossi, A., Liao, M., Li, X., Alian, A., Griner, S.L., et al. (2012). Fabs enable single particle cryoEM studies of small proteins. Structure *20*, 582–592.

Wu, S., Armache, J.-P., and Cheng, Y. (2016). Single-particle cryo-EM data acquisition by using direct electron detection camera. Reprod. Syst. Sex. Disord. *65*, 35–41.

Wu, X., Zhou, T., Zhu, J., Zhang, B., Georgiev, I., Wang, C., Chen, X., Longo, N.S., Louder, M., McKee, K., et al. (2011). Focused evolution of HIV-1 neutralizing antibodies revealed by structures and deep sequencing. Science *333*, 1593–1602.

Wu, X., Zhang, Z., Schramm, C.A., Joyce, M.G., Do Kwon, Y., Zhou, T., Sheng, Z., Zhang, B., O'Dell, S., McKee, K., et al. (2015). Maturation and diversity of the VRC01-antibody lineage over 15 years of chronic HIV-1 infection. Cell *161*, 480–485.

Xiao, T., Takagi, J., Coller, B.S., Wang, J.-H., and Springer, T.A. (2004). Structural basis for allostery in integrins and binding to fibrinogen-mimetic therapeutics. Nature *432*, 59–67.

Xiong, J.-P., Stehle, T., Zhang, R., Joachimiak, A., Frech, M., Goodman, S.L., and Arnaout, M.A. (2002). Crystal structure of the extracellular segment of integrin alpha Vbeta3 in complex with an Arg-Gly-Asp ligand. Science *296*, 151–155.

Xiong, J.-P., Mahalingham, B., Alonso, J.L., Borrelli, L.A., Rui, X., Anand, S., Hyman, B.T., Rysiok, T., Müller-Pompalla, D., Goodman, S.L., et al. (2009). Crystal structure of the complete integrin alphaVbeta3 ectodomain plus an alpha/beta transmembrane fragment. J. Cell Biol. *186*, 589–600.

Xiong, J.P., Stehle, T., Diefenbach, B., Zhang, R., Dunker, R., Scott, D.L., Joachimiak, A., Goodman, S.L., and Arnaout, M.A. (2001). Crystal structure of the extracellular segment of integrin alpha Vbeta3. Science *294*, 339–345.

Xu, K., Acharya, P., Kong, R., Cheng, C., Chuang, G.-Y., Liu, K., Louder, M.K., O'Dell, S., Rawi, R., Sastry, M., et al. (2018). Epitope-based vaccine design yields fusion peptide-directed antibodies that neutralize diverse strains of HIV-1. Nat. Med. *24*, 1.

Xu, X., Vysotskaya, Z. V, Liu, Q., and Zhou, L. (2010). Structural basis for the cAMP-dependent gating in the human HCN4 channel. J. Biol. Chem. *285*, 37082–37091.

Yan, Y., Wang, X., Lou, P., Hu, Z., Qu, P., Li, D., Li, Q., Xu, Y., Niu, J., He, Y., et al. (2019). A nanoparticle-based HCV vaccine with enhanced potency. J. Infect. Dis.

Yang, H., Hu, M., Guo, J., Ou, X., Cai, T., and Liu, Z. (2016). Pore architecture of TRIC channels and insights into their gating mechanism. Nature *538*, 537–541.

Ye, F., Hu, G., Taylor, D., Ratnikov, B., Bobkov, A.A., McLean, M.A., Sligar, S.G., Taylor, K.A., and Ginsberg, M.H. (2010). Recreation of the terminal events in physiological integrin activation. J. Cell Biol. *188*, 157–173.

Yet, M.G., Shao, M.C., and Wold, F. (1988). Effects of the protein matrix on glycan processing in glycoproteins. FASEB J. *2*, 22–31.

Yi, F., Danko, T., Botelho, S.C., Patzke, C., Pak, C., Wernig, M., and Südhof, T.C. (2016). Autism-associated SHANK3 haploinsufficiency causes Ih channelopathy in human neurons. Science *352*, aaf2669.

Zagotta, W.N., Olivier, N.B., Black, K.D., Young, E.C., Olson, R., and Gouaux, E. (2003). Structural basis for modulation and agonist specificity of HCN pacemaker channels. Nature *425*, 200–205.

Zakeri, B., Fierer, J.O., Celik, E., Chittock, E.C., Schwarz-Linek, U., Moy, V.T., and Howarth, M. (2012). Peptide tag forming a rapid covalent bond to a protein, through engineering a bacterial adhesin. Proc. Natl. Acad. Sci. U. S. A. *109*, E690-7.

Zhang, K. (2016). Gctf : Real-time CTF determination and correction. J. Struct. Biol. *193*, 1–12.

Zheng, J., and Zagotta, W.N. (2004). Stoichiometry and assembly of olfactory cyclic nucleotide-gated channels. Neuron *42*, 411–421.

Zheng, J., Trudeau, M.C., and Zagotta, W.N. (2002). Rod cyclic nucleotide-gated channels have a stoichiometry of three CNGA1 subunits and one CNGB1 subunit. Neuron *36*, 891–896.

Zheng, S., Palovak, E., Armache, J., Verba, K.A., Cheng, Y., and Agard, D.A. (2017). MotionCor2 : anisotropic correction of beam-induced motion for improved cryo-electron microscopy. Nat. Publ. Gr. *14*, 331–332.

Zhong, H., Molday, L.L., Molday, R.S., and Yau, K.-W. (2002). The heteromeric cyclic nucleotide-gated channel adopts a 3A:1B stoichiometry. Nature *420*, 193–198.

Zhou, T., Hamer, D.H., Hendrickson, W.A., Sattentau, Q.J., and Kwong, P.D. (2005). Interfacial metal and antibody recognition. Proc. Natl. Acad. Sci. U. S. A. *102*, 14575–14580.

Zhou, T., Georgiev, I., Wu, X., Yang, Z.-Y., Dai, K., Finzi, A., Kwon, Y. Do, Scheid, J.F., Shi, W., Xu, L., et al. (2010). Structural basis for broad and potent neutralization of HIV-1 by antibody VRC01. Science *329*, 811–817.

Zhou, T., Zhu, J., Wu, X., Moquin, S., Zhang, B., Acharya, P., Georgiev, I.S., Altae-Tran, H.R., Chuang, G.-Y., Joyce, M.G., et al. (2013). Multidonor analysis reveals structural elements, genetic determinants, and maturation pathway for HIV-1 neutralization by VRC01-class antibodies. Immunity *39*, 245–258.

Zhou, T., Lynch, R.M., Chen, L., Acharya, P., Wu, X., Doria-Rose, N.A., Joyce, M.G., Lingwood, D., Soto, C., Bailer, R.T., et al. (2015). Structural repertoire of HIV-1-neutralizing antibodies targeting the CD4 supersite in 14 donors. Cell *161*, 1280–1292.

Zhou, T., Doria-Rose, N.A., Cheng, C., Stewart-Jones, G.B.E., Chuang, G.Y., Chambers, M., Druz, A., Geng, H., McKee, K., Kwon, Y. Do, et al. (2017). Quantification of the Impact of the HIV-1-Glycan Shield on Antibody Elicitation. Cell Rep. *19*, 719–732.

Zhu, J., Luo, B.-H., Xiao, T., Zhang, C., Nishida, N., and Springer, T.A. (2008). Structure of a complete integrin ectodomain in a physiologic resting state and activation and deactivation by applied forces. Mol. Cell *32*, 849–861.

Zivanov, J., Nakane, T., Forsberg, B.O., Kimanius, D., Hagen, W.J., Lindahl, E., and Scheres, S.H. (2018). New tools for automated high-resolution cryo-EM structure determination in RELION-3. Elife *7*.

VITA

PhD Graduate Student of Biochemistry at the University of Washington in Seattle studying Structural Biology and Molecular Biophysics. My experience includes cryo-electron microscopy, glycoproteomics, protein heterogeneity, and the biophysical and immunological characterization of antibody/antigen interactions. I utilize CryoEM to solve structures of bacterial, human, and viral membrane proteins both alone and in complex with therapeutic antibodies to better understand their modes-of-action. I frequently supplement structural observations with surface plasmon resonance, biolayer interferometry, and mass spectrometry to help guide research in the areas of vaccine design and protein therapeutic development.